

HZG Report 2018-1 | ISSN 2191-7833

A.B. Abibe

Friction-based Injection Clinching Joining (F-ICJ): a new joining method for hybrid lightweight structures

(Vom Promotionsausschuss der Technischen Universität Hamburg-Harburg im Jahr 2015 als Dissertation angenommene Arbeit)

HELMHOLTZ-ZENTRUM GEESTHACHT



HZG Report 2018-1

A.B. Abibe

Friction-based Injection Clinching Joining (F-ICJ): a new joining method for hybrid lightweight structures

(Vom Promotionsausschuss der Technischen Universität Hamburg-Harburg im Jahr 2015 als Dissertation angenommene Arbeit)

HELMHOLTZ-ZENTRUM GEESTHACHT

Die HZG Reporte werden kostenlos abgegeben.
HZG Reports are available free of charge.

Anforderungen/Requests:

Helmholtz-Zentrum Geesthacht
Zentrum für Material- und Küstenforschung GmbH
Bibliothek/Library
Max-Planck-Straße 1
21502 Geesthacht
Germany
Tel.: +49 4152 87-1690
Fax.: +49 4152 87-1717
E-Mail: bibliothek@hzg.de

Druck: HZG-Hausdruckerei

Als Manuskript vervielfältigt.
Für diesen Bericht behalten wir uns alle Rechte vor.

ISSN 2191-7833

Helmholtz-Zentrum Geesthacht
Zentrum für Material- und Küstenforschung GmbH
Max-Planck-Straße 1
21502 Geesthacht

www.hzg.de

Friction-based Injection Clinching Joining (F-ICJ): a new joining method for hybrid lightweight structures

(Vom Promotionsausschuss der Technischen Universität Hamburg-Harburg im Jahr 2015 als Dissertation angenommene Arbeit)

André Bastos Abibe

199 pages with 121 figures and 17 tables

Abstract

Designers of modern transportation structures use a multi-material design strategy to reduce weight and satisfy emissions policies. Joining these new structures constitutes an engineering challenge, essentially due to the physical and chemical differences of dissimilar materials. A traditional method of joining dissimilar structures is by staking. Staking of polymers consists of deforming a polymeric stud that passes through a hole in the joining partner, to firmly fasten them together. However, there is a lack of scientific information on the changes related to the process with materials joined by staking, and how these localized changes affect the global properties of a larger structure. The aim of this investigation is to gain a fundamental understanding and description of the scientific and technological aspects of a new staking technology, Friction-based Injection Clinching Joining (F-ICJ, European patent application 14182938.2). F-ICJ uses a metallic tool to generate frictional energy and apply axial force on the polymeric stud, deforming it into a stake. Specially designed cavities in the metal partner are used to accommodate the softened stake material, accomplishing strong flush joints in a rapid and effective way. This PhD work clarifies, for the first time, the joint formation mechanisms and the influence of the process-related microstructural changes on the local material properties and quasi-static mechanical behavior of joints produced by the new F-ICJ process. For this purpose, structural engineering materials relevant to industry, aluminum 6082-T6 and both unreinforced and carbon-fiber reinforced polyetherimide – PEI) were selected.

Joint formation mechanisms and material flow were explained by monitoring the process and its thermal history, along with microstructural analyses using reflected and transmitted-light optical microscopy. It has been shown that relative movement of the rotating tool and the stationary polymer creates by friction a shear layer of softened, flowing polymer around the tool. This shear layer comprises polymer in a thermomechanically affected microstructural zone (PTMAZ). Material flow in the shear layer is the main mechanism that dictates joint formation in the F-ICJ process.

Process-related changes in the polymer were evaluated using microstructural analyses, photoelasticity, microhardness testing, and thermal analyses. High axial forces can form a plastically-deformed zone (PDZ) with local compressive stresses, where the free volume from plastic yielding decreases its local strength. In the PTMAZ, heat and deformation effects decrease chain packing density, and local strength is reduced by fast cooling during stake consolidation. No evidence of extensive thermo-mechanical degradation of the material in the PTMAZ was detected by thermal analyses (DSC and TGA) for the optimized joints. The combined analytical approach indicates that the decrease in local strength in PTMAZ and PDZ results from less compact macromolecular structures, with more free volume than the as-received material.

The quasi-static mechanical behavior of F-ICJ joints was assessed by lap shear and cross tensile testing. Strain distribution (digital image correlation) and stress concentration (finite element method) were used to describe the failure behavior. Scanning electron micrographs of the fracture surfaces were used to identify the failure micromechanisms and the effects of microstructural features on mechanical behavior.

A fractional factorial design of experiments was selected to evaluate and understand the effects of the process parameters on heat development, microstructure, and global mechanical properties of single-spot joints. It was shown that heat development mainly depends on the setup parameters of the friction phase and to a lesser degree on the cooling regime during consolidation. Lap-shear strength is only slightly affected by heat input and process-related microstructural changes, but cross-tensile strength is sensitive to heat generation and the local changes in the stake head.

As part of an exploratory proof of concept of the new F-ICJ technology, statistical models were used to obtain an optimized joining condition. The mechanical performance of F-ICJ joints was found comparable to state-of-the-art staking, with a higher strength-to-weight ratio. The optimized joining condition was used in an exploratory scaling-up study to assemble multi-spot sheet and stiffener subcomponents. This preliminary investigation indicated solvable challenges for the industrial-scale use of F-ICJ. The subcomponents were submitted to quasi-static, four-point bending tests to assess the mechanical behavior of multi-spot structures joined by the F-ICJ process.

This PhD work successfully describes the development and fundamental characteristics of the new F-ICJ metal-polymer joining technology, by materials science-based understanding and optimization, from coupon to subcomponent. All in all, the scientific discussion and theories proposed contribute to extended knowledge of staking-based joining technologies.

Friction-based injection clinching joining (F-ICJ): eine neue Füge­technik für hybride Leichtbaustrukturen

Zusammenfassung

In Strukturbauteilen moderner Transportmittel wird Multimaterialdesign angewendet, um Gewicht zu reduzieren und Emissionsrichtlinien zu erfüllen. Das Fügen dieser neuen Strukturen ist eine technische Herausforderung, im Wesentlichen aufgrund von physikalischen und chemischen Unterschieden zwischen ungleichartigen Materialien. Eine der traditionellen Methoden zum Fügen artfremder Materialkombinationen ist das Niet­en (auf Englisch: staking). Nietverfahren basieren auf der Umformung eines Kunststoffstifts, der in einem Durchgangsloch eines Fügepartners platziert ist, um beide Teile formschlüssig zu fügen. Prozessbedingte Veränderungen von durch Nietverfahren gefügten Materialien, und der Einfluss dieser lokalen Veränderungen auf die globalen Eigenschaften einer größeren Struktur sind bis heute wissenschaftlich kaum untersucht. Diese Arbeit hat das grundlegende Verständnis und die Beschreibung der wissenschaftlichen und technologischen Aspekte eines neuen Nietverfahrens, des Friction-based Injection Clinching Joining (F-ICJ), europäische Patentanmeldung 14182938.2), zum Ziel. F-ICJ verwendet ein metallisches Werkzeug, um Reibungsenergie und Druck in den Kunststoffstift einzubringen, und ihn zu einem Niet zu verformen. Gezielt eingebrachte Aussparungen im Fügepartner nehmen dabei den erweichten Kunststoff auf, sodass stabile Versenk­niete schnell und effektiv realisiert werden können. Die vorliegende Doktorarbeit beschreibt zum ersten Mal die Füge­mechanismen und den Einfluss der prozessbedingten Gefügeänderungen auf lokale und quasi-statische mechanische Eigenschaften von mit dem neuen F-ICJ Prozess erstellten Verbindungen. Als Fügepartner wurden die branchenrelevanten strukturellen Werkstoffe Aluminium 6082-T6, sowie Polyetherimid - PEI mit und ohne Verstärkung durch Kohlefasern ausgewählt.

Fügemechanismen und Materialfluss wurden anhand von Prozessüberwachung und Temperaturverlauf analysiert, und im Zusammenhang mit Mikrostrukturanalyse mittels Auf- und Durchlichtmikroskopie diskutiert. Es wurde gezeigt, dass die Relativbewegung zwischen dem rotierenden Werkzeug und dem stationären Polymer eine Scherschicht aus erweichtem, fließendem Polymer um das Werkzeug erzeugt. Die Scherschicht wird als Polymer-thermomechanisch-beeinflusste Zone bezeichnet (PTMBZ). Der Materialfluss in der Scherschicht ist der wichtigste Fügemechanismus im F-ICJ Prozess. Prozessbedingte Veränderungen im Polymer wurden anhand von Mikrostrukturanalyse, Spannungsoptik, Mikrohärteprüfung und thermischer Analysen ausgewertet. Hohe axiale Kräfte können eine plastische-verformte Zone (PVZ) mit lokalen Druckspannungen erzeugen, in der freies Volumen durch plastische Verformung des Kunststoffs die lokale Festigkeit verringert. In der PTMBZ reduzieren Temperatur- und Verformungseffekte die Kettenpackungsdichte und damit die lokale Festigkeit, aufgrund der schnellen Abkühlung während der Nietkonsolidierung. Keine Anzeichen für umfangreichen thermomechanischen Abbau des Materials in der PTMBZ wurden durch Thermische Analyse (DSC und TGA) für die optimierten Verbindungen detektiert. Der kombinierte analytische Ansatz zeigt, dass die Reduktion der lokalen Festigkeit in PTMBZ und PVZ eine Folge von, im Vergleich zum unbeeinflussten Material, weniger kompakten makromolekularen Strukturen mit mehr freiem Volumen ist.

Quasi-statisches mechanisches Verhalten von F-ICJ Verbindungen wurde durch Scherzug- und Kopfzugversuche untersucht. Dehnungsverteilung (digitale Bildkorrelation) und Spannungskonzentration (Finite Elemente Methode) wurden ausgewertet, um den Versagensablauf zu beschreiben. REM-Aufnahmen der Bruchflächen wurden verwendet, um Versagensmechanismen und den Einfluss der Mikrostruktur auf das mechanische Verhalten zu identifizieren. Ein Teilfaktorplan wurde durchgeführt, um die Auswirkungen der Prozessparameter auf Wärmeentwicklung, Mikrostruktur und globale mechanische Eigenschaften von Single-Spot-Proben zu bewerten und zu verstehen. Die Wärmeentwicklung wird hauptsächlich von den Einstellparametern der Reibungsphase bestimmt, und wird nur in geringerem Maße durch die Konsolidierungsphase beeinflusst. Die Scherzugfestigkeit ist weitestgehend konstant, während die Kopfzugfestigkeit empfindlicher auf Wärmeeinbringung und lokale Gefügeänderungen im Nietkopf reagiert.

Im Rahmen eines explorativen „Proof of Concept“ der neuen F-ICJ-Technologie wurden statistische Modelle verwendet, um optimierte Fügebedingungen zu erhalten. Die Festigkeit der F-ICJ Verbindung war vergleichbar mit dem Stand der Technik anderer Nietverfahren und zeigt bessere spezifische Werte in Relation zum Gewicht. Der optimierte Prozess wurde in einer explorativen Skalierungsstudie verwendet, um Multi-Spot Teilkomponenten zu fertigen. In dieser vorläufigen Untersuchung lösbare Herausforderungen für die industrielle Verwendung von F-ICJ wurden identifiziert. Die Multi-Spot Teilkomponenten wurden mittels quasi-statischer Vierpunkt-Biegung geprüft, um das mechanische Verhalten von durch den F-ICJ Prozess verbundenen Strukturen zu bewerten.

Diese Doktorarbeit hat erfolgreich die Entwicklung und die grundlegenden Eigenschaften der neuen F-ICJ Metal-Polymer-Verbindungstechnik beschrieben, durch materialwissenschaftlich basiertes Verständnis und Optimierung, von Kleinproben bis zum Fügen von Mehrelementteilkomponenten. Die wissenschaftliche Diskussion und die vorgeschlagenen Theorien haben dazu beigetragen, das Wissen um auf Nietverfahren basierende Fügeprozesse signifikant zu erweitern.

List of abbreviations

ANOVA	Analysis of variance
BM	Base material
BPB	Base plate bending failure
-CF	Carbon-fiber reinforced
CFRP	Carbon-fiber reinforced plastic
CP-TLOM	Transmitted-light optical microscopy with crossed polarizers
CoF	Consolidation force
CoT	Consolidation time
CT	Cross tensile
DIC	Digital image correlation
DMA	Dynamic mechanical analysis
DSC	Differential scanning calorimetry
EDS	Energy dispersive X-ray spectroscopy
E-ICJ	Electrical-heating Injection Clinching Joining
F-ICJ	Friction-based Injection Clinching Joining
FEM	Finite element method
FF-DoE	Fractional factorial design of experiments
FF	Frictional force
FP	Frictional pressure
FT	Frictional time
FoF	Forging force
FoP	Forging pressure
FoT	Forging time
FRP	Fiber reinforced plastic
FSpJ	Friction Spot Joining

FSSW	Friction Stir Spot Welding
FSW	Friction Stir Welding
-GF	Glass-fiber reinforced
GMT	Glass-mat-reinforced thermoplastic
GP	Guinier-Preston zones
GPC	Gel permeation chromatography
HPo	Head pull-out failure
HT	Heating time
HV	Vickers microhardness
IB	Incomplete bending
ICJ	Injection Clinching Joining
IR	Infrared
LS	Lap shear
LSCM	Laser scanning confocal microscopy
MA	Microstructural analysis
MHAZ	Metal heat-affected zone
MTMAZ	Metal thermomechanically-affected zone
μ CT	Computed microtomography
OEM	Original equipment manufacturer
OFAT	One-factor-at-a-time experiment
PCB	Printed circuit boards
PDZ	Plastically deformed zone
PA	Polyamide
PA66	Polyamide 66
PEI	Polyetherimide
PEEK	Polyether ether ketone
PHAZ	Polymer heat-affected zone

PP	Polypropylene
PTFE	Polytetrafluoroethylene
PTMAZ	Polymer thermomechanically-affected zone
RLOM	Reflected-light optical microscopy
RNA gantry	Automated joining system “Reibnietanlage”
RS	Rotational speed
RSM400	Lab-scale joining system
SB	Secondary bending failure
SEM	Scanning electron microscopy
SE-SEM	Scanning electron microscopy, secondary electrons signal
S	Standard error of the regression
SPo	Stake pull-out failure
SR- μ CT	Synchrotron radiation computed microtomography
SSS	Stake-shaft shearing
ST	Stake temperature
STZ	Strengthened transition zone
T _c	Crystallization temperature
T _g	Glass transition temperature
T _m	Crystalline melting temperature
Tr	Tube renewal time
TGA	Thermogravimetric analysis
TLOM	Transmitted-light optical microscopy
UCTF	Ultimate cross tensile force
ULSF	Ultimate lap shear force

List of symbols

A_{CS}	Cross-sectional area of the stake
A_{PTMAZ}	Cross-sectional area of the PTMAZ
A_{pore}	Cross-sectional area of the pores
C_{opt}	Stress-optical coefficient
E	Elastic modulus
E_r	Reduced elastic modulus
E_{work}	Energy input from mechanical work
\dot{E}	Rate of energy input
\dot{E}_{work}	Rate of mechanical work generation
\dot{E}_f	Rate of mechanical work generation from friction
\dot{E}_d	Rate of mechanical work generation from deformation
F	Force
FF	Axial force during the friction phase
F_f	Frictional force
F_N	Normal force
FT	Frictional time
h	Thickness of the molten layer
h_r	Residual indentation depth
h_{max}	Maximum indentation depth
H_T	True hardness
HV_{PTMAZ}	Hardness at the PTMAZ
k	Exponential decay constant
M	Torque/Bending moment
M_{total}	Total torque

$(n_1 - n_2)$	Birefringence
p	Contact pressure
p_0	Maximum contact pressure
p_c	Contact pressure at the chamfer
p_N	Normal contact pressure
p_s	Contact pressure at the stake
r	Radius
RA_{pore}	Relative pore area
RA_{PTMAZ}	Relative PTMAZ area
\dot{Q}_S	Heat flow from interface friction (solid friction)
\dot{Q}_M	Heat flow from internal friction (shearing) in the molten layer
t	Time
t_0	Initial time
t_{am}	Time to achieve Tg for amorphous polymers
t_c	Time to achieve Tc for semicrystalline polymers
T_c	Crystallization temperature
Tg_{am}	Glass transition temperature of the amorphous polymers
Tg_{sc}	Glass transition temperature of the amorphous portion of semicrystalline polymers
T_{max}	Maximum temperature
t_{sc}	Time to achieve Tg for the amorphous portion of semicrystalline polymers
V	Relative velocity
V_p	Pile-up volume
y	Specimen thickness
β	Characteristic angle of the indenter
$\dot{\gamma}$	Shear rate
δ	Retardation of light

δ_{res}	Relative residual depth
Δx	Displacement
$\dot{\Delta T}$	Rate of temperature change
ε	Strain
$\varepsilon_{plastic}$	Residual plastic strain
ε_y	Strain in the Y direction
η	Viscosity
μ	Coefficient of friction
σ	Stress
$(\sigma_1 - \sigma_2)$	Difference in normal stresses
$+\sigma_F$	Representative tensile stress
σ_{max}	Maximum principal stress
σ_{res}	Residual stress
σ_y	Yielding stress
σ_{y-BM}	Yielding stress of the base material
σ_{y-PDZ}	Yielding stress of the PDZ
τ	Shear stress
τ_{am}	Relaxation time of amorphous polymers
τ_{sc}	Relaxation time for the amorphous portion of semicrystalline polymers
v	Deformation rate
ϕ_s	Heat flux density
ω	Angular velocity
$\bar{\omega}$	Average angular velocity

Table of Contents

CHAPTER 1 . INTRODUCTION.....	1
CHAPTER 2 . MOTIVATION AND OBJECTIVES.....	4
CHAPTER 3 . LITERATURE REVIEW.....	5
3.1 POLYMER-BASED MATERIALS AS METAL REPLACEMENT IN LIGHTWEIGHT STRUCTURES.....	5
3.2 OVERVIEW OF JOINING METHODS FOR HYBRID LIGHTWEIGHT STRUCTURES.....	6
3.2.1 Advanced welding-based methods.....	6
3.2.2 Advanced mechanical joining methods.....	7
3.3 STAKING.....	8
3.3.1 Hot air staking.....	11
3.3.2 Thermal staking.....	11
3.3.3 Infrared and laser staking.....	12
3.3.4 Ultrasonic staking.....	13
3.3.5 Recent advances in staking processes.....	13
Ultrasonic upsetting.....	13
Thermoclinching.....	14
Injection Clinching Joining (ICJ).....	15
Friction Staking (FricStaking).....	16
3.3.6 Design considerations for staked joints.....	17
3.4 PHYSICAL-CHEMICAL PHENOMENA IN FRICTION-BASED POLYMER JOINING TECHNIQUES.....	18
3.4.1 Heat generation in friction-based polymer joining of polymers.....	19
3.4.2 Effects of thermomechanical processing on polymers.....	22
3.5 MAIN CHARACTERISTICS AND PROPERTIES OF BASE MATERIALS USED IN THIS WORK.....	24
3.5.1 Polyetherimide.....	24
3.5.2 Aluminum alloy 6082-T6.....	26
CHAPTER 4 . THE NEW FRICTION-BASED INJECTION CLINCHING JOINING PROCESS.....	28
4.1 PRINCIPLES OF THE PROCESS.....	30
4.2 PROCESS PARAMETERS AND VARIABLES.....	33
4.3 ADVANTAGES AND LIMITATIONS OF F-ICJ.....	34
CHAPTER 5 . EXPERIMENTAL APPROACH.....	35
CHAPTER 6 . MATERIALS AND METHODS.....	37
6.1 MATERIALS.....	37
6.1.1 Aluminum alloy 6082-T6 (AA6082).....	37
6.1.2 Polyetherimide (PEI).....	38
6.1.3 Short carbon fiber reinforced PEI (PEI-CF).....	39
6.2 JOINING EQUIPMENT.....	40
6.2.1 Joining tool.....	40
6.2.2 Single-spot joining for lab-scale investigation.....	41
6.2.3 Multi-spot joining process for proof-of-concept scaling up.....	42
6.3 METHODS.....	43
6.3.1 Joining procedure.....	43

6.3.2	Monitoring of joining process temperature.....	44
6.3.3	Microstructural analysis.....	45
6.3.4	Synchrotron radiation X-ray computed microtomography (SR- μ CT).....	46
6.3.5	Qualitative analysis of residual stresses.....	46
6.3.6	Physical-chemical changes on the polymer partner.....	47
6.3.7	Local mechanical properties.....	48
6.3.8	Quasi-static global mechanical behavior	49
6.3.9	Joint formation mechanisms	49
6.3.10	Effect of process parameters on joint properties.....	50
6.3.11	Joint optimization.....	51
6.3.12	Process transferability.....	51
6.3.13	Exploratory scaling up of the process to multi-spot subcomponents	53
CHAPTER 7 . INVESTIGATION OF THE JOINT FORMATION MECHANISMS IN F-ICJ.....		55
7.1	GENERAL ASPECTS OF JOINT FORMATION IN F-ICJ.....	55
7.2	JOINT FORMATION USING A TWO-PHASE PROCESS CONFIGURATION (FRICTION AND CONSOLIDATION PHASES).....	56
7.2.1	FRICTION PHASE: STUD MELTDOWN.....	57
7.2.2	FRICTION PHASE: DWELL TIME	60
7.2.3	CONSOLIDATION PHASE.....	65
CHAPTER 8 . PROCESS-RELATED CHANGES IN THE MATERIALS JOINED BY F-ICJ.....		68
8.1	CHANGES IN THE METALLIC PARTNER.....	68
8.2	CHANGES IN THE POLYMERIC PARTNER.....	70
8.2.1	Plastically deformed zone (PDZ) and base material (BM)	71
8.2.2	Polymer thermomechanically-affected zone (PTMAZ).....	74
8.2.3	Physical-chemical changes in the microstructural zones of F-ICJ joints.....	75
8.3	INTERPRETATION OF THE LOCAL VISCOELASTIC PROPERTIES.....	77
8.4	TYPICAL DEFECTS IN F-ICJ JOINTS	80
8.4.1	Porosity in the shear layer.....	80
8.4.2	Remnant weld line.....	81
8.4.3	Stake-shaft shearing (SSS)	82
CHAPTER 9 . QUASI-STATIC MECHANICAL BEHAVIOR OF F-ICJ JOINTS.....		84
9.1	MECHANICAL BEHAVIOR IN LAP-SHEAR CONFIGURATION	84
9.2	MECHANICAL BEHAVIOR IN CROSS-TENSILE CONFIGURATION	94
CHAPTER 10 . PROCESS-MICROSTRUCTURE-PROPERTY RELATIONSHIPS IN F-ICJ JOINTS....		104
10.1	EFFECTS OF THERMAL DEVELOPMENT ON MICROSTRUCTURAL FEATURES	104
10.2	INFLUENCE OF THE JOINT'S MICROSTRUCTURAL FEATURES ON QUASI-STATIC MECHANICAL PERFORMANCE	108
10.3	STATISTICAL ANALYSIS OF THE EFFECT OF PROCESS PARAMETERS ON JOINT PROPERTIES.....	111
10.3.1	Effects of the factors on stake temperature (ST)	114
10.3.2	Effects of the factors on ultimate lap shear force (ULSF).....	116
10.3.3	Effects of the factors on ultimate cross-tensile force (UCTF)	118
CHAPTER 11 . PROOF OF CONCEPT		120
11.1	JOINT OPTIMIZATION	120

11.2	TRANSFERABILITY TO THE GANTRY SYSTEM	121
11.3	COMPARISON OF F-ICJ JOINTS TO THE STATE OF THE ART	125
11.4	PROCESS SCALING-UP	126
11.4.1	Quasi-static mechanical testing of the subcomponents	128
CHAPTER 12 . SUMMARY OF THE RESULTS.....		131
CHAPTER 13 . CONCLUSIONS		135
CHAPTER 14 . RECOMMENDATIONS FOR FUTURE WORK		137
REFERENCE LIST		138
APPENDIX A . F-ICJ PATENT APPLICATION		X
APPENDIX B . EQUIPMENT SPECIFICATIONS: RSM400 AND RNA GANTRY.....		XI
APPENDIX C . CLAMPING SYSTEM FOR SINGLE-SPOT F-ICJ SPECIMENS		XII
APPENDIX D . PRELIMINARY ANALYSIS FOR THE NUMBER OF STAKES AT THE MULTI-SPOT SPECIMENS		XIII
APPENDIX E . JOINT FORMATION USING A THREE-PHASE PROCESS CONFIGURATION (FRICTION, FORGING, AND CONSOLIDATION PHASES).....		XIV
APPENDIX F . COLORED BIREFRINGENCE MICROGRAPHS		XV
APPENDIX G . DETAILED THERMAL ANALYSIS CURVES		XVI
APPENDIX H . MECHANICAL PERFORMANCE OF JOINTS PRESENTING STAKE-SHAFT SHEARING		XVIII
APPENDIX I . MECHANICAL PERFORMANCE OF NON-JOINED F-ICJ SPECIMENS		XIX
APPENDIX J . EXPERIMENTAL RESULTS FROM THE SPECIMENS OF THE DESIGN OF EXPERIMENTS		XX
APPENDIX K . EFFECT OF HEAT INPUT ON WELD LINE FORMATION AND PTMAZ LOCAL STRENGTH.....		XXIII
APPENDIX L . VALIDITY OF MICROSTRUCTURAL OBSERVATIONS FOR MECHANICAL TESTING SPECIMENS		XXIV
APPENDIX M . REDUCED REGRESSION MODELS FROM THE FF-DOE AND MODEL VALIDATION TABLES		XXVI
APPENDIX N . MICROSTRUCTURE AND LOCAL MECHANICAL PROPERTIES OF OPTIMIZED JOINTS PRODUCED AT THE RSM400		XXIX
APPENDIX O . TORQUE AND ENERGY INPUT RESPONSES AT THE RSM400 AND RNA GANTRY		XXX
APPENDIX P . IMPROVED TOOL DESIGN FOR F-ICJ		XXXI

CHAPTER 1. INTRODUCTION

The European Commission published a white paper in 2011 stating the proposed strategy for achieving competitive and resource-efficient transport throughout the continent [1]. Reflecting the global trend of environmental policies, the proposal involves a regulatory framework for innovative transport, including regulations for greenhouse gases that aim at a reduction of 70 % of the 2008 emission levels by 2050. The already strict emissions legislation for the passenger vehicle industry and aviation are expected to be further imposed throughout the century.

Around the world, one of the main strategies in the transport industry to help achieve these targets is lightweight construction [2-5]. A lighter vehicle not only uses less fuel, but also compensates for the extra weight of the new emission-reduction technologies and safety measures used by manufacturers [6, 7]. It has been expressed recently that “lightweight construction is the main discipline” in the automotive sector [8, 9], while the aircraft industry has been exploring weight reduction for the latest-generation of aircraft [5]. Weight reduction is achieved through the ongoing replacement of traditional structural materials, such as common steels and cast iron, for high-strength steels, lightweight alloys, and fiber reinforced polymer composites [10].

The importance of weight reduction and the associated material selection has been reported in systematic academic studies. The life-cycle assessment of aluminum, magnesium, and fiber reinforced engineering plastics (FRP) lightweight strategies for compact cars was analyzed by Raugei *et al.* [11]. This study showed that the isolated potential of each of these strategies is limited in the long term. Duflou *et al.* [12] showed that in comparison to steel-based structures, FRPs can improve damping and impact energy absorption while reducing weight of the vehicle. Innovation in production and recyclability is of the highest importance for a wide application of engineering plastics in the automotive sector. Timmis *et al.* [13] conducted a similar study of the life-cycle assessment of large passenger aircraft that compared a best-case scenario for aluminum-intensive and FRP-intensive aircraft and concluded that weight reduction in aircraft is essential in the long term to decrease fuel consumption. Life-cycle assessment studies indicate in general that when considering lightweight structures as an emissions-reduction strategy, FRPs have great potential for long-term use, but currently are prohibitive in terms of costs and recyclability, especially in the case of carbon-fiber reinforced plastics (CFRP). However, significant research on recyclability [14] and cost reduction [15] of these materials to overcome these limitations is ongoing. Structures based solely on lightweight alloys are currently reliable and their mechanical behavior well-understood, but they present less potential for weight reduction; the observed trend for achieving weight reduction is a mixed material design [7, 10].

One of the main engineering challenges of multi-material lightweight design is the assembly method. Lightweight metals, high-strength steels, plastics, and polymer composites are used together, forming a structure with a wide range of physical and chemical properties. The traditional joining technologies of adhesive bonding, mechanical fastening, and welding usually do not satisfy the requirements of the industry for such material combinations. The long curing times of adhesives, weight penalty of fasteners, and the physical-chemical dissimilarity

between materials for welding are driving forces behind the development of new joining technologies specifically for multi-material structures [16].

Among the alternatives for such structures is staking, which is a traditional joining technology for dissimilar materials. Staking methods have been successfully applied for joining of non-structural dissimilar parts in the industry. However, there is insufficient technical and scientific information about the mechanical behavior of staked joints and process-related changes in the joined materials. New advanced staking methods have been introduced recently. One of these new staking technologies, “Injection Clinching Joining” (ICJ), was developed at the Helmholtz-Zentrum Geesthacht for hybrid joining of thermoplastics [17]. Initial investigations of ICJ showed improved mechanical performance, but relatively long joining cycles [18]. This PhD work assesses the fundamentals of a new friction-based variant of the ICJ process. This is achieved by the investigation of joint formation mechanisms, process and microstructure property relationships, quasi-static mechanical behavior, and exploratory proof-of-concept for multi-spot structures. A combination of commercially available materials was selected for this initial study, consisting of the lightweight aluminum alloy 6082-T6 and the engineering thermoplastic polyetherimide (PEI).

The original contribution of this work is the development and optimization of the new Friction-based Injection Clinching Joining process (F-ICJ), an advanced staking process. This new technology has been devised, patented, and developed in the course of this work by Abibe *et al.* (European patent application EP 14182938.2, 2014, Appendix A). Moreover, this work provides the first deep scientific investigation of phenomena occurring in materials joined by staking, and evaluates how these phenomena influence the global joint performance.

Following this introductory chapter, this thesis is divided into the following chapters:

Chapter 2 defines the motivation and objectives of the work, based on the knowledge gaps stated in the introduction.

Chapter 3 discusses the relevant literature on this subject: the trend of weight reduction through metal replacement; new advanced joining methods; innovations in staking-based technologies; heat development and physical-chemical changes in polymers subject to thermomechanical treatment (friction); and the relevant characteristics of the base materials used.

Chapter 4 introduces the new F-ICJ joining process that was developed within the scope of this work. Its basic principles, process parameters and variables are described, as well as an initial assessment of its advantages and limitations.

Chapter 5 comprises the experimental approach used in this study, focusing on the proposed objectives.

Chapter 6 describes the equipment, materials, specimen geometries, and characterization methods used to obtain and analyze the results.

The results and corresponding discussions are spread over five chapters:

Chapter 7 addresses understanding the mechanisms of joint formation in F-ICJ by the application of a joining-equipment stop-action procedure. With this procedure the individual

stages of joint formation can be investigated. Process and temperature monitoring were coupled to investigate the heat development throughout the stop-action stages. These observations are combined with microstructural analysis using optical microscopy (reflected and transmitted light) to understand the evolution of joint formation. Process-related physical-chemical changes in the materials are used to support the interpretation of these results.

Chapter 8 analyzes how the process affects the microstructure of the joining partners. The metallic partner, which suffers less significant microstructural change, was evaluated with optical microscopy. The more complex thermal and mechanical effects in the polymer were analyzed by combining techniques of microstructural analysis (microscopy), residual stresses (photoelasticity), and local properties (microhardness and thermal analyses). Finally, the formation mechanisms of joint defects and their possible influence on mechanical behavior are described.

Chapter 9 evaluates the quasi-static mechanical behavior of single-spot joints in lap-shear and cross-tensile configurations. An analytical interpretation of the stress state in each test is introduced and correlated with finite-element models. The mechanical behavior is analyzed by mechanical testing and the strain distribution in lap-shear configuration is evaluated by digital image correlation. The failure modes are evaluated with reflected-light optical microscopy and scanning electron microscopy, and are correlated to microstructural changes.

Chapter 10 deals with the relationships between joining process conditions, generated microstructure, and joint properties. Statistical modeling through design of experiments is used to define the relevance and effect of the process parameters on heat development and mechanical performance. A materials science and engineering approach is used to investigate these relationships, based on the observations from the previous chapters.

Chapter 11 presents an exploratory proof of concept of scaling up the F-ICJ process to a multi-spot structure. Validated statistical models are used to obtain an optimized high-strength joint. The transfer of the lab-scale process to a multi-spot capable system is performed. A first impression of the joining process and mechanical behavior from multi-spot systems is described.

The final remarks of this work are distributed across three chapters:

Chapter 12 summarizes the main results obtained in this work.

Chapter 13 describes the main contributions and conclusions of this PhD study for the further understanding of polymer-metal joining technologies.

Chapter 14 provides a list of recommendations of further work for scientific and technology advancement in this field.

CHAPTER 2. MOTIVATION AND OBJECTIVES

The need for solutions in the assembly of modern lightweight structures provides the main motivation for this PhD work.

Advanced staking technologies are a potential solution for the joining of dissimilar materials. However, an understanding of the changes in the materials joined by staking processes and how these localized changes affect the global properties of structures is lacking. This scientific background is necessary for a precise assessment of the relevance of these technologies for engineering structural applications. From the technological aspect, identifying and understanding the process on a larger scale is fundamental for its technical advancement.

Considering the previously stated gaps in knowledge about joining multi-material structures, this thesis describes a new staking-based technology called Friction-based Injection Clinching Joining (F-ICJ). For this purpose an industry-relevant case-study hybrid joint of polyetherimide (unreinforced and short carbon-fiber reinforced) and aluminum alloy 6082-T6 was chosen. This work has the following objectives:

- Describe the joint formation mechanisms in the new F-ICJ process and process-related changes in the joined materials;
- Establish and understand the relationships between the joining process, microstructure, and mechanical behavior of F-ICJ joints;
- Optimize the quasi-static mechanical performance of F-ICJ joints at the coupon level;
- Investigate scaling up of the F-ICJ process to a subcomponent structural assembly, and provide a first assessment of its feasibility for multi-spot structures.

CHAPTER 3. LITERATURE REVIEW

3.1 Polymer-based materials as metal replacement in lightweight structures

Exploring all the structural, environmental, and economical aspects, no single material or joining technology alone is applicable in a lightweight structure [19]. The concept of “the right material in the right place” is shared by many original equipment manufacturers (OEMs) [3, 4, 20]. Instead of relying on a few strong materials in a structure, several lightweight alloys and high-strength steels are combined with engineering plastics and polymer composites. Body stiffness is maximized by optimizing beam profiles and joints, using longitudinal and transverse beams, using multifunctional reinforcements, optimizing joint positioning, and applying tailored blanks, among other strategies [21]. This approach allows for improved structural integrity and reduced weight, with the joining processes exerting great importance on the mechanical behavior of the structure [19, 21]. The optimization of lightweight design must therefore consider the joining processes and their mechanical performance. To achieve this, several design steps are involved: identifying the load carrying properties of the joints, optimizing the joining process and joint design, and enhancing the assembly configuration (thickness, number of spots, pitch) [22].

Interest in thermoplastic polymers for structural and non-structural parts is increasing rapidly, due to the better processability and recyclability of these materials in relation to thermosets. Continuous fiber reinforced thermoplastics are preferably used as structural sheets or profiles, and these can be more easily joined by the available methods due to their geometrical simplicity. Metallic extruded profiles and stamped sheets can be replaced by these composites. Unreinforced engineering thermoplastics and isotropic composites (discontinuous fibers) are more frequently used with complex geometries and therefore are injection or compression molded. These materials are used in secondary body in white structures (reinforced engineering thermoplastics), and in car and airplane interiors (unreinforced engineering plastics or low-strength composites), replacing cast or machined aluminum parts.

Continuous fiber reinforced composites have strength-to-weight ratios even higher than some steels. Such outstanding properties show that their dominance for structural parts is currently only hindered by prohibitive costs and long cycles [23-25]. A current demand by the industry is for shortening of processing times for polymer composite parts, for example by developing alternative processing methods or by improving present ones [26]. Continuous fiber reinforced composites can be currently processed without the use of an autoclave, significantly shortening cycles and reducing costs [26], but the material properties are not on the same level as the traditional methods [27]. Discontinuous fiber reinforced plastics (FRP) are more flexible in terms of processing and cycle times, because they can produce simple geometries by sheet and bulk molding compounding, or more complex parts through compression and injection molding [28, 29]. Constant innovation in processing technologies and material development for discontinuous FRPs has resulted in these materials partially replacing metallic components. Lamborghini and Callaway have developed “forged composite”, a recycled carbon-fiber compression-molding process that is intended to substitute aluminum alloys [30]. This technology is widely used in the Lamborghini Sesto Elemento prototype car, and has been applied in a similar fashion to the C-column of the 2016 BMW 7 series [31]. Although it has

been used with epoxy resins, it can be easily applied with thermoplastic matrices. SABIC Innovative Plastics developed a new carbon-fiber reinforced polyetherimide (PEI-CF) that is stronger than aluminum alloy 7075-O and with a strength-to-weight ratio comparable to 7075-T6 [32]. In a case study, injection-molded tray arms for aircraft seats achieved a 46 % weight reduction and at least 75 % cost reduction. A new grade of carbon-fiber reinforced poly ether ether ketone (PEEK-CF) has replaced aluminum and titanium brackets in aircraft [33, 34] and aerospace fuel housings [35]. These examples confirm the trend of partial substitution of metals for engineering plastics, leading to a multi-material structure.

3.2 Overview of joining methods for hybrid lightweight structures

Hybrid metal-polymer structures are a relatively new concept, and specific methods for the assembly of such structures have only recently been explored. Joining of metal-polymer joints has been traditionally carried out using mechanical fastening and adhesive bonding [16]. Although these methods are well-established for similar joints, they are not usually directly applicable for joining dissimilar parts. Generally speaking, state-of-the-art mechanical fastening techniques introduce extra weight to the structure, while adhesive bonding often needs extensive surface treatment and curing times [16]. Moreover, the technical knowledge of both traditional methods is mainly based on the joining of metals. The limitations of mechanical fastening and adhesive bonding lead engineers and designers to find new ways of joining dissimilar structures. The new technologies are mostly aimed at thermoplastic reinforced plastics as a result of the increasing interest in these materials. Formability and re-melting of thermoplastics provide new possibilities for joining mechanisms compared to rigid thermosets. Although there are innovations such as hybrid riveting-bonding [36, 37] or fiber-metal laminates [38, 39] for bolted joints, and expanded knowledge of adhesion and adhesive joint design [40, 41] for adhesive joints, several alternative new methods are also being explored. These are here divided into advanced welding-based methods and advanced mechanical-joining methods.

3.2.1 Advanced welding-based methods

These technologies rely on welding-based energy supply techniques to create direct-adhesion joints between polymer and metal. A schematic illustration is shown in Figure 3-1. The metallic partner is placed on top and the workpieces are clamped together to ensure intimate contact. A heat source is used to warm, and in some cases deform, the metallic partner. Heat flows from the heated-up volume to the metal-polymer interface, softening or melting the top layers of the polymer workpiece. After cooling the resolidified polymer adheres to the metallic partner. In the case of friction-based processes, a non-consumable rotating tool not only heats but also deforms the joining partners [42, 43].

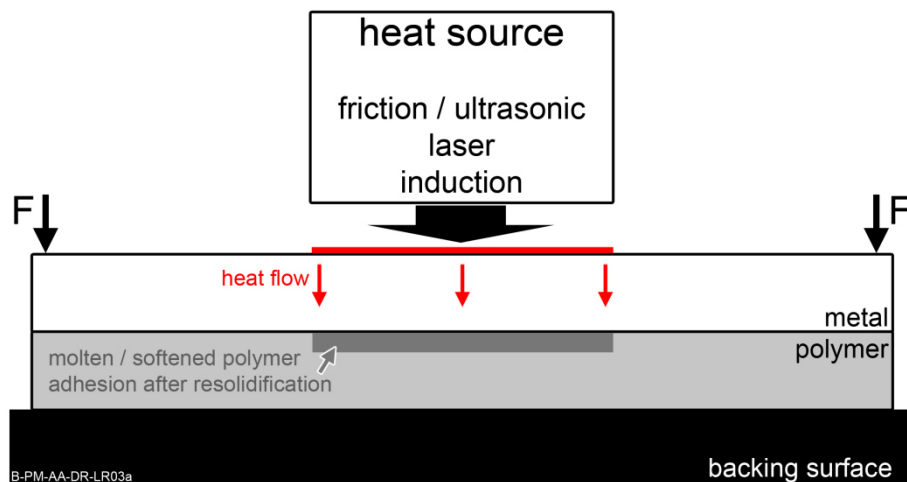


Figure 3-1: Basis of metal-polymer welding-based joining methods.

Great interest in these joining processes is evident from the investigations of several groups for spot joints. A large project carried out at TU Kaiserslautern investigated joint formation mechanisms, mechanical performance and the scale-up of induction [44-47] and ultrasonic [48-50] joining processes. Friction Stir Spot Welding (FSSW) creates metal-polymer joints by heating and deforming the metallic partner, which in turn melts the polymer and it flows outward from the joining area [51, 52]. Friction Spot Joining (FSpJ, [53]) is an alternative process that affects only thin layers of the polymer while also creating an undercut (nub) for mechanical anchoring on the metal. FSpJ has been demonstrated with unreinforced thermoplastics and nanocomposites by Junior *et al.* [54, 55]. Goushegir *et al.* [42] investigated the bonding mechanisms of FSpJ, showing that the combined effects of adhesion and mechanical interlocking are responsible for joint strength.

In some cases, the heat source is able to produce not only spot joints, but also linear ones. Laser-assisted joining has been explored for heating the metallic partner [56-58]. The process is also possible by heating the metal-polymer interface directly through a transparent polymer [57, 59]. Strong joints can be produced, achieving in some cases short-range chemical bonding at the interface [59]. Processes based on the friction stir welding (FSW) of metals have been successfully demonstrated for metal-polymer joints [43, 60-62]. Joints are achieved using a pin-less tool, which rubs the top surface of the metallic partner while translating, without large penetration. Bonding mechanisms similar to FSpJ are therefore present. Attempts to reproduce the stirring effect from FSW using a pin-and-shoulder tool show that this is a challenging approach [63, 64]. The stir zone presents a mixture of chipped metal particles and potentially degraded polymer, leading to decreased joint strength.

3.2.2 Advanced mechanical joining methods

In this category are technologies that differ from traditional mechanical fastening by shortening the joining cycles, increasing strength, or both. Auxiliary joining parts of fast assembly or improvements in the mechanical interlocking are strategies to achieve this.

The foremost example that does not use auxiliary parts is over-molding. Over-molding techniques have become popular in the automotive industry with the introduction of hybrid front-ends in the mid-90s [21, 65]. The original injection over-molding technology as presented by Zoellner and Evans [66] uses metal stampings with holes for mechanical interlocking of the injected polymer. Analyses from Grujicic *et al.* [65, 67] and Paul *et al.* [68] show that a combination of direct adhesion and mechanical interlocking effects seems to be more advantageous, improving the ultimate strength and energy absorption in mechanical loading.

Commercially available advanced mechanical fastening technologies are widely used, especially in the automotive segment [19]. Mechanical clinching [69, 70], self-pierce riveting [71-73], and Rivtac® [74] are cold-forming methods that have been shown suitable for some metal-polymer material combinations. Unlike traditional mechanical fastening, these methods do not require the pre-drilling of holes. More recently, thermal joining methods were demonstrated by Meschut *et al.* [75], based on resistance and friction welding. These technologies combine thermal and mechanical joining concepts. An auxiliary joining partner is thermally joined (by resistance or friction welding) to a substrate, entrapping another joining partner. Overlap joints can be improved by using hybrid joining with adhesives, suggesting that the mechanical fastening contribution is larger than the adhesive contribution [36]. Also combining thermal processes and mechanical fastening, friction riveting (FricRiveting [76, 77]) produces metallic-insert and overlap joints on polymer-based materials using frictional heating and axial pressure. Recent feasibility studies for amorphous, non-reinforced engineering thermoplastics by Amancio-Filho [78] and Rodrigues *et al.* [79] showed that strong point-on-plate joints can be achieved with aluminum rivets. Further development of the technology by Blaga *et al.* [80] and Altmeyer *et al.* [81] achieved joints with continuous and short fiber reinforced composites using commercially-pure titanium rivets, establishing geometrical parameters that influence joint strength. The process is also able to produce joints using thermoset substrates [82].

3.3 Staking

The previous sections described recent innovations in metal-polymer joining. The design flexibility and fast processing of discontinuous FRPs make it an attractive alternative to metallic parts in the transport industry. When processed by compression or injection molding, the freedom of design allows for a range of mechanical joining technologies, such as over-molding, press and snap fits, or staking [83]. However, a post-molding assembly is regarded as giving more freedom for design than in-mold assembly (over-molding) [84], and press or snap fits are too sensitive to creep and stress relaxation failure [83]. The suitability of a joining technology will depend on the structural requirements and part design. One of the most traditional and flexible methods of joining molded plastics to other materials is staking. It has been used since the 1950s, but only in the 1980s did it achieve quality levels adequate for large-scale industrial use [85].

The basic principles of staking are shown in Figure 3-2. A polymer workpiece with an integral stud is pre-assembled with another workpiece with a matching through-hole (Figure 3-2a). A forming tool approaches the polymeric stud, and uses axial force to deform it (Figure 3-2b).

After the tool retreats a staked joint is created (Figure 3-2c). The main advantages and limitations of state-of-the-art staking are described in Table 3-1.

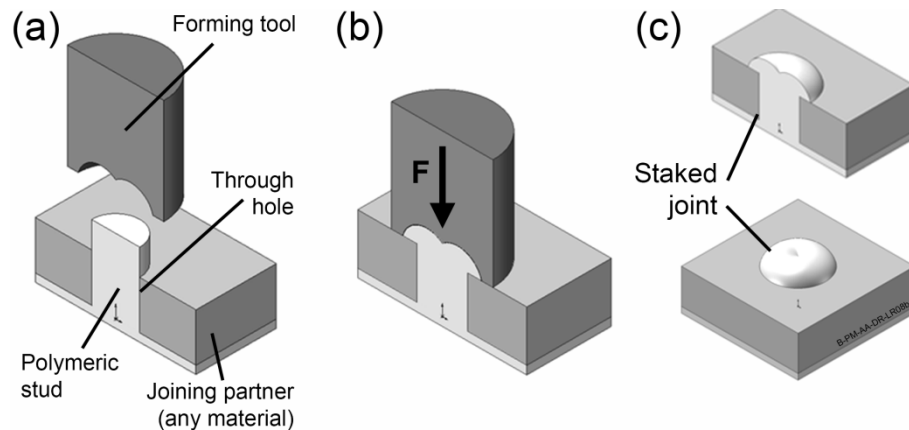


Figure 3-2: Principles of staking. (a) Pre-assembly; (b) forming; (c) staked joint. Adapted from [86].

Table 3-1: Advantages and limitations of state-of-the-art staking methods for dissimilar materials [83, 87].

Advantages	Limitations
Speed of assembly	Longer cycles for thermally-resistant polymers
Disassembly for recycling	Permanent joints
Low investment, simple tooling	Shape recovery from relaxation
No auxiliary elements, reducing weight	Surface finishing, due to large stake heads
Little or no surface preparation needed	Tool positioning/clearance can be difficult
Loose tolerances can be used	Two-sided accessibility required (usually)

Staking is a simple joining method, often used for dissimilar joints when at least one component is a thermoplastic polymer. It also is an alternative joining technique when incompatible polymers need to be joined. Parts need to be molded with studs throughout the desired joining spots, but this adds little to the final costs of molding tools. Staking is often used for the assembly of printed circuit boards (PCB), plastic housings and for trim and bodywork automotive panels [85]. The current design of industrial staking machines is able to join dozens of stakes per cycle, and in different planes and positions [88]. Automated staking uses electronic equipment to assure adequate alignment of tools and studs prior to joining, and for quality control afterwards.

There are two types of staking processes: cold staking and hot staking [83, 87]. Cold staking is carried out as described in Figure 3-2, with formation of the stud into a stake accomplished by the axial force of the forming tool. In cold staking the stud is below the relevant thermal transition's temperature range of the thermoplastic – T_g for amorphous polymers, and T_m for semicrystalline polymers. Joining is accomplished by plastic deformation, using forces above the yielding strength of the thermoplastic. This process variant is suitable only for ductile

polymers, because brittle polymers and composites will usually fail when cold formed. Additionally, long consolidation times are required to avoid recovery effects. Recovery corresponds to the stored elastic energy upon stress release and is a time-dependent effect [89]. The recovery phenomenon associated with cold forming can be accelerated by heat, making the use of cold-staked structures mostly unsuitable for elevated in-service temperatures. The plastic deformation from cold forming of the polymer also makes it more susceptible to crazing and chemical attack [83, 90]. These characteristics of cold staking make it unsuitable for high-end applications and so it is mostly used in simple assemblies.

Hot staking is a more relevant process variant technologically, which is widely applied in the automotive and electronics industry. Hot staking differs from the cold variant by forming the stud into a stake while it is softened, or melted, above its transition temperature. This allows the polymer to flow easily and therefore lower joining forces are necessary. Recovery is avoided since the polymer will solidify or consolidate to its final shape without the creation of significant residual stresses. The shrinking during cooling of the formed parts in hot staking tightens the joints further. Nevertheless, higher energy consumption is required and thermal degradation of the polymer may occur [85, 86]. It is also recommended to cool the system down before tool retreat, to avoid sticking of melted material to the tool surface.

Heating of the stud prior to joining can be achieved by various energy sources, such as hot air, hot tool, infrared radiation, laser beam, and friction. Examples of the industrial applications of staking in the automotive industry are on interior trims such as seat and door assemblies [91], exterior components such as bumpers and taillights [92], and structural parts such as front-end assemblies [93]. Some of these examples are illustrated in Figure 3-3.

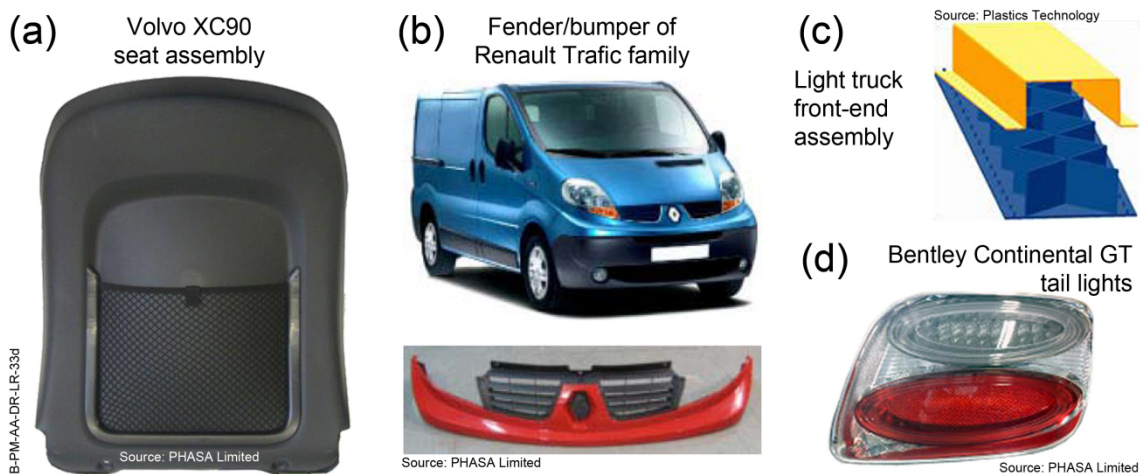


Figure 3-3: Examples of automotive staking applications: (a) Volvo XC90 seat assembly [91]; (b) fender/bumper of Renault Traffic minivan family [92]; (c) light truck front end assembly [93]; (d) Bentley Continental GT tail lights [92].

Although staking is widely applied in the industry, most information on the technology is obtained in the form of press releases and technical guidelines from machine suppliers [85, 94-96], or textbooks that compile the supplier's information [83, 97]. Few scientific works

describing material behavior and the process-microstructure-property correlations are available. The next sections briefly describe state-of-the-art staking methods and highlights of the results from publications, when available.

3.3.1 Hot air staking

These staking methods use a flow of hot gas towards the stud to melt/soften it. Uniform heating of the stud can be achieved, because it involves a constant temperature air flow. The process has low energy efficiency due to the low heat capacity of air. Therefore, short heating times require more energy at the heating source. Due to the high temperatures, especially at the stud surface, slight discoloration may occur [83, 85, 86].

The most common example is hot air cold staking (HACS) [83, 85, 98]. A jet of hot air at 150-400 °C is directed by nozzles at the stud, which is subsequently formed by a cold (or non-heated) tool. This is usually performed industrially in two phases: the part is positioned below the hot air nozzles and heated; it is subsequently moved below the forming tool and staked. The joining cycle ranges from 8 to 20 seconds.

Yeh *et al.* [98] joined polycarbonate (PC), blends of PC with copolymer acrylonitrile butadiene styrene (ABS), and polyoxymethylene (POM) studs to plates of ABS and talc-reinforced polypropylene (PP) using HACS. Pull-out strength and failure mode were correlated to the process parameters of heating time, stake height, and stake head shape. No microstructural analysis was performed, only temperature measurements and the mechanical tests. No correlation could be traced between process parameters, joint strength, and failure mode. The failure mode and strength could be correlated to material choice and stiffness relations between the stake's plate and the hole's plate.

Hahn and Finkeldey [99] produced what is probably the most complete work in state-of-the-art staking. Intended for the use of staking in automotive applications, the main staking methods were evaluated in a preliminary step and HACS was selected as the most promising for reinforced thermoplastics. A parameter study for glass-mat reinforced PP (GMT-PP) and injection-molded PP-GF was performed, evaluating joint strength, polymer degradation, and aging. This was followed by durability tests in fatigue and corrosion. The best joints were achieved with GMT-PP in a "long-stake" configuration. This condition was compared to other mechanical joining methods and adhesive bonding. Finally, a very brief section describes the assembly of a multi-stake structure in terms of joining forces. The work fulfills all process development and durability aspects, but does not use a materials science and engineering approach to understand joint behavior.

3.3.2 Thermal staking

Also known as heat staking or hot-die staking, in this process the stud is heated when in contact with the forming tool, which is electrically heated above the polymer's transition temperature. The stud therefore melts as it is formed into a stake. Cycles last from 6-10

seconds. This process is simple and well-suited for glass-reinforced polymers [94]. Its drawbacks are high energy consumption and, since the tool does not cool down between cycles, there is risk of degradation due to the elevated tool temperature [83].

3.3.3 Infrared and laser staking

Infrared staking is currently applied in the industry by the proprietary “Infrastake” technology (Extol Inc., USA [100]). The process uses the joining module displayed in Figure 3-4a, which has a concentrator on one end. The concentrator has a reflective inner wall, a forming tool and a technical-grade low-wattage infrared lamp. The stages of the Infrastake process are shown in Figure 3-4b. When the parts are clamped, the lamp is turned on. The inner walls are designed to reflect the light towards its opening, which is the position of the stud. The focused light rapidly heats the stud, and the tool forms the stud while a jet of compressed air cools the system, then the tool retracts [96, 101].

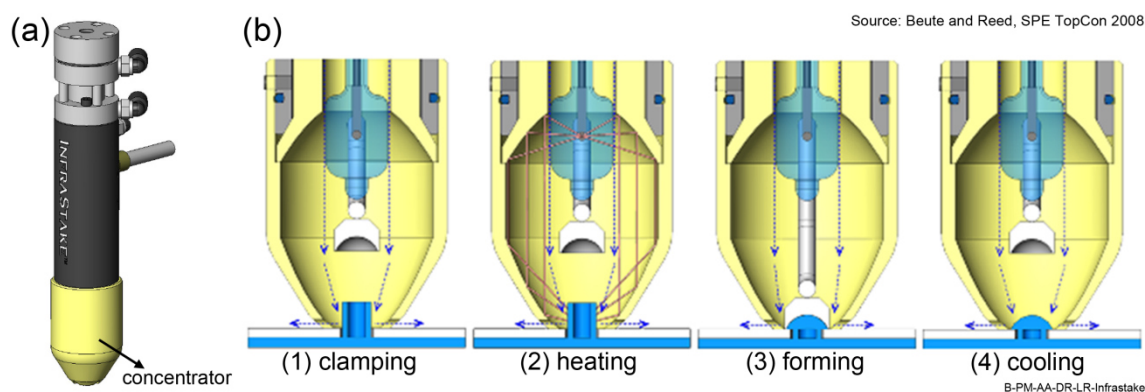


Figure 3-4: Infrastake: (a) joining module; (b) process phases. Blue arrows are compressed air, red arrows are infrared radiation. Adapted from [101], as permitted by Society of Plastics Engineers.

This process has low energy consumption, because only a single 35 W or 100 W lamp is used, and it requires low joining forces. The focused beam reduces the risk of damage to sensitive components such as PCB plaques. In a study by Beute [102], glass fiber reinforced polyamide (PA-GF) joints produced in 9-second cycles showed a decrease in strength with larger hole clearances, but performed better than concurrent ultrasonic staking joints. The author claimed that both semicrystalline and amorphous polymers can be joined, and the process is more efficient with dark, opaque polymers. Light-colored, translucent, or transparent polymers absorb the radiation less efficiently, requiring longer joining times. The process cycles can be optimized by adjusting the light intensity and the compressed air flow.

Laser heating can also be used for staking applications. It does have the advantages of a precisely focused beam and fast heating, but requires higher initial capital investment than infrared systems [103]. New developments in laser staking use through-transmission welding of a soft, transparent polymer to the top surface of the stud, so that the transparent part acts

as a stake head. The authors report that this strategy avoids the sticking of polymer to the tool surface and provides better process quality control [95].

3.3.4 Ultrasonic staking

In ultrasonic staking, a sonotrode (forming tool) attached to an ultrasonic vibration source is brought in contact with the stud, melting and forming it into a stake. Heating is achieved from interfacial friction between tool and stud, and internal molecular friction in the polymer. The process heats the stud rapidly and small stakes can be formed within cycles of one second. Tool feeding speed must match the stud meltdown rate in order not to crack or deform the stud. No significant heat build-up is present in the forming tool, so sequential joining without cooling between cycles is possible. Only a relatively thin layer is melted, therefore any recovery effects are claimed to be minimized or completely avoided [83]. The process is adequate for amorphous polymers, and fair-to-good for semicrystalline plastics, but it is not suitable for self-lubricating or plastics with a low coefficient of friction [83, 97, 104]. Ultrasonic staking is flexible and well-established in the industry, due to all its advantages. The process works well for closely positioned staking points, but it can be difficult to apply for multi-staked structures with more than four stakes far away from each other [94]. Also, for reinforced plastics accelerated tool wear is expected [86, 105].

Hahn and Finkeldey [105] compared ultrasonic and hot-air staked joints between DC04 steel and glass-fiber reinforced automotive plastics. Long glass-fiber reinforced plastics showed better mechanical resistance with hot-air staking, due to the glass fiber orientation that was induced. For short fibers, ultrasonic staking was better, likely because of the smaller heat-affected volume. The glass fibers caused premature wear of the sonotrodes with more wear observed with the long fiber reinforced composites.

3.3.5 Recent advances in staking processes

As previously mentioned, traditional staking methods are widely applied for dissimilar assemblies in automotive structures, but mostly limited to low-strength thermoplastics and blends. The challenges of advanced polymer-metal joining and the new processing possibilities for polymer composites create further interest in innovations for staking that suit these requirements. In this section some of the newest staking approaches are described.

Ultrasonic upsetting

Herrmann Ultraschall (Germany) has patented [106] and Brückner *et al.* have developed [107] a new ultrasonic-based staking method, named ultrasonic upsetting. In this process a tubular stud is used and the sonotrode concentrates the heat generation on approximately the middle of the stud's height. The sonotrode then presses on the top of the stud, causing a selective deformation only in the middle of the stud. This deformation zone clamps the joining partners

together. The steps of the process are illustrated in Figure 3-5. Tool contact with the joining partner is completely avoided, making the process suitable for joining sensitive components.

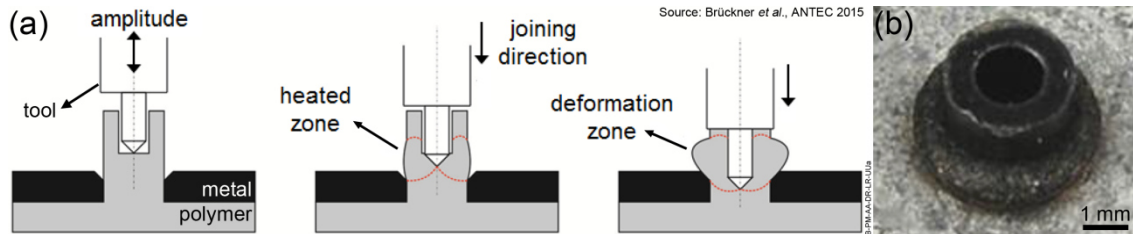


Figure 3-5: Ultrasonic upsetting: (a) process steps; (b) surface view of a joint. Adapted from [108], as permitted by Society of Plastics Engineers.

PA66-GF hollow-stake ultrasonic upsetting joints were demonstrated by Brückner *et al.* [108] to be stronger than hollow stakes produced with hot-air and thermal staking, and comparable to solid stakes from these processes. In the present state of the art, the process quality is mostly dependent on the design of the stud and the sonotrode. With an efficient design the process was successfully applied to reinforced and unreinforced thermoplastics and blends with satisfactory surface finishing in cycles of 1.5-3.0 seconds [109].

Thermoclinching

Gude *et al.* [110] developed a method of creating form-locked joints similar to stakes using continuous fiber reinforced composites. This “thermoclinching” process is based on metal clinching, and uses a tapered pin and a die to create the joint. The process is shown in Figure 3-6a. As an initial step, a notch is machined on the surface of the composite and the sheet is pre-heated to increase formability. Next, a tapered pin is pressed against the softened and notched sheet, which is pushed through the through-hole. The excess material on the opposite side is then pressed by a die, and cools down under pressure. After heating, the joint is created in 0.5 seconds and cooled for 35 seconds for consolidation. The heating time is not reported in the literature. An advantageous fiber orientation can be achieved, as showed in Figure 3-6b.

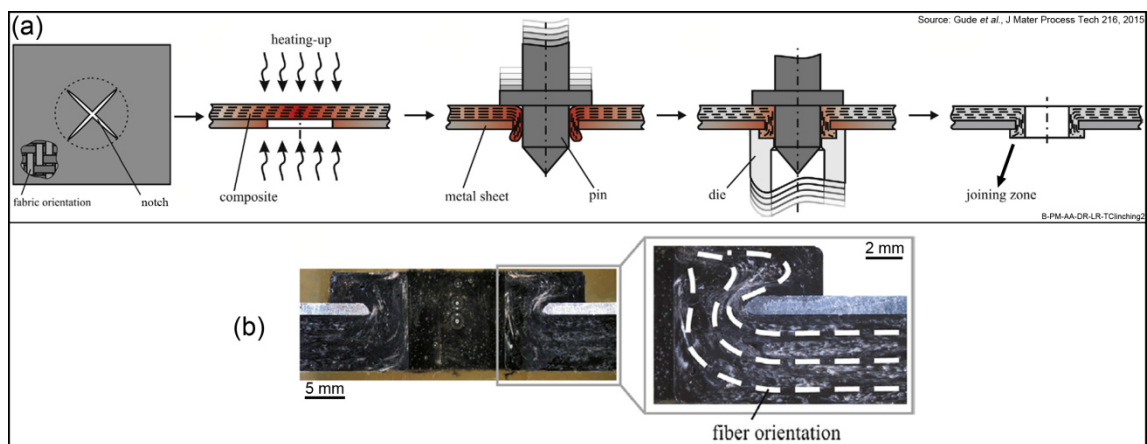


Figure 3-6: (a) Thermoclinching process steps; (b) cross section of a PP-GF joint and fiber orientation. Adapted from [110], with permission from Elsevier.

The heating temperature has a significant effect on surface finishing of these joints, and satisfactory joints can be achieved without signs of thermal degradation [111]. The die pressure also affects the formation of voids in the polymer. The final joint geometry dictates failure mode under lap shear loading, with thin walls leading to stake shear and shallow head leading to head pull-out failure [110].

Injection Clinching Joining (ICJ)

ICJ is a new concept for a staking method, patented by the Helmholtz-Zentrum Geesthacht [17] and developed by Abibe *et al.* [18]. In ICJ, instead of using the large protruding stake heads, as seen in most methods, a flush design is used, relying on cavities inside the through hole to improve mechanical performance. Heating of the stud prior to forming allows the polymer to flow radially when pressed, filling the cavities as in an injection molding process (Figure 3-7a). In a feasibility study using electrical heating as an energy source (E-ICJ), sound PA66-GF/AA2024 joints could be produced [18]. The process steps are shown in Figure 3-7b. A prototype machine was developed for this study, which consists of a hot case, heated by electricity, and a punch-piston coaxially assembled with the hot case. Heat transfer is performed by convection inside the hot case and conduction from the punch-piston. The joining partners are pre-assembled and aligned with the system. The hot case encloses the polymeric stud while clamping the polymer and metal plates and it is heated for a preset time. After conclusion of the preset heating phase the punch-piston applies axial pressure and deforms the stud, pushing the softened/melted material into the cavities. After cooling and consolidation the punch-piston is retracted, finishing the process.

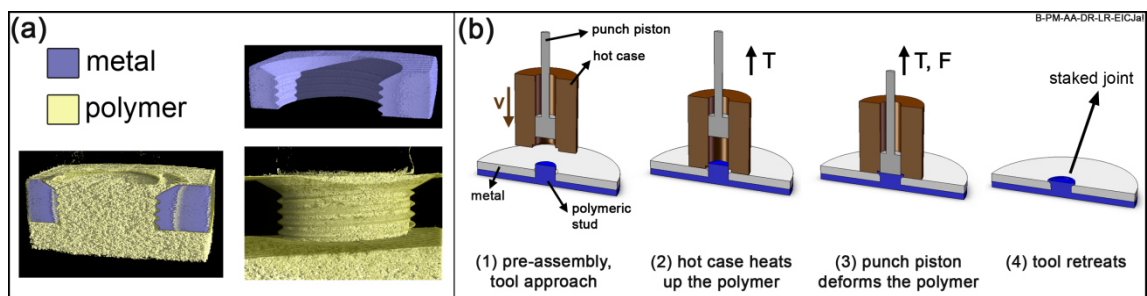


Figure 3-7: (a) Cavity filling in an ICJ process observed through μ CT; (b) electrical-heating ICJ. Adapted from [112].

Microstructural analysis of E-ICJ joints show a clearly defined thermomechanically affected zone in the polymer (PTMAZ), visible by matrix flow and deformation or breaking of reinforcements. Part of the material flows into threaded cavities and a chamfer, and this secures a tight joint. In joints with efficient cavity filling, the global strength in lap shear loading improves significantly, as well as forming a slightly larger stake head [113]. It has been concluded that joint strength depends on the large volume of the stake head and on efficient cavity filling. Although mechanical performance can be greatly improved even with flush stakes in E-ICJ [113], the joining cycles are not attractive for industry; ranging from tens of seconds to a few minutes in these studies [18, 113]

Friction Staking (FricStaking)

FricStaking has been developed recently at Helmholtz-Zentrum Geesthacht as an alternative to ICJ, mainly to shorten the long joining cycles [114, 115]. The process is performed using a tool set composed of a clamping ring, sleeve and pin (Figure 3-8a). The pin and sleeve can rotate and move axially, while the clamping ring applies pressure to keep the plates together. In the process (Figure 3-8b), the parts are initially pre-assembled and aligned with the tool, with the sleeve's internal diameter enclosing the stud and with the pin on top of the stud. The pin and sleeve rotate, generating frictional heat and softening the polymer. A sequence of rotating upward and downward movements of the pin and sleeve reforms the stud into a stake. The clamping ring helps to define the final shape, which is a flat-headed solid stake.

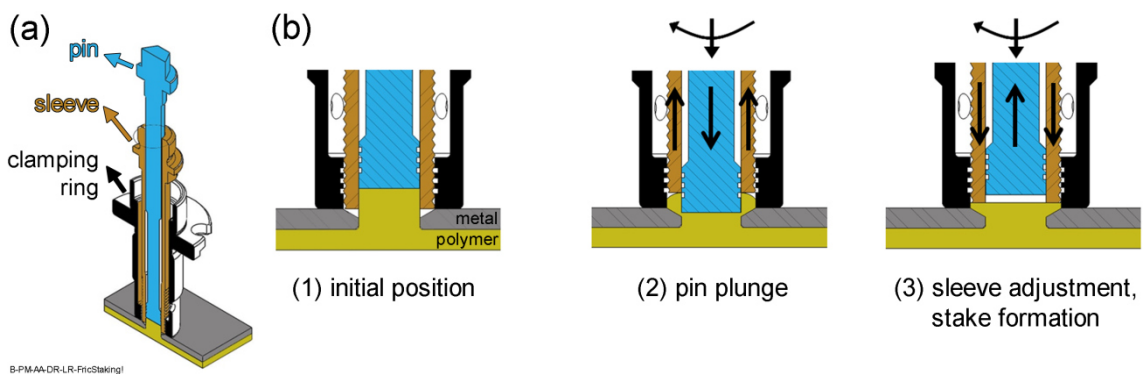


Figure 3-8: FricStaking: (a) tool set; (b) process steps. Adapted from [86].

PEI was joined to aluminum 6082 in a one-factor-at-a-time study exploring the effect of rotational speed on joint properties [115]. In this study, cavities such as those described for ICJ were used in the metallic partner to improve mechanical interlocking. Joining cycles of 4-5 seconds were achieved, with a further cooling time of 10 seconds. Increasing the rotational speed improves the surface finishing, but microstructural analysis shows a larger volume of pores and defects in the polymer. These flaws reflect on the quasi-static global mechanical properties, with increasing rotational speed reducing lap shear and cross tensile properties.

3.3.6 Design considerations for staked joints

Dimensioning of the joining partners and of the tool cavities in staking processes is crucial to achieve sound, durable joints. In this section some design considerations relevant to stake formation and efficient assembly are described. The design is basically constrained by the strength requirements of the structure, determining the types and levels of load involved. This information helps to decide the number of joint spots necessary and the diameter the stakes should have to stay within the safety limits of the structure [83]. Conventional stake designs are showed in Figure 3-9.

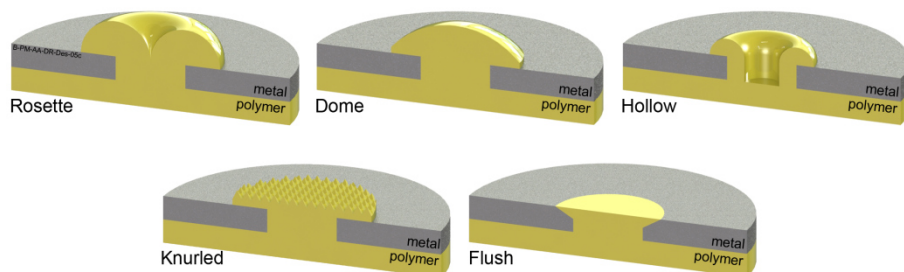


Figure 3-9: Conventional stake designs for metal-polymer joints.

The shape of the forming tools defines the final geometry of the stake head that is created. Each of the designs has its own purpose [83, 86]. Rosette stakes need only low forming forces

and provide good strength, but need precise alignment and are sensitive to tool wear. Dome stakes allow for looser alignment tolerances and still provide good strength, but use more material. Hollow stakes are used when a large cross-section is needed for strength, but would create sink marks. A hollow design uses thin walls to avoid sink marks, while maintaining a large enough cross section. Knurled stakes are a flexible design for which no precise alignment is needed, and they work well with any stud design. Joint strength is generally below the other designs and the appearance is poor. Flush stakes in conventional staking are used when surface appearance is relevant, but the strength is the lowest for these stakes. A 90° chamfer is normally used in this case [85], which can create stress concentrations inside the joint.

The stud height or length should be defined along with the tool cavity used. The tool cavity defines the shape of the stake head and the stud length should be sufficient to fill this cavity. The stake head must satisfy the strength requirements and aesthetic purposes of the application. It is recommended that the stud be slightly larger than the tool cavity volume, so that the polymer is compacted during forming and a tight joint is created. Small studs will create incomplete stake heads. The free length of the stud should not exceed a value twice its diameter, in order to avoid buckling or lateral deformation when forming [83]. Up to a 4:1 length-to-diameter ratio the feeding rates have to be carefully controlled to avoid these deformation effects or root cracks in the stake [97].

Stress concentration points should be avoided when designing staking joints. The polymeric partner should use radii at its base that matches the bottom surface geometry of the other joining partner. For threaded cavities a larger pitch between threads is desirable, in order to reduce the notching effect in the polymer partner. For flush stake heads the chamfer should present a smooth transition to the through hole or threaded cavity [83].

It is recommended that the matching parts use lead-in geometries such as a chamfer on the bottom surface of the joining partner and on the top surface of the stud, to facilitate the pre-assembly [85]. A larger clearance also assists faster pre-assembly, but may decrease joint strength. A clearance of 10 % of the diameter is the recommended industrial practice [85], but in hot staking the loss of melted/softened material from the stake head to the clearance should be avoided [83]. Too large clearances also facilitate out-of-plane deformation and decrease joint stiffness [116].

3.4 Physical-chemical phenomena in friction-based polymer joining techniques

This section explains some of the relevant physical and chemical phenomena that occur in polymers during and after a friction-based polymer joining or welding process. These concepts are important for understanding the joint formation mechanisms and local changes in the material, which may influence the in-service mechanical behavior of joints.

3.4.1 Heat generation in friction-based polymer joining of polymers

The heat generated in such processes can be interpreted as based on the theories of friction welding [76, 117]. Friction welding processes can be divided into five stages, as illustrated in Figure 3-10. This figure shows the axial displacement of the moving parts or non-consumable joining tools during the welding/joining process.

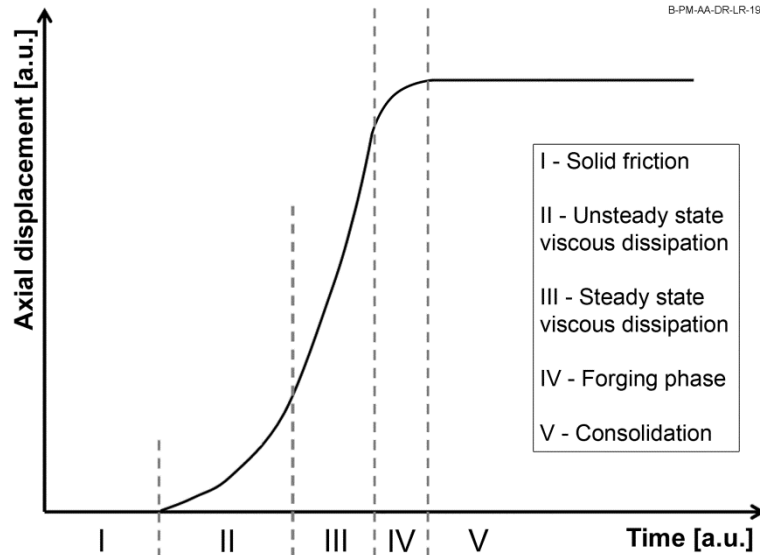


Figure 3-10: Schematic curve of axial displacement during a friction welding/joining process. Based on [118].

Phase I is characterized by solid friction (Coulomb friction). The solid-solid interface is subjected to a normal pressure, inducing friction, which heats the materials until the polymer is softened (amorphous) or melted (semicrystalline). During this notably short phase, the axial displacement has almost no change (approximately zero), whereby the temperature increases locally due to the plastic deformation of microscopic roughness peaks on the surfaces.

Phase II is known as “unsteady state viscous dissipation” [97]. It starts when a softened/melted polymer layer is created at the interface. In this phase, energy is mainly generated by viscous heating of the melted polymer. Thermal energy is released from breaking of the secondary bonds among the chains, because of the tool’s shearing action, chain disentanglement and flow. At the beginning the softened/melted film is thin, therefore the shear rate is high, which induces high viscous heating and an intense melting rate at the interface [118]. In addition, the material flow to the side is small when there is a thin softened/melted polymer layer. However, the thickness of the softened/melted polymer layer increases with time, which reduces the shear rate and the melting rate. Thus the squeeze flow is further supported.

Eventually an equilibrium between the polymer softening/melting at the interface and the squeezed outflow is reached, and the axial displacement increases linearly over time [118]. The process is steady and phase III occurs, known as “steady state viscous dissipation.”

Phase IV is known as the “forging phase” and starts when the relative movement ceases and a consolidation pressure is applied. The melted polymer continuously flows outwards until its viscosity increases and consolidation is achieved during cooling [119]. This stage helps to eliminate defects such as air bubbles in the softened/melted volume. The last phase (phase V) is called the “consolidation phase.” At this stage, there is no further axial displacement from meltdown. Axial pressure is further applied on the solidifying polymer, which avoids any undesired deformation during cooling due to shrinkage and recovery effects.

Frictional heating evolves from relative movement between two solids that are in close contact. While several models are available to describe the heat development in metal friction welding, for polymers it is notably difficult to model the frictional heat generation precisely. Due to the low thermal conductivity, local softening and melting change the conditions at the interface, especially in phase II of a friction welding process [120]. It is possible to estimate the heat generation during more stable conditions, such as the solid-solid friction (phase I) and during the steady-state regime (phase III). Rooney and Grewell [117] defined for spin welding of polymers the rate of energy input \dot{E} during solid friction as a function of the frictional force F_f and relative velocity V . Therefore the rate of energy input can be estimated as directly proportional to the product of the applied normal force F_N and the coefficient of friction μ , multiplied by the product of the radius r and the angular velocity ω , as shown in Equation (3-1).

$$\dot{E} = F_f \times V = (F_N \mu) \times (r \omega) [J \cdot s^{-1}] \quad (3-1)$$

For the steady state phase III, Rooney and Grewell [117] also defined a relation for heat flux density ϕ_s , which is directly proportional to the viscosity η , radius r , angular velocity ω , and thickness of the molten layer h , as shown in Equation (3-2).

$$\phi_s = \frac{\eta r^2 \omega^2}{h} [J \cdot s^{-1} \cdot m^{-2}] \quad (3-2)$$

Potente and Reinke [121] described the heat flow in spin welding of tubes, separating it into contributions of the heat generation due to interface friction between the solid polymers (\dot{Q}_S , Equation (3-3)) and internal friction (shearing) in the molten layer (\dot{Q}_M , Equation (3-4)). The solid friction’s contribution is similar to what Rooney and Grewell described in Equation (3-1), but accounts for the external and internal radii of the tubes (r_2 and r_1) and contact pressure p instead of normal force F_N . The molten layer’s contribution takes into account the average radius of the tube r and the thickness of the molten layer h . As in Equation (3-2), this internal friction model uses the viscosity η of the molten layer as a material property, as opposed to the coefficient of friction μ as used in Equation (3-1) and Equation (3-3) for solid friction.

$$\dot{Q}_S = \left(\frac{\mu p \omega}{3} \times \frac{r_2^3 - r_1^3}{r_2^2 - r_1^2} \right) [J \cdot s^{-1} \cdot m^{-2}] \quad (3-3)$$

$$\dot{Q}_M = \eta \left(\frac{r \omega}{h} \right)^2 [J \cdot s^{-1} \cdot m^{-3}] \quad (3-4)$$

It can be noted that Equations (3-1) and (3-2) bear a resemblance to Equations (3-3) and (3-4), respectively. It can be concluded that for friction welding of polymers the axial pressure and rotational speed, as well as the geometry of the parts, affect the heat input on the materials. The heat input itself will influence material properties such as viscosity [89, 117] and the coefficient of friction [120], dynamically changing the heat generation conditions during the process.

The complexity of the heat generation during viscous friction can be further noted from Equation (3-2) and Equation (3-4). As Rooney and Grewell noted [117], the viscous friction contribution described by these equations is self-limiting as a result of the effect of squeeze flow, which reduces h . Due to the shear thinning behavior of polymers ($\eta = \tau/\dot{\gamma} = \tau h/V$) a reduction in h reduces the viscosity η as well. Since in both equations the heat generation (ϕ_s in Equation (3-2) and \dot{Q}_M in Equation (3-4)) is directly proportional to the viscosity η and inversely proportional to the molten layer's thickness h , this leads to a self-limiting process. The observed effect is that during viscous heating the molten layer becomes thinner because of squeeze flow (increasing ϕ_s or \dot{Q}_M), but shear thinning decreases polymer viscosity and consequently reduces the efficiency of heat generation. Therefore the heat generation achieved in this molten layer is limited and the temperature of the molten layer reaches a plateau during the steady state viscous dissipation phase [117].

Temperature dependence of the coefficient of friction μ and viscosity η combined with time dependence of the molten layer thickness h make precise calculations of heat input and temperature fields in polymer friction welding/joining rather complex. A common approach to estimate heat generation is to calculate the energy input in terms of mechanical work applied during the process [122-124]. The rate of mechanical work generation \dot{E}_{work} can be calculated using Equation (3-5). It considers the frictional contribution \dot{E}_f , which is the product of angular velocity ω and frictional torque M , and a deformational contribution \dot{E}_d , which is the product of the axial force F and deformation rate v . By considering this contribution over the time of the process, the total energy input from mechanical work E_{work} can be calculated, as in Equation (3-6), where M_{total} is the total torque (the integral of torque over time), and Δx is the displacement.

$$\dot{E}_{work} = \dot{E}_f + \dot{E}_d = M\omega + Fv \quad [J \cdot s^{-1}] \quad (3-5)$$

$$E_{work} = \int_{t_0}^t M\omega dt + \int_{t_0}^t Fv dt = M_{total}\omega + F \Delta x \quad [J] \quad (3-6)$$

It is known that the deformational contribution in friction-based joining processes constitutes only about 1 to 2 % of the total energy input and so can usually be neglected for energy input calculations [76, 123, 124]. Equation (3-6) is a straightforward way of estimating the energy input and the experimental data for its calculation is easily obtained from modern welding/joining systems.

3.4.2 Effects of thermomechanical processing on polymers

Typically a friction joining process uses the relative motion between the parts in contact to build up heat at their interface, softening and deforming the material. While for a polymer-polymer system both workpieces are deformed, for dissimilar polymer welds or a metal-polymer joint, only the softer part is generally affected. The heating and deformation change the polymer microstructure and at the end of the process a new local configuration is present.

Thermoplastic polymers exist as amorphous or semicrystalline materials. This nomenclature contemplates the level of local order of the macromolecules in the solid state. A molten polymer is a series of entangled macromolecules with a certain level of mobility. Below their glass transition temperature (T_g), amorphous polymers form glassy solids without long-range order, maintaining a random topological configuration of entangled chains with free volume (holes or empty spaces between chains). The cooling from semicrystalline polymers to below their crystallization temperature (T_c) activates nucleation and growth of three-dimensionally ordered regions, the crystallites. Only parts of the bulk acquire this level of order and the remaining volume has an amorphous conformation [125]. The chain conformation and order levels of the polymers are therefore a function of their processing and cooling regimes. The diagram in Figure 3-11 shows the relevant transitions for amorphous and semicrystalline polymers during the cooling regime after thermomechanical processing by relative movement (rotation) and axial pressure. The described effects can be associated with a friction-based joining process.

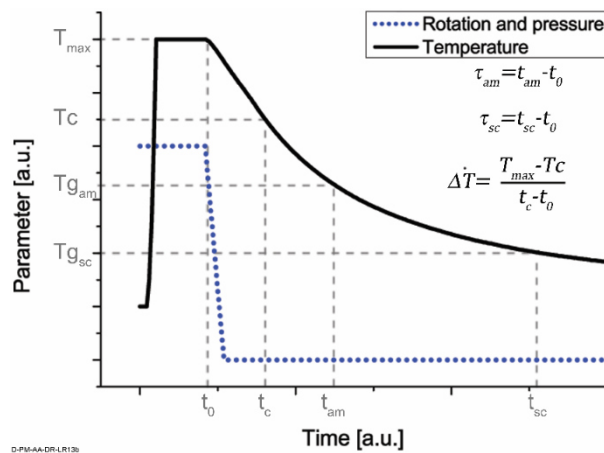


Figure 3-11: Relevant transitions and relaxation times during and after thermomechanical work.

This diagram shows schematically the thermal history of thermomechanical processing of a polymer, as it occurs during and after a friction-based joining process. Initially the process temperature reaches a plateau T_{max} , and as the shearing action (rotation and pressure) ceases, the temperature decreases in an exponential decay. For the amorphous polymer, the glass transition temperature $T_{g_{am}}$ defines the point at which the mobility of chains is reduced, due to lower internal energy, and the molten material solidifies into a glass [125]. The time τ_{am} therefore defines how long the macromolecules have to rearrange into the lowest energy

level possible for the amorphous polymer. The chains in a polymer glass tend to achieve the most packed configuration, eliminating free volume and increasing density, but this is only possible as long as the temperature allows chain movement (during τ_{am}) [126]. A faster cooling rate decreases τ_{am} , and will create a less dense solid with more free volume, while slower cooling rates increase τ_{am} and polymer density. The density of amorphous polymers is a function of the entanglement of its chains and this dictates its mechanical and viscoelastic properties [127, 128].

The cooling rate ΔT is important for the semicrystalline polymer, since it dictates the concurrent mechanisms of crystal nucleation and growth. The crystalline structure formed by a system is defined by the ΔT as it reaches or surpasses the crystallization temperature T_c [125]. Below T_c the time τ_{sc} corresponds to τ_{am} of an amorphous material. During τ_{sc} a certain level of mobility is expected in the amorphous phase and further secondary crystallization may occur until an equilibrium is reached [129].

Generally in polymer thermal welding processes, the temperature and pressure promote interdiffusion of the molecules of each workpiece, creating a bond between them [130]. This interdiffusion can be interpreted in terms of the reptation theory of de Gennes [131], which describes chain movement related to thermal fluctuations. The theory predicts that the chains move inside confined spaces (tubes) between entanglements and eventually disengage from the tube and assume a new conformation [132]. This effect is illustrated in Figure 3-12a: the chain ends disengage from their initial tube over time. The “tube renewal time” T_r is reached when in equilibrium a new tube is defined for the new chain conformation. This movement also happens at the interface between two parts, if sufficient energy is available to promote chain mobility. The interdiffusion across an interface is illustrated in Figure 3-12b. In this case, the chains at the surface of a workpiece are not in equilibrium and as the two workpieces are pressed together these chains are free to change their conformation. As the chain ends are able to disengage from tubes by reptation, they may diffuse across the interface in a tendency to achieve equilibrium with more energetically favorable conformations [132].

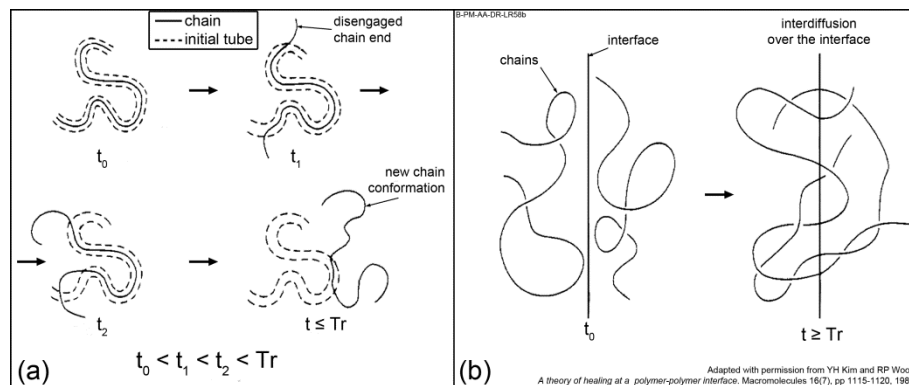


Figure 3-12: (a) Chain-end disengagement leading to new chain conformations according to the reptation theory. T_r is the tube renewal time; (b) interdiffusion of chains across an interface. Adapted with permission from [132]. Copyright 1983 American Chemical Society.

This effect is, however, not limited to high temperature processes as it has been reported to occur in the same fashion for glassy polymers below their T_g temperature range [133, 134], but presenting much lower diffusion coefficients than high-temperature interdiffusion [135]. In friction-based metal-polymer joining, the thermomechanical processing of the polymer may create polymer-polymer interfaces between molten flowing front and stationary volumes [78, 81]. Interdiffusion, as described here, is the healing mechanism during cooling in such interfaces.

3.5 Main characteristics and properties of base materials used in this work

3.5.1 Polyetherimide

Polyetherimide (PEI) is an amorphous, transparent engineering thermoplastic. It was developed as an alternative to polyimides, which present excellent mechanical and thermal properties, but poor processability [136]. It has been commercialized since 1982 by GE Plastics (subsequently acquired by SABIC Innovative Plastics, Saudi Arabia) with the commercial name Ultem. PEI is a condensation polymer, more commonly polymerized from solution or melt in one-step processes. More detailed information on synthetic routes for the production of PEI can be found in [137]. The generated chemical structure of PEI is shown in Figure 3-13. The chain backbone contains ether linkages that provide improved processability and aromatic imides that provide stiffness and thermal resistance.

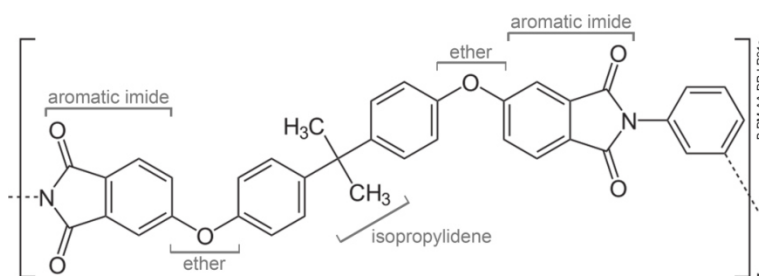


Figure 3-13: Representation of the chemical structure from PEI.

The main characteristics of PEI are high mechanical strength and thermal stability, outstanding flame resistance, transparency, food and drug compliance, excellent electrical properties, and good chemical and environmental stability [136-138]. Johnson and Burlhis [136] thoroughly reported on the mechanical, chemical, thermal, and rheological properties of unreinforced PEI. They showed that creep properties at high temperatures are excellent for amorphous polymers, owing to their high glass transition temperature of 215-220 °C. Its creep behavior along with a high heat distortion temperature (at 1.8 MPa) of 190-210 °C [138] make this material a good choice for high-temperature use. A series of fatigue and tribological data for several unreinforced and reinforced PEI grades is available in [139], which shows significant improvement in long-term mechanical performance for fiber reinforced grades. Mechanical

performance is improved by using glass or carbon fibers as reinforcement, while tribological properties are improved by compounding with carbon nanofibers [137].

PEI is hydrophilic, but to a much lesser degree than polyimides, absorbing up to 1.45 % of water by weight in the range of 20-100 °C [140]. In such saturated conditions, Merdas *et al.* [141] noted a plasticization effect of water on PEI, reducing T_g and yielding strength, but unexpectedly decreasing strain at break. The lower ductility may be due to surface defects observed on the water-saturated samples. Water absorption of 1.25 % was shown as sufficient to degrade the creep behavior of PEI [142].

PEI has a high melt strength and so can be injection-molded or extruded using melt temperatures of 370-390 °C without degradation. Chemical degradation of PEI occurs by the mechanisms of crosslinking and chain scission [143, 144], with crosslinking dominating at temperatures in the range 320-380 °C, and decomposition starting with a random chain scission process at 450-600 °C [137, 144]. Random chain scission occurs preferably at the bonds of isopropylidene, ether (oxygen-phtalamide), and phenyl-phtalamide. Secondary degradation, as pyrolysis and hydrolysis, occur at higher temperatures (620-700 °C) [137]. As PEI applications are intended for high temperature use, a number of studies have explored their thermal degradation mechanisms under different processing conditions. Combining molecular weight measurements made by gel permeation chromatography (GPC) and T_g measurements by dynamic mechanical analysis (DMA), Augh *et al.* [144] identified crosslinking as the dominant mechanism for degradation of PEI-CF after autoclave and oven heating at 300-330 °C. The effects of crosslinking were overlapped with chain scission at harsher conditions (350 °C for 3 hours and at 400 °C for 1 hour), confirming the results observed by Kuroda *et al.* [143]. Amancio *et al.* [145] joined unreinforced PEI to AA2024 using the FricRiveting process and studied the effect of rotational speed on degradation. Thermal degradation by chain scission was observed using GPC, but in levels that did not affect the properties of PEI. Ageorges and Ye [146] joined PEI-CF to AA7075 by resistance welding, finding that thermal degradation affected joint strength and that optimal joints could be achieved, either at low power levels and long times, or high power levels and short times.

PEI can be welded or joined with any of the usual thermoplastic assembly technologies. According to the technical guidelines [104, 147], mechanical joining using snap fits, inserts, thread-forming and thread-cutting screws, riveting, and staking are applicable, while adhesives based on epoxy, polyurethane, and silicone are the most successful for bonding of PEI [147]. Aside from company information, there are several scientific papers on advanced welding-based or mechanical-joining technologies involving both unreinforced and reinforced PEI grades. The motivations for these works are usually weight reduction, recyclability of thermoplastic materials, and overcoming the limitations of traditional joining methods.

With regards to polymer-polymer joining processes, there are a number of works with unreinforced and reinforced PEI in vibration, hot plate, and resistance welding. Stokes [148] investigated vibration welds of PEI, reporting an increase in strength with higher weld pressure at three frequency levels. At a frequency range of 250-400 Hz and weld pressure of 6.9-13.8 MPa, joints with the same strength as the base material could be achieved. With hot plate welding [149] PEI joints are less successful, reaching 85 % of the base material's strength. This difference is probably due to the weld morphology combined with porosity formation. Resistance welding of glass-fiber and carbon-fiber reinforced PEI laminates has been studied

by Hou *et al.*, exploring welds without [150] and with [151] a metallic mesh as heating elements. Both cases presented joints comparable to reference compression molded specimens, indicating the potential of resistance welding for PEI composites. Dubé [152] studied the fatigue life and mechanical behavior in fatigue of unidirectional PEI-CF and textile PEI-GF composites using the metallic mesh. Although their fatigue life was better than that observed using adhesive bonding, poor adhesion to the steel's resistive element seemed to deteriorate their performance.

Further interest in PEI joints to metallic components is seen in the literature. Ageorges and Ye [146] demonstrated the application of resistance welding of PEI-CF and PEI-GF to aluminum 7075-T6 for aircraft applications. Degradation of the PEI matrix seemed to affect lap shear strength. Moreover, the heat input levels necessary for joint formation in this study led to local annealing of the aluminum alloy. PEI/AA6082 joints were explored by Abibe *et al.* [115] using Friction Staking. The thermomechanical process affected part of the material by reducing local strength and forming porosities. Higher heat input increased pore formation in the affected region. The new FricRiveting technology has been explored with unreinforced PEI/AA2024-T351 joints in a feasibility study demonstrating the technology [78]. In this case, porosity formation was also observed as not being affected by rotational speed levels [145], but increasing with longer heating times [76]. More recently, Blaga *et al.* [80] showed the feasibility of FricRiveting with glass-fiber laminate PEI composites and titanium grade 2. The aircraft-grade PEI had the fiber network reoriented and partially destroyed during the process, but the remaining material assisted in opposing axial loading of the inserted rivet. In a further study, showing FricRiveting as a possible civil construction technology [153], PEI-GF/AA2198 overlaps were friction-riveted using titanium grade 2 rivets. These joints presented mechanical performance comparable to bolted joints, but with faster joining cycles.

Global consumption of PEI is estimated to be between 5000 and 10000 tonnes per year [138]. The growing relevance of PEI as an engineering thermoplastic has recently caused drastic increases in industrial demand, causing a global shortage of PEI grades [154, 155]. Applications of PEI are motivated by its characteristics of high strength and thermal resistance, flame retardant behavior and health/food compliance. Its main markets and applications are food service, healthcare, automotive, aircraft, electrical, and lighting [138, 147]. Its uses in aerospace and aircraft often focus on its flame retardant and low smoke emission properties. PEI laminate composites and sheet molding compounds are used in aircraft secondary structures and interiors, such as flooring, luggage bins, and fairings [156]. In the automotive sector PEI is used as an aluminum replacement, for example for transmission components and throttle bodies [147]. Another common use is in lighting as reflectors, since it can be metallized and is thermally stable [157].

3.5.2 Aluminum alloy 6082-T6

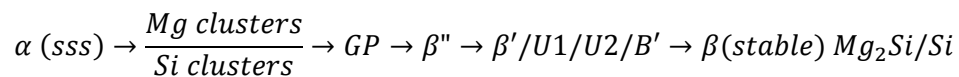
The aluminum alloy 6082 (AA6082, or AlSi1MgMn) is a heat-treatable lightweight alloy of the 6xxx series. The main alloying elements of this series are magnesium and silicon (Al-Mg-Si alloys), but for AA6082 manganese is also added. Magnesium adds to corrosion resistance, silicon increases its age-hardening response and manganese controls the grain size, increasing ductility and toughness [158-160]. This alloy has good corrosion resistance,

formability, machinability, weldability and immunity to stress corrosion cracking [161, 162]. Along with its high strength (for a 6xxx-series alloy), these properties support the use of AA6082 as a structural alloy in construction, transportation equipment, bicycle frames, and shipbuilding [160, 161]. The nominal chemical composition of the alloy is shown in Table 3-2.

Table 3-2: Chemical composition of AA6082 [161].

Element	Mn	Fe	Mg	Si	Cu	Zn	Ti	Cr	Other	Al
Weight	0.4-	0.5	0.6-	0.7-	0.1	0.2	0.1	0.25	0.15	Bal.
[%]	1.0		1.2	1.3						

The T6 temper consists of solution heat treatment followed by quenching and posterior artificial aging. The artificial aging for 6xxx series alloys uses temperatures from 160 °C to 205 °C for up to 18 hours [163]. This temper is used on the formed products to increase their strength through precipitation hardening during artificial aging [161]. The precipitation hardening follows the following sequence [164, 165]:



where $\alpha(sss)$ denotes supersaturated solid solution. Atomic level clusters are formed from Si and Mg atoms, and eventually form small particles as Guinier-Preston (GP) zones. These are precursors to the formation of coherent β'' precipitates, which have the most effective strengthening effect in 6xxx series alloys. Other metastable precipitates ($\beta'/U1/U2/B'$) may be formed, depending on the composition, heat treatment, shelf time after quenching, and aging conditions [164-167].

AA6082 presents good weldability with traditional arc welding, but a trend of using more advanced joining technologies is seen in the literature. Borsellino *et al.* [168, 169] investigated adhesive-bonded AA6082 joints. Their wettability is affected by mechanical surface treatments, and joint strength is influenced by the type of adhesive and surface treatments. Pereira *et al.* [170] correlated process parameters with joint properties and microstructure in resistance-spot welds of AA6082. Increasing the nugget size improved joint strength and could influence the failure modes. Several works explore the feasibility of friction stir welding (FSW) with this alloy, relying strongly on microstructure evolution and local mechanical properties to optimize mechanical performance [159, 162, 167].

The lightweight potential is reinforced by the interest in AA6082 as a material for hybrid structures. Lucchetta *et al.* [171] investigated injection over-molding of PP-GF on AA6082. The surface roughness and temperature of the AA6082 plate have an influence on the joint strength, due to a facilitation of micromechanical interlocking. A similar conclusion was reached by Wirth *et al.* [61] using a friction-based joining process. Mechanical joining by clinching of AA6082 with amorphous polymers was explored by Lambiase [172]. Adequate tool designs were used to enable forming without cracking of the AA6082 part, and a functioning process parameter range could be established.

CHAPTER 4. THE NEW FRICTION-BASED INJECTION CLINCHING JOINING PROCESS

This chapter is an introduction to a new joining technology “Friction-based Injection Clinching Joining” or F-ICJ for short (Abibe *et al.* European Patent Application EP14182938.2, Appendix A). This new process was devised, patented, and developed during the course of this PhD work. In this chapter the fundamental concepts involved in the creation of this technology are presented.

The F-ICJ process explores frictional heating as an energy-efficient means to rapidly create sound polymer-metal staked joints. F-ICJ is based on the concepts of staking, injection molding, and mechanical fastening. While with state-of-the-art staking technologies strong joints are achieved by creating a large stake head to clamp both joining partners together (Figure 3-9), F-ICJ uses the concept of cavity filling from the original ICJ process [173] to improve mechanical performance and appearance [18, 113]. Such an approach allows the process to create strong joints in a smooth surface structure (e.g. flat and flush stake heads), which cannot usually be achieved with traditional staking methods.

Geometric aspects of the joining partners and the tool are important for joint design. The dimensions of the thermoplastic stud and of the cavity profile are defined according to the requirements for strength of the structure [83]. During the process, the stud is deformed into a stake, with the thermoplastic flowing into cavities in the joining partner. The thermoplastic workpiece is preferably injection or compression molded, while the holes in the other workpiece are preferably machined. For complex geometries that can further improve the mechanical interlocking, metal injection molding and additive manufacturing may be used. The shape of the tip of a non-consumable tool is designed with the purpose of creating an efficient material flow to allow cavity filling. Some of the possible joint designs are shown schematically in Figure 4-1.

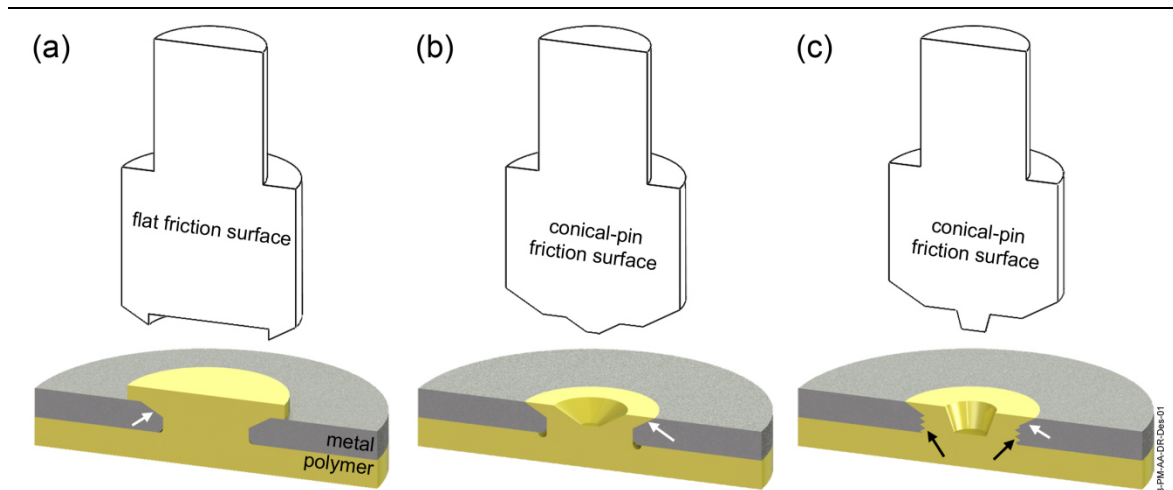


Figure 4-1: Design of F-ICJ joints with different cavities and tool profiles. (a) flat stake head created with a flat frictional surface tool and chamfer cavities (white arrows); (b) flush stake created with a conical-pin tool and chamfer cavities (white arrows); (c) flush hollow stake created with a conical-pin tool, with mechanical anchoring in the threaded cavities (black arrows) and chamfer cavities (white arrows).

The tool and through-hole in F-ICJ can also be designed to provide more freedom in manufacturing by allowing certain levels of hole clearance during pre-assembly of the parts. Large structures joined by staking methods have to deal with tolerances and differential thermal expansions. As mentioned in Section 3.3.6, this is usually solved by using hole clearances of up to 10 % of the stud diameter [85], which may increase out-of-plane deflection and facilitate loss of stiffness [84, 116]. In traditional staking methods, the forming tool only affects the polymer volume above the top surface of the joining partner. Whereas in F-ICJ, by the use of a conical-pin tool, material flow is induced throughout most of the stud during joining, and, depending on the size of the induced shear layer, the hole clearances can be eliminated, or reduced to optimal levels, without much extension of the joining cycle. This effect can be enhanced by using similar tool designs to friction stir welding (FSW) with geometrical features such as prismatic pins, threaded pins, and concave frictional surfaces, which further improve material flow around the pin [174-176].

Applications of staking-based joining technologies have been presented in Section 3.3. The concept of F-ICJ aims for a high performance level of staking joints. The main targets are secondary and tertiary structures using discontinuous FRPs in the transport industry, but also as a general alternative to other staking applications. The potential to achieve this objective lies in the simple design of joining partners, inexpensive machinery and tooling, and the short joining cycles of F-ICJ. Furthermore, the process can successfully join thermoplastic polymers and fiber reinforced plastics to other solid materials.

4.1 Principles of the process

The simplest description of the F-ICJ process is illustrated in Figure 4-2. In this configuration, a thermoplastic workpiece with a solid stud is joined to another workpiece that has a through-hole with a chamfer cavity. A non-consumable tool attached to a rotating machine is used to create the joint. The thermoplastic part and the other joining partner are pre-assembled (preferably on a backing plate) and aligned with the moving axis of the non-consumable tool (Figure 4-2a). After this positioning step, the rotating tool moves towards the thermoplastic stud (Figure 4-2b). The contact between the rotating tool and the stud generates frictional heat at their interface, gradually softening or melting the polymer, and allowing the tool to penetrate further into the stud (Figure 4-2c). The friction phase heats and deforms the thermoplastic stud, decreasing the polymer's molten viscosity and inducing flow. Next, the tool's rotation is stopped and axial pressure acts further upon the softened or melted polymer, pushing it into the cavities and shaping the final stake geometry (Figure 4-2d). The tool remains in this position until the thermoplastic is consolidated to below its glass transition temperature (Figure 4-2e). The tool retreats and the F-ICJ joint is created. An example of an F-ICJ joint and a cross section is shown in Figure 4-3. The white dotted line in Figure 4-3b represents the boundary of the polymer's thermomechanically affected zone (PTMAZ) or shear layer, where the polymer is locally heated and deformed.

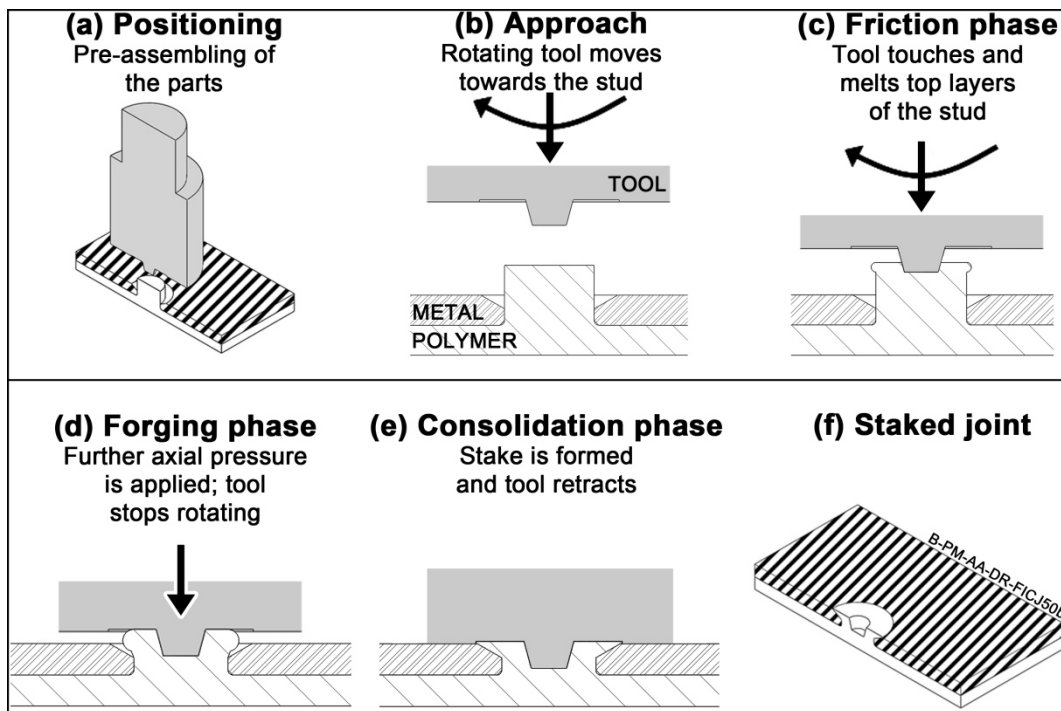


Figure 4-2: Schematic description of F-ICJ process.

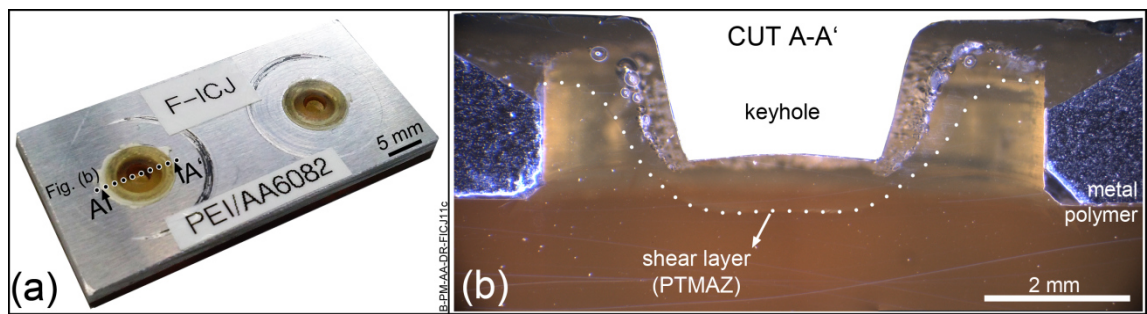


Figure 4-3: (a) Surface view of an F-ICJ joint; (b) cross section of a stake observed in a stereomicroscope. A process-affected volume (shear layer) can be identified (white dotted line).

Joint formation and heat development in a friction-based process such as F-ICJ are mainly dependent on the interaction between the metallic tool and polymeric stud. Thermal and mechanical energy are provided by their relative movement and applied axial force (Section 3.4). Material properties and the varying levels of tool rotational speed and axial force yield different responses in joint formation. For example, with some polymers a complete meltdown of the stud can rapidly be achieved while in the friction phase, obviating the need for a forging phase. A forging phase with higher forces decreases the joining time by increasing the stud meltdown rate. However, a forging phase should only be used with ductile polymers, or after a significant volume of the stud has been heated above the relevant thermal transition of the material. Otherwise the negative effects of cold staking may occur [83], such as recovery and residual stresses. The process setup should therefore be defined according to an optimized joining cycle that is adequate to the material to be joined.

Friction-based joining/welding processes can be controlled either by the applied force or the applied stud meltdown rate. A process with force control regulates the joining force so that it maintains a set level, and the stud meltdown rate is a response. Alternatively, the process can use stud meltdown rate control, obtaining force curves as responses. In either case the joining force or the stud meltdown rate can be kept constant, or can be changed during the friction, forging, and consolidation steps.

The duration of each process phase (friction, forging, consolidation from Figure 4-2) must be based on a given material's response to a heat input level that is attained as a result of the joining parameters that are setup on the joining equipment. Time or displacement limits can be used to define the transition between friction and forging steps – the moment at which the tool stops rotating. Time-limited processes switch to the next phase after a certain preset time. Displacement-limited processes transition to the next phase when a defined axial position is reached.

In the current state of the art of F-ICJ, a force-controlled and time-limited process is used. This configuration is typically used for friction-based joining processes. Schematic process monitoring diagrams, including the controlling parameters as setup, are displayed in Figure 4-4, for force-controlled configurations without a forging phase (two-phase process) and with a forging phase (three-phase process).

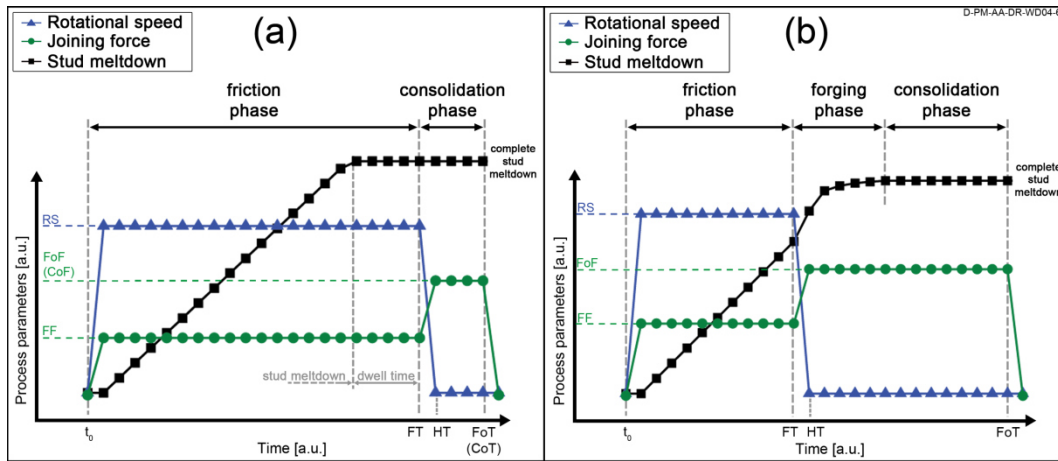


Figure 4-4: Schematic force-controlled F-ICJ joining diagram and process parameters for (a) a process with friction and consolidation phases (two-phase process); and (b) a process with a friction, forging and consolidation phases (three-phase process).

In a two-phase process (friction and consolidation phases) where a complete meltdown is achieved during the friction phase, a forging phase is absent (Figure 4-4a). In this process configuration the friction phase is divided into two stages of variable duration: a stud meltdown stage and a dwell time stage. At the beginning of the friction phase the stud is softened, or melted, by the tool at a certain stud meltdown rate. A complete stud meltdown is achieved when the clamping surface of the tool touches the top surface of the joining partner; therefore in a two-phase process complete stud meltdown is not a response of the process, it is a function of the tool and joining partner geometries. After stud meltdown is completed, the friction phase can be extended with tool rotation, characterizing a dwell time stage. The duration of the dwell time is a function of the preset frictional time and of the stud meltdown rate. During dwell time the tool rotates in the same position, stirring and mixing the stake material. After the dwell time, natural cooling under pressure is used during the consolidation phase. Forced cooling may be applied to avoid tool temperature build-up in sequential joining with this process. The joining force or pressure may be increased during the consolidation phase as shown in Figure 4-4a, but a constant force may also be used throughout the process.

A three-phase process configuration (friction, forging and consolidation phases) as shown in Figure 4-4b is characterized by an increase in joining force and a decrease in rotational speed before complete stud meltdown is achieved. The friction phase is composed only of a stud meltdown stage (without dwell time). During the friction phase, the heat build-up softens the polymer, while the transition to the forging phase, with a higher axial force, yields a higher meltdown rate. In this configuration stud meltdown is a response of the process and a function of the energy input and axial forces. Such a process configuration is adequate when the heat supply during the friction phase is sufficient to bring a large volume of the stud above its glass transition temperature. If the polymer has insufficient fluidity at the start of the forging phase, the tool-related compressive stresses might lead to pronounced cold-forming effects, such as microcracks and/or excessive shear banding [83], weakening the joint. As complete stud meltdown is achieved, the forging phase ends and a consolidation phase starts. The duration of this consolidation phase is a function of the preset forging time and of the duration of the forging phase.

4.2 Process parameters and variables

For a time-limited F-ICJ process using force control (as with the one used in this project), the programmable process parameters involved are rotational speed (RS), frictional time (FT), frictional force (FF), forging time (FoT), forging force (FoF). These values are illustrated in the schematic examples of Figure 4-4. Depending on the joining equipment, axial forces are a result of setup manometric pressures, in which case the force parameters FF and FoF are a function, respectively, of the preset frictional pressure (FP) and forging pressure (FoP).

RS is the angular velocity imposed by the spindle on the non-consumable tool. It influences heat generation directly, as described in Section 3.4.1. Additionally, the relative movement between the stationary polymeric stud and the rotating tool induces shear stresses in the polymer. The combination of an increase in temperature and shear stresses facilitates polymer flow. FT is the time span in which the spindle rotation is active; therefore it defines when RS starts to decelerate to zero. The longer the FT, the more heat and shear can be generated for formation of the stake, increasing local temperature and the size of the thermomechanically affected volume. FF (or FP) is the axial force (or pressure) applied at the spindle. The tool touches the polymeric stud with this force, and this force is maintained over the time span of the FT. The intensity of FF (or FP) defines the feeding rate of the tool and consequently the stud meltdown rate. It also determines how intimate the contact between the rotating tool and the stud is, and a strong contact between tool and polymer results in more efficient frictional heat generation [177]. RS, FT, and FF or FP are active during the friction phase and are responsible for frictional heat generation.

In a two-phase process configuration (Figure 4-4a), the friction phase is followed by a consolidation phase. In this case FoF (or FoP) can be referred to as consolidation force (CoF, or pressure – CoP) (see Figure 4-4a), since no forging occurs. FoF (CoF) at the consolidation phase must ensure a tight contact between the joining partners, allowing the consolidation to occur without a loss of shape over time due to dimensional recovery [83]. The CoT defines the time span of the consolidation phase and this should be long enough for the stake to cool down to below the relevant transition temperature of the polymer (glass transition for amorphous polymers; crystalline melting for semicrystalline polymers). CoT in a two-phase process corresponds to the preset FoT.

At the end of the friction phase in a three-phase process configuration (Figure 4-4b), the forging phase starts and is followed by a consolidation phase. The combined time span for both phases is defined by the preset FoT, and the duration of each of the phases (forging and consolidation) is a function of how fast complete stud meltdown is achieved. The FoT should be long enough for the stake to achieve its final shape and consolidate without significant dimensional recovery. The FoF (or FoP) is the axial force (or pressure) applied during the span of the FoT. It can be equal to or higher than the FF (or FP) and must be sufficient to deform the stud until the clamping surface of the tool touches the top surface of the joining partner. In the case of a three-phase process configuration (Figure 4-4b) the FoF or FoP influences the meltdown rate and contributes to deformational energy input.

The main process variables in F-ICJ are the stud meltdown, stud meltdown rate, duration of dwell time, heating time (HT in Figure 4-4), energy input, and stake temperature (ST). Stud meltdown is the measurement of stud length that is consumed to form the final stake geometry. It is measured by the distance covered by the spindle after the tool first touches the polymeric stud. Stud meltdown can be related to the initial free length of the stud and tool geometry, in order to verify if complete meltdown was achieved. For a given tool and geometry combination of the workpieces, the stud meltdown will be constant for sound joints, since the whole volume of the stud is formed into a stake. The meltdown rate is the speed at which the stud is consumed to create the stake. It is a function of RS, FF or FP, and of FoF or FoP in three-phase processes. The stud meltdown rate must ideally match the squeeze outflow rate in a friction process (Section 3.4). If the meltdown rate is too fast, it causes overfeeding of the tool, which can induce cold-forming defects. By contrast, exceedingly slow rates extend the joining time. The duration of dwell time depends on the preset frictional time, and the duration of the stud meltdown stage (and therefore, depends on stud meltdown rate). During dwell time extra stirring and mixing of the polymer increases energy input at the stake and facilitates material flow. HT is the duration of the heating phase in a cycle, from the start of the process until the rotation stops. Unlike FT, HT also considers the deceleration of the spindle. The energy input is a function of RS (ω), axial forces (F), total torque (M_{total}), and stud meltdown (Δx) as described in Equation (3-6). It has a direct influence on the heat input applied in the process. The heat input in the polymer can be estimated by the ST and can be measured by thermography or thermometry. Measurements of ST assist in interpretation of the microstructure and of the local properties of the joint.

The main microstructural variables in F-ICJ are the size of the process-affected zones and porosity formation in these zones. The process parameters induce certain thermomechanical conditions in the polymer that allow flow, mainly due to local temperature increases and to shear stresses. The higher temperatures in this region promote the evolution of volatiles, or the elimination of structural water in hydrophilic polymers. These effects are seen by the formation of pores. Pore formation and the size of the process-affected zone may affect the joint's global behavior and this can be quantified and investigated by experimental measurements. These will be addressed in detail in Section 10.2.

4.3 Advantages and limitations of F-ICJ

Aside from the advantages and limitations inherent in all the staking processes listed in Table 3-1, F-ICJ currently exhibits the following benefits: (i) simple machinery required; (ii) high energy efficiency with frictional heating; (iii) further weight reduction when using a conical-pin tool (creates hollow stakes); (iv) improved mechanical properties by the use of cavities; (v) excellent surface finishing; (vi) suitable for most thermoplastics and discontinuous FRPs; (vii) short joining cycles; (viii) suitable for joining complex geometries. The current main limitations identified are: (i) need for extra machined cavities in the metallic partner (for flat and flush stake joints) to enhance mechanical performance; (ii) a more complex tool geometry might be necessary to avoid damage to the surface of the joining partner; (iii) can only create stakes from cylindrical studs; (iv) unsuitable for continuous fiber reinforced composites.

CHAPTER 5. EXPERIMENTAL APPROACH

This thesis follows an incremental development structure, from an understanding of processing phenomena and mechanical behavior, to an interpretation of process-microstructure-property relationships, and through to a proof of concept of its feasibility. For this reason the work was divided into five main phases. A diagram of the phases of this experimental concept is shown in Figure 5-1.

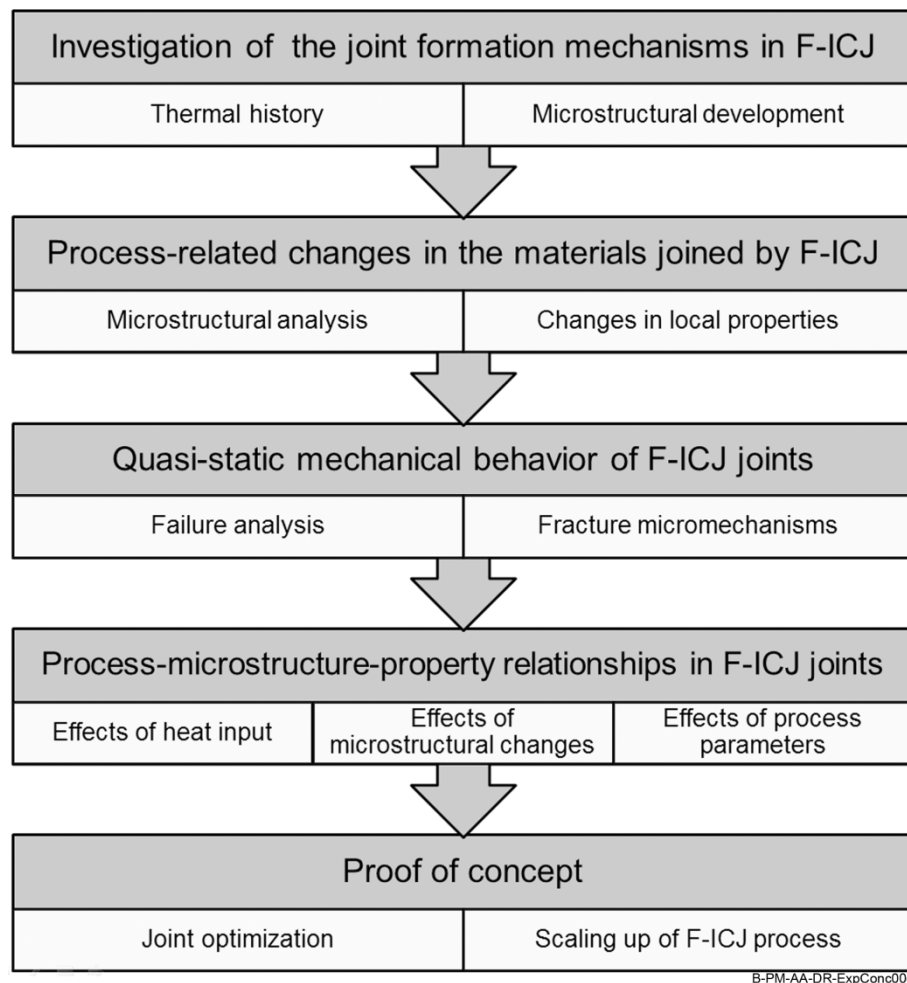


Figure 5-1: Experimental concept of this thesis.

The first phase consisted of an investigation of the physical and thermomechanical phenomena occurring during the joining process. A joining equipment stop-action procedure of a force-controlled two-phase process configuration (Figure 4-4a) was carried out to understand the joint formation mechanisms. The microstructure and heat development of specimens at various stages of the joining process were analyzed, shedding light on the thermomechanical effects that assist joint formation. This experimental investigation explained how the stake is formed, as well as the origin of microstructural features and defects in the polymer.

The second phase used the mechanisms described in the first phase to interpret the microstructural changes occurring in the materials. Local mechanical properties (microhardness), residual stresses (photoelasticity) and physical-chemical changes (thermal analyses) in the polymer were investigated. The results of these analyses were correlated with microstructural analyses to describe how the process affects the joined material. Typical defects in F-ICJ joints were described and their causes identified.

With a comprehensive understanding of joint characteristics, the quasi-static mechanical behavior of F-ICJ joints under lap-shear and cross-tensile loading was investigated in the third phase. Mechanical performance of joints tested in these configurations was evaluated through strain distribution monitoring (digital image correlation) and visualization of stress distribution (finite element method). Failure behavior was described, combining microstructural analyses (reflected-light optical microscopy) and observation of fracture micromechanisms (scanning electron microscopy). Effects of the microstructural changes in the polymer were correlated with failure modes, as well as crack initiation and propagation mechanisms.

In the fourth phase of this work, the relationships between processing conditions, generated microstructure, and corresponding properties were established. The influence of heat development on microstructural changes was determined by evaluating the statistical significance of their correlation. The same approach was used to evaluate the effect of these microstructural changes on the mechanical properties of F-ICJ joints. Design of experiments and analysis of variance were used to analyze the significance of process parameters (RS, FT, FoT, FP, and FoP) on heat development and quasi-static mechanical performance of joints, based on validated regression models.

The fifth phase is a proof of concept of this technology. The validated statistical models were used with a desirability function to achieve an optimized F-ICJ joint. This condition was transferred to an automated gantry joining system for the assembly of multi-spot subcomponents. A sequential automated process was carried out to simulate process behavior in an industrial application. The joined subcomponents were loaded in four-point bending and a preliminary assessment of their mechanical behavior was performed.

CHAPTER 6. MATERIALS AND METHODS

6.1 Materials

The selection of materials for this work was determined by the proposed applications of new staking-based joining technologies, focusing on the feasibility of F-ICJ for lightweight transport industry materials. The dimensions of the metallic workpiece (Section 6.1.1), the polymeric workpiece (Sections 6.1.2 and 6.1.3), and the tool's frictional surfaces (Section 6.2.1) were defined based on the envisioned application and on standard design guidelines for stud and stake geometry. Therefore plates 2 mm thick were used, as is common in the transport industry. The cavity in the metal was designed to accommodate some polymer for extra mechanical anchoring, but limiting notch effects. The length of the stud was calculated to be able to fill the cavities and tool geometries with some extra, as recommended in the literature [83, 85].

6.1.1 Aluminum alloy 6082-T6 (AA6082)

2 mm thick AA6082 rolled sheets (Aalco Metals Ltd, UK) were used in this work. The base material's microstructure is shown for the three directions in Figure 6-1a. The sheets were cut into the test geometries and through-holes were machined on these coupons. The 6 mm diameter through-hole geometry used in this work had a 120° chamfer on the top surface as the cavity for mechanical anchoring of the stake, and a 90° chamfer on the bottom surface to allow positive-radius stake bases to be used. The design of the hole is shown in Figure 6-1b. Relevant mechanical and physical properties of AA6082 are shown in Table 6-1.

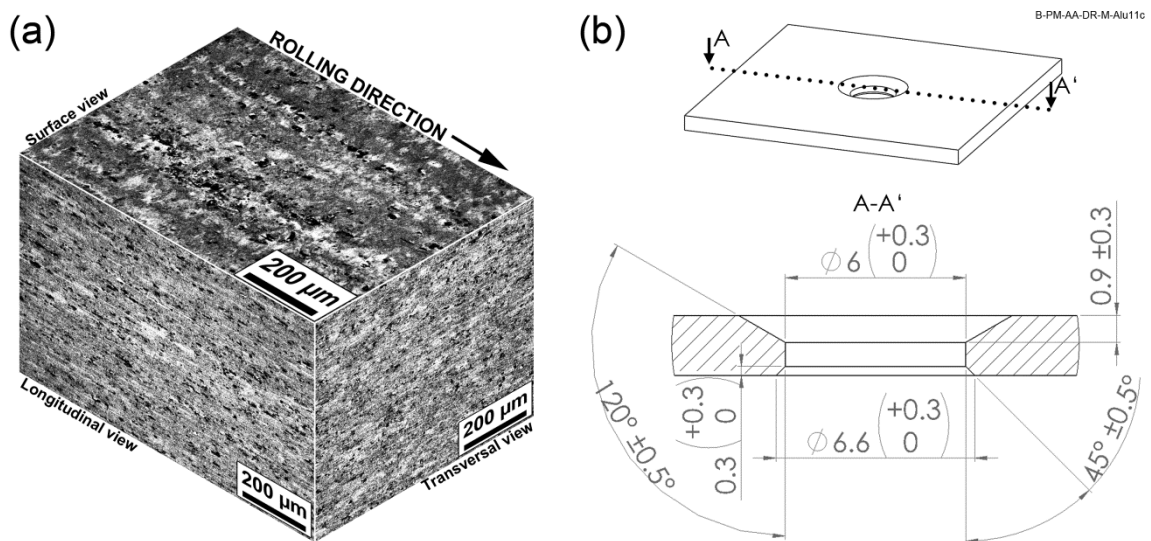


Figure 6-1: (a) Microstructure of the AA6082 rolled sheets (Airbus reagent, described in Section 6.3.3); (b) geometry of the through hole in the AA6082 sheets.

Table 6-1: Physical and mechanical properties of AA6082 in T6 condition.

Melting point [°C]	Thermal expansion coefficient [K ⁻¹]	Thermal conductivity [W.m ⁻¹ .K ⁻¹]	Yielding stress [MPa]	Ultimate tensile strength [MPa]
555 ^a	24 x 10 ⁻⁶ ^a	180 ^a	316 ± 6 ^b	343 ± 6 ^b

^a Data from the literature [178].

^b Experimentally obtained.

6.1.2 Polyetherimide (PEI)

6.35 mm thick extruded PEI plates (Duratron U1000 PEI, Quadrant Plastics, Switzerland) were used in this work. PEI plates were cut to specimen shapes, and the coupons were machined to create a 2 mm thick plate with an integral stud and a positive radius on its base, as illustrated in Figure 6-2a. The specimens were used in the as-received condition, presenting 0.48 ± 0.00 % moisture content in weight. The birefringence pattern shows low levels of residual stresses along the thickness, as a result of differential cooling in the extrusion process. The local mechanical properties are constant in this region, as shown by the microhardness overlay. The geometry of the stud is illustrated in Figure 6-2b. Key physical and mechanical properties of PEI are shown in Table 6-2.

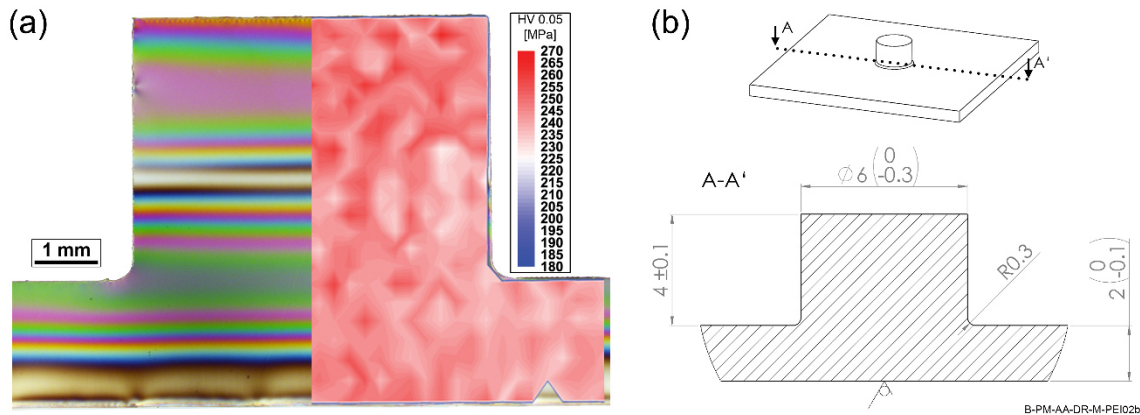


Figure 6-2: (a) Overlay picture showing birefringence pattern (right-hand side) and microhardness (left-hand side) distributions in the mid cross section of the stud; (b) geometry of the machined stud.

Table 6-2: Physical and mechanical properties of PEI (Duratron U1000).

Glass transition temperature (DSC) [°C]	Onset of decomposition (TGA) [°C]	Thermal expansion coefficient [K ⁻¹]	Thermal conductivity [W.m ⁻¹ .K ⁻¹]	Tensile yielding stress [MPa]	Compressive yielding stress [MPa]
216 ± 0.6 ^a	542 ± 1 ^a	50 x 10 ⁻⁶ b	0.24 b	123 ± 1 ^a	152 ^b

^a Experimentally obtained.

^b Data from the literature [179, 180].

6.1.3 Short carbon fiber reinforced PEI (PEI-CF)

Unreinforced PEI is transparent and amorphous; therefore the material flow in an F-ICJ process with it is difficult to assess. Reinforcements or fillers in the polymer matrix are useful to visualize material flow, since they are broken and/or reoriented during processing. PEI reinforced with 40 % in weight of short carbon fibers (RTP 2187, RTP Company, USA) was injection molded to shapes with the same stud geometry as the PEI specimens (Figure 6-2b). This material was only used for investigation of joint formation mechanisms (Section 6.3.9). Figure 6-3 shows the as-molded fiber orientation of the PEI-CF specimens, Table 6-3 shows key physical and mechanical properties of PEI-CF.

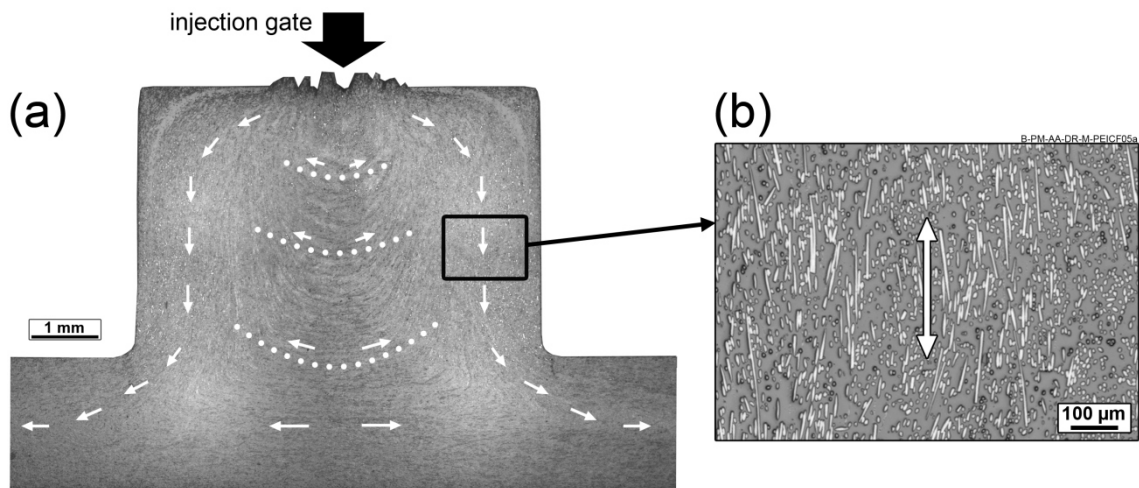


Figure 6-3: (a) As-molded fiber orientation at the PEI-CF specimens; (b) close-up view of the stud microstructure. White arrows represent local fiber orientation.

Table 6-3: Physical and mechanical properties of PEI-CF (RTP2187) [181].

Deflection temperature at 1.8 MPa [°C]	Ultimate tensile strength [MPa]	Ultimate flexural strength [MPa]
210	241	345

6.2 Joining equipment

6.2.1 Joining tool

Non-consumable tools for F-ICJ were machined from 316L stainless steel bars. This material was selected because of its low thermal conductivity (for steel). This reduces the heat sink effect of the tool, allowing the generated heat to be more efficiently used for stake formation. Moreover, 316L is an accessible, well-known steel grade. This material's composition and relevant properties are shown in Table 6-4 and Table 6-5, respectively.

Table 6-4: Chemical composition of 316L stainless steel [182].

Element	Cr	Ni	Mo	Mn	Si	C	P	S	Fe
Weight [%]	16.0- 18.0	10.0- 14.0	2.0- 3.0	2.0	1.0	0.03	0.045	0.03	Bal.

Table 6-5: Physical and mechanical properties of 316L stainless steel [182, 183].

Maximum service temperature [°C]	Thermal expansion coefficient [K ⁻¹]	Thermal conductivity [W.m ⁻¹ .K ⁻¹]	Yielding stress [MPa]	Ultimate tensile strength [MPa]
425	15.9 x 10 ⁻⁶	16.2	170-310	450-620

A simple F-ICJ tool design is comprised of a fastening shank, a set of frictional surfaces, and a clamping surface (Figure 6-4a). The fastening shank fits inside the spindle of the friction welding machine or other rotational drive system. The frictional surfaces (light-gray filled areas in Figure 6-4a) generate frictional heat upon contact with the thermoplastic stud. The clamping surface (dark-gray filled areas in Figure 6-4a) limits the final position of the tool during joining, and firmly clamps the joining partners together during consolidation. It extends slightly further than the top frictional surface of the tool, forming an outer ring that diminishes the loss of flash material to the surroundings. In time-limited processes, a feature known as the clamping surface limits the final position of the tool. Alternatively, in a displacement-limited process, the final position of the tool is defined beforehand, preferentially at a position where the clamping surface presses the two parts together.

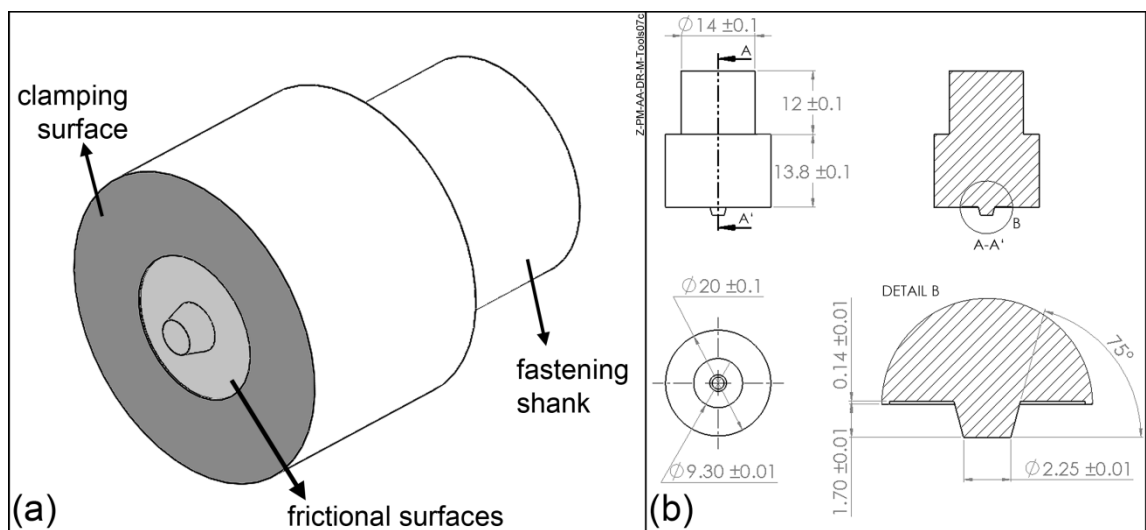


Figure 6-4: (a) Features of an F-ICJ non-consumable tool; (b) tool design used in this work.

This work used a conical-pin tool configuration as displayed in Figure 6-4b. This design was chosen based on previous studies that compared a conical-pin tool and a flat tool [184], and compared conical-pin tools of different angles and heights [185].

6.2.2 Single-spot joining for lab-scale investigation

For joining of single-spot overlap specimens a commercially available friction welding system (RSM400, Harms+Wende, Germany) was used. The RSM400 is a machine originally designed for the friction welding of metals and polymers (such as stud and spin welding). It uses a two-step joining cycle consisting of a friction phase limited by a preset frictional time, and a forging phase limited by a preset forging time. A joining cycle is defined at the RSM400 by the following process parameters: rotational speed, frictional time, frictional pressure, forging time, and forging pressure.

Joining pressures of up to 1.0 MPa (5.5 kN) for each of the phases can be set, as well as a rotational speed in the range of 6000-23400 rpm for the friction phase. At the end of the process the spindle retreats on command of the user, making it possible to use an additional holding time (axial force fixed at 0.3 kN) after the forging phase. A monitoring system is available that records the signals for rotational speed and joining pressure in F-ICJ. Further specifications of this system are available in Appendix B (Table B-1). An overview of the joining setup is shown in Figure 6-5a, and a detail view of the joining partners prior to joining is shown in Figure 6-5b.

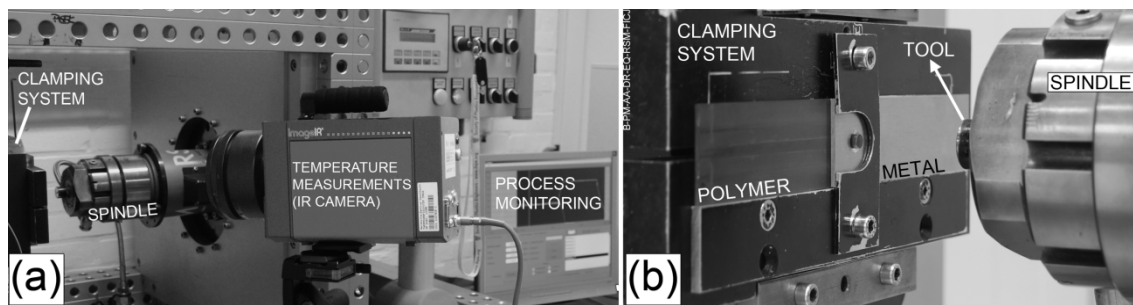


Figure 6-5: (a) Overview of the RSM400 system along with the monitoring devices; (b) close-up view of the spindle, tool, and the joining specimens in the clamping system.

A sample holder with a clamping system adaptable to all single-spot F-ICJ specimen geometries was used to position the joining partners. The center of the clamping system was aligned with the moving axis of the machine's spindle. The system in its standard setup does not work as a backing plate, having a 10 mm diameter hole underneath the stud (see Appendix C); in this way one-side accessibility can be simulated for F-ICJ, but an adjusting pin can be used to work as a backing surface. In the current joining jig (clamping system and sample holders) the alignment of the stud with the spindle was a manual process. This is, however, susceptible to misalignment due to the tolerances of the joining partners.

The RSM400 was used mainly for the investigation at coupon level of the process-related changes in the materials (Chapter 8), quasi-static mechanical behavior of F-ICJ joints (Chapter 9), process-microstructure-property relationships (Chapter 10), and for joint optimization (Section 11.1).

6.2.3 Multi-spot joining process for proof-of-concept scaling up

In order to pursue the preliminary assessment of F-ICJ as a series production process, the scaling up of F-ICJ to multi-spot joining cycles was addressed. However, due to limitations in specimen positioning and process automation, the RSM400 is impractical for multi-spot joining in its current configuration. In the course of this work, a new automated friction welding gantry system [81] was made available and adapted to the F-ICJ process. The automated gantry system (RNA, H.Loitz-Robotik, Germany) with a commercially available friction welding head (RSM410, Harms+Wende, Germany) was used for the scale-up investigation. A joining cycle is defined at the RNA gantry by the following process parameters: rotational speed, frictional time, frictional force, forging time, and forging force.

The gantry system works with rotational speeds in the range 6000-21000 rpm and axial forces up to 24 kN. Monitoring curves from rotational speed, joining force and spindle displacement can be obtained for F-ICJ through the user interface. Further specifications of this system are available in Appendix B (Table B-2). An overview of the system is shown in Figure 6-6a. XYZ coordinates can be programmed at the RNA's user interface for up to 20 individual positions. In this manner, sequential multi-spot joints can be produced (Figure 6-6b), making possible the

joining of small parts and subcomponents up to 0.5 m³. As in the RSM400, time-limited processing conditions were used.

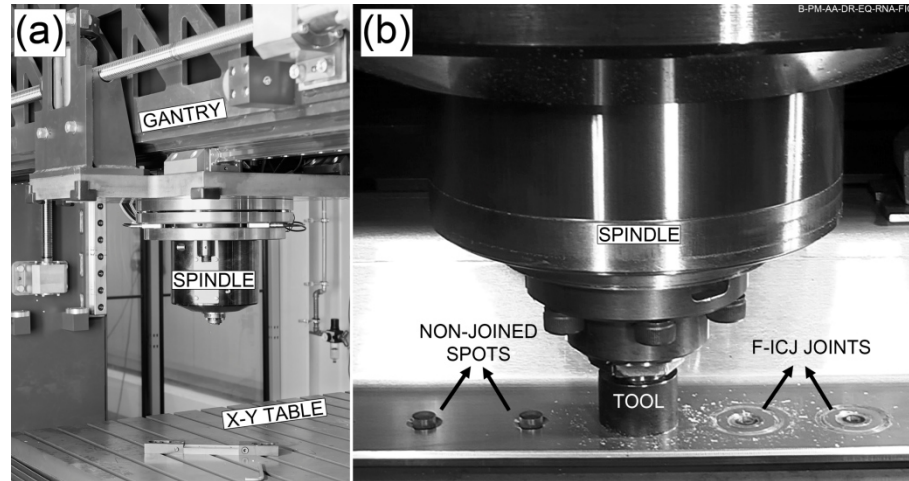


Figure 6-6: (a) RNA gantry system with a friction welding spindle and X-Y moveable table; (b) close-up of a sequential multi-spot joining process.

The RNA gantry was used at coupon level for the investigation of joint formation mechanisms (Chapter 7) applying a stop-action procedure. Some of the results of changes in the polymeric partner (Section 8.2) and of the quasi-static mechanical behavior of F-ICJ joints (Chapter 9) were performed on joints produced by the RNA gantry. It was mainly used for the assembly of multi-spot subcomponents in the proof of concept phase of this work (Chapter 11).

6.3 Methods

6.3.1 Joining procedure

Prior to joining, PEI workpieces were cleaned with water and dried with pressurized air to avoid swelling from solvents, while AA6082 workpieces were wiped with acetone.

For the single-spot joints, the workpieces were pre-assembled and manually positioned in the clamping system; whenever necessary the position was adjusted to align the stud with the spindle axis. The parameters were setup on the RSM400 and the process was manually started. After the end of the forging/consolidation time, 7.5 seconds were used as an additional holding time prior to tool retreat. The joint was subsequently removed from the clamping system, documented and prepared for investigation. The same procedure was performed for single-spot joints joined on the RNA gantry during joint formation and proof of concept studies.

Multi-spot joints on the RNA gantry were pre-assembled and positioned on the XY table. Stud positions for the corner studs (1-4) were determined by moving the tool while attached to the

spindle, and aligning the tool with the corner studs. The positions of the remaining studs were interpolated from the corner-stud coordinates. With all 20 target positions defined and the parameters setup, the sequential joining process was started. At the end of the process the subcomponent was removed, documented and prepared for further analyses.

6.3.2 Monitoring of joining process temperature

Preliminary trials of temperature monitoring with thermocouples in the polymer workpiece proved problematic and not reproducible. The polymer's low conductivity and varying microstructure often provided no reliable measurement of process temperature. Thermal imaging has been shown to produce reliable results that can be correlated to the heat input in a joining process [79, 186]. Therefore, in order to establish an estimate of the joining process temperature an infrared thermal camera (Image IR8800, InfraTec, Germany) was used to monitor tool and stake temperatures. Both the tool and the aluminum workpiece surfaces were painted with a matt black paint to avoid reflectance effects. The camera was placed at a distance of about 0.5 m of single-spot specimens, with a line of view at approximately 30° from the surface plane of the joints, capturing images as shown in Figure 6-7a and b. A temperature calibration in the range of 20-300 °C was used for all experiments, except for one stop-action joint that exceeded this range; in that case the joint was repeated with a calibration of 150-700 °C. The camera recorded at a frame rate of 10 fps, from the start of the process and until the stake temperature fell below 30 °C. The maximum temperature at the stake after tool retreat was recorded as the stake temperature (ST) value for a joint (Figure 6-7c), which was used as the estimated heat input.

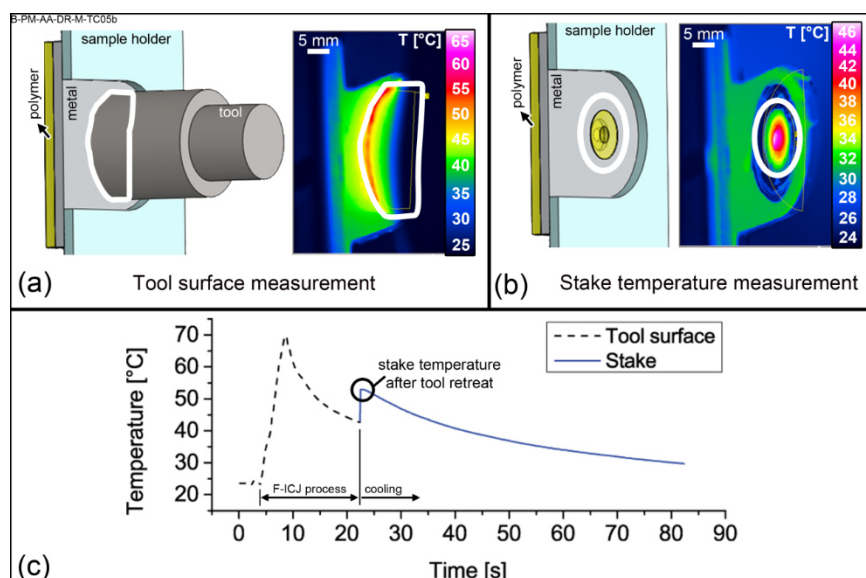


Figure 6-7: Schematics of the temperature measurement setup and snapshot of the camera's view for (a) tool surface temperature; and (b) stake temperature. White areas are the measurement regions; (c) example of the measurement curve.

6.3.3 Microstructural analysis

Microstructural analyses were performed on the cross-section of a simple overlap joint configuration (Figure 6-8a). This geometry is referred to as the microstructural analysis specimen (MA). The MA specimens were cut with a precision saw and ground and polished with standard methods. For microstructural investigations of the aluminum joining partner, the grain structure was revealed using electrolytical etching with Barker's reagent (5 ml HBF_4 in 200 ml distilled water, $U = 30 \text{ V}$ for 120 seconds) and chemical etching with Airbus reagent (5 ml HF in 95 ml H_2O and 10 ml H_2SO_4 in 90 ml H_2O). Several types of microstructural analyses were used for the polymer, according to the objective of the investigation. Reflected-light optical microscopy (RLOM) was used for general cross-sectional observation of the joints and for measurement of microstructural features. Transmitted-light optical microscopy (TLOM) was used with thin sections of the joints (about 1 mm thick) to observe joint formation effects in the stop-action study. For RLOM and TLOM a Leica DM IRM optical microscope (Leica Microsystems, Germany) was used. Laser scanning confocal microscopy (LSCM, model VK-9700, Keyence, Japan) and scanning electron microscopy with secondary electrons (SE-SEM, model Quanta FEG 650, FEI, USA) were used for understanding microstructural features.

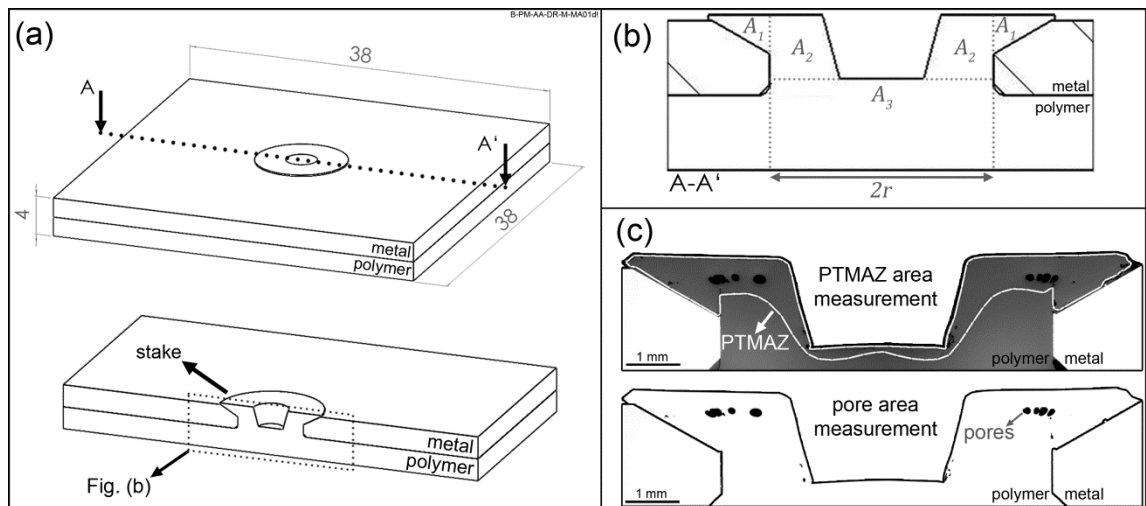


Figure 6-8: (a) Microstructural analysis (MA) specimen; (b) schematic of the cross-section of a joint and the area used for microstructural measurements; (c) example of measurements of the PTMAZ area and the pore area in an F-ICJ joint.

The relative pore area RA_{pore} and relative PTMAZ (shear layer) area RA_{PTMAZ} were defined as the extent of the stake's cross-sectional area in which these features are present. The joint's cross-sectional area A_{CS} was divided into sub-areas A_1 , A_2 , and A_3 from Figure 6-8b. Since the materiallographic procedure does not always accomplish a perfectly centered cross-section, the sub-areas A_1 , A_2 , and A_3 have to be normalized in respect to the specimen's through-hole diameter $2r$ (see Figure 6-8b). The PTMAZ area A_{PTMAZ} and total pore area A_{pore} measured on a specimen (as in Figure 6-8c) were divided by the cross-sectional area A_{CS} to obtain the values of relative PTMAZ area RA_{PTMAZ} and relative pore area RA_{pore} for two replicates. The

equations for the microstructural features are shown in Table 6-6. ImageJ software was used for the measurements of the areas and cross-sectional diameter from RLOM images.

Table 6-6: Equations for measurement of microstructural features.

Feature	Cross-sectional area A_{CS} [mm ²]	Relative PTMAZ area RA_{PTMAZ} [%]	Relative pore area RA_{pore} [%]
Equation	$2A_1 + 2A_2 + A_3$	$\left(\frac{A_{PTMAZ}}{A_{CS}}\right) \times 100 \%$	$\left(\frac{A_{pore}}{A_{CS}}\right) \times 100 \%$

6.3.4 Synchrotron radiation X-ray computed microtomography (SR- μ CT)

SR- μ CT analysis of selected specimens was used for further understanding of material flow in F-ICJ joints. Microstructural analysis specimens (Figure 6-8a) were milled to a cylindrical shape with a diameter of 10 mm. Microtomographic analysis was performed at the High Energy Materials Science (HEMS) beamline at PETRA III [187]. The monochromatic X-ray beam is attenuated by the sample and captured by a CCD camera, after being transformed into visible light by a fluorescent screen.

For tomographic reconstruction of the 3D datasets, the algorithm “back projection of filtered projections” [188] was used. 32-bit floating-point image stacks with isotropic voxel size of 3.77 μm^3 were obtained in these measurements. Segmentation and further image processing was performed using the open-source software FIJI [189] and applying mask-image filters for further visualization and the volume rendering in VG Studio MAX 2.2 (Volume Graphics, Germany)

6.3.5 Qualitative analysis of residual stresses

Transmitted-light optical microscopy with crossed polarizers (CP-TLOM) was used to qualitatively evaluate residual stress fields in the polymeric joining partner. A standard microscope filament lamp, producing a continuous white light spectrum, was used as a light source. Crossed polarizers reveal the optical anisotropy in the material, seen as a color pattern. This optical anisotropy is denominated birefringence, and transparent polymers such as PEI present birefringence from the application of stresses [131, 190]. The original color pattern observed in the PEI base material is shown in the right-hand side of Figure 6-9. Fringes of the same color are denominated isochromatics. Each isochromatic is associated with a fringe order and indicates a stress level that resulted from processing or thermal effects. For the extruded PEI plates in this study, zero-order fringes (black fringes) are seen at the color image, both at the stud’s mid-height and close to the bottom surface. An almost symmetrical color pattern towards both top and bottom surfaces is observed, with any observed asymmetry being due to the machining of the top surface. This configuration is a typical result of the skin-core effect of the extrusion process [125].

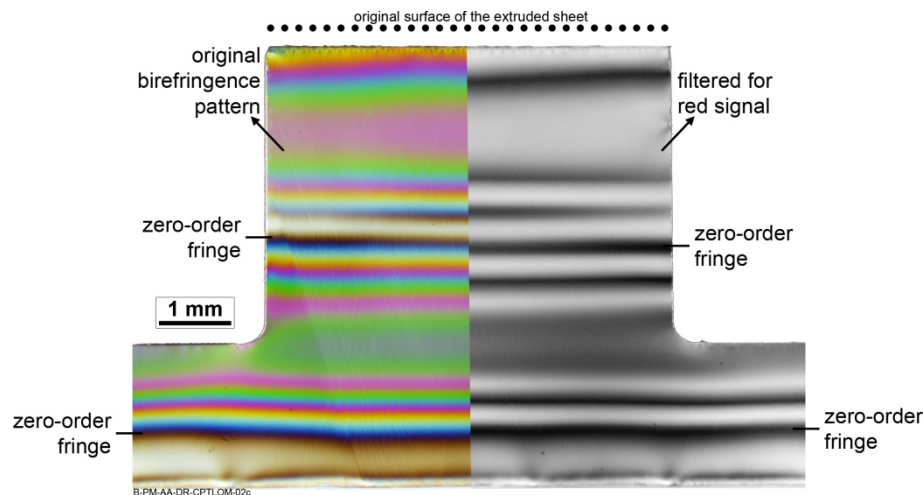


Figure 6-9: Transmitted-light optical microscopy with crossed polarizers (CP-TLOM) of the PEI base material. Left-hand image is the original output; right-hand image is filtered for red signal only.

The number of fringe orders can be analyzed for a qualitative analysis of the residual stress levels in the joints [191]. In order to facilitate the visualization of the number of fringes in this work, a digital filter for the red signal was applied on the CP-TLOM images, as seen in the right-hand side of Figure 6-9. With this simplified method, the approximated fringe orders can be more clearly distinguished. The residual stress fields were qualitatively evaluated to assist in interpretation of local mechanical properties and failure mechanisms in the joints.

6.3.6 Physical-chemical changes on the polymer partner

Differential scanning calorimetry (DSC) and thermogravimetric analysis (TGA) were carried out to identify the physical-chemical properties of as-received PEI and the processed polymer. Shards of material from the PTMAZ were extracted with a scalpel from the volume above the chamfer, roughly the volume corresponding to areas A_1 from Figure 6-8b. The properties of the processed polymer were compared to the as-received material to identify process-related changes.

DSC was carried out with a heat flux DSC 200 F3 Maia (Netzsch, Germany). The runs were performed on 5.0 ± 0.1 mg samples, using a heating rate of $20 \text{ K}\cdot\text{min}^{-1}$ from $30 \text{ }^\circ\text{C}$ to $250 \text{ }^\circ\text{C}$ in inert atmosphere (N_2 , $20 \text{ ml}\cdot\text{min}^{-1}$). Two heating and cooling cycles were used. The first heating cycle was used to identify the in-service properties of the F-ICJ-processed PEI. The second heating cycle eliminates any previous thermal history and specimen preparation effects and allows identification of evidences of thermomechanical degradation [192]. Mid-point glass transition temperatures (T_g) for first and second heating cycles were recorded.

TGA was carried out with a TG 209 F3 Tarsus (Netzsch, Germany). The runs were carried out on 5.0 ± 0.1 mg samples, using a heating rate of $20 \text{ K}\cdot\text{min}^{-1}$ from $25 \text{ }^\circ\text{C}$ to $800 \text{ }^\circ\text{C}$ in inert

atmosphere (N_2 , 20 ml.min⁻¹). The temperature for onset of decomposition was recorded, in order to investigate changes in the decomposition behavior.

6.3.7 Local mechanical properties

Changes in local mechanical properties were investigated using Vickers indentation microhardness. Indentation hardness is a useful method for determining local structural changes in polymers [193]. The testing procedure was performed according to ASTM E384-10e1 [194] using an indentation load of 0.495 N, indentation distance of 200 μ m, and a holding time of 15 s with a ZHV microindenter (Zwick Roell, Germany). Microhardness maps were obtained from the two measurement configurations shown in Figure 6-10a and b. The standard configuration with five profiles (Figure 6-10a) was used for most of the specimens, whereas a detailed configuration (Figure 6-10b) was used for chosen conditions. Stereomicroscopy images of indented MA specimens were used to correlate the positions of the indentations with the microstructure (Figure 6-10c). The microhardness values were associated with the indentation's coordinates to create contour plots of the distribution of local strength and define the boundaries of microstructural zones.

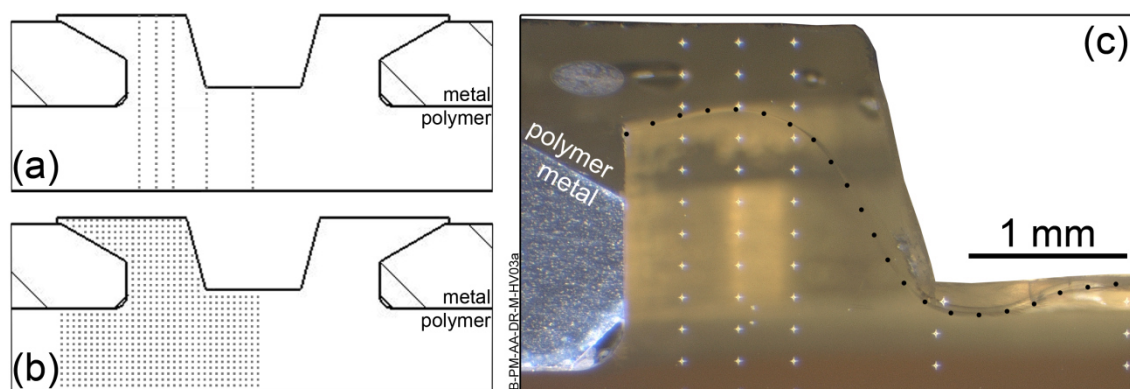


Figure 6-10: Local mechanical property measurements. (a) Standard map of five profiles; (b) detailed map; (c) microstructural zones and indentation positions observed with a stereomicroscope for a five-line profile as from (a). The black dotted line follows the shear layer boundary.

For a better understanding of the local properties of the microstructural zones, 3D profiles of chosen indentations in each region of interest were analyzed using LSCM. Elastic and plastic responses of the indented material were interpreted and correlated with local mechanical properties.

6.3.8 Quasi-static global mechanical behavior

Quasi-static mechanical behavior of F-ICJ joints was investigated under two loading conditions, in similar fashion to the tests reported in the literature [98, 99, 113]. Specimen geometry for each condition is shown in Figure 6-11. Lap shear (LS) performance of the joints was evaluated using a universal testing machine (model 1478, Zwick Roell, Germany) at room temperature and a crosshead speed of 2 mm.min⁻¹; the test procedure was based on ASTM D5961-10 [195]. A digital image correlation system (DIC – Aramis, GOM, Germany) was used to monitor the deformation of the polymer workpiece during the LS tests. The surfaces of interest were painted with a random black dotted pattern over a white background. The bottom surface of the polymer workpiece was painted to determine the strain distribution at this region. For out-of-plane deflection, the side surfaces of the polymer and metal workpieces of LS specimens were painted. Stake-head strength was investigated using cross-tensile (CT) testing on the universal testing machine at room temperature and crosshead speed of 2 mm.min⁻¹. The procedure was based on the standard DIN EN ISO 14272 [196].

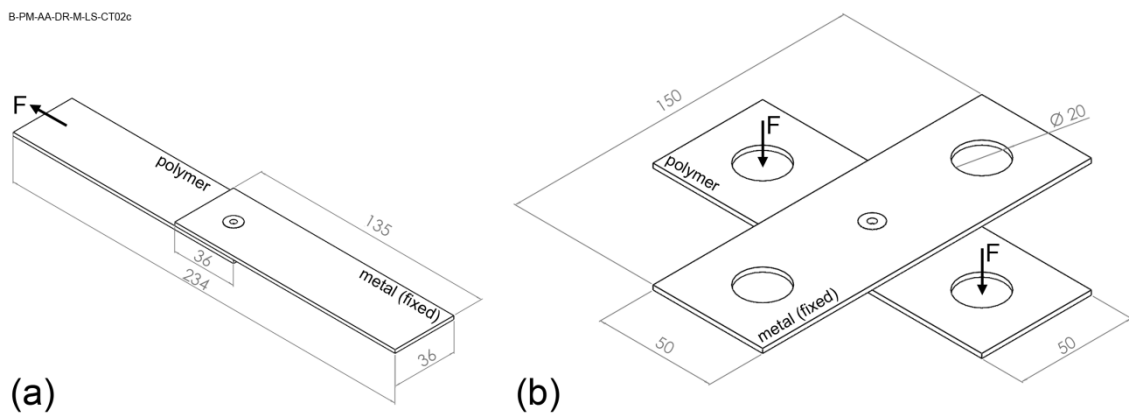


Figure 6-11: (a) Lap shear (LS) specimen; (b) cross tensile (CT) specimen.

The fracture surfaces of the broken specimens were analyzed to identify the micromechanisms dictating crack propagation. The regions of interest were observed in an SEM using secondary electrons (Quanta FEG 650, FEI, USA). The polymeric specimens were sputtered with a thin layer of gold and ground with copper tape and/or silver paste to improve conductivity and reduce charging at the surfaces. Energy-dispersive X-ray spectroscopy (EDS, system EDAX TEAM, EDAX, USA) coupled to the SEM was used to qualitatively identify the composition of particles on the fracture surfaces. Overviews of chosen fracture surfaces were scanned with the LSCM to create 3D images of the failures (VK-9700, Keyence, Japan).

6.3.9 Joint formation mechanisms

A joining equipment stop-action procedure was adopted to obtain further in-depth information of the joint formation mechanisms. The stop-action study consists of stopping the joining process at specific stages and observing the joint formation and microstructural

characteristics. One joint is produced for each step under investigation. Stop-action joints from relevant moments of the joining process were obtained for the process configurations described in Figure 4-4. Stake temperature measurements, microstructural evolution and material flow were analyzed to describe joint formation.

6.3.10 Effect of process parameters on joint properties

A statistical approach was chosen to evaluate the effects of the process parameters on joint characteristics. In the current configuration, F-ICJ involves five main process parameters: rotational speed (RS), frictional time (FT), forging time (FoT), forging pressure (FoP), and frictional pressure (FP). For a thorough understanding of the main effects and interactions of these parameters, a fractional factorial design of experiments (FF-DoE) was chosen [197]. In previous works [185], screening experiments using a one-factor-at-a-time approach were used to determine a parameter window for the FF-DoE. Three replicates of the principal fraction of a 2^{5-1} half factorial (resolution V, Table 6-7) were performed for each of the three responses: stake temperature (ST), ultimate lap-shear force (ULSF), and ultimate cross-tensile force (UCTF). ST is used as an indicator of process temperature (or indirectly, heat input) to correlate with microstructural changes in MA specimens. ULSF and UCTF measure the joint's mechanical performance. The replicates were performed in a randomized order. The analysis of the FF-DoE was performed with Minitab statistical software.

Table 6-7: Levels of the fractional factorial design of experiments.

Level	Factors				
	RS [rpm]	FT [ms]	FoT [ms]	FoP [MPa (N)]	FP [MPa (N)]
-1	8000	2500	2500	0.7 (3733)	0.3 (1525)
+1	12000	5000	5000	1.0 (5363)	0.5 (2726)

Regression models for the FF-DoE responses were obtained with Minitab software. Stepwise regression through backward elimination of predictors [197] was used in the full regression models, in order to achieve a reduced model. The objective was to obtain a reduced model with satisfactory prediction ability and without involving superfluous predictors, which improves the explanatory power of the model for interpretation of the results [197, 198]. Starting from the full model, including all main factors and all second level interactions, the least significant (higher p-values) factors were excluded from the model in a stepwise manner until all predictors presented p-values smaller than 0.1. All steps of backward elimination were analyzed, and the reduced models with lowest standard error of the regression (S) and highest values of adjusted R^2 were selected. These criteria were used because models with lower S values can predict a response more accurately, and models with high values of adjusted R^2 indicate that the predictors in the model add explanatory power to the model, meaning a simpler model with low error [197]. The distribution of residuals was analyzed for all models to ensure model adequacy. The reduced regression models were validated using additional

experiments within the FF-DoE processing window, with three replicates for the ST model, and five replicates for the ULSF and UCTF models. The explanatory power of each validated model for its response was assessed.

To evaluate the significance of the effects of factors on the responses an analysis of variance (ANOVA) using partial F-tests for each predictor of the reduced models was used at 5 % confidence level. The influence of the significant factors and second level interactions on the responses ST, ULSF and UCTF was described in terms of the joint formation mechanisms and local changes in the polymer. In this DoE, the effects of the main factors and second level interactions are aliased with fourth and third level interactions; however these interactions are less likely to be relevant [197] and were not investigated.

6.3.11 Joint optimization

For the purpose of achieving a high-strength joining condition, the validated statistical models were used with a desirability function [199, 200] from Minitab to obtain an optimized joint with high ULSF and UCTF. The lowest acceptable limit for the desirability function was defined as the average ultimate force observed for all LS and CT specimens. The ideal value defined in the desirability function was set to the maximum force predictable by the reduced models [200]. Stake temperature for all specimen geometries was also measured to verify the similarity of heat input for the optimized condition in all testing geometries.

6.3.12 Process transferability

This PhD work focused on coupon-scale development of the F-ICJ technology, which was performed with the RSM400 system (Section 6.2.2). As previously explained, the lab-scale RSM400 friction joining equipment is not appropriate for automated joining of multi-spot structures. For the proof of concept of the F-ICJ technology in multi-spot structures, the knowledge and joining conditions produced at the RSM400 were transferred to the automated RNA gantry system.

In order to try to reproduce the RSM400 joint on the RNA gantry system, a parameter setup was defined that corresponds to the actual rotational speed and joining force curves from the RSM400 system. The rotational speed and joining force curves are defined by the controlling parameters (RS, FT, FP, FoT, FoP) for the process, therefore a match between these curves in both joining systems indicates satisfactory setup reproduction [81]. The actual values measured by the RSM400's monitoring system were used, and the average RS and durations of the stud meltdown and dwell time for a two-phase process were determined. As the RSM400 uses values of pressure, its axial force was measured with a load cell over its operational range and a calibration curve was established for pressure-to-force conversion.

In order to assess the effect of any differences in functioning of the machines on material properties, the energy input from each machine was compared. A torque sensor (model 9049, Kistler, Switzerland) was used to obtain the materials' torque response for the matching joining

cycles of both machines. Equation (3-6) was adapted to the F-ICJ process, yielding Equation (6-1) for energy input in F-ICJ. The frictional contribution can be described by the product of the average angular velocity $\bar{\omega}$ and the integral of the torque M over the frictional time FT . The deformational contribution is calculated by the product of the frictional force FF and the integral of the tool displacement rate over FT .

$$E_{F-ICJ} = \bar{\omega} \int_{t_0}^{FT} M dt + FF \int_{t_0}^{FT} v dt = M_{total} \bar{\omega} + FF \Delta x [J] \quad (6-1)$$

Both constants FF and $\bar{\omega}$ are calculated from the experimental curves during frictional time. The tool displacement Δx is constant for the same joint and tool geometry: it is the distance covered by the clamping surface from start of friction until it touches the metal part, amounting nominally to 3.56 mm. In this work the maximum FF used was 2726 N, therefore the deformational component $FF \Delta x$ contributed with a maximum of 10 J to energy input, which amounts to less than 1% of total energy input. For simplification, only the rotational component $M_{total} \bar{\omega}$ was used in this work.

The total torque M_{total} is experimentally obtained from the torque curves as shown in Figure 6-12. It is obtained from the friction phase, including both stud meltdown and dwell time. Especially during dwell time, part of the measured torque is from the tool rubbing on the metal surface. While it does not directly represent energy applied to the polymer, it influences heat input to the stake by heating the metal part. An increase in temperature of the metal part either indirectly heats the polymer by conduction, or decreases the efficiency of heat loss from the stake to the metal part. The peak in torque observed during deceleration is the result of a combined effect of polymer solidification and higher coefficient of friction at lower speeds, making its contribution to heat generation complex to estimate. Therefore, the deceleration contribution is neglected and only frictional time was used for calculating total torque M_{total} .

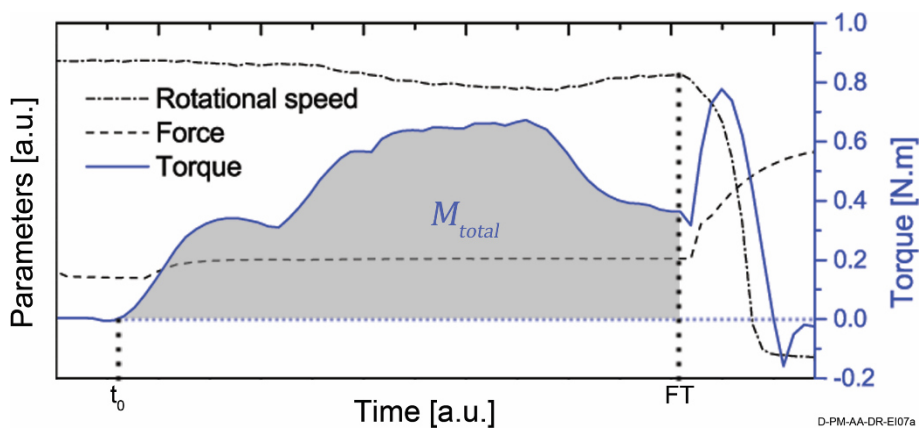


Figure 6-12: Calculation of total torque during frictional time from the monitoring process curves.

Finally, the transferability experiment was performed by comparison of monitoring curves, energy input, microstructural and mechanical properties of the joints.

6.3.13 Exploratory scaling up of the process to multi-spot subcomponents

To explore the effects of applying F-ICJ on a multi-spot subcomponent level, an exploratory scaling up study was conceived. A sheet and stiffener specimen geometry was selected as an approximate version of skin and stringer assemblies in aircraft, and B or C columns in cars. A 20-stake subcomponent was designed, based on preliminary finite element method (FEM) analyses [201] (Appendix D) and similar studies from the literature [45, 46]. The subcomponent structure was joined with the RNA gantry system (Section 6.2.3) using the optimized joining condition that resulted from the investigations described in Section 6.3.11. The specimen geometry is shown in Figure 6-13a and a schematic view is illustrated in Figure 6-13b. The position of each stake was programmed at the RNA gantry interface, and the stakes were automatically joined in the order shown in Figure 6-13c.

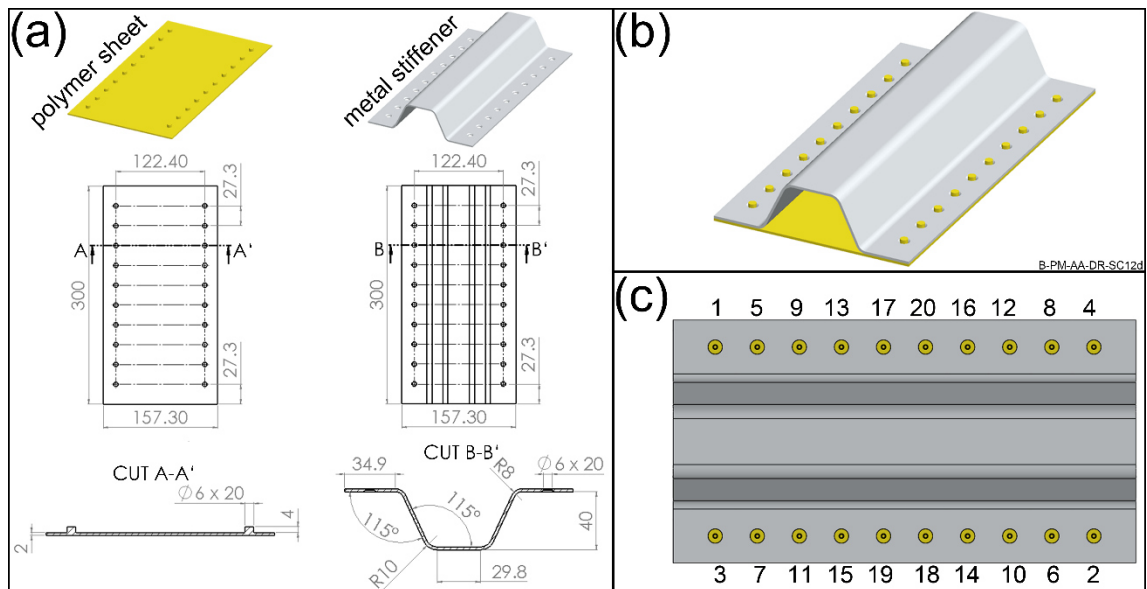


Figure 6-13: (a) Subcomponent specimen geometry. Stud and hole geometry are the same as the coupon specimens; (b) schematic view of pre-assembled subcomponent; (c) joining order.

In order to investigate possible deviations from a single-spot process, stake and tool temperatures were measured with an infrared thermal camera; in the same fashion as the single-spot joints. The camera was placed at a distance of 1.7 m of the multi-spot subcomponents, and at an angle of approximately 20° to the XY table. This configuration permitted the visualization of six stakes, covering the temperature measurement region shown in Figure 6-14. Stake temperatures from these stakes and the maximum tool temperature after joining were recorded.

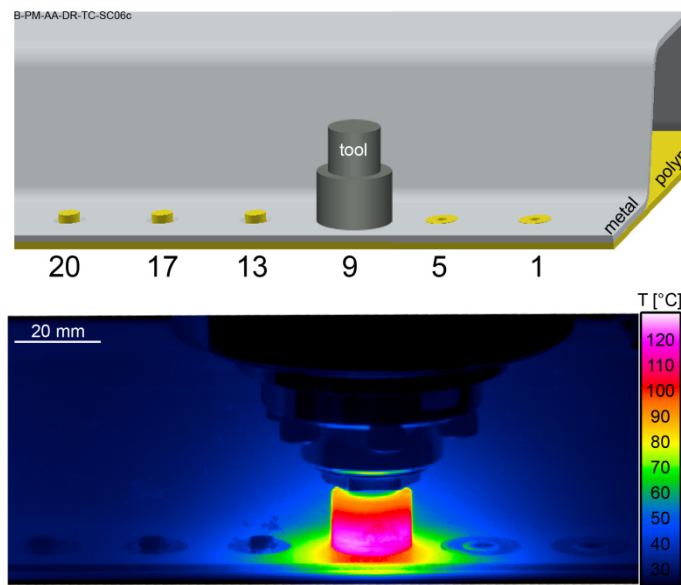


Figure 6-14: Schematic view and snapshot of the temperature measurement region for multi-spot subcomponents.

Four-point bending tests, based on [45, 46], were selected to evaluate the quasi-static mechanical behavior of the joined subcomponents. This mechanical test was chosen as an exploratory tool to obtain a first impression of the mechanical behavior in F-ICJ metal-polymer hybrid structures; the actual structural performance of a stringer-skin or B/C column structure was beyond the scope of this preliminary analysis. The test setup is shown in Figure 6-15. Tests were performed on a universal testing machine (model 1484, Zwick Roell, Germany) at a speed of $40 \text{ mm} \cdot \text{min}^{-1}$.

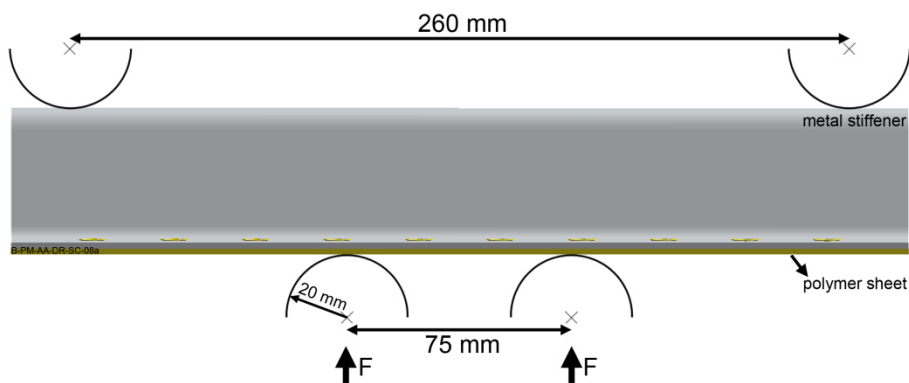


Figure 6-15: Four-point bending of multi-spot subcomponents.

CHAPTER 7. INVESTIGATION OF THE JOINT FORMATION MECHANISMS IN F-ICJ

A thermomechanical process such as F-ICJ induces great changes to the structure of the materials. In order to better understand the joint formation mechanisms and material changes, the sequence of events involved in the process were studied. The process configurations described in Figure 4-4 were explored, analyzing specimens from the stop-action procedure, using microstructural analysis, temperature measurements, and joining process diagrams, as described in Section 6.3.9. This study was performed with unreinforced PEI and PEI-CF, while the metallic partner was aluminum 6082-T6.

7.1 General aspects of joint formation in F-ICJ

Based on the customary friction-based joining process configurations that were described in Section 4.1, F-ICJ joints were produced using both two and three phase configurations for the material combination of interest. The typical appearance of joints created with two and three phase process configurations are shown in Figure 7-1. The surface of the two-phase process joint is smooth and flush to the aluminum surface (Figure 7-1a). The three-phase process joint has a stake head with a rougher surface, and it protrudes above the aluminum surface (Figure 7-1b). In addition, only partial cavity filling is achieved for a three-phase process. A brief analysis of the microstructure of these joints is shown in Figure 7-1c and Figure 7-1d. The birefringence pattern observed by transmitted-light optical microscopy with crossed polarizers (CP-TLOM) helps to observe the extension of cold forming in each case (white dotted boundaries). A significantly larger cold-formed volume is observed for the three-phase process configuration (Figure 7-1d). Cold forming in staking-based methods has several disadvantages related to residual stresses and recovery, which have previously been addressed in Section 3.3; therefore a smaller or absent cold-formed volume is generally preferred.

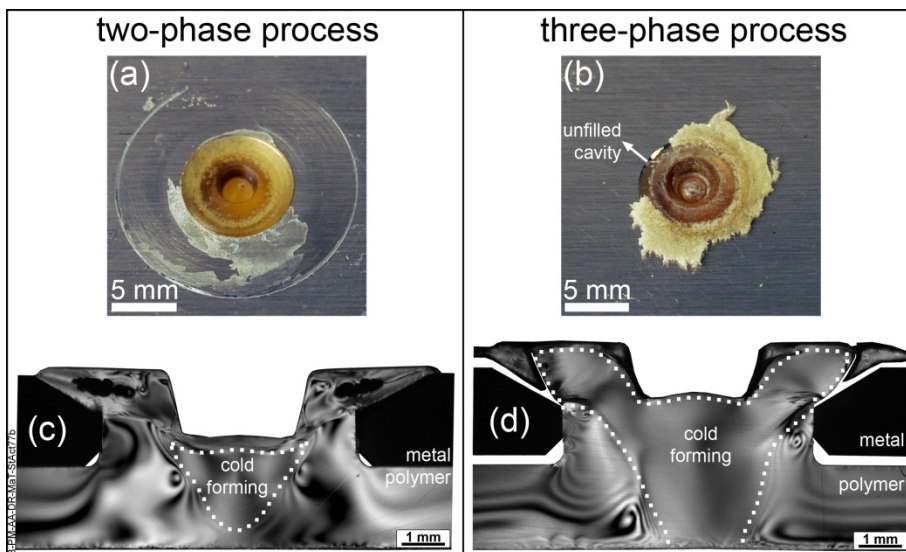


Figure 7-1: Surface finishing in joints from: (a) two-phase process; and (b) three-phase process; and birefringence pattern in joints from: (c) two-phase process; and (d) three-phase process. Boundaries of the highly stressed cold-formed zones are marked with square dotted lines (CP-TLOM images).

Figure 7-1 represents the general behavior observed in the course of this work for each process configuration. It was concluded that for a brittle, glassy polymer such as PEI the two-phase process configuration (Figure 4-4a and Figure 7-1a and c) can create sound joints over a large range of process parameters. By contrast, the three-phase process configuration (Figure 4-4b and Figure 7-1b and d) could only create joints with excessive cold forming of the stake. The result is a joint with a large volume under plastic strain and an excessive amount of discontinuities (shear bands, remnant weld line). However, a sound joint of PEI could possibly be created with the three-phase configuration, for example by using longer cycles in order to effectively heat the stud and avoid excessive plastic deformation. As for this material combination the two-phase process configuration (friction and consolidation phases) shows more potential to create sound joints, in this chapter only this configuration will be investigated in further detail. An analysis of the joint formation mechanisms for a three-phase process configuration is available in Appendix E.

7.2 Joint formation using a two-phase process configuration (friction and consolidation phases)

For this investigation a two-phase process configuration (described in Section 4.1) with a parameter set that creates a sound joint with above-average mechanical performance was selected. Figure 7-2a shows the process diagram for the F-ICJ joining cycle with this process configuration, and Figure 7-2b details only the friction phase of the same diagram. The diagrams from Figure 7-2 show monitoring signals from tool displacement (black squares), joining force (green disks), and rotational speed (blue triangles). Additionally, stake temperature measurements (orange downward triangles) from seven stages of the stop-action

study were performed (Figure 7-2a), with four of them during the friction phase (Figure 7-2b). The transition from friction to consolidation phase is distinguished by a decrease in rotational speed. In this example, the forging force is higher than the frictional force, so an increase in joining force is also seen at the phase transition. Rotational speed and joining force are setup process parameters. The tool displacement and stake temperature are observed responses. In Figure 7-2b five stages of the friction phase are marked with gray stars on the tool displacement curve. These points will be used to understand the joint formation mechanisms described in this section, using the stop-action study.

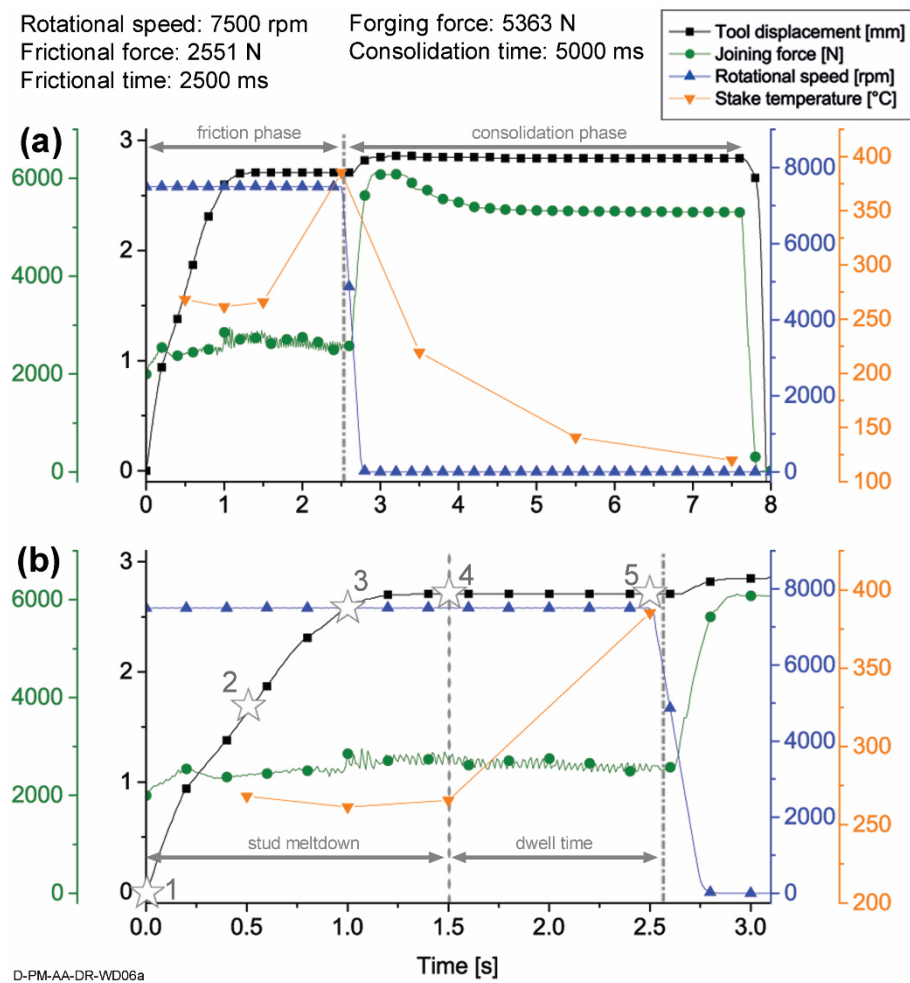


Figure 7-2: (a) Process diagram for a two-phase F-ICJ joining configuration; (b) detail of curves during the friction phase.

7.2.1 Friction phase: stud meltdown

In Figure 7-2a the whole joining cycle is shown, which consists of a friction phase (RS: 7500 rpm, FF: 2551 N, FT: 2500 ms) followed by a consolidation phase (FoF: 5363 N, CoT: 5000 ms). During the friction phase (Figure 7-2b) there are two steps: a “stud meltdown” step followed by a “dwell time” step. During the stud meltdown (Stages 1 to 4 in Figure 7-2b), the

tool plasticizes and deforms the stud into the desired stake geometry until the clamping surface touches the top surface of the joining partner. The tool displacement achieves a plateau (Stage 4 of the friction phase) while the tool still rotates. The stud meltdown rate before this plateau is of 1.97 mm/s. At this point the tool does not move further forward, because its clamping surface is slightly rubbing against the metallic partner's surface. Stake temperature measurements show only a slight fluctuation of around 250-270 °C over the course of the stud meltdown step. This kind of equilibrium in frictional processes is dependent on the influence of RS and force on local properties of the materials. This is in accordance with the self-limitation of heat generation during viscous friction [117], as described in Section 3.4.1 (Equations (3-2) and (3-4)). Moreover, in a metal-polymer sliding friction system, the coefficient of friction is reduced at higher relative velocities and axial pressures, reaching a temperature equilibrium [202].

Although significant heat is generated at the polymer-tool interface, part of it is conducted to heat sinks such as the tool, clamping system, and spindle, in the same manner as other friction-based welding processes [123]. Stake temperatures measured during the stud meltdown step range between 250-270 °C, which is about 50 °C above the glass transition temperature and about 270 °C below the onset of decomposition of PEI. Transmitted-light optical microscopy (TLOM) images of the cross-sections from Stages 1 to 4 of the stud meltdown step, obtained from the stop-action procedure, are shown in Figure 7-3.

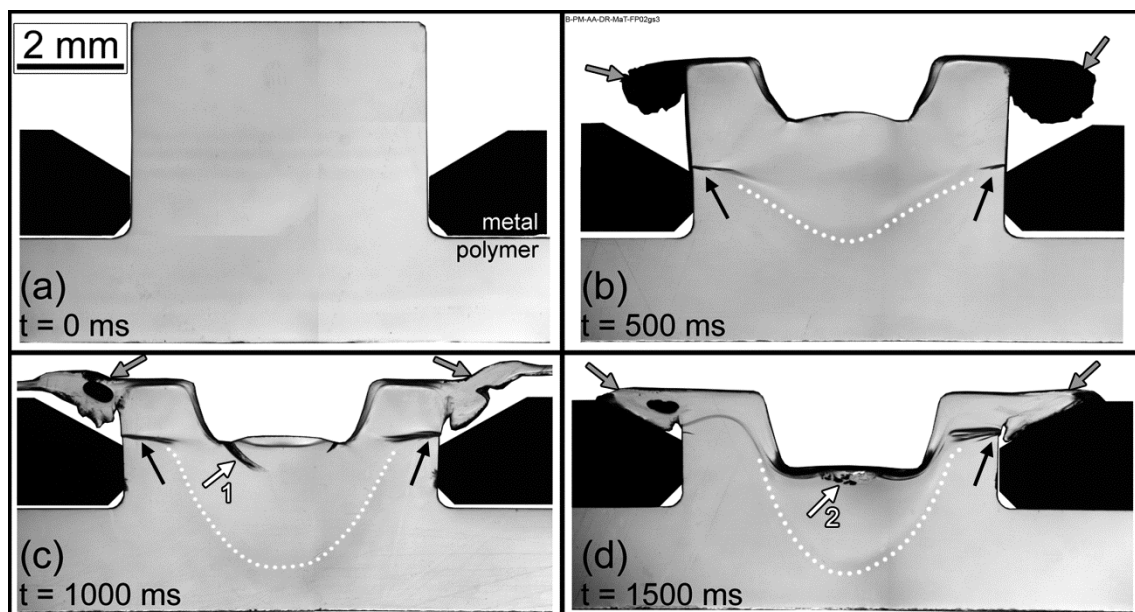


Figure 7-3: Evolution of joint formation during stud meltdown in the friction phase of a two-phase process configuration; (a) parts before joining; and after a friction time of (b) 500 ms; (c) 1000 ms; (d) 1500 ms (Stages 1-4 from Figure 7-2b, TLOM images). Black arrows show shear banding zones; white arrows show microcracks (1) or pores (2); gray arrows show squeeze flow material; the dotted lines approximately indicate the plastically deformed zone (PDZ).

During these stages, various phenomena can be identified: the formation of a plastically deformed zone (PDZ), formation of a shear layer, microcracking and porosity in the shear layer (white arrows), formation of flash material from squeeze flow (gray arrows), increase of the stud diameter, and shear banding (black arrows). The PDZ is depicted by a white-dotted line in Figure 7-3b-d. This region is directly beneath the tool's conical pin and undergoes hydrostatic pressure from the axial force applied during the friction phase. Microcracks below the keyhole also appear to be due to axial force from the tool (white arrow 1 in Figure 7-3c). In the next stage (Figure 7-3d) these microcracks are eliminated, but there is instead a formation of porosities (white arrow 2 in Figure 7-3d) below the keyhole in what appears to be a coalescence of cracked regions, as a result of increased polymer fluidity in the shear layer. Cracks and the PDZ are effects of excessive stress induced by the frictional forces. For this stop-action study, the setup value of frictional force was 2551 N, which when applied onto the area of tool's conical pin (3.98 mm²) yields a compressive stress of 640 MPa, far above the compressive yield stress of PEI (152 MPa, [180]). Such elevated stress applied on this glassy volume causes plastic yielding. These effects may be avoided by using lower frictional forces.

The shear layer (Figure 7-4a) is a result of the rotational movement of the tool's frictional surfaces pressing against the solid polymer [97], and it can be seen around the keyhole extending to the top of the stake head. The thickness of this shear layer is a function of the rotational speed of the tool and of the rheological properties of the material [203]. Furthermore, viscous friction between the polymer chains increases the temperature locally at the shear layer (see Section 3.4). Therefore the material of the shear layer is thermomechanically processed. Due to the application of shear stresses and to the increased temperature, the shear layer's viscosity decreases. Pressure from the tool-feeding action pushes this low-viscosity volume outwards as a squeeze flow, forming flash material (indicated by gray arrows in Figure 7-3b-d). A close-up view of the shear layer and squeeze flow material is shown in Figure 7-4a. In addition, as a result of the axial forces during the friction phase, the stud is plastically deformed with an increased diameter (Figure 7-4b). This plastic deformation is a result of the axial force pushing the free length of the stud into the chamfer cavity, but this deformation occurs outside the thermomechanically affected zone, with the polymer's temperature below its glass transition. Deformation of glassy amorphous polymers under compression occurs by shear yielding with the formation of shear banding [204], which can be seen in the TLOM image in Figure 7-4b. This effect can be attenuated by decreasing the joining force during the friction phase (frictional force).

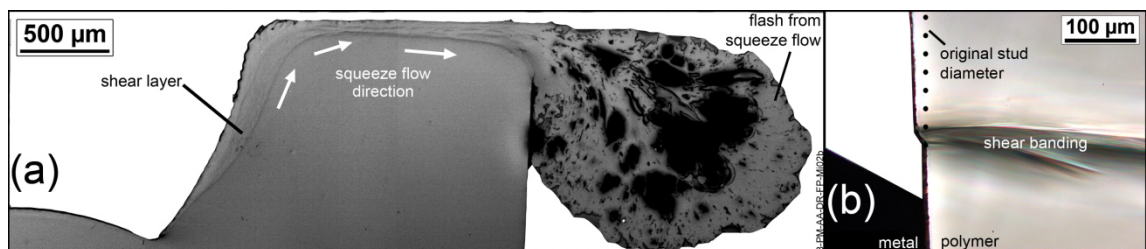


Figure 7-4: Microstructure after 500 ms of friction time (Figure 7-3b, Stage 2 of the friction phase). (a) Formation of the shear layer and flash material from squeeze flow (RLOM); (b) plastic deformation with increase of stud diameter and shear banding (TLOM).

The formation of a shear layer can also be seen in the carbon-fiber reinforced PEI (PEI-CF). In a fiber reinforced plastic material the material flow is more easily detected visually due to breakage and/or reorientation of the fibers. Figure 7-5 shows in detail the top of the stake head from specimens after 1000 ms of friction time (Figure 7-3c, Stage 3 of the friction phase). Figure 7-5a reveals the shear layer in unreinforced PEI, and Figure 7-5b in PEI-CF. In this region the original injection-molded PEI-CF has the fibers oriented vertically and parallel to the plane of observed cross-section, as seen in Figure 6-3. The original orientation is visible in the base material region in Figure 7-5b, whereas in the shear layer the fibers are either broken due to shear, or re-oriented radially around the rotation axis of the tool (perpendicularly to the observed cross-section). Although the thermal conductivity and rheological behaviors of these materials are different, the shear layer shape and size are comparable, because the same joining parameters were used.

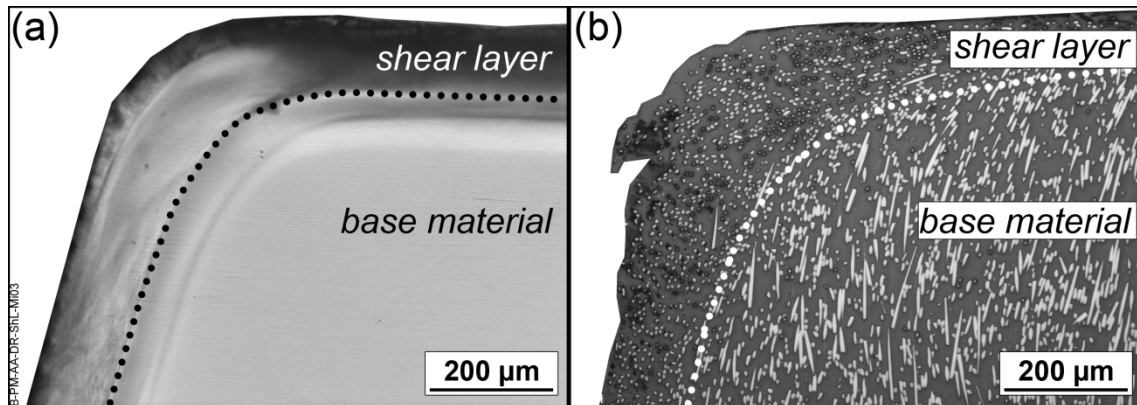


Figure 7-5: Shear layer around the top of the stake head for (a) unreinforced PEI (TLOM); and (b) PEI-CF (RLOM). Stop-action specimens after 1000 ms of friction time (Figure 7-3c, Stage 3 of the friction phase).

7.2.2 Friction phase: dwell time

At the end of stud meltdown, the clamping surface of the tool is pressed against the top surface of the metallic partner and so does not move further forward. However, the tool still rotates and its frictional surfaces are stirring/mixing the polymer of the shear layer. In Figure 7-2b this is shown as the dwell time step. During the dwell time, the temperature plateau changes, as seen by the stake temperature increase from between 250-270 °C up to 385 °C (orange downward triangles, Figure 7-2b).

A schematic illustration of the interaction of the tool and joining partners during dwell time is shown in Figure 7-6a. During the dwell time, a constant shearing action of the tool on the polymer under pressure promotes further viscous heating at the shear layer (light gray area in Figure 7-6a). The heating effect is further improved during the dwell time, since the shear layer is confined between rotating tool (white area), metal partner (blue area), and unaffected base material (dark gray area). In this situation no squeeze flow to the cavities is present and the shear layer only flows radially around the tool's conical pin (as shown by the symbols in Figure

7-6a) and is constantly sheared by the tool action. Therefore the dwell time has a pronounced effect on viscous heat generation, which affects the formation of a shear layer and consequently the promotion of cavity filling. The material flow at the shear layer was investigated by synchrotron radiation X-ray computed microtomography (SR- μ CT, Section 6.3.4) using carbon fiber reinforced PEI (PEI-CF). The region of interest is shown by the hatched area in Figure 7-6b. Slices of the SR- μ CT volume rendering are displayed in Figure 7-6c, according to the positions S1-S4 indicated in Figure 7-6a. In the images of the slices from Figure 7-6c, white arrows show material flow (fiber orientation) in the shear layer. Fiber orientation in the base material is towards the image as shown by the symbols. Dotted lines indicate boundaries between the shear layer and base material regions at each slice.

Slice S1 from Figure 7-6c is the uppermost part of the shear layer, and shows fiber orientation following the tool rotation direction (white arrow). The material is oriented according to the shear imposed by the top frictional surface of the tool. In unreinforced PEI, this means that in the shear layer a certain degree of chain orientation is expected in the same fashion as observed for the carbon fibers in PEI-CF.

Slice S2 shows the polymer-polymer interfaces between the shear layer and the unaffected base material (dotted lines in Figure 7-6c). As seen from the S2 position in Figure 7-6a, this slice cuts through the base material, shown in Figure 7-6c by the boundaries of the white dotted lines. The unaffected base material is in its original orientation from the injection molding process (refer to Figure 6-3). Material flow in the shear layer can be observed on both sides of this unaffected volume: close to the tool's conical pin (keyhole in S2, Figure 7-6c) and over the chamfer cavity.

In slice S3 fiber orientation is only featured around the keyhole as a result from the shearing action of the tool's conical pin. Slice S4 displays the material flow below the keyhole, which features orientation from the lower frictional surface of the tool.

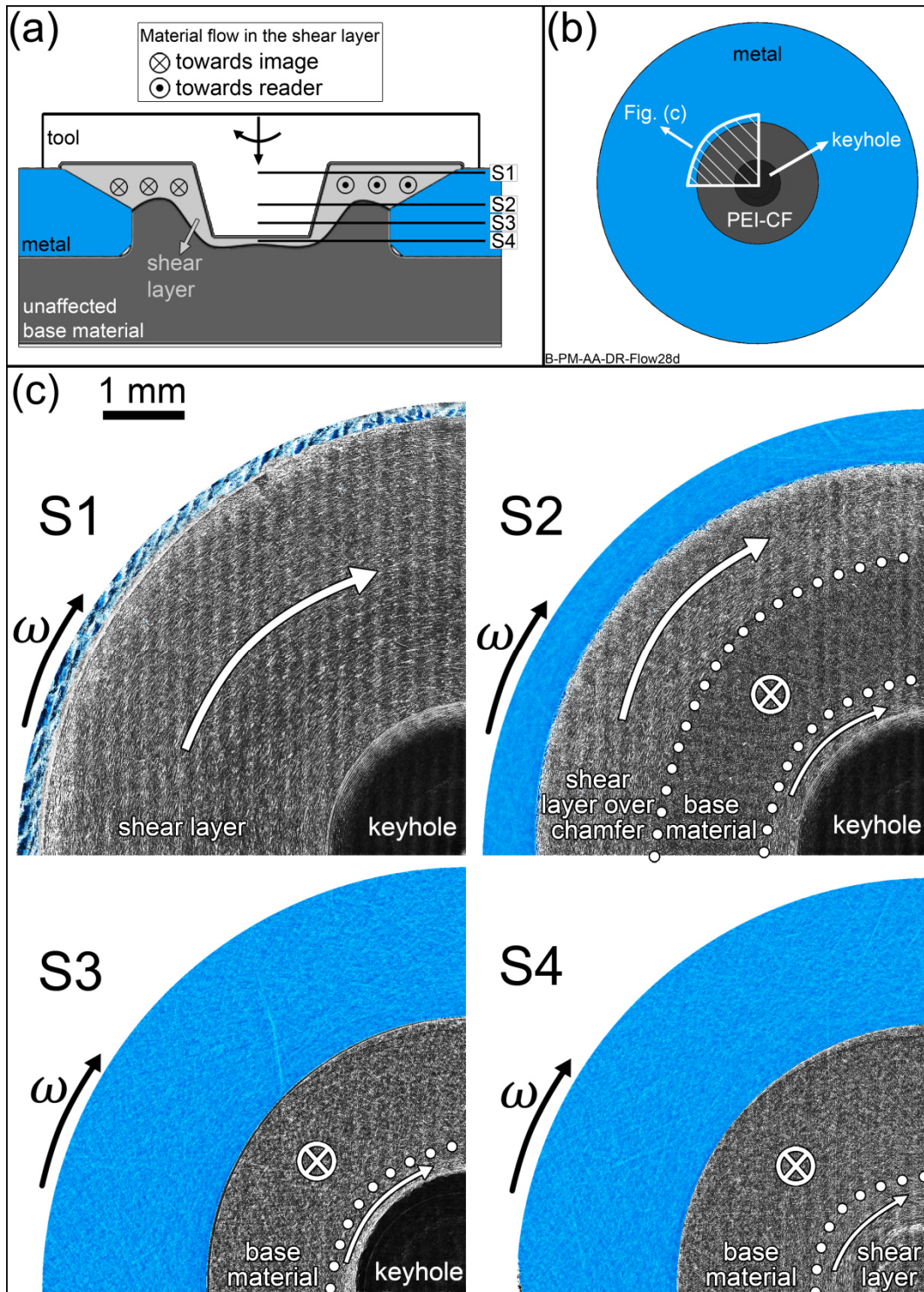


Figure 7-6: (a) Schematic illustration of the material flow in the shear layer during dwell time; (b) schematic surface view of an F-ICJ joint showing the region of interest observed by SR- μ CT; (c) material flow in a PEI-CF joint at different positions of the shear layer. Positions S1-S4 are indicated in (a). White arrows indicate material flow in the shear layer. Dotted lines indicate boundaries between the shear layer and the unaffected base material.

Figure 7-7 shows the difference in shear layer formation before and after dwell time in stop-action specimens (Stages 4 and 5 from Figure 7-2b). In the stop-action specimen prior to dwell time (Figure 7-7a) the shear layer is relatively thin and does not reach the regions of shear banding (white arrow). In the stop-action specimen after dwell time (Figure 7-7b), the temperature and shear stresses increase the thickness of the shear layer. This extension of shear layer thickness can eliminate small discontinuities, as seen from shear banding being present in Figure 7-7a, but absent in Figure 7-7b in the same region. This elimination of discontinuities is a result of the mixing/stirring action of the tool that induces material flow in these volumes.

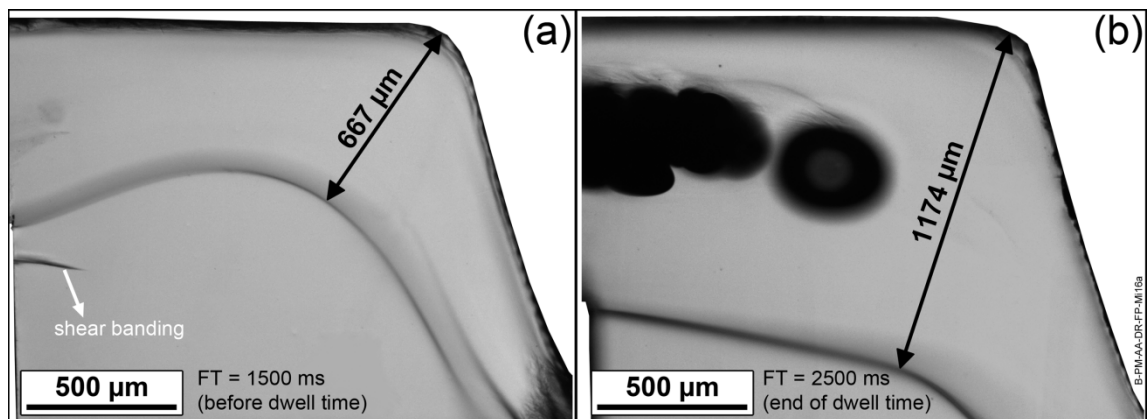


Figure 7-7: Effect of the dwell time on joint formation. Shear layer in a stop-action specimen (a) before the dwell time (Stage 4 of the friction phase); (b) after 1000 ms of dwell time (Stage 5 of the friction phase). TLOM images.

Figure 7-8 shows two F-ICJ joints after complete joining cycles, but one of them was processed without a dwell time (Figure 7-8a) and one with (Figure 7-8b). The absence of a dwell time causes the formation of volumetric flaws in the form of microcracks beneath the keyhole, as observed in Figure 7-8a. For a joint processed with a dwell time (Figure 7-8b), the shear layer extends beyond the usual shear banding and microcracking zones; as previously seen in Figure 7-7, the tool mixing/stirring action induces material flow in these zones and eliminates the discontinuities. This reinforces the idea that material mixing/heating could heal occasional cracks and eliminate shear banding (see Section 3.4.2). However, the use of a dwell time appears to increase a porous volume in the shear layer (Figure 7-8b), likely due to the extra heating that causes partial decomposition of smaller hydrocarbons or the evolution of structural water [140, 145]. Another possible origin of pore formation in the shear layer volume is coalescence of the microcracks and/or smaller pores during the squeeze flow (as in the flash from Figure 7-4a).

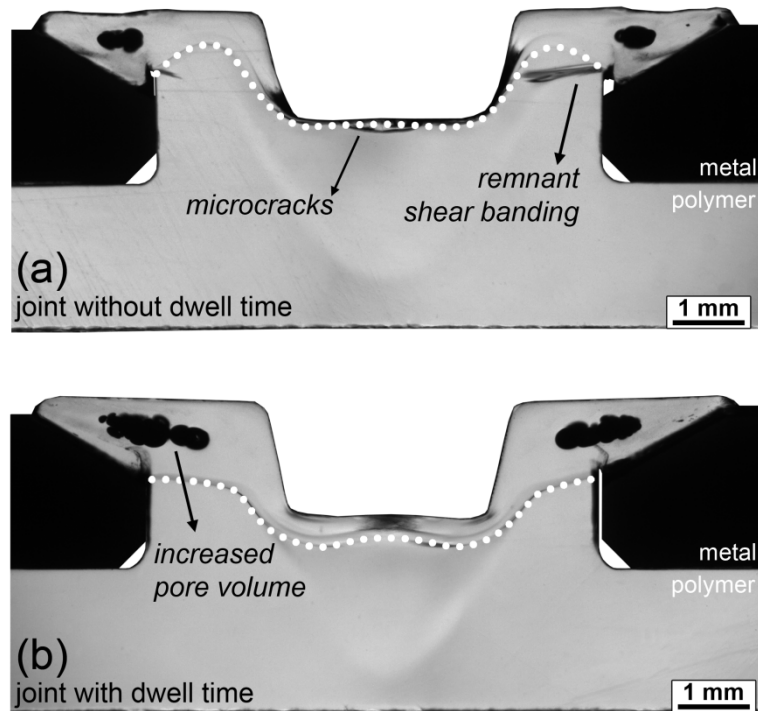


Figure 7-8: Effect of the dwell time on the final joint microstructure. (a) Joint without a dwell time; (b) Joint with 1000 ms of dwell time (TLOM images).

During stud meltdown, flash material is formed from squeeze flow and pushed into the chamfer cavity, as seen in the sequence of images in Figure 7-3 (gray arrows). As it fills the chamfer cavities, the polymer from squeeze flow forms a polymer-polymer interface with the solid material at the stake shaft; this is seen in the example of Figure 7-9a for a PEI-CF stop-action specimen at the end of stud meltdown and before dwell time (Stage 4 in Figure 7-2b). This is a discontinuous polymer-polymer interface in the fashion of a remnant weld line between the material from squeeze flow in the chamfer cavity and the stake shaft material (usually an unaffected polymer volume). The carbon fibers from PEI-CF in Figure 7-9 help to see the material flow and understand the weld line formation and healing process. The polymer from squeeze flow has a smaller fiber size, as a result of fiber breakage during the friction phase, whereas the stake shaft has the original fiber orientation of the base material (vertical and parallel to the observation plane, as seen in Section 6.1.3).

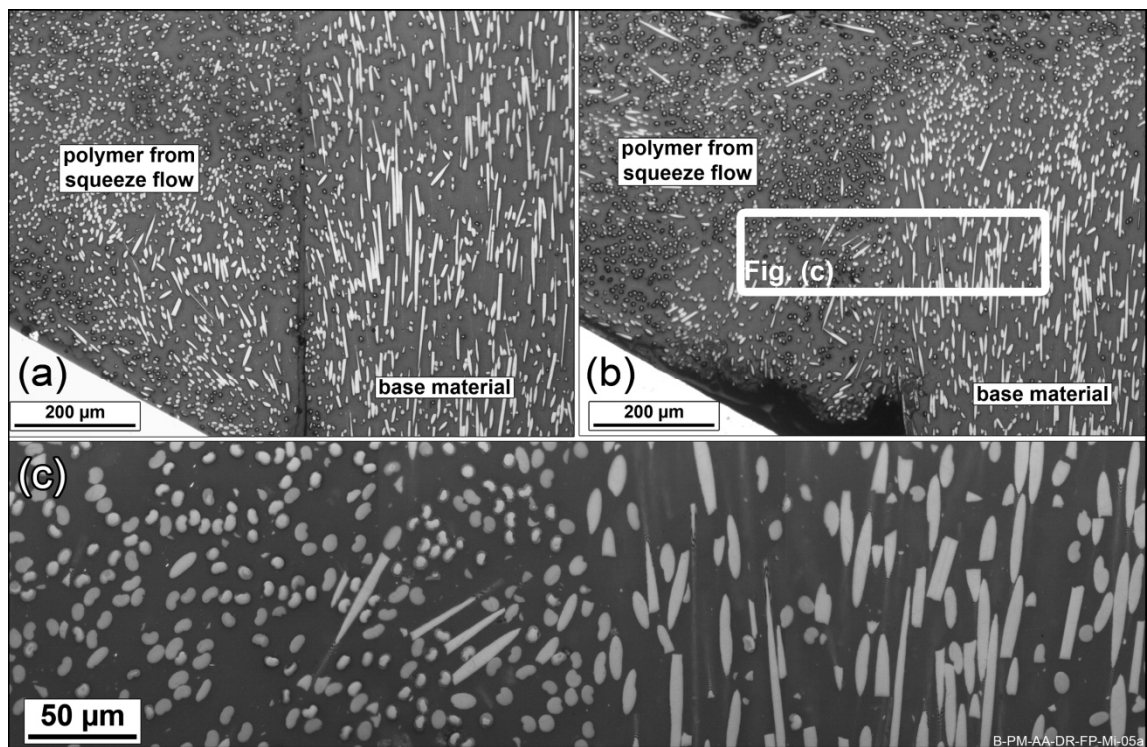


Figure 7-9: Effect of dwell time on the polymer-polymer interface. Interface in a stop-action specimen (a) before dwell time; and (b) after 500 ms dwell time; (c) detail of the microstructure from (b), showing the healed interface (RLOM images).

The remnant weld line is a discontinuity that does not contribute to load transfer and is therefore undesired. Normally it can be eliminated by promoting interdiffusion of the macromolecules between the surfaces (see Section 3.4.2). Most commonly this is achieved by supplying energy in the form of heat and promoting intimate contact between the surfaces [125, 205]. In Figure 7-9b the same region is shown for a PEI-CF stop-action specimen after 500 ms of dwell time. In this case the different orientation of the fibers is still clearly visible, but there is an intimate contact between the volumes. Higher magnification, as in Figure 7-9c, shows the two different zones (with different fiber orientations) without a discontinuous interface between them. Heating during the dwell time promotes interdiffusion of the polymer chains between the volumes, which aids healing of the weld line (as described in Figure 3-12b). Another way of eliminating the weld line is to use processing conditions with higher heat input. Heat generation further decreases the polymer's viscosity, and can extend the shear layer up to the position of the weld line, which eliminates it by inducing material flow, as shown by the removal of shear banding in Figure 7-7 and Figure 7-8.

7.2.3 Consolidation phase

After the friction phase, no further heat is generated and the joint cools down under pressure from the tool in the consolidation phase. The cooling regime is shown in Figure 7-10, based on data from infrared thermal camera measurements. The black squares are measurements from

the stop-action study during the consolidation phase. The blue triangles are measurements after consolidation, during ambient cooling. Exponential decay fits are shown for each phase.

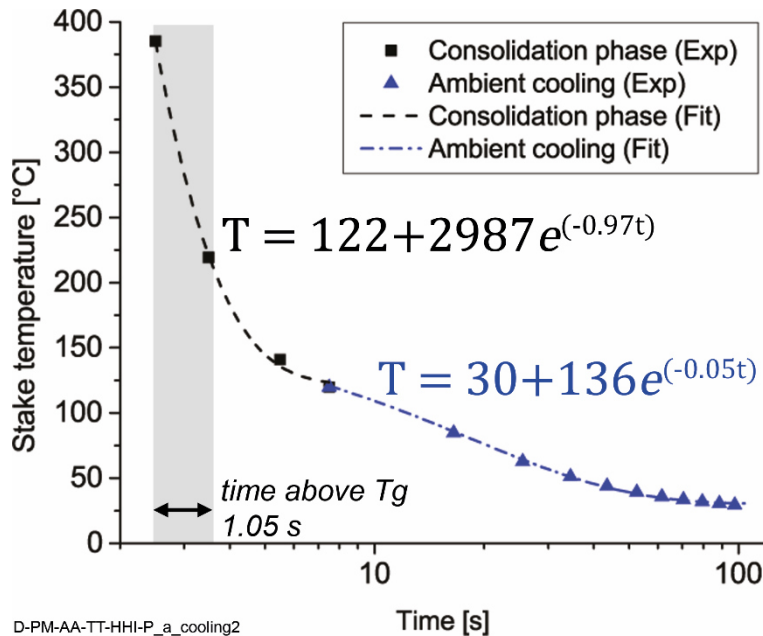


Figure 7-10: Cooling curves during (black squares and dashed line) and after (blue triangles and dash-dotted line) the consolidation phase of a two-phase process.

What is observed in F-ICJ is rapid cooling during consolidation due to contact with the steel tool and spindle system (from 385 °C to 120 °C, k of 0.97 s⁻¹); followed by a slower cooling period under ambient conditions (from 120 °C to 29 °C, k of 0.05 s⁻¹). The much higher values of the decay constant k during consolidation are a result of the heat sink effects of the tool and spindle system [123]. Stake temperature steeply decreases over the consolidation phase, reaching temperatures below glass transition after 1 second of consolidation. At the end of consolidation, the stake temperature was 120 °C, which is 95 °C below the T_g of PEI. Above T_g the polymer chains may still diffuse, but below T_g little or no significant topological rearrangement of macromolecules is expected. The fast cooling and constant geometrical restriction applied by the axial force on the tool induce a lack of further significant structural changes to the joint during consolidation. Figure 7-11 shows the microstructure of the joints during the consolidation phase.

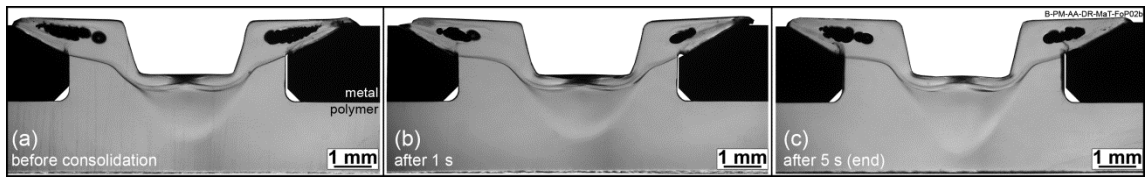


Figure 7-11: Evolution of joint formation during the consolidation phase: (a) stop-action specimen from the end of the friction phase, before consolidation starts (Stage 5 of the friction phase in Figure 7-2b); (b) stop-action specimen after 1 s consolidation; and (c) joint after 5 s consolidation, the end of the phase (TLOM images).

In the two-phase process configuration, the friction phase is most important for joint formation since that is the phase where heat is generated. The dwell time step contributes greatly to further heating of the shear layer, allowing healing of the discontinuities created during stud meltdown, such as shear bands and weld lines. The stake is cooled below T_g rapidly during the consolidation phase, and no additional changes to the polymer take place as it cools down further.

CHAPTER 8. PROCESS-RELATED CHANGES IN THE MATERIALS JOINED BY F-ICJ

The previous chapter described the joint formation mechanisms in F-ICJ mainly as a function of the interaction of the tool with the polymer, generating material flow in a shear layer which cools down under pressure. The heat and deformation applied to the joint will affect both joining partners to different degrees. This chapter describes the local changes in the metallic partner as well as the polymeric partner, with indications of typical defects in F-ICJ joints.

8.1 Changes in the metallic partner

Because most of the interaction of the tool with the joining partners is limited to the polymer, the achieved temperatures during a typical F-ICJ process are not high enough to cause significant heat transfer to the metal. The metal-polymer interface at the chamfer is shown in Figure 8-1. The polymer shear layer reaches 250-385 °C for short periods (refer to Figure 7-2 and Figure 7-10). Heat flows from the shear layer to the polymer's base material, to the steel tool, and to the aluminum partner. This heat flow is not sufficient to cause metallurgical changes, and no obvious alterations to the microstructure of the aluminum partner are observed, in comparison with the 6082-T6 base material.

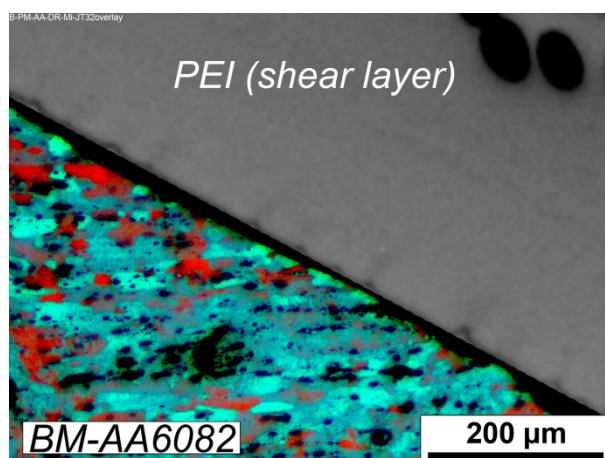


Figure 8-1: Metal-polymer interface at the chamfer. Overlay of RLOM (PEI) and polarized RLOM (aluminum, Barker's reagent).

However, significant heat transfer to the aluminum may occur during dwell time, while the rotating tool slightly rubs the top surface of the metallic partner (Figure 8-2a) leaving a ring-like mark (Figure 8-2b). This rubbing causes a partial dynamic recrystallization of a thin layer (around 50-150 μm thick) on the metal surface, due to thermomechanical work. This creates a thermomechanically-affected zone in the metal (MTMAZ), as is seen in other friction-based welding processes [175, 206]. This effect can be seen by comparing the microstructure of the

base material (Figure 8-2c) with the rubbed surface of the AA6082 partner (Figure 8-2d). The thin MTMAZ is indicated with a dashed white line. An adjacent heat-affected zone (MHAZ) may also be present, with dissolution or coarsening of precipitates in heat-treatable alloys, such as AA6082-T6 [206].

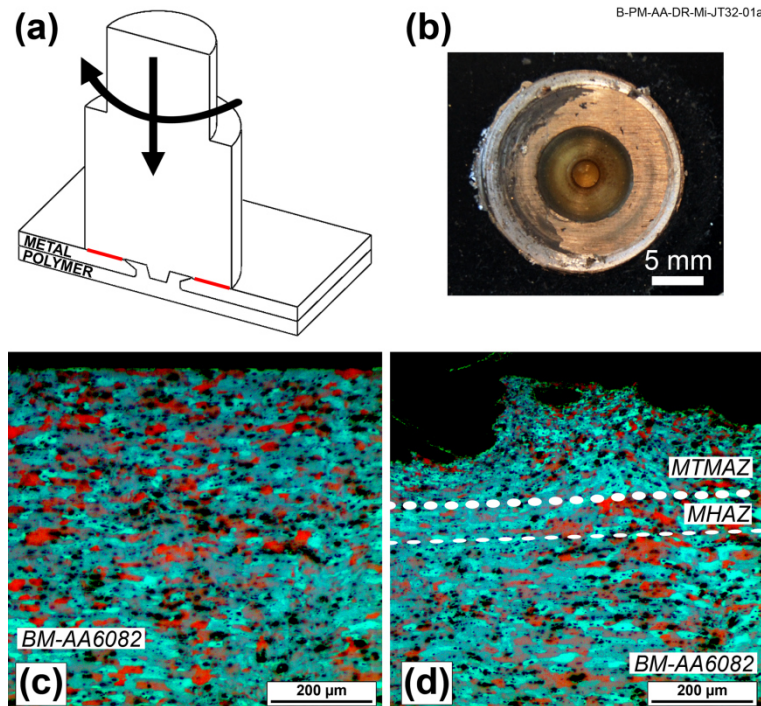


Figure 8-2: (a) Schematic representation of tool rubbing on the metallic partner; (b) detail of the surface of a joint with which tool rubbing took place; (c) microstructure of AA6082-T6 base material close to the surface in a non-affected area; (d) microstructure of a region of tool contact close to the surface, showing a thin process-affected layer (MTMAZ/MHAZ). Polarized RLOM images, Barker's reagent. Processing conditions: RS: 12000 rpm; FT: 5000 ms; FP: 0.5 MPa (2726 N); FoP: 1.0 MPa (5363 N); CoT: 5000 ms.

It has been reported in the literature that such thermomechanical treatment can soften Al-Mg-Si alloys [159, 167]; softening is a result of the heat and deformation overaging the alloy by causing decomposition of coherent β'' precipitates and coarsening of semi and non-coherent precipitates. Changes to the local properties in these regions are difficult to determine, due to the small size of the MTMAZ and MHAZ in F-ICJ joints, but it is known from the literature that lower hardness is generally observed in the TMAZ and HAZ of precipitation-hardenable friction-welded 6xxx alloys [206].

Since these phenomena occur in a notably thin layer of the metal that is away from the actual stake, and because the polymeric partner is usually where the final failure occurs during loading, minor metallurgical changes will not affect global behavior of the joint. Nevertheless, local frictional heating of the aluminum surface due to rubbing may enhance the heat transferred to the stake, or decrease heat diffusion from the polymer's shear layer to the metal.

8.2 Changes in the polymeric partner

A typical F-ICJ joint results from the effect of heating and deformation imposed by rotational and axial movement of the tool in contact with the polymeric stud. Its microstructure is highly influenced by heat input, tool geometry and configuration of process parameters. Such an F-ICJ joint is shown in Figure 8-3, with details of its microstructural zones and joint features.

The use of transmitted-light optical microscopy (TLOM) through a thin section of an F-ICJ joint makes it possible to observe the microstructural features and discontinuities in the amorphous polymer. A dark line across the diameter of the stake shaft delineates a polymer-polymer interface (Figure 8-3b). The volume above this interface interacted with the frictional surfaces of the conical-pin tool, and has been heated and deformed by its rotation and axial force. This is a polymer thermomechanically-affected zone (PTMAZ), which is characterized by material flow and the presence of volumetric discontinuities such as pores, remnant weld lines and microcracks (Figure 8-3c).

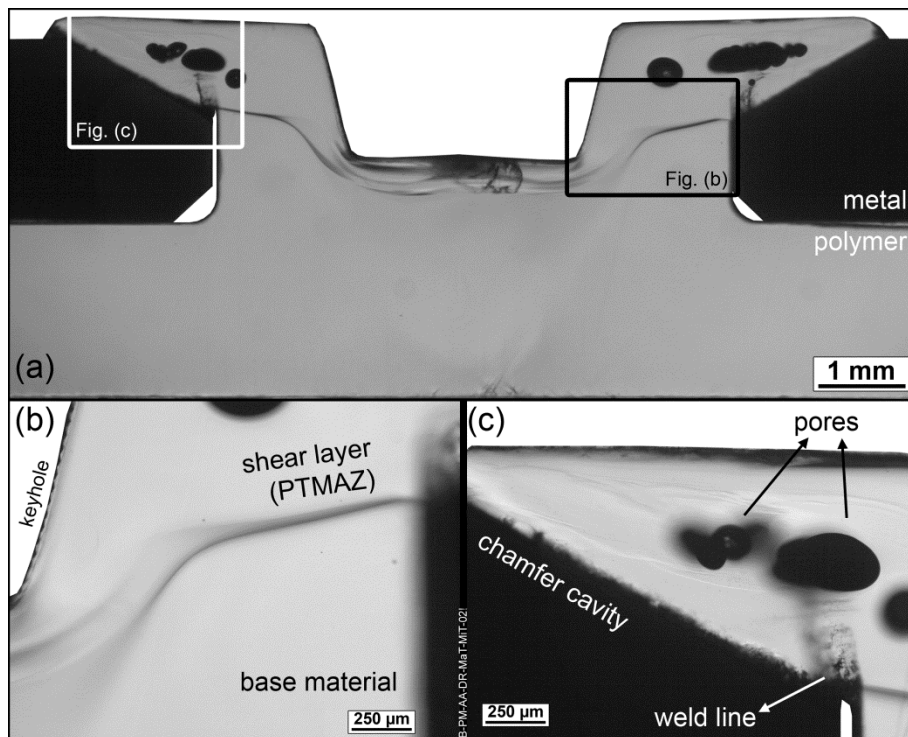


Figure 8-3: Microstructural features of an F-ICJ joint created with a conical-pin tool and chamfer cavities: (a) overview of joint cross-section; (b) polymer-polymer interface; (c) pores and remnant weld lines in the PTMAZ (TLOM images). For processing conditions see Table 11-2.

To better visualize the microstructural zones and understand their local properties, further characterization methods can be of assistance. The right-hand side of Figure 8-4 presents a

micrograph of the joint from Figure 8-3 by transmitted-light optical microscopy with crossed polarizers (CP-TLOM) that displays birefringence patterns. To complement the analysis and help to understand possible changes in local mechanical properties, a microhardness map (Section 6.3.7) with the same joining condition is overlaid on the left-hand side of Figure 8-4. The coupled analysis reveals three microstructural zones with different local mechanical properties: a PTMAZ, a plastically deformed zone (PDZ), and unaffected base material (BM). At this resolution of the microhardness map (200 μm between indentations) no sharp transition zone between the PTMAZ and the BM can be identified that would otherwise characterize an extensive polymer heat-affected zone (PHAZ).

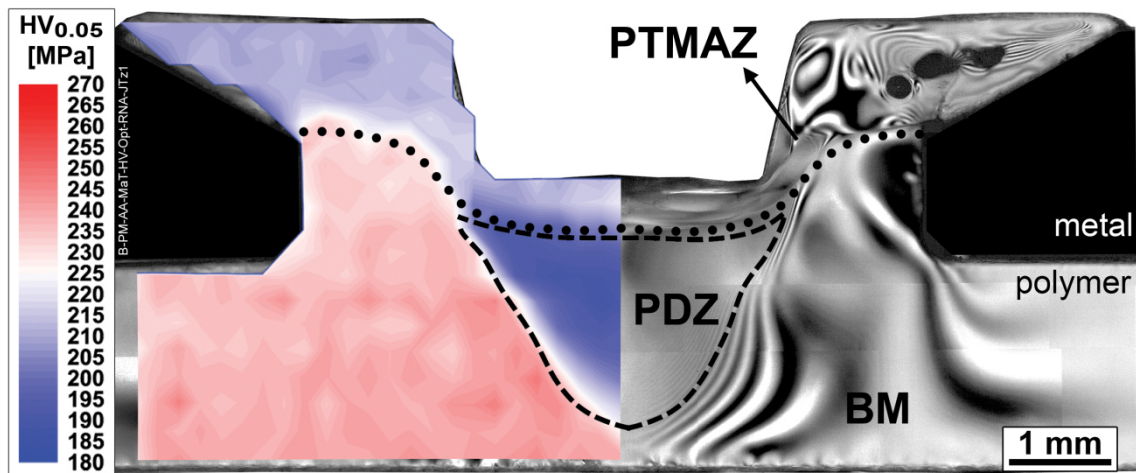


Figure 8-4: Overlay of a microhardness map (left) on a CP-TLOM micrograph of the F-ICJ joint from Figure 8-3. Dotted lines are the boundaries of the polymer thermomechanically-affected zone (PTMAZ); dashed lines are the boundaries of the plastically deformed zone (PDZ). For processing conditions see Table 11-2.

8.2.1 Plastically deformed zone (PDZ) and base material (BM)

Beneath the shear layer boundary of the PTMAZ (dotted line in Figure 8-4), two zones can be identified. The highest-strength volume BM has base material properties and is not affected by the process.

The lowest-strength PDZ (boundaries marked by a dashed line in Figure 8-4) is directly below the conical pin's line of action, and has 12-16 % less local strength compared to the base material. The temperature of this volume is not significantly altered by the rotating action of the tool, as this volume is in a glassy state during processing. A well-formed PDZ is only observed for conditions where the joining force is notably high (above 2400 N in this work), creating stresses above the yielding point of the solid polymer; therefore it follows that the PDZ is plastically deformed by compression.

PEI undergoes strain softening under compression in the 7-13 % strain range [207], as shown schematically in Figure 8-5a. Strain softening in polymer glasses is related to the difference in conditions (energy or stresses) that is required to initiate yielding and to propagate it: yielding

stress is greater than the stress required for propagation [208]. In the case of the polymer in the PDZ, its mechanical history during F-ICJ may be schematically represented by the solid stress-strain curve in Figure 8-5b. The polymer in the PDZ is stressed up to a point in the strain softening region, and after removal of load a residual plastic strain $\varepsilon_{plastic}$ is present. When reloading a previously yielded amorphous polymer during the microhardness test (dotted curve in Figure 8-5b) a new, lower yielding stress is reached (σ_{y-PDZ}), because the necessary conditions for initiation of yielding were previously achieved (σ_{y-BM}). A peak of yielding stress is usually still present, due to a certain level of physical aging (hardening as a result of the reduction of free volume at temperatures close to but below T_g [209]) during cooling or at room temperature.

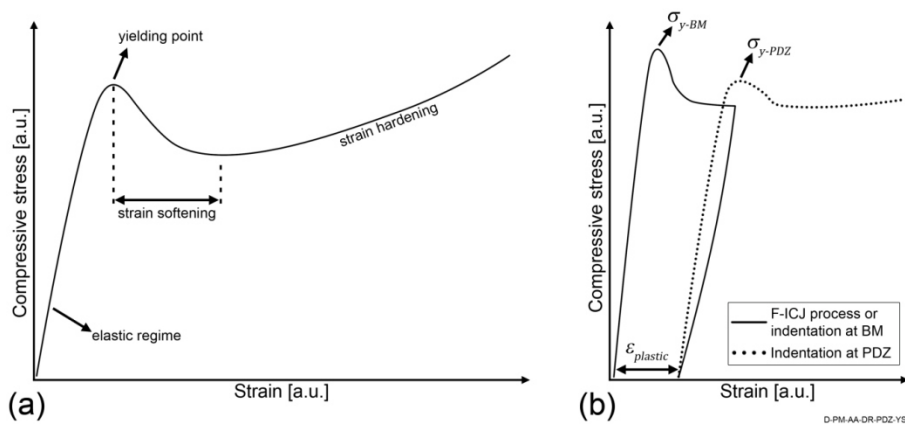


Figure 8-5: (a) Behavior of PEI under uniaxial compression (based on [90, 207]); (b) yielding of PEI up to strain softening (solid curve), and reloading the yielded PEI during microhardness (dotted curve).

Plastic deformation by yielding is described as conformational changes of the macromolecules, leading to increased free volume in amorphous polymers [204, 208-210], which is detected as reduced hardness in indentation testing [127, 128]. In Figure 8-5b the solid line can also represent the microhardness testing in the BM region. Since a Vickers indentation applies a representative strain of 8-10 % on the tested volume [193, 211], this corresponds to the strain softening region of PEI in the PDZ [180].

Identification of the shape and limits of the PDZ can be additionally supported by the birefringence pattern with crossed polarizers. Birefringence patterns are associated with the residual stresses in a material through the stress-optic law (Equation (8-1) [131]).

$$\sigma_{res} = (\sigma_1 - \sigma_2) = (n_1 - n_2) C_{opt} = \frac{\delta}{y} C_{opt} [MPa] \quad (8-1)$$

Where σ_{res} is the residual stress, $(\sigma_1 - \sigma_2)$ is the difference in normal stresses in the specimen, $(n_1 - n_2)$ is the birefringence, C_{opt} is the stress-optical coefficient of the material, δ is the retardation of light in the specimen, and y is the specimen thickness. Photoelasticity [191] can be used to quantify stresses in birefringence patterns by defining these parameters.

However, a quantitative measurement of residual stresses through the photoelastic effect requires adequate equipment and complex analyses [212, 213], which were not within the scope of this work. Such analyses can be performed more commonly using a color image and obtaining the intensity of the red-green-blue signals, or by using a Michel-Levy chart. These methods assist in the definition of the number of fringes in a certain region, which are a measurement of the retardation δ [214]. In this work a grayscale image filtered from the red signal (as described in Section 6.3.5) is used to qualitatively estimate the number of fringes in a given region of the joint. An increasing number of fringes (larger retardation δ) can be associated with an increasing level of residual stresses (see Equation (8-1)) [131]. The colored birefringence images used in this work are displayed in Appendix F.

Figure 8-6a is one half of the cross-section previously presented in Figure 8-4; the transition region between the PDZ and BM zones is highlighted with a black rectangle. This highlighted region is shown in greater detail in Figure 8-6b. In this image, a first-order fringe is on the right-hand side, and increasing orders of isochromatic fringes can be observed towards the PDZ on the left of the figure. The brighter, well-defined fringes in the base material region are low-order fringes, indicating lower stresses, while the lighter shades in the PDZ are high-order fringes, indicating high residual stresses [212, 215]. The high-order fringes correspond to higher retardation (δ) values, which indicate higher residual stresses, as described in Equation (8-1). Therefore yielding in the PDZ creates a highly-stressed volume, whereas away from the PDZ and into the BM the fringe orders are of the same level as observed in the as-received material (Figure 6-9) where no significant residual stresses are present.

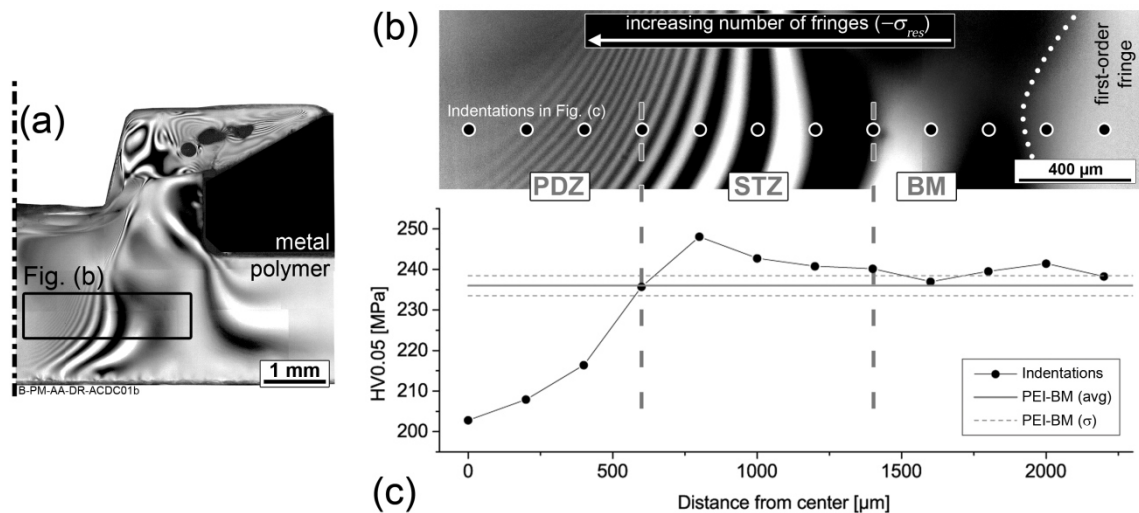


Figure 8-6: (a) Half of a cross-sectional view of a joint featuring a PDZ; (b) birefringence of the PDZ-BM transition highlighted in (a), with number of fringes ($-\sigma_{res}$) increasing in the PDZ direction (CP-TLOM); (c) indentation profile highlighted in (b), showing the the formation of a strengthened transition zone (STZ) between the PDZ and BM. The gray horizontal lines in (c) correspond to the PEI base material's hardness.

In Figure 8-4, it can be observed that local mechanical strength is decreased at the PDZ. The black dots in Figure 8-6b represent the position of the indentations of the profile shown in

Figure 8-6c, covering the transition between PDZ and BM. The horizontal gray lines in Figure 8-6c indicate the as-received hardness of PEI and its standard deviation; the black disks are the indentation measurements of the profile. It is possible to see that a strengthened transition zone (STZ) is detected between the BM and PDZ. It is known that compressive stresses increase hardness values [216, 217], whereas plastic deformation decrease them [127, 128]. Therefore, there are two competing effects taking place. The combined analysis demonstrates that in the PDZ and STZ significant compressive residual stresses ($-\sigma_{res}$) are present, but in the PDZ the effect of free volume from yielding dominates and hardness is lower, whereas in the STZ no yielding is present and the $-\sigma_{res}$ increases hardness. In the BM, none of these effects play a role and the hardness fluctuates around the levels of the base material.

8.2.2 Polymer thermomechanically-affected zone (PTMAZ)

Following the polymer-polymer interface line in Figure 8-3b, the volume previously described as the PTMAZ presents 8-12 % lower strength than the base material. The PTMAZ corresponds to the shear layer described in Chapter 7. This is a volume that has been affected by frictional heat and shear stresses, and changes in local properties are tied to the thermomechanical processing and its subsequent thermal history. Unlike the PDZ, no effects of cold forming are seen, because this volume is above the material's T_g during processing. A number of competing phenomena may act in this volume to change its microhardness: chain reorientation, topological conformation, and molecular weight changes [193]. In the PTMAZ, the chains are most likely oriented parallel to the direction of indentation, due to the radial flow induced by the tool (see Figure 7-6), which would increase its microhardness [218]. Conformational changes that alter the topology of entanglements occur from quenching (increasing free volume) or physical aging (reducing free volume). Lower hardness in this case indicates more free volume [127, 128, 219]. Reduction of molecular weight by chain scission tends to reduce microhardness, because a larger fraction of chains with low molecular weight represent more chain ends and degradation products [220]. By contrast, thermally-induced crosslinking increases local strength as a result of a rigid network [193]. In the PTMAZ of F-ICJ joints, the chain reorientation probably has a low contribution, because local strength is lower than the BM. Therefore a combination of entanglement topology and molecular weight changes can be investigated as the possible causes of the microhardness reduction.

Chain conformation topology in F-ICJ is related to the available energy for chain diffusion at the end of the friction phase. During the friction phase, the PTMAZ reaches temperatures far above the T_g (Figure 7-2) and it cools down rapidly during consolidation (Figure 7-10). At the end of the consolidation phase the polymer is well below T_g in a frozen state [131]; this does not allow the chains to achieve a densely packed conformation, and so reducing the local strength [127, 204]. This indicates that the cooling regime in the PTMAZ is probably faster than for the manufacturing process of the base material. The extruded thick PEI sheets either use slow cooling after exiting the die, or are annealed after extrusion to achieve a random-coil macromolecular configuration [125]. Either way the industrial process allows the polymer chains to achieve a more packed configuration than the as-joined PTMAZ.

8.2.3 Physical-chemical changes in the microstructural zones of F-ICJ joints

In order to verify the theory of increased free volume in the PDZ, and whether changes to the molecular weight also affect the local strength in the PTMAZ (i.e. an indication of process-related physical-chemical changes in the polymer, such as chain scission or crosslinking), a joint with the same joining conditions as of Figure 8-4 was subsequently annealed for 24 hours at 200 °C ($T_g - 15$ °C). The time and temperature of annealing were based on the maximized physical aging of PEI as reported by Belana *et al.* [221]. Annealing of amorphous polymers promotes accelerated physical aging. Physical aging is the natural tendency of the macromolecules to conform into a low-energy configuration creating a densely packed structure and eliminating mobile defects, thereby decreasing free volume [209, 219]. A CP-TLOM micrograph with an overlay of local strength distribution of the aged joint is shown in Figure 8-7a. The physical-chemical properties of samples extracted from the PTMAZ from the as-joined condition (Figure 8-4) and the aged condition (Figure 8-7a) are compared with base material's properties in Figure 8-7b.

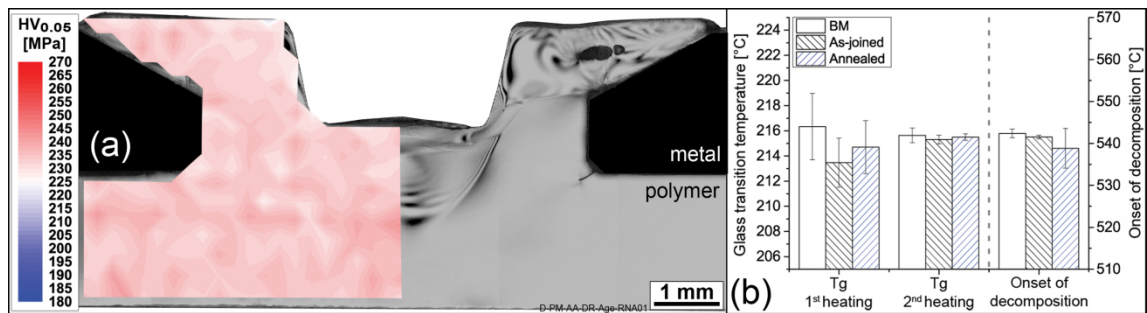


Figure 8-7: (a) Microhardness distribution overlay on a CP-TLOM micrograph from an annealed F-ICJ joint (same processing condition as Figure 8-4); (b) first- and second-heating T_g (DSC), and onset of decomposition (TGA) of the PTMAZ from as-joined and annealed joints compared to the BM.

Figure 8-7a shows the same joining condition as Figure 8-4 after annealing. From the microhardness distribution no microstructural zones can be distinguished, and the average measured microhardness is 233.0 ± 3.7 MPa across the whole joint. The homogeneity of local mechanical properties over the joint indicates that any differences between the base material and PTMAZ or PDZ in the as-joined specimen were due to an unsteady topological conformation of increased free volume. The photoelastic effect also shows considerable stress relief around the PDZ and in the BM regions compared to the as-joined specimen (Figure 8-4). Low-order fringes indicate low residual stresses in the shear layer and around it. However, they apparently are not large enough to affect the local strength. These results show that if thermal degradation is present in the F-ICJ joints, it does not affect their local mechanical properties.

To investigate if a certain level of degradation is present, physical-chemical properties related to chain length can be studied. A reduction of average chain length reduces the entanglement density in amorphous polymers, reducing the energy necessary to achieve the rubbery plateau (T_g) during heating or deformation [90], and also reducing the energy necessary for

decomposition. The hypothesis of thermomechanical degradation is evaluated in Figure 8-7b with measurements of Tg (DSC) and onset of decomposition (TGA) (refer to Appendix G for DSC and TGA curves). For Tg, the first heating indicates the state of the polymer in service conditions of a joint. The first-heating Tg has a larger standard deviation probably due to sample preparation effects such as residual stresses from scalpel cutting [192]. It is observed that the as-joined specimen has a small reduction in average first-heating Tg (2.9 °C) in relation to the base material, while the aged specimen has reduction of 1.6 °C. These variations are small and considering the previously mentioned effects of specimen preparation, it is difficult to assume that the variations are produced by extensive thermal degradation. Measurements of second-heating Tg and of the onset of decomposition eliminate the thermomechanical history and possible specimen-preparation induced effects; they show the pure physical-chemical properties of the material. Average measurements of both values show that virtually no variation is seen between BM and the PTMAZ from as-joined and annealed conditions, reinforcing the hypothesis that no extensive thermal degradation takes place.

The physical-chemical changes in the PTMAZ can be further analyzed, to compare its measured properties with the base material behavior. The processing temperatures measured in the stop-action study are compared to the decomposition behavior of the PEI base material from TGA in Figure 8-8a. The diagram is an averaged thermogravimetry (TGA) curve of three replicates of the PEI base material. The F-ICJ processing temperature range observed with an infrared camera in the stop-action study (Figure 7-2b) is marked with a gray rectangle in the range 250-385 °C. The weight loss at the processing range is of 0.07-0.15 %, which could result from structural water loss [140]. Crosslinking of PEI is expected at temperatures from 320 °C upwards, while chain scission occurs above 400 °C [145]. The maximum temperatures observed in F-ICJ (250-385 °C) are around 160 °C below the onset of decomposition for this material (542 ± 1 °C), and lay within the normal industrial processing range of 320-400 °C for PEI [137, 222]. Moreover, the PEI in F-ICJ joints in this work is only exposed for up to five seconds (during the friction phase) to these temperatures, comparatively brief compared to the plasticization times in common injection molding and extrusion (i.e. residence times of the polymer in the screw).

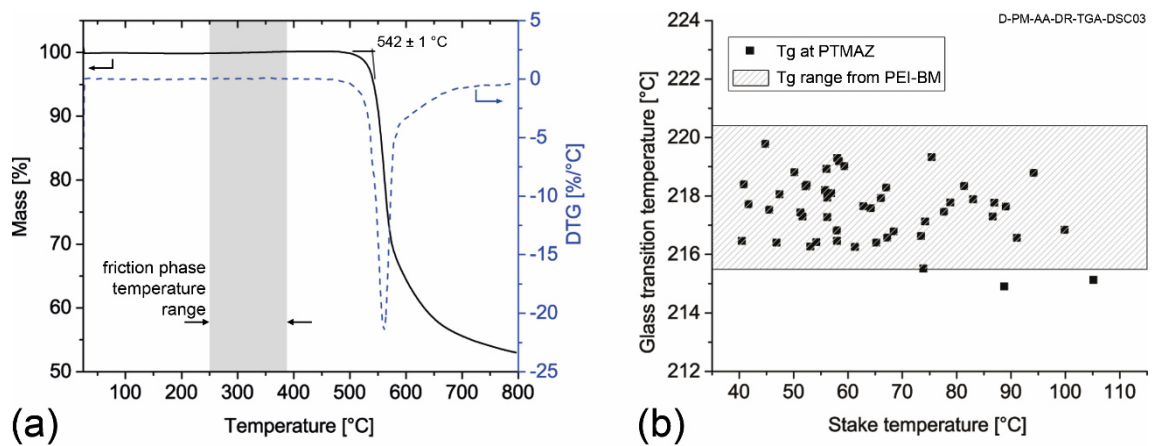


Figure 8-8: (a) Thermogravimetry curve of the as-received PEI base material and the processing temperature range during the friction phase of F-ICJ; (b) Tg range of PEI base material (hatched area) compared to Tg measurements of the PTMAZ under various conditions.

The second-heating Tg of the PTMAZ under several F-ICJ conditions, with stake temperatures ranging from 40.5 °C to 105.1 °C, is compared with the base material's glass transition relaxation range (hatched area) in Figure 8-8b. The wide heat input level applied on these joints does not change the Tg greatly, with only two data points straying outside the base material's relaxation range. This coupled analysis shows once again that no extensive degradation is expected to occur in F-ICJ, and any changes to molecular weight are not bound to affect the global properties of the joints. This conclusion is further supported by the literature. Amancio *et al.* [145] observed thermal degradation in PEI-AA2024 friction riveted joints, however the levels were not significant for changes to their quasi-static mechanical properties. Similarly, Hahn and Finkeldey [99] verified evidences of thermo-oxidative degradation in glass-fiber reinforced polypropylene joined by hot-air cold staking. In their study, the as-joined specimens were apparently not affected by degradation, but high heat-input specimens aged for 42 days at 140 °C had up to 50 % decrease in strength.

8.3 Interpretation of the local viscoelastic properties

Observation of the shapes of indentations in different zones contributes to further understanding of local changes to the polymer. Three-dimensional measurements of selected indentations in each microstructural zone (BM, PTMAZ, PDZ) were performed. At this depth of analysis, an evaluation of the material's responses of sink-in and/or pile-up in these regions can provide a qualitative view of local viscoelastic properties. Sink-in and pile-up are the local effects of material flow that are induced by the indentation. Sink-in is observed as flow in the direction of the indentation (commonly forming a pin-cushioned shape, typical of elastic recovery); pile-up is observed as an extrusion of the material upwards, above the original surface level around the indentation [211, 216]. Examples of the shapes of the indentations in the microstructural zones of an F-ICJ joint are shown in Figure 8-9a. The profiles from the BM and PTMAZ indentations are similar, with pronounced elastic recovery in a pin-cushioned indentation and little pile-up. This is the usual indentation shape for amorphous polymers in

the glassy state [211, 223, 224]. The PDZ indentation presents an indentation closer to a square shape, with less pronounced elastic recovery, and more intensive pile-up. The pile-up volume V_p was measured by establishing a baseline of the polished specimen surface and measuring the volume above it from the 3D scans, based on the approach by Blunt and Sullivan [225]. Profiles along the faces of the indentations were traced, and compared to the maximum depth h_{max} reached by a Vickers indenter as shown in the diagram in Figure 8-9a.

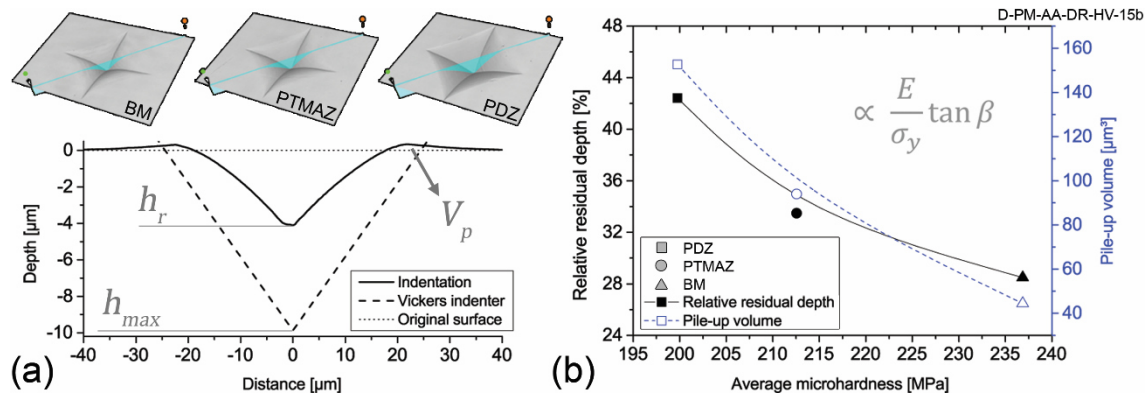


Figure 8-9: (a) Shape of indentations in each microstructural zone and typical profile measurement of the residual indentation depth compared to the maximum depth of the Vickers indenter; (b) measurements of relative residual depth (black solid line and symbols) and pile-up volume (blue dashed line and open symbols) as a function of local strength in the microstructural zones.

The relative residual depth is described by Equation (8-2) [226].

$$\delta_{res} = 100 \% \left(\frac{h_r}{h_{max}} \right) = \frac{1}{1 + 2H_T/E_r \tan \beta} \quad (8-2)$$

Where δ_{res} is the relative residual depth, h_r is the residual depth, h_{max} is the maximum depth achieved by the indenter, H_T is the true hardness of the material, E_r is the reduced elastic modulus (a function of specimen and indenter material properties), and β is the characteristic angle of the indenter. For the purpose of this analysis, E_r can be directly related to PEI's elastic modulus as it is only dependent on the materials of the indenter and specimen; and H_T is known to be directly proportional to yielding stress σ_y [211, 226-228]. β has a value of 19.7° for a Vickers indenter and is constant [193]. Simplifying Equation (8-2) we obtain the relation shown in Equation (8-3) as proposed by Sakai [226].

$$\delta_{res} \propto \frac{E}{\sigma_y} \tan \beta \quad (8-3)$$

The right side of this relation is a measure of the reciprocal value of elastic strain experienced by the indented material [193]. Therefore, low values of E/σ_y represent highly elastic materials, whereas high E/σ_y value represent more plastic behavior, with less elastic recovery. In the PTMAZ and PDZ of F-ICJ joints we observe a larger δ_{res} than the BM (Figure 8-9b),

indicating either increase in E or decrease in σ_y . Considering the previously described local mechanical changes (hardness) in the PDZ (increased free volume from plastic strain) and in the PTMAZ (increased free volume from fast cooling) it can be concluded that these volumes present a decrease in σ_y and little or no change in the absolute value of E , based on Equation (8-3). The black data in Figure 8-9b shows a decrease in relative residual depth with increasing microhardness values in accordance with Equation (8-3). This behavior has been widely confirmed in FEM studies of indentations on materials with a varying E/σ_y ; materials with higher E/σ_y ratios (such as work-hardened metals) have more plasticity and increased pile-up, while materials with lower E/σ_y ratios (such as polymers or annealed metals) have more elastic recovery and sink-in [216, 217, 229]. It is seen from the blue data in Figure 8-9b that pile-up also increases with decreasing σ_y . Pile-up is a typical response of high E/σ_y materials and increases with increased plasticity [217, 229]; the compressive stresses in the PDZ may also contribute to increased pile-up [216, 217].

In other words, a summarized interpretation of Figure 8-9 is that the shapes of the indentations are related to the viscoelastic response of the microstructural zones under mechanical load. The F-ICJ process changes the local properties in the PTMAZ and PDZ, thus increasing the plastic response in these zones (higher E/σ_y values). The measured values of depth recovery and pile-up are the polymer's responses to an applied indentation. Both measurements can be interpreted in terms of elastic and viscous responses of the material, such as elastic modulus and hardness [230] or storage and loss moduli [128, 227]. In the PTMAZ and PDZ, the lower local strength is obviously correlated to a change in σ_y , which as previously shown is an effect of the increase in free volume. However, the σ_y alone does not describe elastic recovery in the indentations. The creation of free volume also affects E in a more subtle manner, which was not detected in the macroscopic quasi-static uniaxial testing as shown in Figure 8-5b.

Hutchinson [219] reviewed several aspects of physical aging and its effect on mechanical properties based on the free volume theory. Several studies are presented that confirm that changes in free volume affect time-dependent properties of polymers, such as creep compliance, dynamic moduli, and the loss tangent. More specifically, it has been observed that increased free volume will decrease storage modulus, increase loss modulus, and shift the creep and relaxation curves to lower times. This interpretation has also been used by Ovaert *et al.* [227] to describe recovery behavior during indentation unloading of polymer coatings with constant storage modulus, but varying elastic modulus. The consequence of these interpretations is that the free volume will increase the loss modulus contribution, allowing more dissipation of energy by plastic flow in the PTMAZ and PDZ. The molecular mechanisms dictating this behavior are not completely understood, but they seem to be related to isothermal relaxation of the free volume and possibly to the beta relaxation [219].

This means, scientifically, that the PTMAZ and PDZ zones with more free volume will dissipate more energy from the applied forces [131]. Therefore they are more susceptible to plastic deformation (as represented by higher E/σ_y values) than the more elastic base material (with lower E/σ_y values). Technologically, these results suggest that under cyclic-loading or creep-loading conditions a premature failure can potentially occur in the high free-volume zones.

Consequently, a restoration of the joint's local mechanical properties by controlled annealing (Figure 8-7a) may be beneficial for long-term properties of F-ICJ joints.

8.4 Typical defects in F-ICJ joints

Improper selection of parameters for any fabrication process may lead to a defective product. For the F-ICJ process, most defective joints result from inadequate heat input, tool feeding rate, or an unsuitable combination of both. This section describes the typical defects in F-ICJ joints and their formation mechanisms.

8.4.1 Porosity in the shear layer

Pore formation in polymer welding/joining processes is mostly a result of thermal effects. As experimentally reported by Tan *et al.* [231], porosities are formed either by small thermal degradation products or by shrinkage of the heat-affected polymer. Similar porosity formation was observed in the PTMAZ under all conditions for the PEI/AA6082 joints in this work (Figure 8-10a). Considering that the porosities are only formed within the PTMAZ (not at its interface with the BM zone), and that they have a smooth inner surface (Figure 8-10b), is an indication that they are products of volatile formation [231]. PEI is a hydrophilic polymer, with up to 1.45 % moisture concentration by weight [140]. The specimens used in this study were not dried prior to or after joining, with the as-received material having experimentally-measured moisture content of 0.48 ± 0.00 % by weight. As discussed in Figure 8-8, no extensive degradation of PEI was expected, therefore most of the pore formation is believed to be due to moisture desorption, with a small part probably originating from evolution of small hydrocarbons or other thermal degradation products.

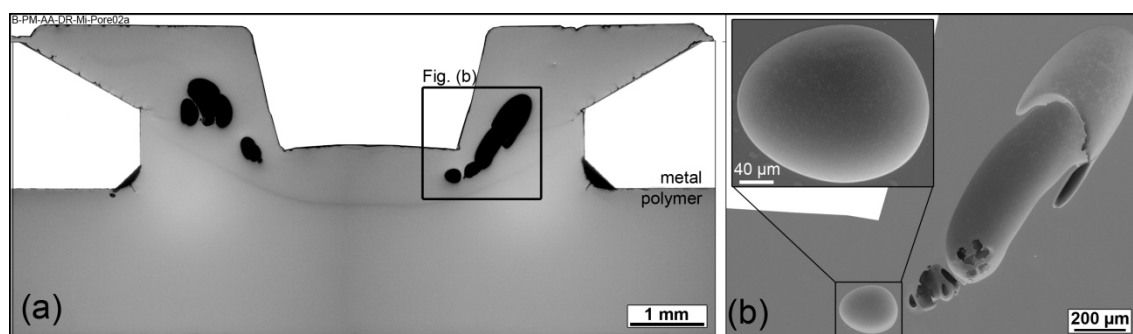


Figure 8-10: (a) Overview of an F-ICJ joint (RLOM); (b) inner surfaces of the pores (SE-SEM). Processing conditions: RS: 12000 rpm; FT: 5000 ms; FP: 0.3 MPa (1525 N); FoP: 0.7 MPa (3733 N); CoT: 5000 ms.

Computed microtomography images (μ CT) of the pores in F-ICJ joints were studied by Schütz [232] under the supervision of the author of this PhD thesis. The μ CT image in Figure 8-11

shows an example of 3D visualization of the pore distribution in an F-ICJ joint, overlaid on a schematic drawing of the stake for better visualization. The pores form a ring-like shape over the chamfer, in a similar fashion to the observations in Section 7.2 (e.g. Figure 7-3b-d and Figure 7-4a).

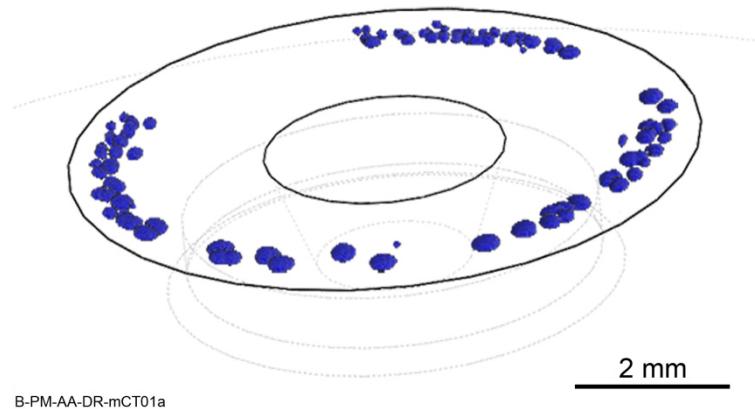


Figure 8-11: Example of 3D visualization through μ CT of pore distribution in an F-ICJ joint (RS: 7500 rpm; FT: 2500 ms; FF: 1525 N; FoF: 3733 N; CoT: 2500 ms). Results adapted from [232].

Porosities are undesirable, because they can act as nucleation points for cracks or shortcuts for crack propagation. The effects of porosities on mechanical behavior will be discussed in Chapter 9 and section 10.2.

8.4.2 Remnant weld line

Weld line formation and healing mechanisms were discussed in Figure 7-8 and Figure 7-9. Ideally, the weld line is healed during a dwell time or consolidation phase of the joining process. If there is not enough thermal energy to allow interdiffusion between the PTMAZ over the chamfer and the stake shaft material during these phases, a remnant weld line will be present in the joint (Figure 8-12a). This weld line is a discontinuous polymer-polymer interface in the stake head. As is known from the failure mechanisms of staked joints, loading will cause rotation of the stake against the chamfer and this is only avoided by the integrity of the stake head [113]. Paz [201] and Tschoepke [233] studied the mechanical behavior of F-ICJ by finite element analysis, under the supervision of the author of this PhD thesis. In Figure 8-12, (b) and (c) show the stress distribution in FEM simulations of lap-shear testing; (b) without a weld line and (c) with. In a qualitative manner, it is clear that the presence of a weld line transfers some of the stresses towards the stake head on the opposing side to the loading direction [233]. This indicates the negative contribution of the weld line to mechanical behavior. The effects of a remnant weld line on the mechanical performance will be discussed in detail in Section 10.2.

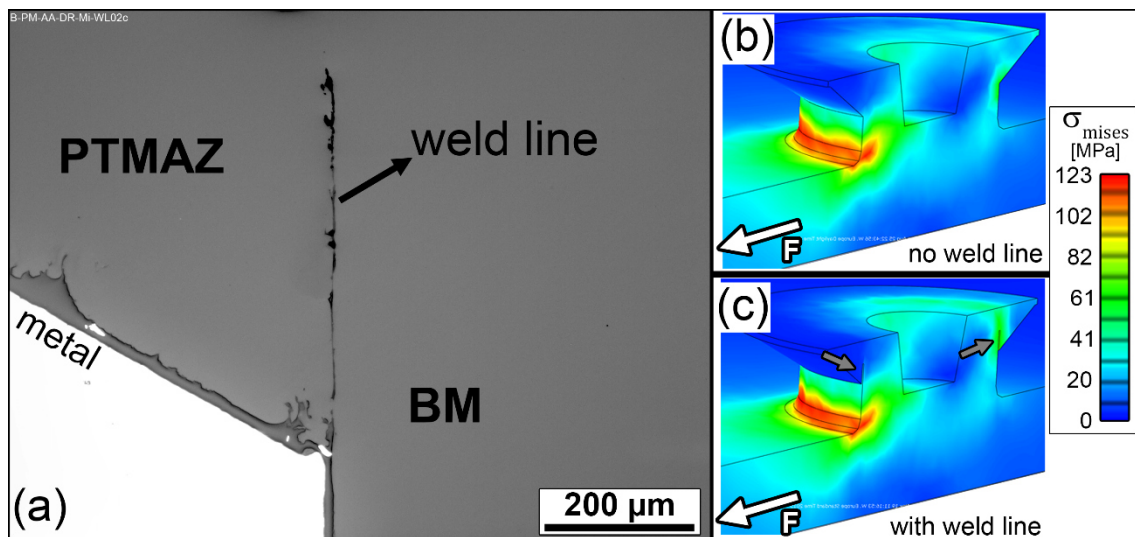


Figure 8-12: (a) Remnant weld line between PTMAZ and BM (RLOM image; RS: 8000 rpm; FT: 2500 ms; FP: 0.3 MPa (1525 N); FoP: 0.7 MPa (3733 N); CoT: 5000 ms); and stress distribution on the stake head for (b) joint without weld line; (c) with a remnant weld line, indicated by gray arrows. FEM results adapted from [233]. The white arrow indicates loading direction.

8.4.3 Stake-shaft shearing (SSS)

The configuration of the clamping system used is able to create joints both with and without a backing surface (see Section 6.2). Joints can successfully be produced with both configurations, using low frictional forces. In joints processed with high joining forces (over 2400 N) and using a backing surface, the microstructure as seen in Figure 8-4 is generated, forming a PTMAZ around the keyhole and a PDZ underneath it. When no backing surface is used with high frictional forces, a different microstructure and local strength distribution is generated, as shown in Figure 8-13.

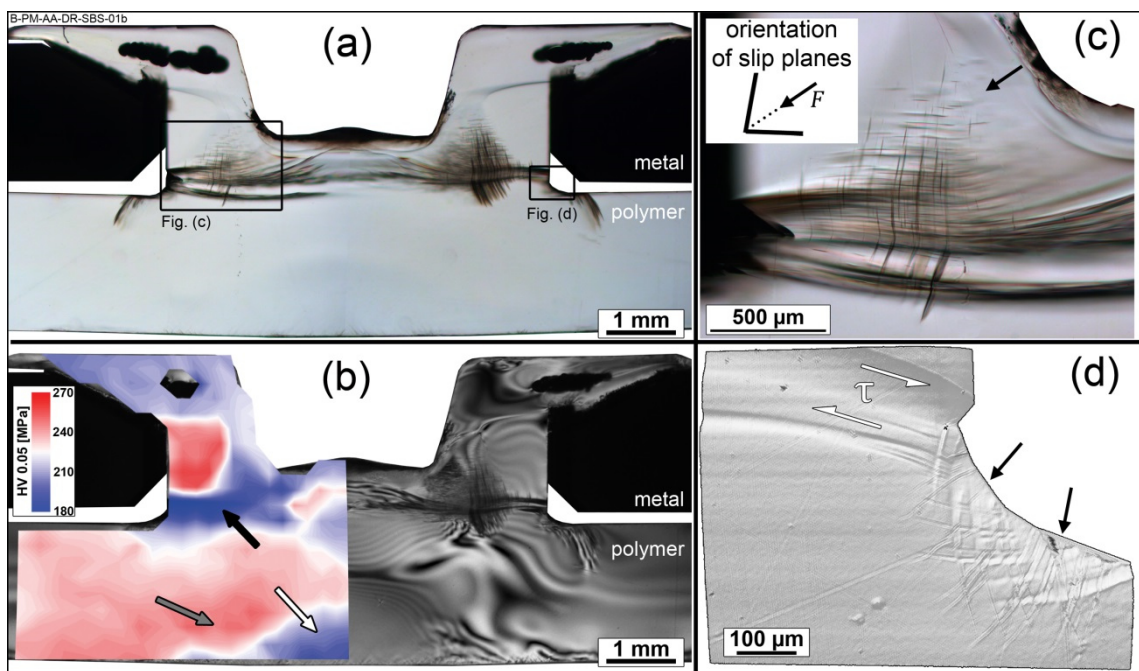


Figure 8-13: Joint produced with high frictional force (2551 N) and without a backing surface, featuring stake-shaft shearing: (a) TLOM micrograph; (b) overlay of microhardness distribution on the stress field image by CP-TLOM (see text for description of the zones indicated by arrows); (c) severe shear banding (TLOM) and schematic orientation of slip planes; (d) 3D surface scan of the shear banding at the stake base (LSCM, 4000 % height magnification). Shear bands indicated by black arrows, shearing of the stake shaft indicated by white half-arrows. Processing conditions: RS: 8000 rpm; FT: 2500 ms; FP: 0.45 MPa (2551 N); FoP: 1.0 MPa (5363 N); CoT: 5000 ms.

In Figure 8-13a, several discontinuities are observed in the plane of the stake base outside of the shear layer. Local strength (microhardness values) around these flaws is very low (Figure 8-13b, black arrows) and at higher magnifications one can observe typical shear-banding morphology in these regions (Figure 8-13c) with slip planes at approximately 41-42° relative to the loading direction in compression (black arrow in Figure 8-13c) [234]. The discontinuities originate from deformation at the base of the stake shaft. The surface profile of the originating region is shown in Figure 8-13d. Shear bands can be seen on the radius of the base, indicating compression yielding in this volume (black arrows in Figure 8-13d). Shear (τ) on the stake shaft (white half-arrows) is observed as a result of the instability created by high tool forces normal to stake length. In Figure 8-13b the photoelastic residual stress field matches the microhardness distribution, with high-order fringes in the low-strength regions. The high feeding rate and axial force cause instability at the base of the stake shaft, plastically deforming it (black arrow in Figure 8-13b). On the bottom surface of the polymer partner, a plastically deformed zone (PDZ, white arrow in Figure 8-13b) is present, and around this region there is a narrow strengthened transition zone (STZ, gray arrow in Figure 8-13b). This STZ results from the same compressive stress effect seen in Figure 8-6c. Although the microstructure is highly affected and several regions of low strength have developed, the quasi-static mechanical performance of such a joint is not greatly affected by this change in microstructure (see Appendix H).

CHAPTER 9. QUASI-STATIC MECHANICAL BEHAVIOR OF F-ICJ JOINTS

Previous works on the quasi-static mechanical performance of staked joints explored their behavior in cross-tensile [98, 102, 105, 107, 115, 235, 236] and lap-shear configurations [99, 113, 115]. However, none of these works provided a deep investigation of the mechanical behavior and failure mechanisms present in staked joints.

This chapter explains the quasi-static mechanical behavior of F-ICJ joints in both lap-shear and cross-tensile testing in detail. The failure behavior and fracture mechanisms are associated with the relevant microstructural features that were studied in the previous chapters.

9.1 Mechanical behavior in lap-shear configuration

The configuration of a lap-shear (LS) test was introduced in Section 6.3.8. Staked specimens from F-ICJ are mechanically-fastened overlap joints of a rigid partner (aluminum) and a more flexible one (polymer). This stiffness mismatch between the partners is reflected during the test as an eccentricity in load transfer, which in turn leads to secondary bending of the weaker partner. In bolted joints, the stiffness mismatch creates a non-uniform contact pressure in the hole, which causes secondary bending [237]. Effects reported are reduction of joint stiffness and its influence on the type of failure. Staked joints are also mechanically fastened joints, but unlike bolted joints, the stake (fastener) is an integral part of one of the joining partners. Bolted joints also have the positive influence of a clamping force, resulting from the fastening torque at the bolt, so that load transfer to the fasteners only occurs after the frictional forces (induced by clamping torque) have been overcome [237]. The joining partners in this work were designed with no clearance gap, having a tight clearance-fit joint. In this case, no extensive load transfer solely due to friction takes place, and a contact between stake shaft and the cavities in the metal part can be assumed to be observed from the beginning of the test. Figure 9-1a shows an analysis of the eccentricity in lap-shear loading based on the work by Ekh [238]. The analysis considers only the main effects acting in lap shear, neglecting the shear and friction components.

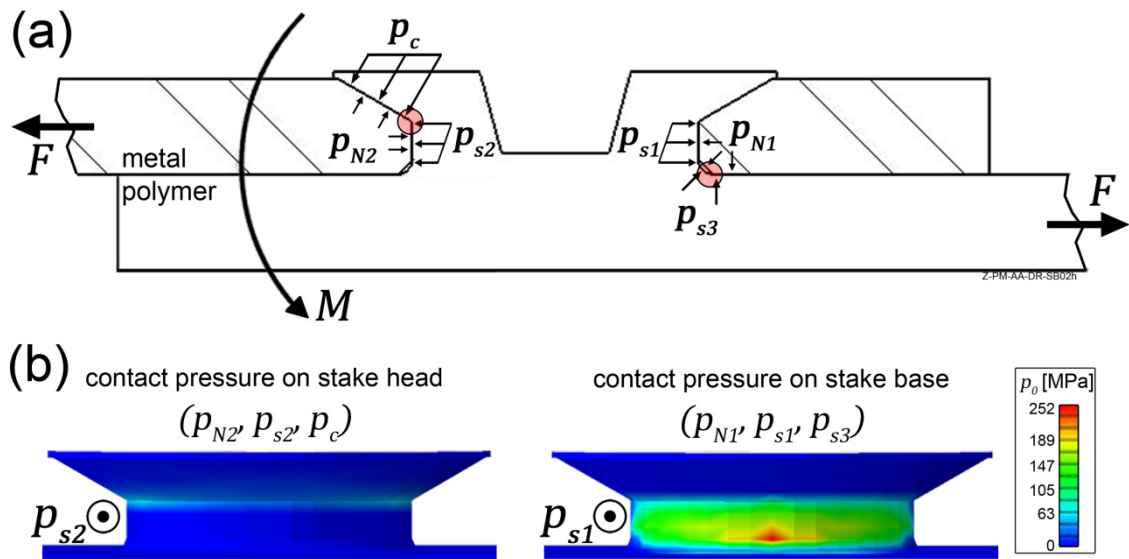


Figure 9-1: (a) Schematic description of the forces acting during lap-shear loading of F-ICJ joints, based on the analysis by Ekh [238]. Red disks are the main stress concentration spots; (b) finite element method (FEM) simulation of the contact pressure on both stress concentration regions, adapted from [233]. FEM LS models followed the same test setup as the actual experiments (see Section 6.3.8).

In lap-shear loading, the lower (polymer) plate is pulled by the force F (which has a reaction force F in the opposite direction on the clamped part). The eccentricity creates uneven contact pressure distributions p_{s1} and p_{s2} from the stake on the hole walls [238, 239], which result in a bending moment M . M causes an out-of-plane deflection, and in a chamfered design this deflection creates a pressure p_c on the chamfer and a pressure p_{s3} on the stake base. The response to these contact pressures are the reaction normal pressures p_{N1} and p_{N2} . The normal pressure p_{N1} along with the pulling force F creates a stress concentration point on the stake base, while p_{N2} creates another stress concentration point on the lower edge of the chamfer (red disks show the stress concentration points). The state of stresses is further supported by FEM simulation of the contact pressures normal to the outer surfaces of the stake (Figure 9-1b). The highest pressures applied by the metallic partner on the stake match the stress concentration points from Figure 9-1a, confirming the interpretation of the stress analysis in LS testing. The higher contact stress at the lower part of the stake base (right-hand side of the picture in Figure 9-1b) is consistent with the analysis from [237] which states that contact pressure increases at the interface between the workpieces. The reaction contact pressure p_{N2} (from p_c and p_{s2}) is concentrated on the lower edge of the chamfer (left-hand side of Figure 9-1b), but at much lower magnitudes than the pressure at the stake base p_{N1} (right-hand side of Figure 9-1b).

The out-of-plane deflection of the metal and polymer plates caused by M is the secondary-bending effect observed in F-ICJ joints, as illustrated in Figure 9-2a by snapshots from digital image correlation (DIC) measurements.

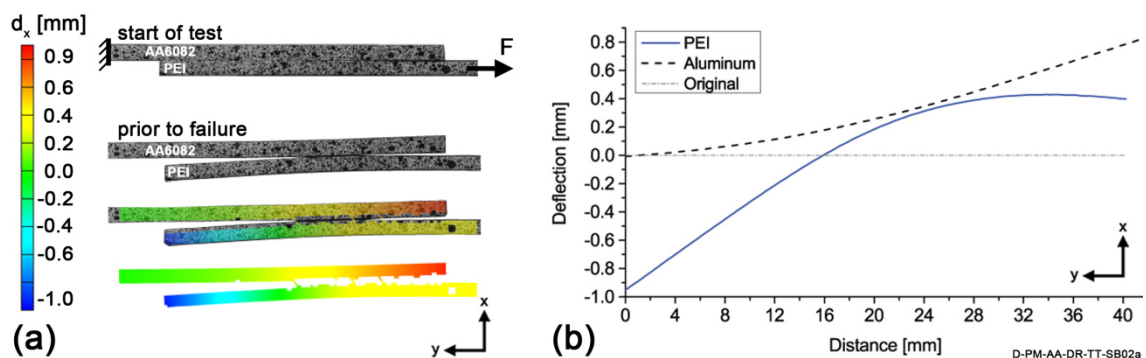


Figure 9-2: (a) Lateral view of specimens at the start of a lap-shear test and prior to failure, with an overlay of the deflection in the x-axis; (b) deflection from secondary bending for PEI (blue solid line) and aluminum (black dashed line) in relation to their original position (gray dash-dotted line).

At the start of the test, both plates are parallel to the loading direction, without any deflection in the out-of-plane x-axis. Ordered from top to bottom of Figure 9-2a, the first two images show the change in shape of both plates prior to failure, and the third and fourth images show the actual local out-of-plane deflection as measured by DIC. The curvature is plotted in the diagram from Figure 9-2b compared to the original position of the plates at the start of the test. A slight bending at the free edge of the aluminum plate is observed. The PEI plate deflects in a more dramatic fashion over a larger distance, as schematically shown in Figure 9-3a. A representative tensile stress $+\sigma_F$ is present over the length of the specimen as a result from the force F applied by the grips. Added to $+\sigma_F$ a gradient of stresses along the plate thickness is created by the bending moment M , focused at the center of rotation from the secondary bending. There are tensile stresses on the top surface and compressive stresses on the lower surface in this region. Figure 9-3b schematically shows the local effect of the bending moment on the base plate.

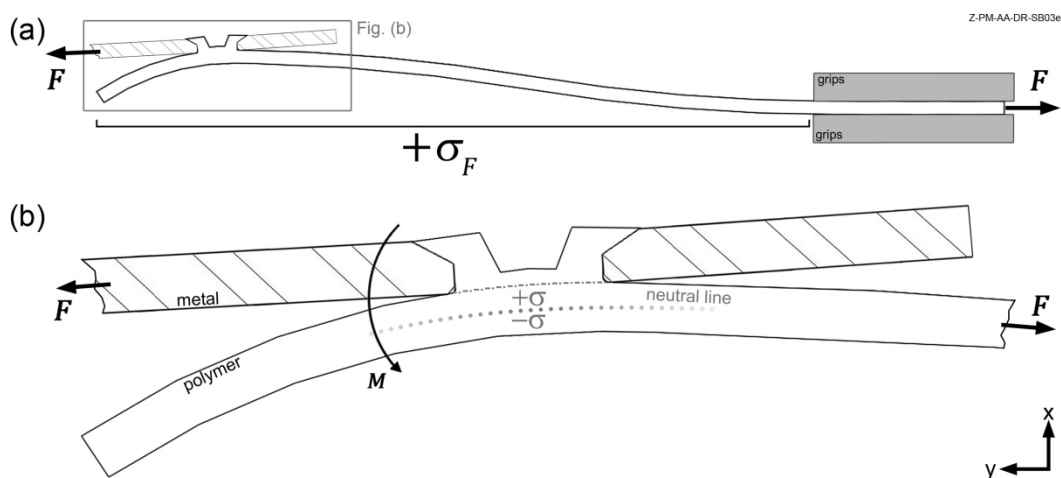


Figure 9-3: (a) Deflection of the polymer plate from secondary bending; (b) stresses on the base plate in an F-ICJ metal-polymer overlap joint.

The effects of the observations in Figure 9-3 were experimentally observed by DIC strain-field measurements on the bottom surface of the PEI plate during the lap-shear test, as shown in Figure 9-4. During the elastic phase (Stages I and II) tensile strain $+\varepsilon_y$ is observed in the areas away from the stake region (close to the plate edge and the grip), while along the plate width (x-axis) compressive strain $-\varepsilon_y$ is seen. The boundaries of these regions are marked by dotted black lines. As the ultimate force is reached and it starts to decrease, an intensification of the secondary bending is seen, and the compressive strain in the stake region extends to a horizontal hourglass-shaped area (dotted lines in Stages III and IV). The compressive strain directly beneath the stake increases until failure by secondary bending (SB). These results indicate that the bending moment effect from Figure 9-3b is most intensely localized around the stake region (the hourglass-shaped region in Stages III and IV), while tensile stresses $+\sigma_F$ from Figure 9-3a dominate in the rest of the plate.

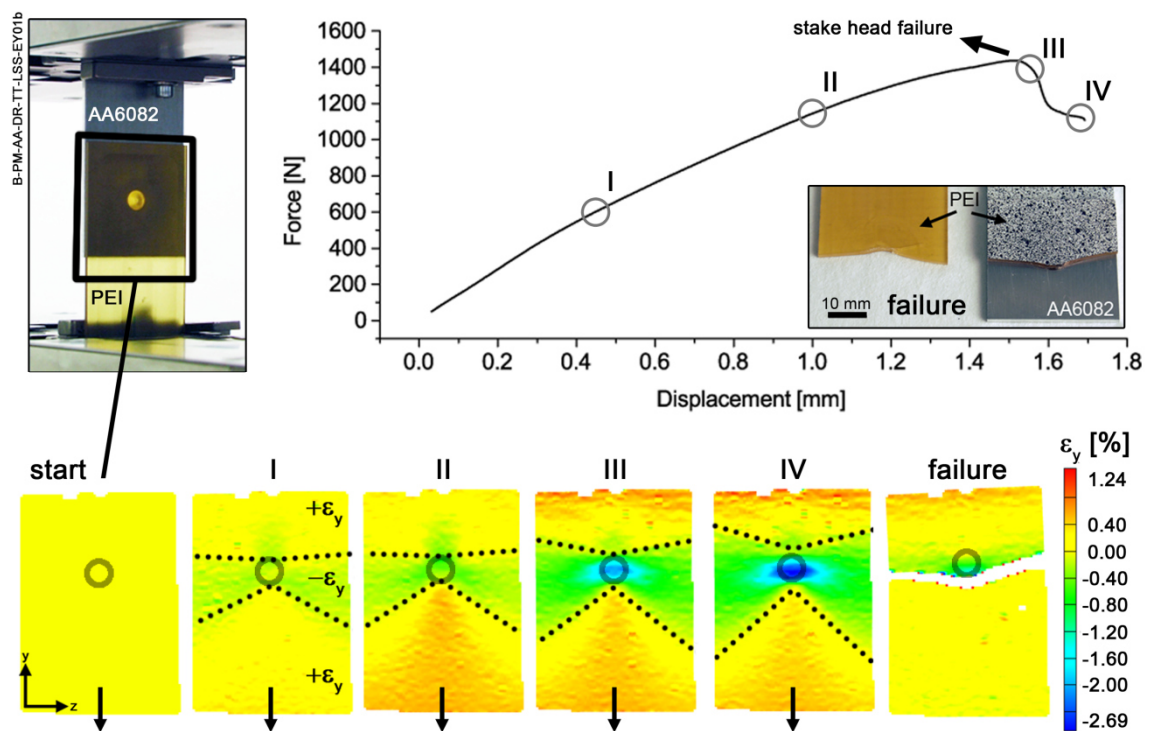


Figure 9-4: Mechanical behavior in lap-shear testing. Snapshots of the strain in y-direction at selected stages of the force-displacement curve show increasing localized compressive stresses $-\varepsilon_y$ (hourglass-shaped boundaries). The position of the stake is indicated by a dark circle in the snapshots.

In lap-shear testing, the polymeric partner undergoes secondary bending, which creates a stress gradient through the thickness of the plate and a stress concentration point on the chamfer edge. The tensile stresses $+\sigma$ on the top surface of the polymeric plate (Figure 9-3), along with the normal pressure p_{N1} (Figure 9-1), nucleate a crack at the stake base, which ultimately brings the polymer plate to catastrophic brittle failure. The stresses on the chamfer nucleate a crack in the stake head, which coincides with the peak force (Stage III of the curve in Figure 9-4); this loss of stake-head strength triggers intensification of the compressive

stresses in Stages III and IV due to greater load transfer to the stake base. For an interpretation of microstructural effects on this behavior Figure 9-5a displays a micrograph of a failed specimen. Two cracks are visible in the material: one in the stake head (Figure 9-5b) and one in the base plate (Figure 9-5c).

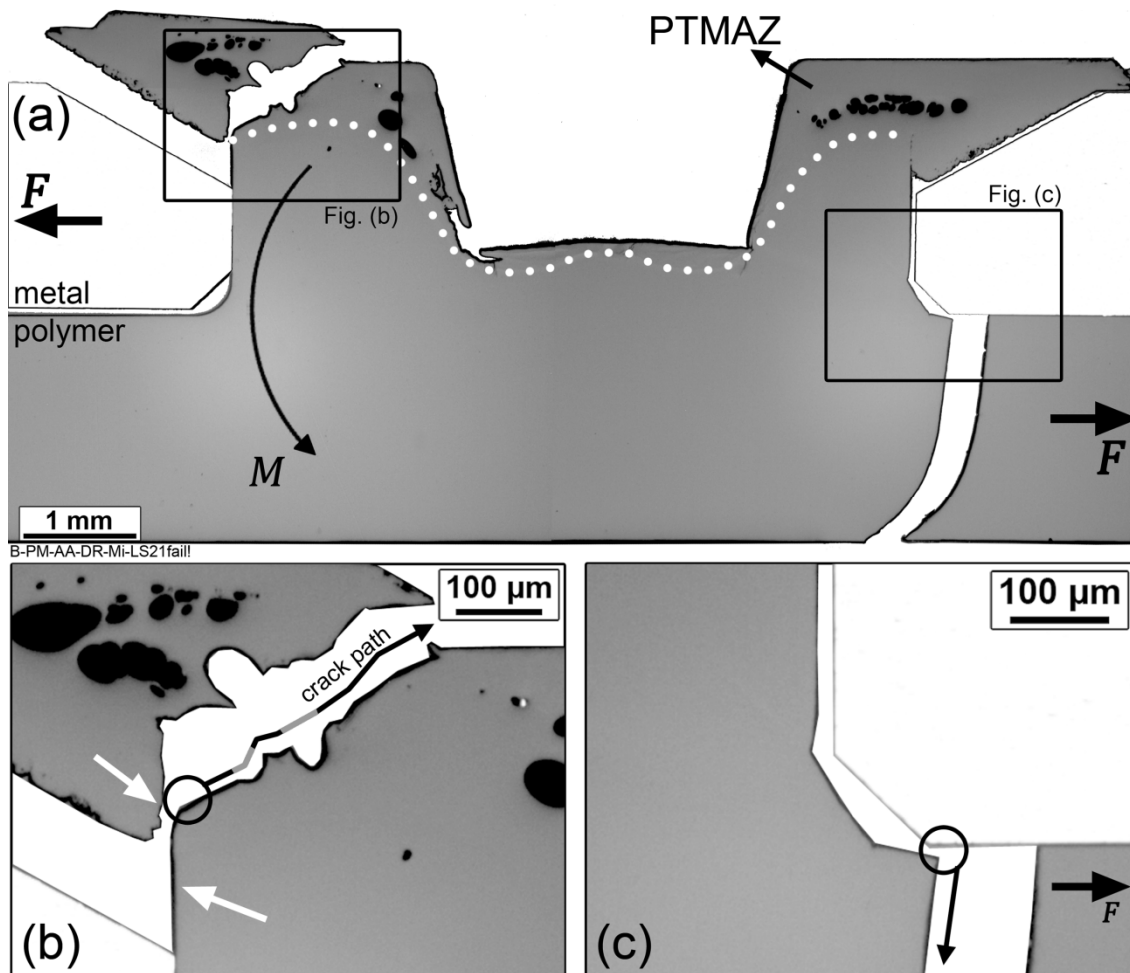


Figure 9-5: (a) Micrograph of a LS joint failure by secondary bending. PTMAZ boundary is marked by the white-dotted line; (b) detail of the radial crack on the stake head. White arrows indicate weld line interfaces; (c) detail of deformation at the stake base (RLOM images). Processing conditions: RS: 8000 rpm; FT: 2500 ms; FP: 0.3 MPa (1525 N); FoP: 0.7 MPa (3733 N); CoT: 5000 ms.

Due to the bending moment M , there is a tendency of the stake to rotate, which creates the reaction pressure p_{N2} on the chamfer. A crack nucleates and propagates radially around the stake head in this region (Figure 9-5b). The crack nucleation and propagation at the stake head may be influenced by the remnant weld line and the porosity distribution. From the figure, it is clear that the crack nucleated on the end of the weld line interfaces (white arrows in Figure 9-5b) from this joint. The volumetric discontinuity does not transfer loads, and stress is concentrated on the tip of weld line, where a crack nucleates (black circle in Figure 9-5b). The

head crack propagates through the lower-strength PTMAZ, where pores are present. In Figure 9-5b, the path is colored gray in the regions where it passed through a pore. This shows that lower strength and discontinuities in the PTMAZ make it a preferential path for a stake-head crack. The microstructural effects of the weld line and porosities on the mechanical performance are assessed in Section 10.2. In Figure 9-5c, a plastic deformation of the stake base with the shape of the lower metallic chamfer is displayed. This is the effect of the contact pressure p_{s1} on the stake. The stress concentration in this deformed zone, combined with bending moment tensile stresses ($+\sigma$) on the top surface of the PEI plate, nucleate another crack that propagates towards the lower surface of the plate. Its propagation constitutes the final failure of a lap-shear joint, by secondary bending. Based on the analysis from Figure 8-4, the volumes of the PEI plate where the main crack propagates are not usually affected by the joining process. In the case of joints with stake-shaft shearing (SSS, Figure 8-13) plastic deformation in the stake base might influence the crack behavior, since the yielded polymer can dissipate more crack propagation energy due to the decreased bonding energy (more free volume) [90]. In this case a more ductile behavior would be expected in the crack initiation region.

A combined analysis of the force-displacement curve in Figure 9-4 and the crack behavior from Figure 9-5 is able to define the mechanism up to joint failure. The curve shows an elastic behavior prior to the ultimate force (Stages I and II), with no extreme strain concentrations in the polymer's bottom surface observed by DIC. When the stake head breaks, the force suddenly decreases (Stage III) and the load is concentrated on the main crack. At this point the compressive strain on the bottom surface of the polymer rapidly increases (Stages III and IV), corresponding to accelerated secondary bending. A staked joint's resistance to out-of-plane deflection from secondary bending is improved by a large stake head or internal cavities in the metallic partner [113]. These additional mechanical anchoring features may decrease the effect of M and hinder stake rotation, consequently reducing p_c at the chamfer. The analysis of these results improves the state-of-the-art description of failure of stake joints, expanding the knowledge reported by experimental observation of staked joints using a ductile thermoplastic (PA66-GF) by Abibe *et al.* [113]. In that case, the same radial crack at the stake head was present and final failure occurred at the main crack in the base plate. For PA66-GF the main crack showed slow crack propagation, except when the PA66-GF was dried before testing, in which case the failure was catastrophic, as is typical of a brittle polymer.

An overview of the micromechanisms controlling crack growth in the polymer plate is displayed with SE-SEM images in Figure 9-6. The crack propagation direction is downwards, from the stake base towards the bottom polymer surface. Four regions are defined: a crack initiation zone "A", a fast-propagation transition zone "B", a stable/unstable growth zone "C", and a fast-propagation banded zone "D". These zones are common to all observed secondary bending failure surfaces. The position of the crack initiation region A validates the stress concentration site predicted in the right-hand side of Figure 9-1b.

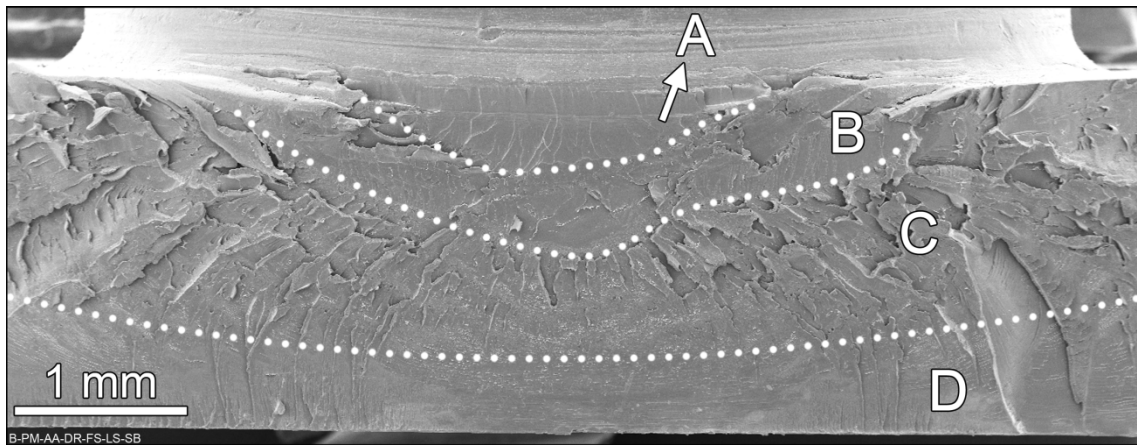


Figure 9-6: Example of the crack propagation regions in secondary bending failure (RS: 8000 rpm; FT: 2500 ms; FP: 0.3 MPa (1525 N); FoP: 0.7 MPa (3733 N); CoT: 5000 ms). See text for a description of the zones.

In the crack initiation region A, river patterns are observed that indicate stable plastic deformation in plane strain [240]. The river patterns in amorphous polymers are a result of the coalescence of craze fronts and subsequent separation on different planes [240, 241]. A detailed view of the crack initiation zone is shown in Figure 9-7. The river patterns are the microflow lines and striations that originate from the black rectangle region. Their bifurcation points indicate the crack propagation direction, as indicated by the white arrows in Figure 9-7a. The black arrow in Figure 9-7b shows the origin of the river patterns in this fracture surface. This crack nucleation point is located around 160 μm below the surface of the specimen. Crack nucleation in the bulk, away from the surface, has been reported for PEI and polycarbonate [242, 243]. Craze formation is triggered by the formation of voids in the material as a result of high local stresses. The maxima of hydrostatic and principal stresses in front of a crack tip are at the boundary between the elastic and plastic zones [242], which lies below the surface. When the plastic zone achieves a critical size, internal voids are formed at the elastic-plastic boundary due to the aforementioned hydrostatic stresses [244], causing the crack to initiate below the surface.

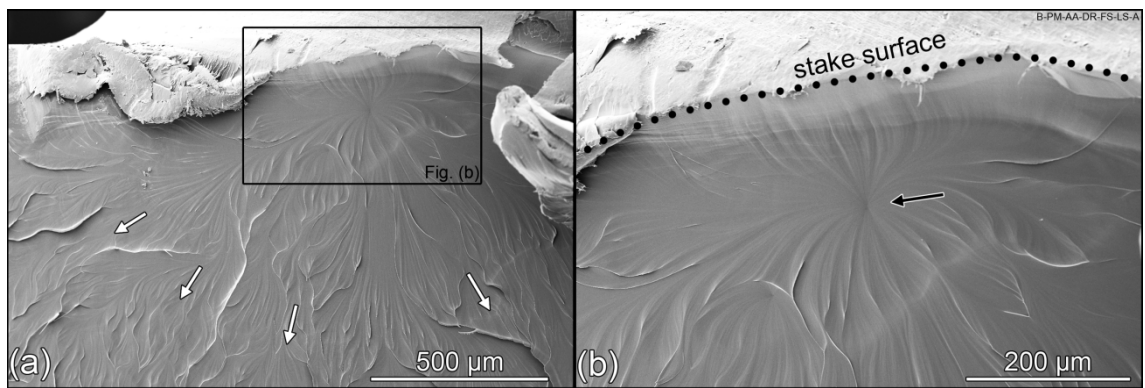


Figure 9-7: (a) Crack initiation region. White arrows indicate crack propagation direction; (b) crack nucleation point (black arrow) below the stake surface. For processing conditions see Table 11-2.

After the crack initiation zone, a transition zone B with mixed features of classic mirror and mist zones is observed (Figure 9-6) [243, 245]. This transition zone is seen in detail in Figure 9-8. The river patterns and striations change into biplanar fracture patterns such as large patches (white arrows) and/or small conical markings (gray arrows) over a very smooth surface. These are features related to the instability of craze growth that cannot dissipate enough crack propagation energy at this stage [241, 243]. These mechanisms are observed on a dominant mirror-like, smooth surface, characteristic of very fast crack propagation without formation of crazes [245]. The transition zone B is followed by zone C, which is dominated by tearing-type shear yielding in the form of large hackles with intermittent patch patterns (black arrows, Figure 9-8), indicating a change from plane strain to plane stress state [246]. These features correspond to a slower crack propagation than zone B.

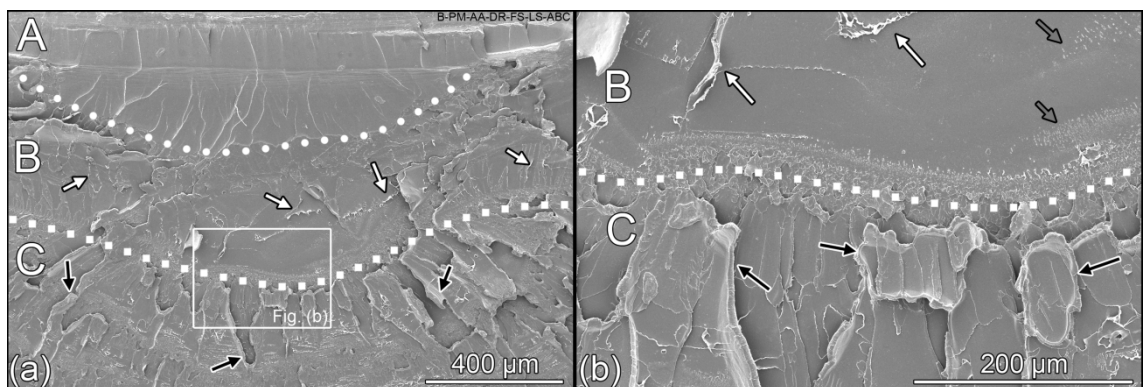


Figure 9-8: (a) Boundaries between crack initiation zone A, transition zone B, and stable/unstable growth zone C; (b) detail of the boundary between zones B and C. White arrows show patches, gray arrows show conical markings, black arrows show hackles. Processing conditions: RS: 8000 rpm; FT: 2500 ms; FP: 0.3 MPa (1525 N); FoP: 0.7 MPa (3733 N); CoT: 5000 ms.

The transition zone B corresponds to the decrease in moment of force discussed in Figure 9-4. The elastic part of the curve corresponds to the sustaining load of both the stake head and the base plate. At some point prior to reaching peak force, a crack nucleates in the base plate and slowly propagates in a craze-controlled stable manner (zone A). As soon as a critical crack size is achieved in the stake head (when it cannot withstand the bending moment M), the load is suddenly transferred to the main crack at the bottom of the stake. The higher stress on the base plate increases the strain energy release rate on the plate crack front, which causes the transition from stable crack growth to fast crack propagation [131, 241], as characterized in zone B. The crack front at this speed eventually reaches the plastic zone envelope ahead of it, which dissipates part of the energy as shear deformation, evidenced by the large hackles in zone C [246]. This forms the transition from plane strain to plane stress at the fracture surface. Another contribution to crack deceleration is from compressive stresses as the crack passes the neutral line of the polymer sheet (Figure 9-3) [245].

Finally, transition from zone C to the fast-propagation banded zone D is displayed in Figure 9-9a. The end of the stable/unstable zone C, composed mostly of patch patterns (black arrows) and small hackles (white arrows), is reached. The change to an end-banded structure, as shown in Figure 9-9b, marks the typical terminal zone of a fracture in amorphous polymers, because the stresses achieve levels below the critical crazing stress [241, 243, 245]. The parallel lines observed in these structures are perpendicular to the crack propagation direction and concentric to the crack nucleation point [243].

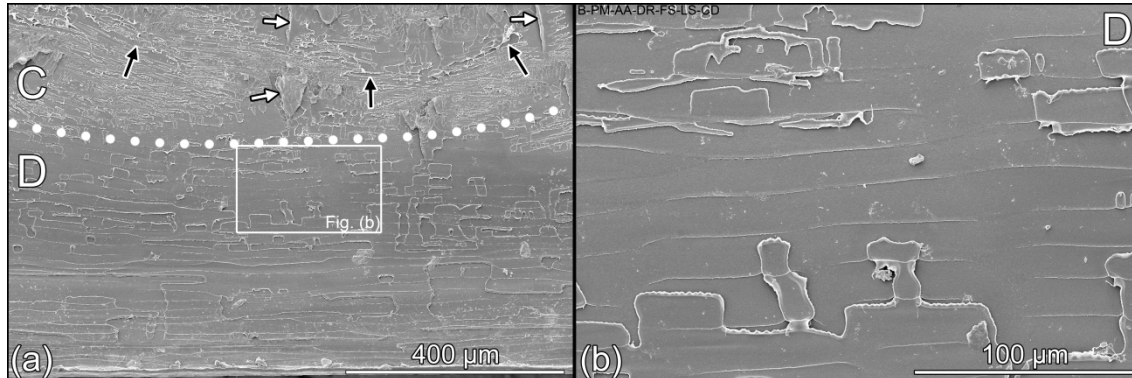


Figure 9-9: (a) Transition between zones C and D. Black arrows are patch patterns, white arrows are hackles; (b) end-bands in the fast-propagation banded zone D. Processing conditions: RS: 8000 rpm; FT: 2500 ms; FP: 0.3 MPa (1525 N); FoP: 0.7 MPa (3733 N); CoT: 5000 ms.

Secondary bending failure (SB), as described here, was observed for 91 % of all comparable F-ICJ LS joints in this work (98 specimens, $n = 108$). In the remaining 9 % of the joints (10 specimens) the main crack did not propagate completely through the plate thickness and/or width (white arrow, Figure 9-10a), consisting of an incomplete secondary bending failure (IB). Otherwise, the failure is identical to SB. The incomplete crack can be the result of crack deceleration mechanisms previously mentioned as active in zone C of the fracture surface. For both SB and IB failures, a complete removal of the stake head was occasionally observed

(11 % of all lap-shear joints, 12 specimens). Complete head removal is shown by black arrows in Figure 9-10b for a specimen presenting SB failure (white arrows). The stake head is removed due to a rebound effect at the moment of catastrophic failure of the base plate. The existing stake-head crack may introduce a notch effect that facilitates removal of the stake head from the rebound.

A comparison between SB and IB failures is shown in Figure 9-10c. Average values of the ultimate lap shear force (ULSF) and the displacements at ULSF and at break do not differ greatly between failure modes. These results suggest that IB is a variation of SB failure, and its occurrence along with stake-head removal is a punctual observation rather than an actual processing effect. Moreover, LS tests of non-joined specimens (polymeric stud inserted into the hole of aluminum specimens) presented the same SB failure, but at a much lower ULSF, probably because without a stake head crack, growth in the base plate is accelerated (see Appendix I).

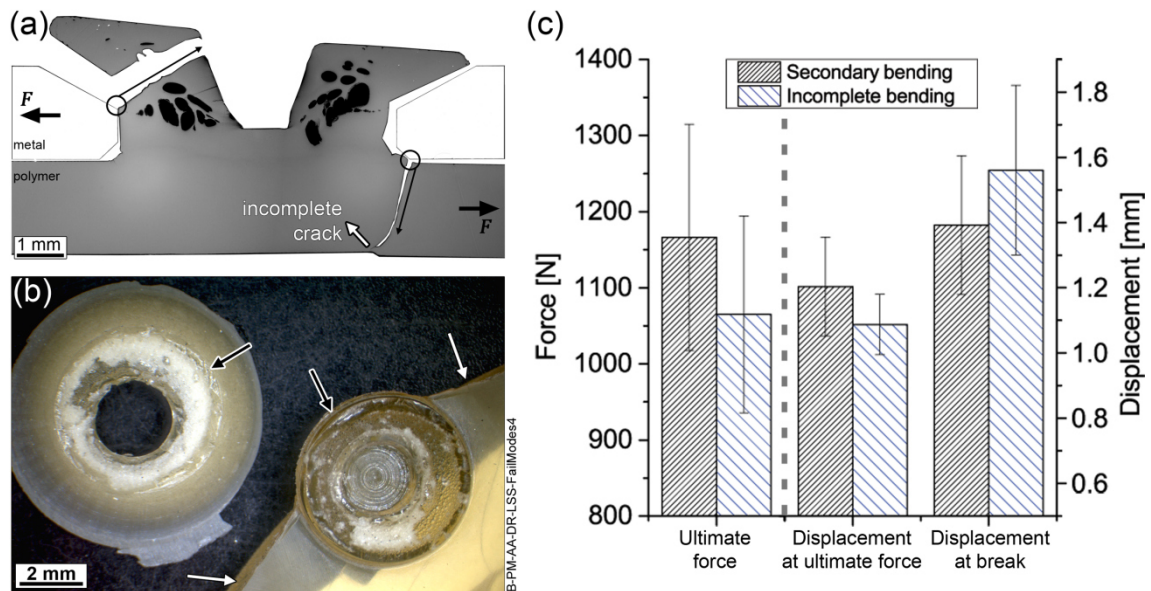


Figure 9-10: (a) Incomplete bending failure (IB) in the base plate, white arrow indicates the end of the crack (RS: 8000 rpm; FT: 5000 ms; FP: 0.5 MPa (2726 N); FoP: 1.0 MPa (5363 N); CoT: 2500 ms.); (b) Example of a specimen showing complete removal of the stake head as a result of the rebound from catastrophic SB failure (RS: 12000 rpm; FT: 5000 ms; FP: 0.5 MPa (2726 N); FoP: 1.0 MPa (5363 N); CoT: 5000 ms). White arrows show SB fracture surfaces, black arrows show the fracture surfaces of stake head removal; (c) comparison of average mechanical properties between SB and IB failures.

In summary, the mechanical behavior of F-ICJ joints under lap-shear loading is related to the interdependence of crack growth in the stake head and the base plate. A premature failure of the stake head can degrade the overall joint performance. In the stake head (radial) crack, weld lines work as a nucleation point and pores are preferential crack paths. The significance of the microstructural features on joint performance will be discussed in the next chapter. The

joint fails by secondary bending of the polymer base plate as the stress concentration in this region increases, leading to crack instability and rapid growth.

9.2 Mechanical behavior in cross-tensile configuration

The cross-tensile test (CT) was previously described in Section 6.3.8. This joint geometry tests the strength of the stake head in tensile loading. A schematic view of the forces acting on the joint is shown in Figure 9-11a. As the aluminum partner remains stationary, the polymer plate is pulled away, only being held by the mechanical interference of the stake head. The pulling force F creates bending moments M on the polymeric plate and their action induces bending stresses $+\sigma$ and $-\sigma$ in the base of the polymeric plate, as shown in the figure. The tensile bending stress $+\sigma$ on the top surface of the polymer plate along with the normal pressure p_N reacting to M create a stress concentration on the stake base (red disk). In addition, as the plate is pulled with a force F the stake is pressed against the chamfer cavity with a contact pressure p_c . Normal pressure p_N counteracting p_c and M force the stake head in the opposite direction, creating stress concentrations at the chamfer edge (orange square). In the FEM simulation [233] in Figure 9-11b it is clear that the stresses are more significant at the stake base than at the head in the CT loading. The correlation of these stress concentration points to failure behavior will be explained in this section.

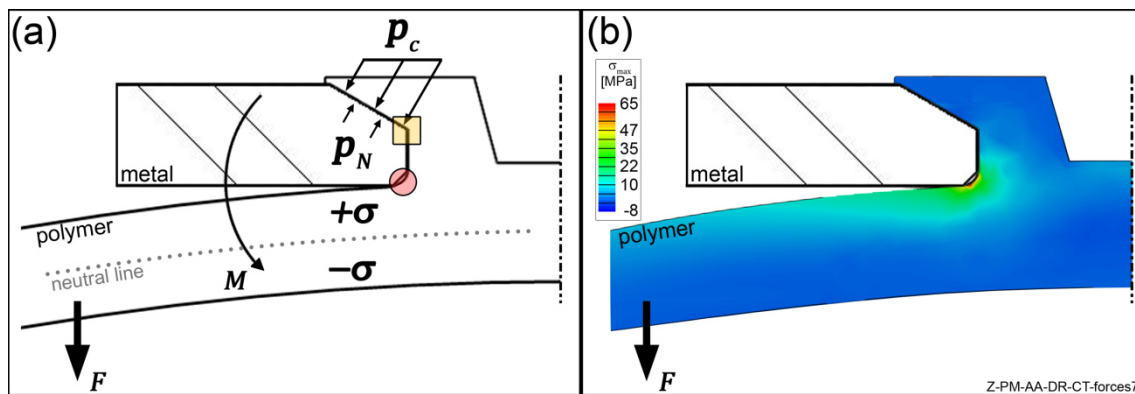


Figure 9-11: (a) Forces acting on the joint in cross-tensile loading. The red disk and orange square represent the main stress concentration points in CT joints; (b) FEM simulation of the maximum principal stresses acting in the joint, adapted from [233]. FEM CT models followed the same test setup as the actual experiments (see Section 6.3.8).

The stress state in cross-tensile testing generally yields a linear force-displacement curve (Figure 9-12a) prior to failure, by either of two concurrent failure mechanisms: base-plate bending (BPB) or head pull-out (HPo), which are represented in Figure 9-12b and c, respectively. The most common failure mode was BPB (Figure 9-12b), which takes place from cracks that propagate from the stake base through the plate's thickness (red disk in Figure 9-11a). This type of failure was observed in 54 % of the comparable joints (61 specimens, $n = 114$). In 37 % of the joints (42 specimens) failure by HPo (Figure 9-12c) was observed. In this

case, the preferred crack nucleation and propagation happens due to reaction stresses p_N around the chamfer (orange square in Figure 9-11a). Both of these failures are catastrophic, with a sudden burst and a linear force-displacement curve.

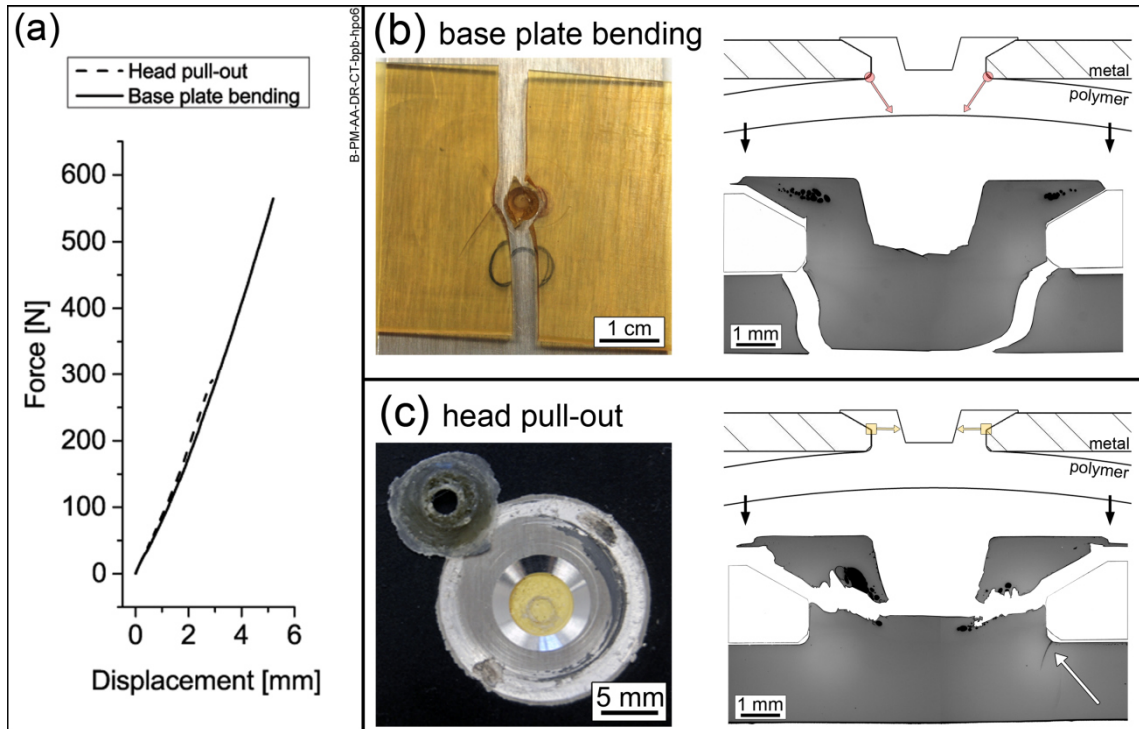


Figure 9-12: (a) Example of linear force-displacement behavior in cross-tensile testing. Overview of (b) base-plate bending failure – BPB (RS: 12000 rpm; FT: 2500 ms; FP: 0.5 MPa (2726 N); FoP: 1.0 MPa (5363 N); CoT: 2500 ms); (c) head pull-out failure – HPo (RS: 8000 rpm; FT: 5000 ms; FP: 0.5 MPa (2726 N); FoP: 0.7 MPa (3733 N); CoT: 5000 ms).

The effects of stress magnitude on each of the stress concentration points can be observed in the failure micrographs in Figure 9-12b and c. Generally, HPo specimens present crack initiation at the base plate (white arrow in Figure 9-12c), whereas for BPB failure, no damage of the stake head is observed. Moreover, the mechanical behavior of the BPB failure is similar to the one observed for the three-point-bending tests of as-machined cross-tensile PEI specimens, which also failed by BPB (Appendix I). These results confirm the hypothesis of concurrent failure mechanisms. The cracks at the polymer base plate are initiated, due to $+\sigma$ and p_N , while the stresses at the chamfer gradually increase. Failure mode depends on whether the base-plate crack achieves a fast propagation regime before the head crack is fully developed and leads to HPo.

Due to the bending nature of the BPB failure mode, it presents similarities to lap-shear secondary bending failure. As seen in Figure 9-13a the polymer plate breaks into two halves, while the stake stays attached to the metallic partner. Each surface of the halves of the plate (or the matching surfaces below the stake) presents sets of micromechanisms corresponding to various crack growth regimes. One of the fracture surfaces is rather flat and exhibits stable

crack growth (top surface of Figure 9-13a, fracture view in Figure 9-13b), while the other surface is concave and presents only fast crack-propagation mechanisms (lower surface of Figure 9-13a, fracture view at Figure 9-13c). On the stable crack-growth side (Figure 9-13b), the fracture morphology is similar to that of secondary bending (SB) failure of lap shear (LS) specimens. A crack initiation zone A with river patterns determines the crack origin and local direction of propagation (Figure 9-13b). The transition zone B with a mirror surface is small or absent in this failure mode. Moreover, it does not cover the whole boundary of crack initiation zone A and appears not to originate from zone A, as in the LS fracture surface. As seen in Figure 9-12b, damage to the stake head is not present in BPB failure, therefore this triggering mechanism for faster crack propagation is absent, and so zone B does not develop in the same fashion as observed in lap-shear failure (Figure 9-8). The rest of the fracture surface reveals a mixture of features from a stable/unstable crack growth zone C and the fast-propagation banded zone D. The white arrows in Figure 9-13b and c are shear yielding deformations as large hackles or shear lips (seen in detail in Figure 9-13d), which are characteristic of zone C; the black arrows indicate the flat surfaces dominated by end bands (seen in detail in Figure 9-13e) that are characteristic of zone D. On the unstable crack-growth side (Figure 9-13c) the typical river patterns indicating a stable crack growth region are absent. The crack on this side nucleates at the stake base and forms a mirror region B to the extent of its fast propagation, followed by a zone of mixed C and D features as seen in Figure 9-13b. It can be assumed that in BPB failure, one side of the stake preferentially develops a stable crack growth regime, which transitions to the C+D zone in a catastrophic propagation fashion throughout the plate width, as seen in Figure 9-13b (top plate half in Figure 9-13a). When this half of the plate is detached from the stake, a sudden load transfer to the other plate half takes place, causing fast crack propagation and forming its mirror zone B as described in Figure 9-13c (lower plate half in Figure 9-13a). Crack deceleration from zone B to C+D occurs as the front reaches the plastic zone (transition from plane strain to plane stress), in the same fashion observed for LS specimens (see Figure 9-8).

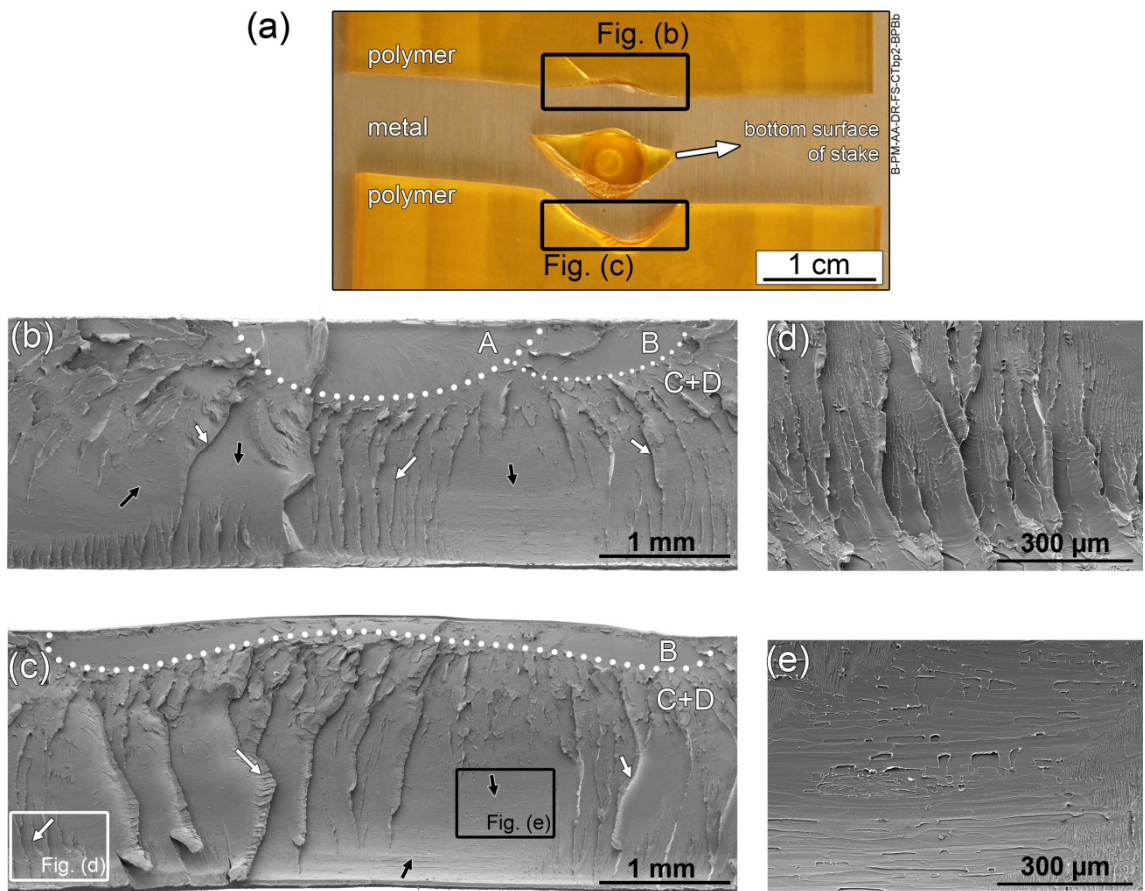


Figure 9-13: (a) BPB failure of a CT specimen (RS: 8000 rpm; FT: 2500 ms; FP: 0.45 MPa (2551 N); FoP: 1.0 MPa (5363 N); CoT: 5000 ms); (b) fracture surface on the stable crack-growth side; (c) fracture surface on the unstable crack-growth side. White arrows are shear micromechanisms shown in detail in (d), black arrows are end-banded regions shown in detail in (e). See text for description of the zones.

An overview of the failure micromechanisms in HPo failure is shown in Figure 9-14 (bottom view of the fractured stake head). The fracture surface shows a clear interaction of the crack path with the porosities. The micromechanisms are the same as those generally observed in the fracture surfaces of amorphous polymers: river patterns close to crack initiation regions, transition zones of unstable crack growth, and end-banded structures close to the terminal fracture surface [240, 241, 243]. Figure 9-14b shows these transitions in a region highlighted in Figure 9-14a, close to the terminal surface (keyhole). Slow crack propagation by river patterns is seen on the left-hand side of the image, with the crazes propagating in the direction of the white arrow towards the pore. As the crack propagates around the pore, new micromechanisms are developed. The micromechanisms show an acceleration of the crack front near to the pores, evident due to unstable crack growth micromechanisms, such as biplanar fracture patterns (gray arrows), and end-bands (black arrows). This transition is marked by the white-dotted line in Figure 9-14b and in an overview of the transition around pores shown in Figure 9-14c (crack propagation direction is indicated by white arrows). In Figure 9-14d, the high pore content volume shows a more fibrillar and slower fracture mechanism in the material between the pores (i.e. the former pore ligament). No vestiges of

crack nucleation sites in this region can be identified. This observation, along with the structure seen in Figure 9-14c, indicate that the pores do not necessarily work as crack nucleation points, but they may influence the crack propagation regime by accelerating crack growth.

In this joint, the tool's alignment with the stud was set slightly off-center, a non-optimal condition that created a certain level of keyhole asymmetry. Therefore, although a radially symmetric loading condition was used, the crack initiation zone was at the narrowest section of the stake (black arrow in Figure 9-14a).

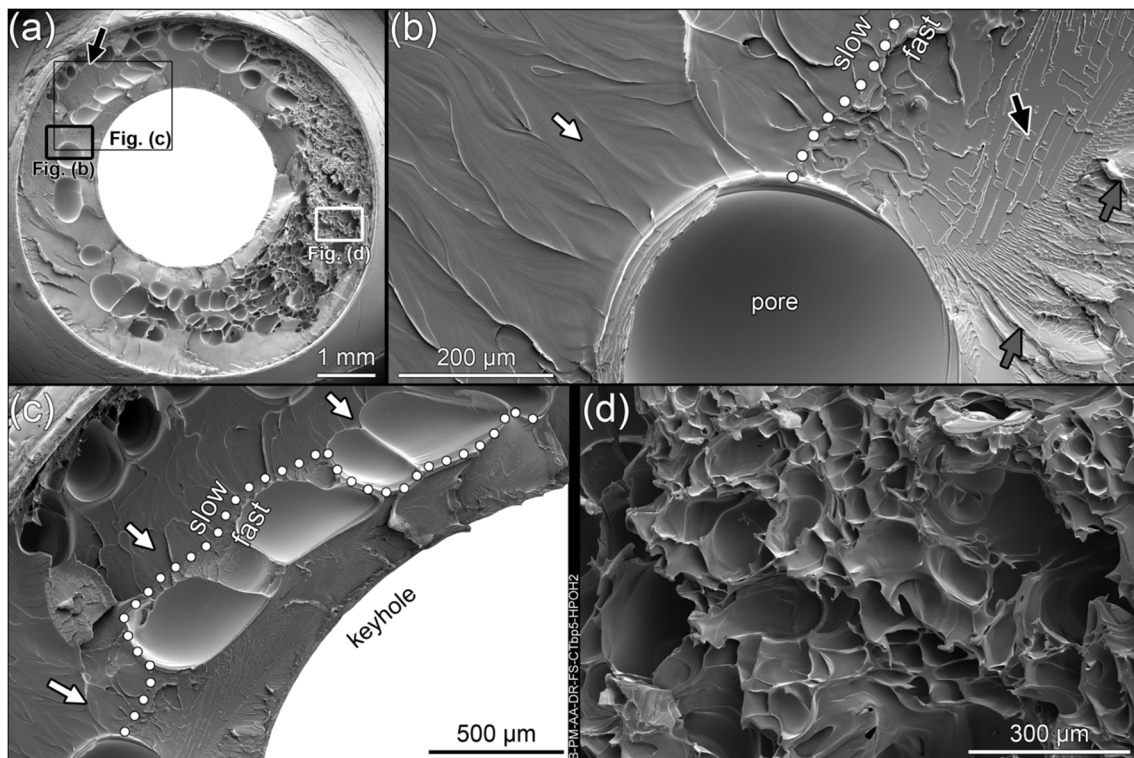


Figure 9-14: (a) Overview of the HPO fracture surface, the black arrow indicates a crack nucleation point; (b) example of fracture regime transitions around a pore; (c) interaction of the crack behavior with proximity to pores. White arrows show crack propagation direction, the dotted line shows transition to unstable crack propagation; (d) detail of the fracture surface close to the high-pore-content region in (a). Processing conditions: RS: 8000 rpm; FT: 2500 ms; FP: 0.45 MPa (2551 N); FoP: 1.0 MPa (5363 N); CoT: 5000 ms.

A closer analysis of crack nucleation on the stake head is discussed in Figure 9-15. A close-up of a crack nucleation site with river patterns of the same origin are shown in Figure 9-15a. This region is highlighted in Figure 9-14a with a black arrow. A higher magnification shows a particle at the crack origin in Figure 9-15b. Energy dispersive X-ray (EDS) analysis was used to investigate the chemical composition of this particle and compare it to the surrounding material. Figure 9-15c shows a peak in the particle's spectrum at the energy level of aluminum, while the spectrum for the surrounding material (PEI marked with a circle in Figure 9-15b) only identifies carbon, oxygen, and gold (from the sputtered conductive coating).

Therefore this particle is a contaminant from the aluminum material. The incompatibility between untreated metals and polymers is well documented in the literature [247], and attributed to dissimilarity of physical-chemical properties, mainly cohesive energy. Their interfacial incompatibility makes the volume around metal particles a possible crack nucleation point, as observed in this case. The contamination of the PTMAZ by particles of the metallic material is found in much smaller contents in optimized joints compared to processing conditions in which excessive tool rubbing occurs (e.g. high axial force during dwell time). An example of cross-sectional view, showing the PTMAZ of such a joint with several particles of aluminum, can be seen in Figure 9-16.

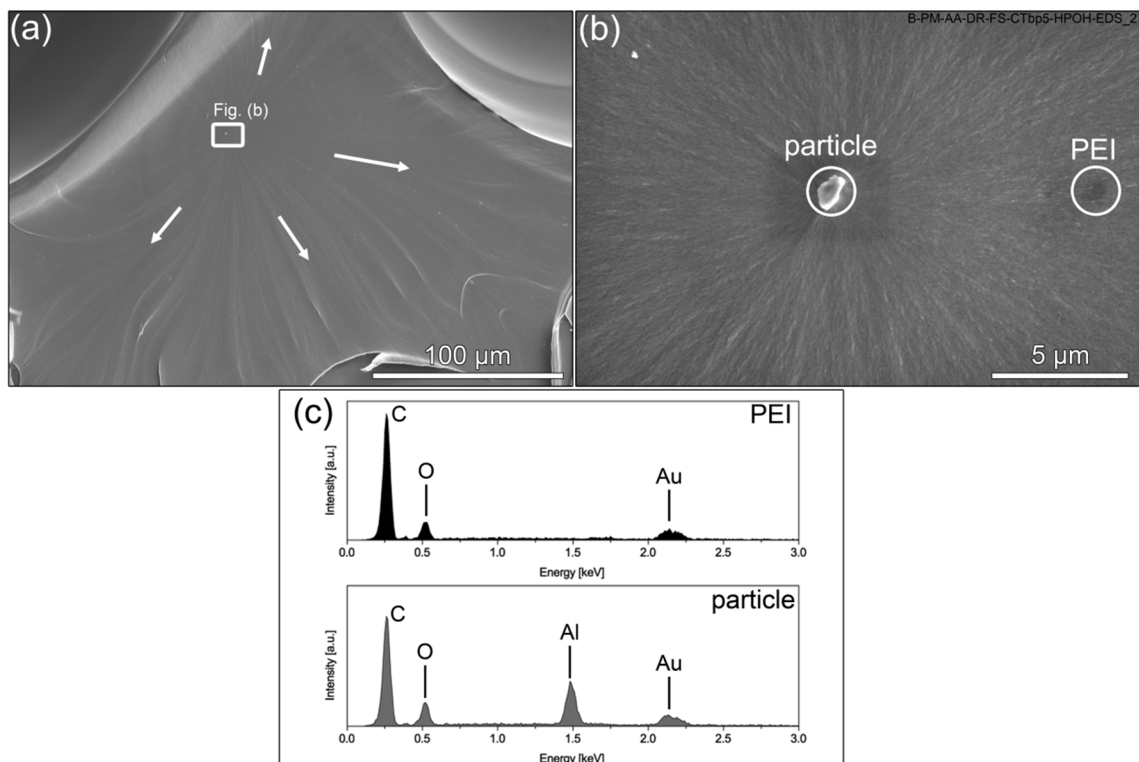


Figure 9-15: (a) Crack nucleation point on the stake head; (b) crack nucleation point at higher magnification, and spots for EDS analyses; (c) EDS spectra for the spots in (b). Processing conditions: RS: 8000 rpm; FT: 2500 ms; FP: 0.45 MPa (2551 N); FoP: 1.0 MPa (5363 N); CoT: 5000 ms.

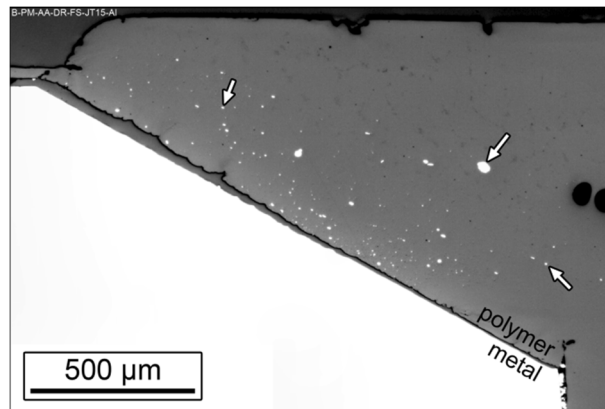


Figure 9-16: Cross-sectional view of a joint with excessive tool rubbing, with white arrows showing contamination by aluminum particles in the PTMAZ (RS: 8000 rpm; FT: 5000 ms; FP: 0.3 MPa (1525 N); FoP: 1.0 MPa (5363 N); CoT: 5000 ms).

These results show that microstructural effects will influence the mechanical behavior. Without considering pores and metal contamination, the FEM analysis from Figure 9-11b did not show significant stresses on the stake head, but the results show that these microstructural features can be critical when predicting the mechanical behavior of the joints under cross-tensile loading.

An alternative behavior was observed for 9 % of the joints (11 specimens), which failed by stake pull-out (SPo, Figure 9-17). With these joints, the ultimate force is achieved and after further displacement with a decreasing force the stake is removed, leaving in the base plate a concave crater (Figure 9-17a and b) or a through hole (see Figure 9-18a). As shown in Figure 9-17b, the crack path observed for this failure mode does not go directly through the thickness of the plate as in BPB, but with simultaneous crack fronts initiating around the stake base (red disks in Figure 9-17b) that move towards the bottom surface of the polymer plate. 82 % (9 of 11) of the observed SPo failures were in joints produced with high frictional forces, presenting plastically deformed zones (PDZ) and stake-shaft shearing (SSS, Section 8.4.3). Figure 9-17c shows the crack path from Figure 9-17b and the boundaries of microstructural zones defined by microhardness testing. As discussed in Section 8.4.3, a strengthened transition zone (STZ) is usually formed around the PDZ in high frictional force joints, as a result of the compressive residual stress gradient around the lower-strength PDZ. For the joint in Figure 9-17c, the STZ has a hardness of 256 ± 7 MPa, 7 % higher than the BM zone (239 ± 4 MPa). These microstructural changes have a clear effect on the mechanical behavior of F-ICJ joints with a PDZ in CT tests; it appears that the crack path preferentially deviates from the STZ and moves towards the weaker PDZ. This effect also explains the mechanical performance of joints with SSS (showed in Appendix H).

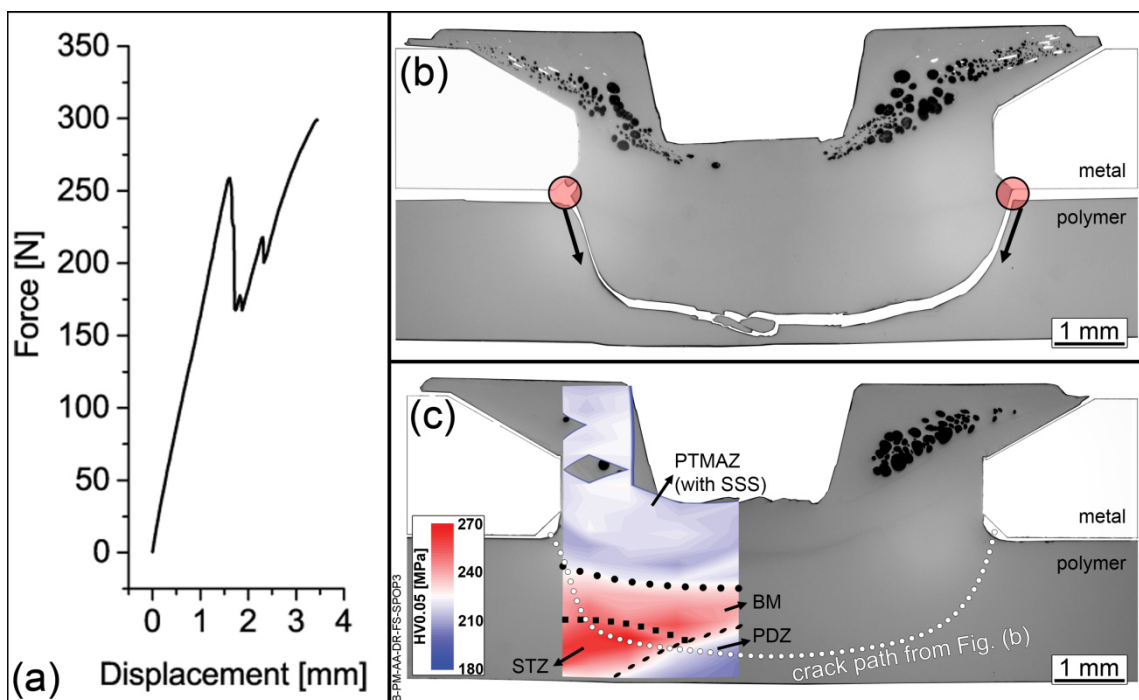


Figure 9-17: (a) Example of a force-displacement curve for stake pull-out (SPo) failure in cross-tensile testing; (b) cross-sectional view of an SPo failure, indicating crack initiation points (red disks) and propagation direction (black arrows); (c) microhardness distribution on high frictional force joints and interaction of the crack path with the STZ (RLOM images). Processing conditions: RS: 12000 rpm; FT: 5000 ms; FP: 0.5 MPa (2726 N); FoP: 0.7 MPa (3733 N); CoT: 2500 ms.

In Figure 9-18a, the matching surfaces in an SPo failure are shown. An overview of the surface on the plate is shown in Figure 9-18b. In this case, the crack deviates from the path observed in Figure 9-17b and c, growing towards the bottom surface as it reaches the PDZ and leaving a through hole in the base plate. Some of the bottom surface of the base plate stays attached to the stake (Figure 9-18a). A large zone A, with river patterns and ridges, shows signs of stable crack growth. This transitions to another region of mixed hackles and end-bands, which indicate unstable and fast crack propagation. The first decrease in force in Figure 9-17a likely indicates the start of crack growth, and final fracture occurs as the crack transitions to the C+D zone. The mirror and mist zone B of fast propagation is absent, because no mechanism of crack acceleration takes place in this failure mode. Figure 9-18c and d show the differences in extension of the crack initiation zone A around the perimeter. The right-hand side and top parts of Figure 9-18b have the largest stable crack-growth zones A, whereas the left-hand side and bottom parts experience a faster transition to unstable crack growth C+D. Figure 9-18e shows details of the terminal fracture zone for the side with a larger zone A, presenting river patterns almost until the end of the crack path. Figure 9-18f is from a similar zone on the side with a larger C+D zone, showing a region dominated by end-bands.

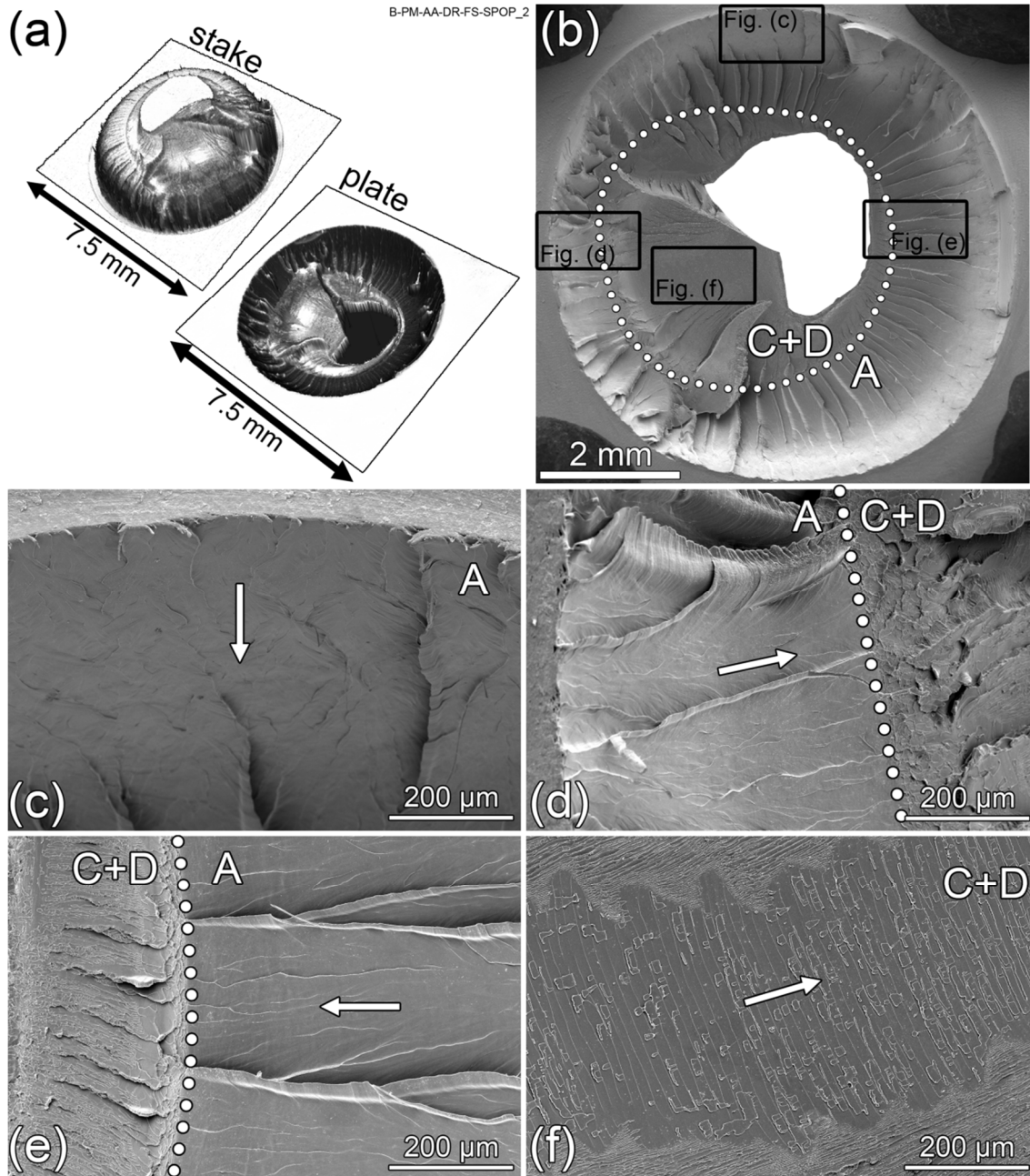


Figure 9-18: (a) 3D view of the stake and plate fracture surfaces; (b) overview of the fracture surface on the plate. The white-dotted line shows the boundary between stable crack growth (A) and fast crack propagation (C+D) zones; (c)-(f) are details of the fracture surface from (b). The white arrows indicate the local crack propagation direction. For processing conditions see Table 11-2. Joint annealed at 200 °C for 24 hours.

Three failure modes were observed in CT testing of F-ICJ PEI/AA6082 joints, where base-plate bending (BPB) and head pull-out (HPo) failure modes are concurrent failure modes, and stake pull-out (SPo) failure occurs as a result of the microstructural changes in high frictional force joints. A general comparison of the mechanical performances of the failure modes is shown in Figure 9-19. Average displacement at break and at ultimate cross-tensile force (UCTF) for BPB and HPo failure modes are very similar, owing to competing mechanisms leading to failure.

UCTF is highest for BPB failure, likely due to failure in the base material, as opposed to failure in the weaker PTMAZ for HPo. Some BPB specimens reached similar or higher ultimate forces than the non-joined PEI CT specimen (see Appendix I), indicating that this failure mode is the closest possible to a sound joint. SPo failure presented the lowest UCTF and displacement values. Their reduced performance is a result of the SPo failure mode occurring more frequently for joints with larger plastically deformed, low strength volumes.

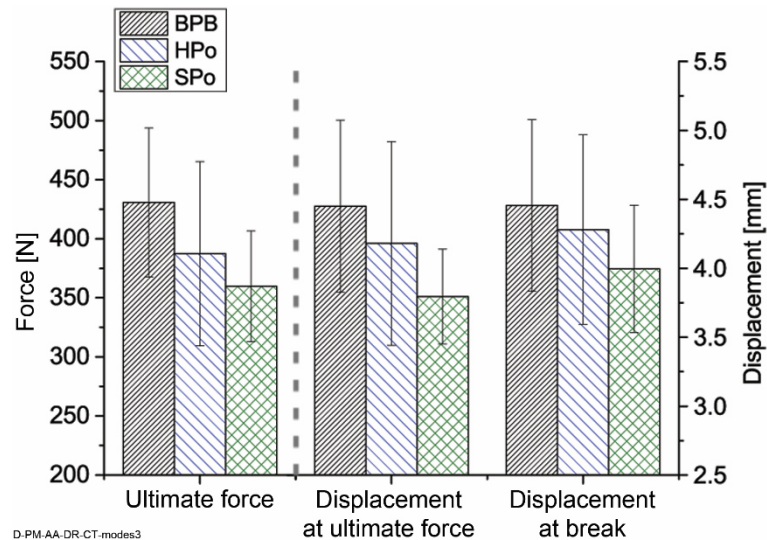


Figure 9-19: Mechanical performance comparison between the CT failure modes.

It has been observed that the microstructural aspects of F-ICJ joints are relevant for the tensile loading of the stake head by CT testing. In the case of sound stake heads, the joint will preferably fail by bending of the base plate (BPB), without damage to the head. However, contamination of the PTMAZ with particles from the joining partner may influence crack nucleation, and porosities accelerate crack propagation. Such effects may lead to failure by head pull-out (HPo). For joints produced with high frictional forces (over 2400 N) and presenting SSS, the failure mode shifts to a plug-like stake pull-out (SPo), as a result of the microstructural zones and their corresponding local mechanical properties.

CHAPTER 10. PROCESS-MICROSTRUCTURE-PROPERTY RELATIONSHIPS IN F-ICJ JOINTS

The previous chapters introduced the joint formation mechanisms and the main microstructural and mechanical characteristics of F-ICJ joints. In Chapter 7 it was shown that the friction phase is particularly important for joint formation, especially due to the formation of a shear layer with effective cavity filling during this phase. In Chapter 8, several features related to formation of this shear layer were described, and it was observed that the microstructure may influence the mechanical behavior, as discussed in Chapter 9. This chapter further analyses the previous observations, in order to discuss the effects of joining process conditions on the microstructure and local properties of the joints, and to correlate these effects to quasi-static global mechanical behavior (lap-shear and cross-tensile properties). The analyses in this chapter are based on those performed on fractional factorial design of experiments (FF-DoE) joints (Section 6.3.10, Table 6-7). Microstructural features were measured as described in Section 6.3.3 and quasi-static mechanical tests were performed as described in Section 6.3.8. Detailed results from these analyses are displayed in Appendix J.

Correlations between the process variables are traced using scatter plots with a linear fitting. Whenever averages are used the fitting applies instrumental weighting of the Y-errors. A linear fitting is used in order to determine how the change of a certain microstructural feature directly affects the response. The adjusted R-square and the significance of the slope of the linear fitting set at a 95 % confidence level (significant when $p < 0.05$) are reported in each diagram.

10.1 Effects of thermal development on microstructural features

The heat development in F-ICJ joints is mainly dependent on the friction phase, as discussed in Chapter 7. During stud meltdown and dwell time, the polymer achieves temperatures much higher than its T_g as a result of shearing and frictional heating. This section investigates the changes in the shear layer (or PTMAZ) according to the heat input – estimated from stake temperature (ST) measurements – and according to friction-phase process parameters (RS, FT, FP). The results in this section are direct measurements from analyses of the microstructural-analysis specimens (MA, two replicates of each condition), as specified in Section 6.3.3.

The area of the PTMAZ A_{PTMAZ} was measured and normalized by the cross-sectional area of the stake A_{CS} to obtain the relative PTMAZ area RA_{PTMAZ} as described in Section 6.3.3. The dependence of RA_{PTMAZ} with ST is shown in Figure 10-1a. Filled symbols are for joints that presented a remnant weld line, whereas open symbols are joints without a weld line. A statistically significant increase in RA_{PTMAZ} with increasing ST is observed ($p = 0.00$). This effect is expected, due to temperature dependence of the polymer's viscosity. The higher the heat input - represented by the increase in stake temperature - in the polymer, the easier it will flow, thereby increasing the volume of the PTMAZ. The scatter plot shows a trend of weld lines being more often present at lower temperatures and with smaller PTMAZ areas. There is no clearly defined range, but joints with ST above 60 °C or with an RA_{PTMAZ} larger than 35 % will rarely present remnant weld lines (the hatched box in Figure 10-1a indicates these limits).

Descriptive statistics of weld line formation are shown in Appendix K (Figure K-1). These results confirm that heat input and material flow in the PTMAZ influence the healing of discontinuities such as weld lines.

In Figure 10-1b, the relative pore area RA_{pore} (pore area A_{pore} normalized by the cross-sectional area A_{CS} of the stake) is plotted as a function of ST. Formation of pores is not significantly dependent on heat input level ($p = 0.11$). This observation agrees with the hypothesis of pores resulting from evolution of structural water and not from extensive thermal degradation (see Section 8.4.1), so that for every condition pores are created from moisture on approximately equal levels. If they had been a product of thermal degradation, RA_{pore} would be expected to increase with higher heat input (higher stake temperatures) levels. By contrast, a significant correlation of RA_{pore} to RA_{PTMAZ} could be observed ($p = 0.00$, Figure 10-1c). This correlation is likely due to the temperature effects described in Figure 10-1a and b, and the fact that a larger PTMAZ affects more material, leading to further evolution of moisture and/or small hydrocarbons (Section 8.4.1). Therefore, any changes in the PTMAZ size are also likely to proportionately increase pore volume.

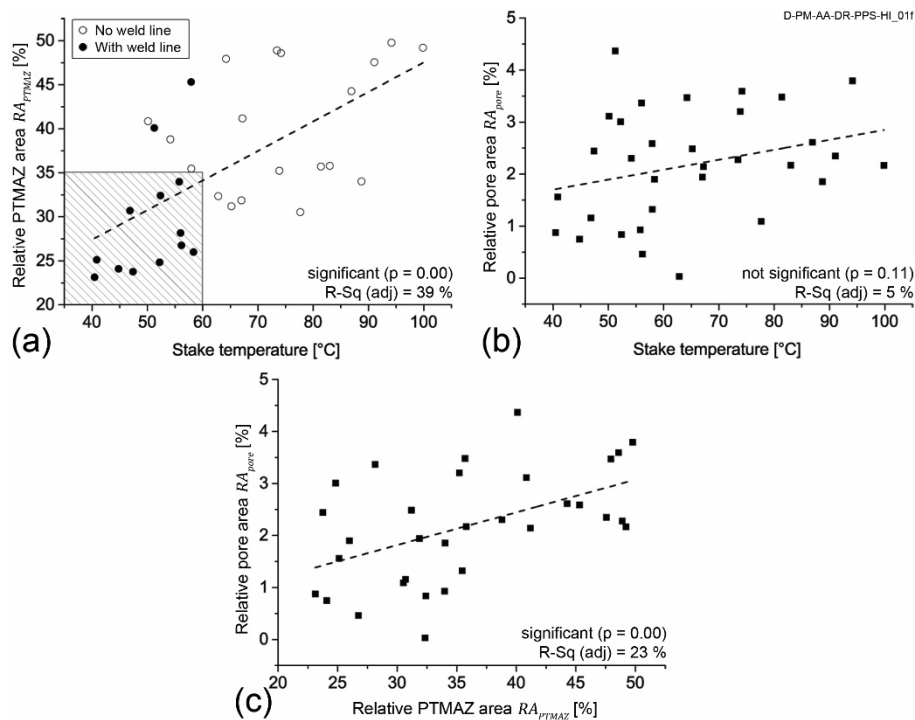


Figure 10-1: (a) Effect of heat input on the size of PTMAZ and weld line formation. The box indicates conditions with a high frequency of weld lines; (b) effect of stake temperature on relative pore area; (c) correlation of pore area to PTMAZ area.

As an alternative approach, the PTMAZ size may be analyzed as a function of dwell time. The studied joints were produced with an FT of 2500 ms (with a short dwell time of 1300-2000 ms) and 5000 ms (with a long dwell time of 3800-4500 ms). Figure 10-2 shows the RA_{PTMAZ} for several conditions indexed by the dwell times. These measurements show that longer dwell

time increases PTMAZ size. These results confirm the shear layer (PTMAZ) formation mechanism, as described in Figure 7-8. During dwell time further stirring/mixing of the polymer creates a larger shear layer, as a result of viscous heating facilitating the material flow.

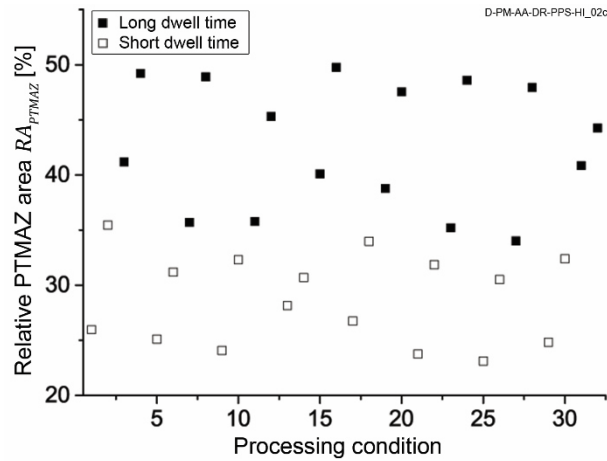


Figure 10-2: Effect of dwell time on relative PTMAZ area. Measurements from two replicates of the conditions from the FF-DoE (Table 6-7).

The PTMAZ presents decreased local strength, as shown by microhardness distribution maps (Section 8.2), due to the increased free volume in the cooling regime after joining. The processing conditions then yield different microstructural zones with different properties. Figure 10-3 shows the effects of frictional time (FT), rotational speed (RS), and frictional pressure (FP) on the size and hardness of the PTMAZ, and Table 10-1 shows the measurements from each of the selected conditions in this figure. Figure 10-3a is a reference joint processed with RS 8000 rpm, FT 5000 ms, and FP 0.3 MPa. Figure 10-3b is a joint processed with a shorter FT of 2500 ms, Figure 10-3c shows a specimen with increased RS of 12000 rpm, and Figure 10-3d shows a joint with increased FP of 0.5 MPa.

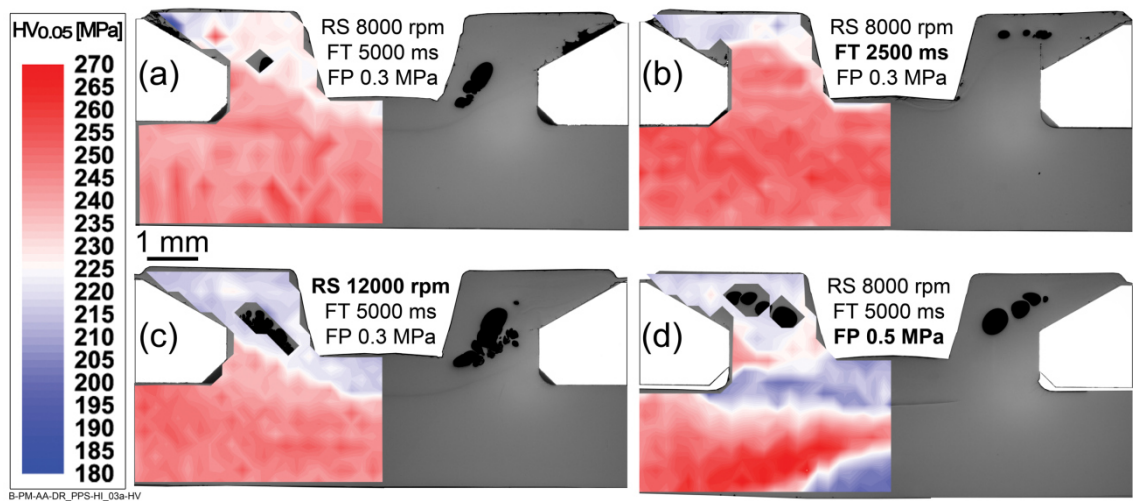


Figure 10-3: Effect of process parameters on microstructural zones. Parameters highlighted in bold in (b)-(d) are changes to those for the reference joint in (a).

Table 10-1: Microstructural changes for selected conditions. Bold parameters in (b)-(d) are changes to those for the reference joint in (a).

Processing condition	ST [°C]	Relative PTMAZ area RA_{PTMAZ} [%]	Relative pore area RA_{pore} [%]	HV_{PTMAZ} [MPa]
(a) RS 8000 rpm FT 5000 ms FP 0.3 bar	67.2	41.2	2.1	226 ± 8
(b) RS 8000 rpm FT 2500 ms FP 0.3 bar	40.8	25.1	1.6	221 ± 6
(c) RS 12000 rpm FT 5000 ms FP 0.3 bar	73.4	48.9	2.3	219 ± 6
(d) RS 8000 rpm FT 5000 ms FP 0.5 bar	81.4	35.7	3.5	218 ± 4

Comparisons of the PTMAZ and pore areas in Figure 10-3a with Figure 10-3b-d are direct observations of changes to energy input. With increasing stake temperature (ST) the RA_{PTMAZ} increases, which causes an increase in RA_{pore} , as previously discussed in Figure 10-1a and c. The microhardness values in the PTMAZ (HV_{PTMAZ}) are within a close range of each other. As one can observe in Table 10-1, despite the energy input range being relatively wide, it seems to influence only the size (RA_{PTMAZ}), but not the local strength (HV_{PTMAZ}) of the PTMAZ. Also, the physical-chemical properties in the PTMAZ were not expected to change significantly with the heat input as discussed in Figure 8-8b. Microhardness of glassy polymers is mainly a function of the chain packing density of the material [128], which for the F-ICJ joints in this work is a result of the cooling regime (see Section 8.2.2). Therefore the effect of energy input is

to change the cooling conditions in the PTMAZ, but for the parameter range used in this work, the energy input levels seem to have no significant effect on local strength, as observed from the hardness testing (see Appendix K, Figure K-2).

10.2 Influence of the joint's microstructural features on quasi-static mechanical performance

In this section, the average measurements of microstructural features for each joining condition are correlated with their average mechanical properties. Although the microstructural features are measured from microstructural-analysis (MA) specimens and not directly from the lap-shear (LS) and cross-tensile (CT) joints, the validity of this analysis is based on the fact that measurements of stake temperature for MA, LS, and CT geometries are comparable for each joining condition (Appendix L, Figure L-1). Therefore one can assume that the same microstructural characteristics of the MA specimens were present in the LS and CT joints.

As previously described, the increase in size of the PTMAZ not only accounts for a larger low-strength volume, but also for an increased porosity level (Section 10.1). Due to the similarity of the effects of these two microstructural features and owing to the fact that the PTMAZ includes the porosities, only the PTMAZ response is evaluated here. The same diagrams for the effects of porosity are provided in Appendix L.

Figure 10-4 shows the effects of the RA_{PTMAZ} on relevant lap shear testing properties. Ultimate lap shear force (ULSF) is not significantly affected by RA_{PTMAZ} ($p = 0.06$, Figure 10-4a), but significant effects are observed for displacement at ULSF ($p = 0.00$, Figure 10-4b) and joint stiffness in the elastic regime ($p = 0.00$, Figure 10-4c). Displacement at ULSF is frequently the moment at which a critical crack size is achieved in the stake head, causing a load transfer to the base plate, as discussed in Figure 9-4 and Figure 9-5. The negative effects of the PTMAZ area on displacement at ULSF (Figure 10-4b) is believed to be the result of two mechanisms: an increase in stiffness due a tighter joint (Figure 10-4c) and an increased volume of porosity (see Figure 10-1c).

The joint becomes tighter with a larger PTMAZ, due to better cavity filling. This hinders stake rotation from secondary bending, increasing the stiffness of the joint (Figure 10-4c). As a result of this, a critical load on the stake head is reached sooner in stiffer joints, causing the displacement at ULSF to be lower in joints with a larger PTMAZ (Figure 10-4b).

The relative porosity content that results from a larger PTMAZ (see Figure 10-1c) may lead to premature failure of the stake head in the same fashion as head pull-out (HPo) failure in CT specimens, and this contributes to the negative slope in the diagram of relative PTMAZ area in Figure 10-4b (for the diagrams about the effects of RA_{pore} on LS properties refer to Figure L-2 in Appendix L).

The ULSF is apparently independent of RA_{PTMAZ} (Figure 10-4a), and the analysis of mechanical behavior in Section 9.1 shows that the ultimate force depends mostly on the stake head failure (Figure 9-4 and Figure 9-5). Displacement at break (Figure 10-4d) is not

dependent on the size of the PTMAZ ($p = 0.97$), because after stake head failure the mechanisms for final joint failure only depend on the polymer base plate.

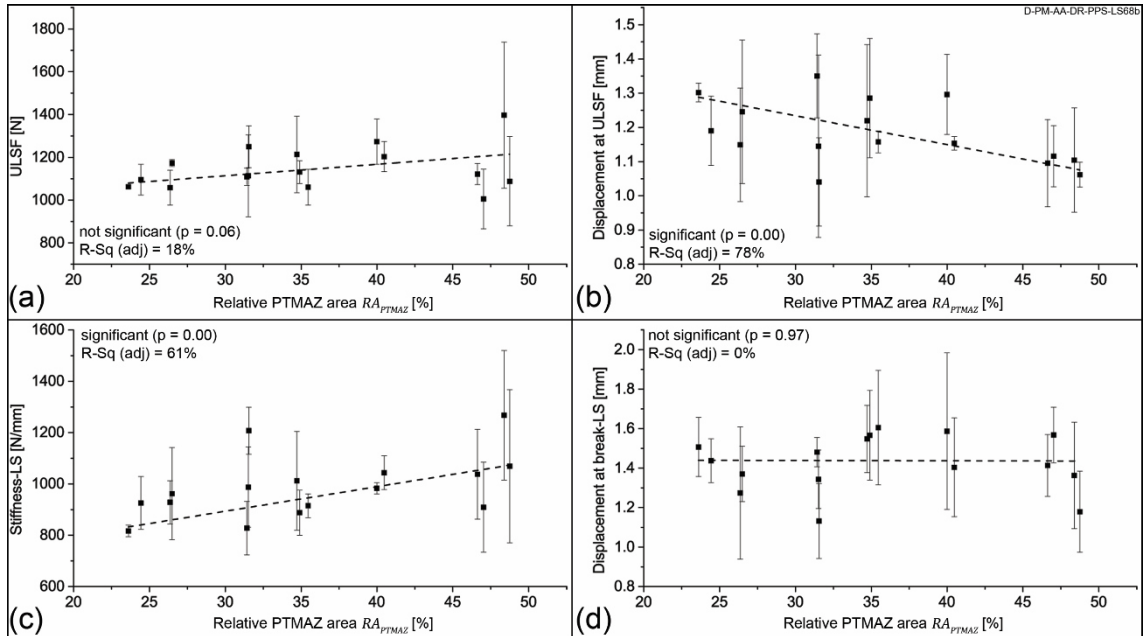


Figure 10-4: Effects of relative PTMAZ area on LS properties: (a) ULSF; (b) displacement at ULSF; (c) joint stiffness; (d) displacement at break.

The effects of the RA_{PTMAZ} on CT properties are shown in Figure 10-5a-d. The symbols and their colors are indexed according to the most frequent failure mode observed for a given joining condition, and the linear fitting is for all conditions independent of failure mode. Since CT testing applies load directly on the stake head (the region with the most intense thermomechanical processing), the mechanical properties of CT specimens are more susceptible to changes in PTMAZ size and pore content. The linearity of most CT force-displacement curves (base-plate bending (BPB) and head pull-out (HPO) failures, Figure 9-12a) causes the correlations of RA_{PTMAZ} with all properties studied in Figure 10-5 to be similar. The CT mechanical properties show a significant negative slope ($p = 0.00$) with increased RA_{PTMAZ} .

The PTMAZ is a weaker polymer volume that contains porosity (see Figure 10-1c) and is the load-carrying part of the joint during CT tests. The porosities in the PTMAZ were shown to accelerate crack propagation in the stake head (Figure 9-14), which may result in lower ultimate cross tensile force (UCTF, Figure 10-5a) and lower displacement at UCTF (Figure 10-5b) values. As a result of the linearity of CT force-displacement curves, the reduction in UCTF and displacement at UCTF consequently lead to reductions in joint stiffness (Figure 10-5c) and displacement at break (Figure 10-5d) with increasing RA_{PTMAZ} .

These results are in agreement with the HPO failures (green triangles) following more closely the general linear fitting (blue dashed line) than the BPB failures (black squares) in Figure 10-5. BPB failure depends on the bending behavior of the base plate during the test and occurs without apparent damage to the stake head (see Section 9.2), thus is rather unaffected

by RA_{PTMAZ} . By contrast, HPO is a failure mode directly dependent on the properties of the stake head (RA_{PTMAZ} and RA_{pore}) and follows more closely the linear fitting. (for the diagrams about the effects of RA_{pore} on CT properties refer to Figure L-3).

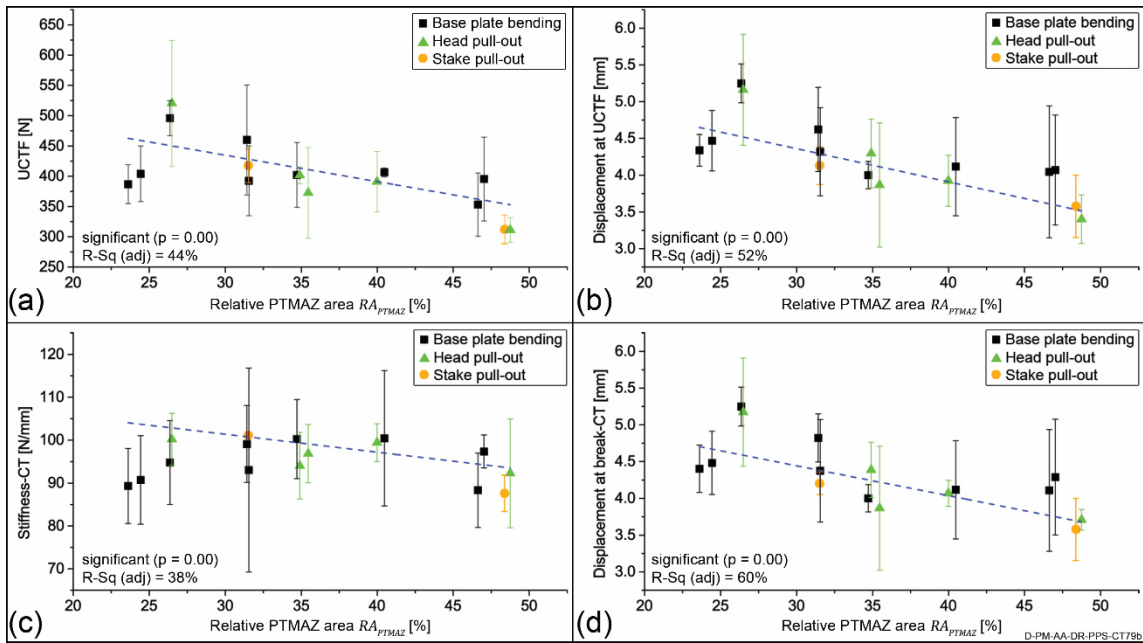


Figure 10-5: Effects of relative PTMAZ area on CT properties, indexed by most frequent failure mode: (a) UCTF; (b) displacement at UCTF; (c) joint stiffness; (d) displacement at break.

Changes in mechanical properties of both LS and CT specimens in terms of the presence of a weld line on the joints are shown in Figure 10-6a-d. From a statistical point of view, the presence of a weld line does not change the average value of any of the mechanical properties for LS and CT specimens over the range of joining parameters evaluated in this work. The results suggest that although a weld line could be a crack nucleation point (Figure 9-5a) its notch effect is overcome by other factors that influence quasi-static joint properties, such as the PTMAZ size and porosity level. However, a remnant weld line may influence other mechanical properties of F-ICJ joints, such as cyclic and long-term mechanical properties.

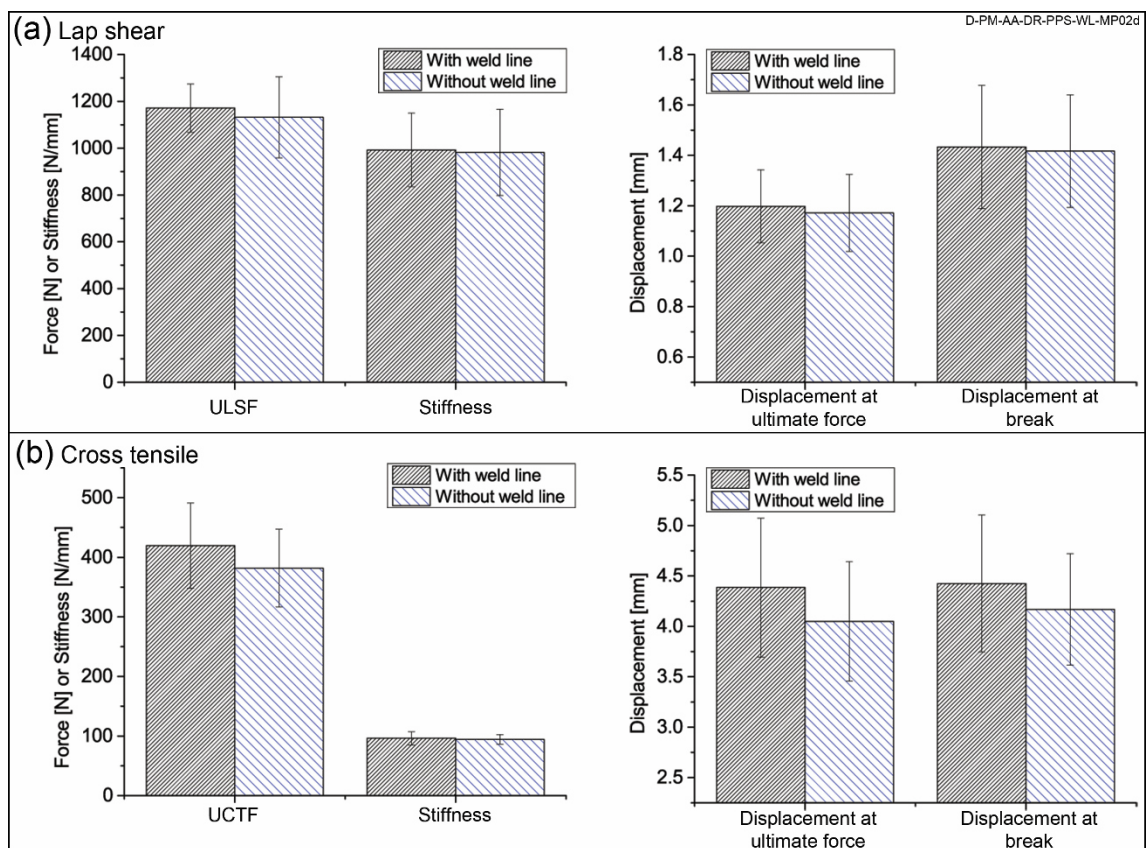


Figure 10-6: Effects of a remnant weld line on LS and CT relevant properties.

10.3 Statistical analysis of the effect of process parameters on joint properties

The design of the experiments used for the main part of this chapter was selected based on preliminary screening experiments for this work. First, tool geometry was investigated for PA66-GF/AA2024 F-ICJ joints [184] (Figure 10-7a). It was concluded that a conical-pin tool improves the mechanical performance compared to flat tools, owing to the better cavity filling ability of a conical-pin design. In a next stage, two geometries of conical-pin tool were investigated for PEI/AA6082 F-ICJ joints [185] (Figure 10-7b). The conical-pin tool with a 75° angle presented slightly better mechanical performance in a one-factor-at-a-time (OFAT) experiment than a 30° tool. The difference results from the thinner walls of the hollow stake created with the 30° tool, which under lap-shear testing act as a shorter path for a radial stake-head crack (see Figure 9-5b).

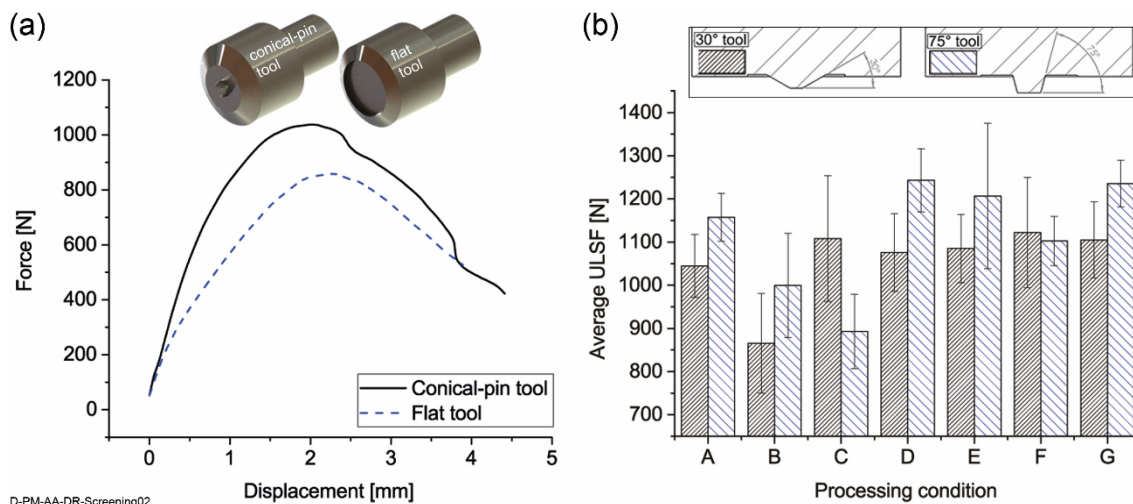


Figure 10-7: Results of preliminary investigations: (a) comparison of mechanical behavior of joints produced with a conical-pin tool and flat tool (adapted from [184]); (b) comparison of average ULSF for two conical-pin tool geometries in a one-factor-at-a-time experiment (adapted from [185]).

The OFAT experiment in Figure 10-7b explored the joint microstructure and lap-shear mechanical performance of a wide range of process parameters within the limits of the friction welding system. Based on the results of these experiments, the parameter range was narrowed down to a window that produced sound joints, with complete stud meltdown achieved during the friction phase of a two-phase process (Figure 4-4a).

Based on the preliminary work shown in Figure 10-7, a parameter window was selected for a fractional factorial design of experiments (FF-DoE, described in Section 6.3.10, Table 6-7). Stake temperature (ST), ultimate lap shear force (ULSF), and ultimate cross-tensile force (UCTF) were analyzed as statistical responses. ST is an indication of the heat input in a given condition, and ULSF and UCTF measure the mechanical performance of F-ICJ joints in two loading configurations. For each response, a reduced linear multivariate regression model was used to interpret the influence of the factors on the response, and the effects of the statistically significant factors from the model are explained here. The factors of the models are the controlling process parameters of an F-ICJ joining cycle (Section 4.2): rotational speed (RS), frictional time (FT), frictional pressure (FP), forging time (FoT), and forging pressure (FoP), as well as their second-level interactions. The explanatory power of the models is therefore limited to the effects these parameters can describe.

The reduced models with coded factors for ST, ULSF, and UCTF are displayed in Appendix M, along with their residual plots. The reduced models were validated using experimental data within FF-DoE and further validation joints, whose processing conditions are listed in Appendix M. Figure 10-8 shows validation plots for the reduced models. Black squares indicate runs from the FF-DoE, and green triangles indicate validation runs. The dotted black line shows a correlation of 1.0 between predicted and actual values, the black dashed lines show 10 % error limits, and the green dash-dotted lines are the prediction intervals for the model. Prediction intervals indicate limits in which the model can predict a single observation [197].

The 10 % limits are used by some authors in polymer welding/joining as acceptable limits due to the variation in properties between different polymer grades and batches [124, 186].

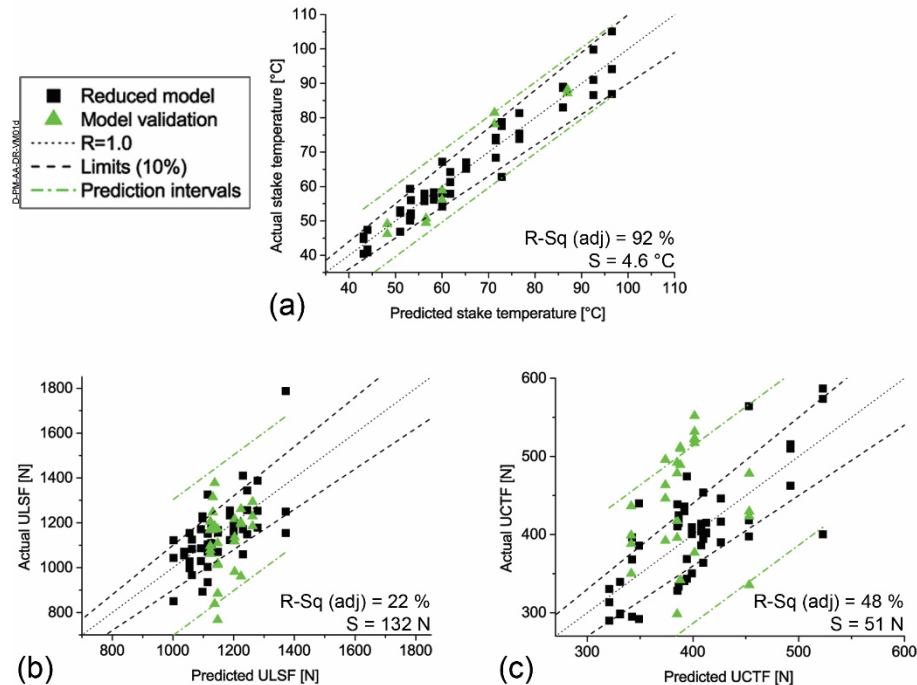


Figure 10-8: Validation diagrams for the reduced models of (a) ST; (b) ULSF; and (c) UCTF.

The validation experiments were successfully predicted within the limits of each model. The temperature model has the best explanatory power, with an adjusted R-squared of 92 % and a standard error of the regression of 4.6 °C (Figure 10-8a). Most data points lie within the 10 % limits, and linearity is well established. Heat generation in F-ICJ is directly related to the process parameters (as seen in Equation (6-1)), which explains the good fitting of the ST model.

For ULSF the model has a very low explanatory power (adjusted R-squared of 22 %) and a large standard error of the regression of 132 N (Figure 10-8b). Furthermore, the predicted values are concentrated within a relatively narrow range of 1000-1400 N compared to the experimental observations of 750-1800 N. As was concluded in the previous chapters, the ULSF is a function of the resistance of the joint to the bending moment M from secondary bending (Section 9.1), which is fairly independent of changes in the microstructure (Figure 10-4a). Since the factors in the regression model mostly affect the local properties of the stake head (such as RA_{PTMAZ} , formation of PDZ or weld lines), they do not contribute greatly to predicting how the ULSF varies within this parameter range. Therefore it follows that ULSF does not significantly depend on the process parameters (factors of the model) in the range used in this work, but other effects that are not included in the model could possibly improve the model's explanatory power (e.g. cavity filling efficiency, out-of-plane deflection during testing, stake-wall thickness, etc).

The UCTF model has an adjusted R-squared of 48 % and standard error of regression of 51 N, so is able to explain almost half of the variability in UCTF (Figure 10-8c). Although to a lesser degree than the ULSF model, the UCTF model also results in a narrower range of predicted values (325-575 N) compared to the experimental ones (275-600 N). The explanatory power of the UCTF model is higher than the ULSF model's as cross-tensile performance depends more directly on joint microstructure than lap-shear performance (see Section 10.2). The microstructural features that affect UCTF (e.g. porosities, formation of stake-shaft shearing) are a function of the heat input (Section 10.1) and joining force (Figure 9-17), which are directly described by the factors used for the reduced models.

The relatively low prediction ability (low adjusted R-squared) of the ULSF and UCTF models can also be accounted for by variances in dimensional tolerances of the joining partners and some impreciseness of the clamping system used. These factors often affected the experiment by producing off-centered joints or causing excessive rubbing of the tool on the metallic surface. The radial asymmetry and the extra heating of the polymer from tool rubbing are not accounted for in the models, and so may affect the responses.

Analysis of variance (ANOVA) of the models was used to evaluate predictor statistical significance to the responses. Further information about the models is shown in Appendix M. The statistically significant process parameters are used to explain the variability in the responses over the next sections, and as described in Section 6.3.10.

10.3.1 Effects of the factors on stake temperature (ST)

Figure 10-9a shows a Pareto chart of standardized effects for the ST model. The value for the standardized effect of each factor is derived from its coefficient in the model divided by its standard error. The dashed vertical line defines the limit on a 95 % confidence level ($\alpha = 0.05$) in which a parameter becomes significant to the response. The significant factors for ST are FP ($p = 0.000$), FT ($p = 0.000$), RS ($p = 0.000$), FT*FP ($p = 0.000$), and FoP*FP ($p = 0.001$). Figure 10-9b shows the effects of FP, FT, and RS, Figure 10-9c shows the effect of the FT*FP interaction, and Figure 10-9d shows the effect of the FoP*FP interaction on mean ST.

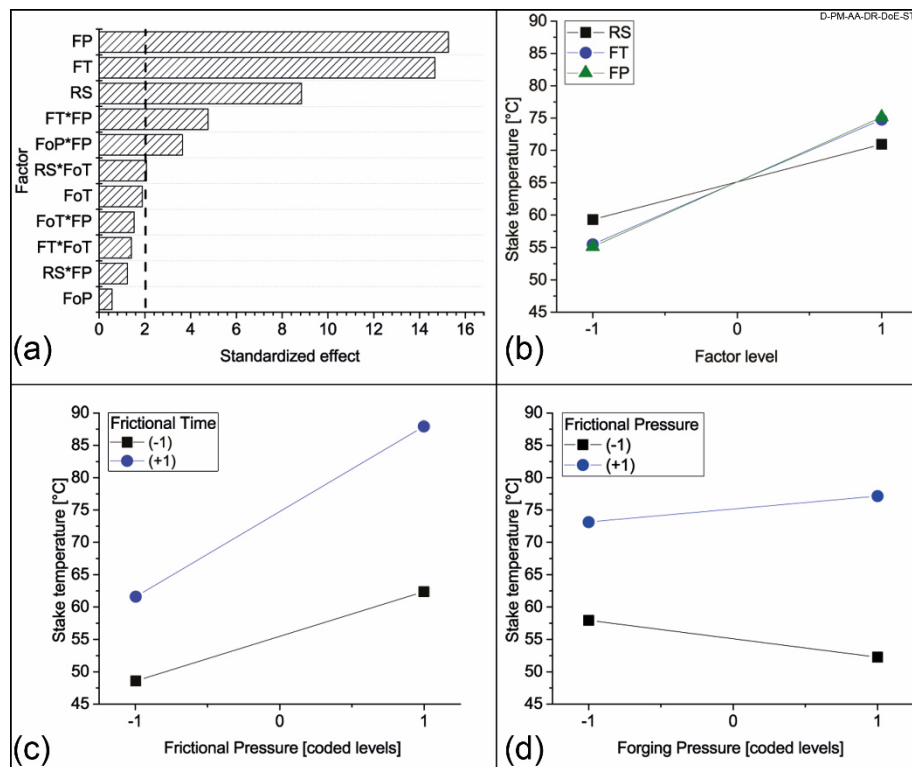


Figure 10-9: Analysis of ST: (a) Pareto chart of standardized effects; (b) plots of significant main effects (RS, FT, FP); (c) effect of the FT*FP interaction; (d) effect of the FoP*FP interaction on the stake temperature.

The RS, FT, and FP main effects have a positive effect on ST (Figure 10-9b), and this can be interpreted based on the energy input equations presented in Section 3.4.1. For a direct interpretation of energy input in F-ICJ, one can use Equation (6-1). RS is represented by the angular speed $\bar{\omega}$, and has a direct influence on the frictional component of heat generation. It will help in heat generation during the solid and viscous friction phases of stud meltdown, and during the tool's rubbing of the aluminum partner. FT determines how long RS is active. FT is the integration interval for the energy input calculation in Equation (6-1), therefore it also has an increasing effect on the energy input. FP increases the stake temperature as a result of a faster stud meltdown rate v that generates more deformation Δx , and of closer contact with the tool when rubbing the top surface of the metallic joining partner (refer to Section 8.1) due to higher forces (FF). Although the effect of tool rubbing significantly adds to heat generation, its precise contribution is difficult to be quantified. Forging time and forging pressure have minimal effects on stake temperature, since in this parameter range the forging pressure acts as a consolidating force and the forging time only determines how long the consolidation step takes place.

The FT*FP interaction (Figure 10-9c) follows the individual trend that is observed for the main effects. By increasing either FT or FP the temperature also increases, but it shows that at longer FT (FT=1) an increase in FP (FP=1) will yield larger increases in temperature than at shorter FT (FT=-1). This effect is observed, because with a longer FT the dwell time is also longer. During the dwell time heat is generated due to viscous friction at the tool and shear-layer interface (Section 7.2.2) leading to a higher amount of generated thermal energy.

Moreover, heat from the tool rubbing during dwell time also heats the metal partner, reducing heat loss from the stake. Both effects are also improved with higher FP, since a more intimate contact between tool and joining partners is achieved. With a shorter FT, the duration of the contact between tool and metallic partner is shorter, so that its contribution to heat development is smaller.

In Figure 10-9d, a small change in slope can be seen between the lower and higher levels of FoP while changing the FP. Heat generation here is dictated by the frictional pressure (FP). FoP has not much influence on heat generation, but may affect the cooling rate by improving the contact between tool and workpieces. At lower FP (FP=-1) the heat generation is lower, and by increasing the FoP (FoP=1), faster cooling during consolidation may reduce the stake temperature (black squares in Figure 10-9d). However, at higher FP (FP=1) the heating is more intense on the tool, due to its contact with the metallic joining partner. Therefore at high FP (FP=1), a stronger contact and high FoP (FoP=1) during consolidation presents a decreased cooling rate, due to decreased losses to the warmer tool (blue disks in Figure 10-9d), which increases stake temperature.

10.3.2 Effects of the factors on ultimate lap shear force (ULSF)

A Pareto chart for the ULSF model is shown in Figure 10-10a. In this case, the interactions FoT*FoP ($p = 0.014$) and FT*FoT ($p = 0.018$) have a statistically significant effect on ULSF. None of the main factors have a significant effect in this model, and the two significant interactions have little influence on the response, as seen by their proximity to the significance limit (dashed line in Figure 10-10a). The results have previously shown that ULSF corresponds to a critical load on the stake head due to secondary bending (see diagram in Figure 9-4) and does not vary greatly within these experiments (as previously described in Figure 10-8b). These observations mean that the parameter setup cannot describe much of the variability in ULSF, which is confirmed by its adjusted R-squared of 22 %. Figure 10-10b and c show the interaction plots for the significant second-order interactions (FT*FoT and FoT*FoP, respectively).

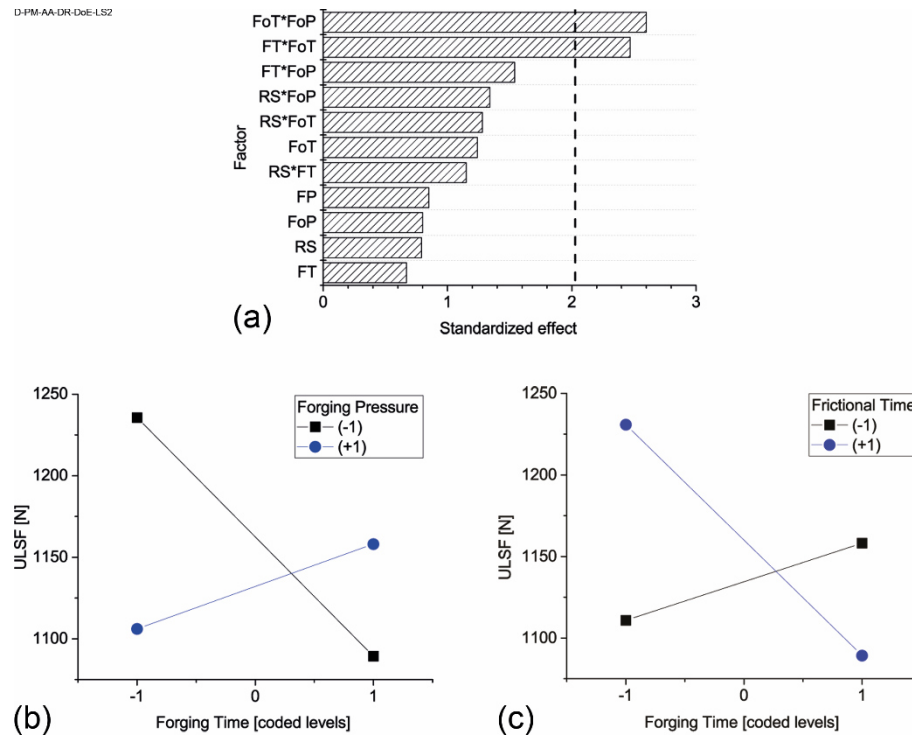


Figure 10-10: Analysis of ULSF: (a) Pareto chart of standardized effects; (b) effect of the FoT*FoP interaction; (c) effect of the FT*FoT interaction.

The FoT*FoP interaction has the strongest influence on ULSF (Figure 10-10b). This indicates that consolidation of the stake head has a strong effect on the tensile performance of overlap F-ICJ joints. As was discussed in Section 9.1, the integrity of the stake head is important for retarding fast crack growth in the base plate. This is in accordance with what was reported by Abibe *et al.* [113] for E-ICJ joints of PA66-GF/AA2024 in which the shape and contact of the stake head with chamfer cavities was important for improving lap-shear strength.

In Figure 10-10b, the interactions plot for FoT*FoP is charted. An increase in FoT (FoT=1) means the tool in contact with the stake for a longer time. After the friction phase the high temperatures of the tool can reduce the cooling rate of the stake's PTMAZ, allowing longer times for relaxation effects to occur, for example, void growth and coalescence. In such cases, longer FoT has a negative effect on joint strength when the forging (consolidation) pressure is not high enough (FoP=-1, black squares in Figure 10-10b). Higher hydrostatic pressures (supported by higher FoP; FoP=1, blue disks in Figure 10-10b) in the cooling phase (consolidation) densify the polymer and reduce the molecular mobility [126], so longer FoT (FoT=1) with a high FoP level (FoP=1) improves the chain packing and may increase joint strength. At lower FoP levels (FoP=-1), mobility is greater and so pore growth and coalescence are more likely over time, decreasing joint strength.

Stake integrity after consolidation is also a result of the FT*FoT interaction (Figure 10-10c). With longer FT (FT=1) more heat is generated (as seen in Figure 10-9b). The extra heat affects both pore content and tool temperature. Therefore with longer FT (FT=1) a longer FoT (FoT=1) can reduce ULSF, because more time with the hot tool against the stake may promote pore growth and coalescence (by slowing the cooling rate). However, with short FT (FT=-1) the heat

generation is less intense (Figure 10-9b), and a longer consolidation step (FoT=1) is advantageous for the formation of a sound stake head.

In summary, these results show that the model has little explanatory power for ULSF variability, indicating that joint strength in lap shear is only slightly dependent on process parameters in the range used in this work. As explained in Figure 10-8b, the process parameters as factors of the model mostly describe the heat generation of the process; the heat generation can be directly correlated with joint microstructure (see Section 10.1), but it was demonstrated that ULSF is fairly independent of microstructural changes in Figure 10-4a. The analysis in Figure 10-10 seems to indicate that the joining parameters of the forging phase (FoT and FoP), which dictate the consolidation of a sound stake, seem to be more important for ULSF in this parameter range.

10.3.3 Effects of the factors on ultimate cross-tensile force (UCTF)

A Pareto chart for the UCTF model is shown in Figure 10-11a. The predictors that have a significant influence on UCTF are RS ($p = 0.007$), FT ($p = 0.000$), FP ($p = 0.008$), and the interaction FT*FP ($p = 0.019$). The effects of RS, FT, and FP on mean UCTF are shown in Figure 10-11b. The interaction plot for FT*FP is charted in Figure 10-11c.

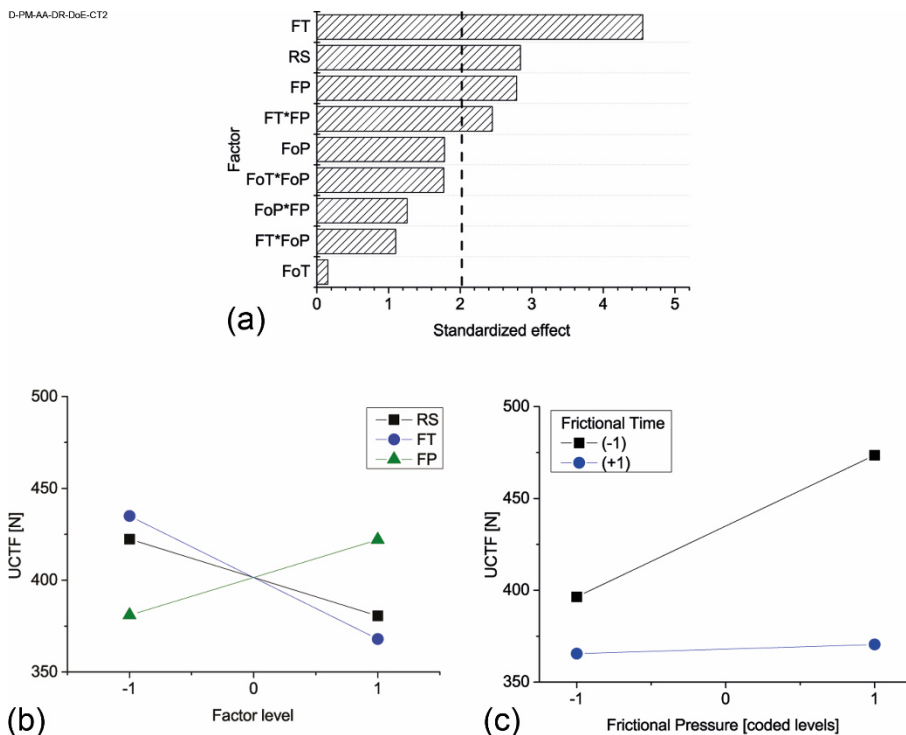


Figure 10-11: Analysis of UCTF: (a) Pareto chart of standardized effects; (b) plots of significant main effects (RS, FT, FP); (c) effect of the FT*FP interaction.

The significant single factors (Figure 10-11b) are all parameters that are active during the friction phase. High levels of both RS and FT reduce mean UCTF and are most likely related to the higher heat input of these conditions (refer to Figure 10-9b). As previously seen, these higher temperatures increase the PTMAZ size and porosity formation in the stake head (Figure 10-1). Since CT testing evaluates the strength of the stake head, UCTF may be influenced by the microstructural changes generated at high temperatures.

FP has a reverse effect, creating stronger joints at higher levels (Figure 10-11b) even though higher FP levels also increase temperature (Figure 10-9b). In this FF-DoE all the specimens were joined without a backing surface, and when joined with a high level of FP (0.5 MPa) they presented stake-shaft shearing defects (Section 8.4.3). The positive effect of higher FP on UCTF can be related to the microstructure described in Figure 8-13 and Figure 9-17c. At the bottom of the stake a strengthened transition zone (STZ) is created around a plastically deformed volume (refer to Figure 8-6). The STZ is positioned within the preferable crack path for the most common failure mode in cross-tensile testing (BPB failure, Figure 9-12b). The force-displacement curve in cross-tensile tests is linear, so even though high FP leads to higher temperatures, the STZ (Figure 8-6) helps to slow down crack growth in its direction, increasing UCTF and displacement. The main effects plot indicates that the positive STZ effect on UCTF is stronger than the negative effect of additional heat at higher FP.

The interaction FT*FP shows the same positive contribution from increasing the FP, both at shorter and longer frictional times, but gain is notably higher for shorter FT (FT=-1, black squares in Figure 10-11c). With longer FT (FT=1, blue disks in Figure 10-11c) the positive effects of FP seem to be counterbalanced by excessive heat input, which can depreciate stake head integrity. With shorter FT (FT=-1) the positive effect of FP (FP=1) is more pronounced on the UCTF, because of the milder heat development in the stake. The effects of these parameters on heat input (as observed by stake temperature) were described in Section 10.3.1.

For the UCTF model, a remarkable influence of heat-generating factors can be seen. RS, FT, and FP are factors that are active during the friction phase. This indicates sensitivity of stake-head strength to the microstructural changes caused by heat generation during the F-ICJ process. The parameters (FoT and FoP) of the consolidation phase and their interactions do not play any important roles.

CHAPTER 11. PROOF OF CONCEPT

This chapter applies knowledge gained on the F-ICJ process and the validated statistical models to create an optimized joint and assess its properties. The optimized joint is reproduced by the gantry RNA system (Section 6.2.3), which is able to produce multi-spot components in an automated way. An exploratory investigation of process scaling-up was achieved by using this optimized condition to join a 20-spot sheet and stiffener subcomponent. The joining process for multi-spot structures and the quasi-static mechanical properties in four-point bending of the subcomponents are evaluated.

11.1 Joint optimization

In order to create an optimized condition, a desirability function was used to determine the processing parameters that would yield a maximized ultimate lap-shear force (ULSF) and ultimate cross-tensile force (UCTF) for an F-ICJ joint (Section 6.3.11). The optimized joining condition that was predicted by the desirability function for the specimens produced in the RSM 400 joining equipment is shown in Table 11-1.

Table 11-1: Process parameters for the optimized condition, as predicted by the desirability function (Section 6.3.11).

Rotational speed (RS) [rpm]	Frictional time (FT) [ms]	Forging time (FoT) [ms]	Forging pressure (FoP) [MPa (N)]	Frictional pressure (FP) [MPa (N)]
8000	2500	5000	1.0 (5363)	0.45 (2551)

This condition was created with the same setup as the FF-DoE on the RSM400 system. However, due to the high FP and absence of a backing plate these joints presented stake-shaft shearing (SSS) (Section 8.4.3). Although SSS presents a strengthened transition zone (STZ) which may improve cross-tensile (CT) strength, SSS was shown to cause several discontinuities in the joints, whose effects are unknown, especially with long-term and dynamic loading. Therefore, the optimized condition was produced both without a backing plate (forming SSS) and with a backing plate (avoiding SSS). The actual mechanical performances of these conditions are shown in Figure 11-1 for the joints produced on the RSM400 compared to the predicted values (white columns) and the standard errors of the regression (S, dashed lines) around the target value.

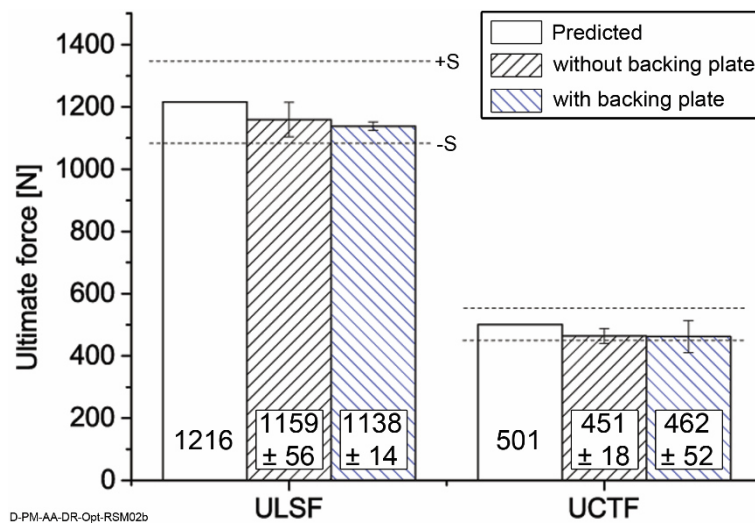


Figure 11-1: Mechanical performance of the optimized condition (with and without backing plate) compared to the predicted value. The dashed lines represent the standard error of the regression around the model’s target value (specimens produced at RSM400 equipment).

The predicted (target) values are ULSF of 1216 N and UCTF of 501 N. The actual values for the optimized joint are lower than the targets, but within the error of the regression and the specifications of the desirability function. The results show that the quasi-static mechanical performance between conditions produced without a backing plate (presenting SSS) and with a backing plate (without SSS) does not differ greatly, as was also observed in Appendix H. All five LS replicates in both conditions presented a complete secondary-bending failure (SB). The five CT replicates of each condition presented three base-plate bending (BPB) and two head pull-out (HPo) failures. Both conditions are similar in terms of static mechanic behavior, and the condition produced with a backing plate (without SSS) was chosen to be further studied as the optimized joint, because its microstructure presents less volumetric discontinuities (see Appendix N).

11.2 Transferability to the gantry system

The optimized process conditions produced with the RSM400 equipment were transferred to the RNA gantry system following the procedure described in Section 6.3.12. The setup joining parameters of the RNA gantry system are shown in Table 11-2. It is noted that the parameter setup on the RNA gantry (Table 11-2) is slightly different from the one of the RSM400 (Table 11-1). On the RSM400 only one friction phase with preset RS, FT, and FP (FF) can be defined, and the duration of the stud meltdown stage and dwell time stage depends on these process parameters. The RNA gantry is able to use up to three friction phases with varying RS, FT, and FF levels. In order to reproduce the RSM400 curves, two friction phases were defined on the RNA, representing the stages of stud meltdown and dwell time. The duration of these stages and the setup RS values on the RNA correspond to the average duration and RS observed in the RSM400 monitoring curves.

It is very important to emphasize that although both joining systems allow the same process variant (force control) to be performed, the differences in hardware and sensor technology (Appendix B) induce mild variability in heat generation for identical setup joining parameters. Bearing this in mind, the comparison of the process monitoring curves from the RSM400 and RNA gantry systems for the optimized specimen condition are displayed in Figure 11-2.

Table 11-2: Parameters for reproduction of the optimized condition with the RNA gantry.

Phase	Duration [ms]	Rotational speed [rpm]	Axial force [N]
Stud meltdown	765	7472	2551
Dwell time	1812	7018	2551
Consolidation	5000	0	5363

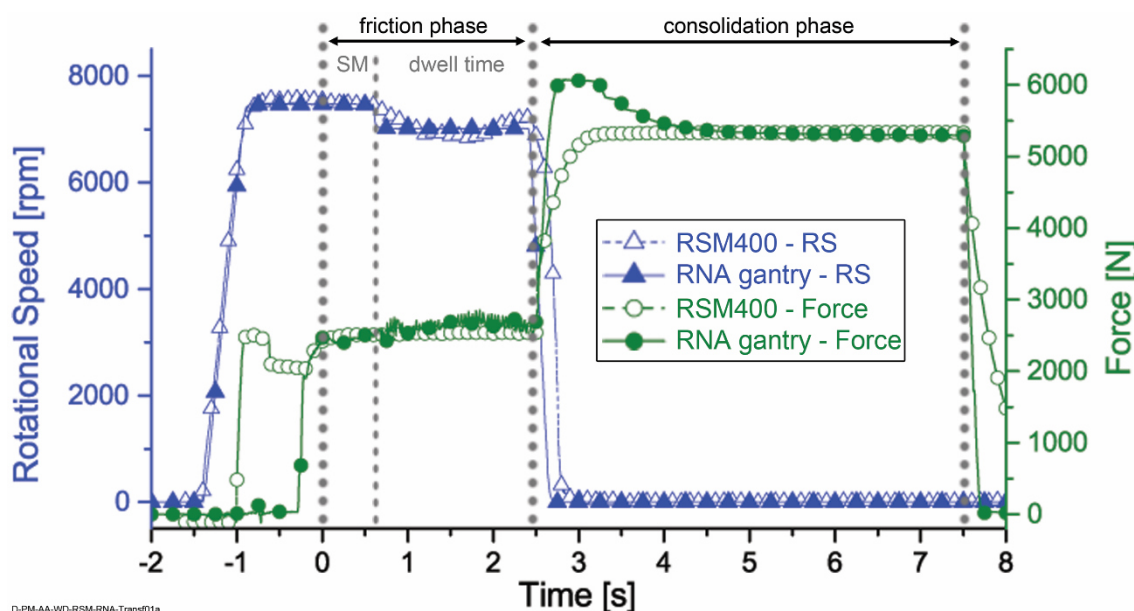


Figure 11-2: Joining diagrams for the transferability study of replicating the RSM400's optimized joining conditions on the RNA gantry system.

It can be seen from the RSM400 curve in this figure that during the dwell time there is a decrease in RS due to tool rubbing on the aluminum surface. This phenomenon was not observed for the original RS curve on the RNA as the machine has a more robust spindle motor (see Appendix B), which is able to accommodate oscillations of rubbing torque. The RS curve of the RNA gantry is very stable at the set level, whereas on the RSM400 the RS can decelerate due to tool rubbing. In order to match the same deceleration effect in the RNA, an artificial RS reduction step (Table 11-2) was programmed during dwell time, as previously described at the beginning of this section.

Another difference between both pieces of equipment is that the experiment designed for the RSM400 used a holding time of 7.5 seconds after the forging phase. This holding time was defined as a result of the preliminary studies described in Figure 10-7 as an extension of the

consolidation time, in order to minimize the chances of dimensional recovery after tool retreat (see Section 3.3). During this time a low force is used (about 0.3 kN) and the tool stays in contact with the joining partners. This holding step is not possible to be performed on the automated RNA gantry system, which retreats immediately after the end of the forging phase. This difference in equipment characteristics makes a direct comparison of stake temperature after tool retraction between conditions of the RSM400 and RNA gantry impossible, because accelerated joint cooling is promoted by longer contact with the tool during holding time for the specimens produced with the RSM400, and this artificially reduces the stake head temperature.

Since no direct comparison of stake temperature was possible, the energy input was used for this transferability stage. The energy input is calculated from the torque curves for both machines during frictional time – from the start of the tool-stud friction until the rotational speed starts to decrease. The torque curves are shown along with a calculation of the energy input (according to Equation (6-1) and the procedure described in Figure 6-12 (Section 6.3.12)) in Appendix O. The process was transferred with a satisfactory match of process curves (Figure 11-2), but due to these minor differences a complete reproduction of the energy input was not achieved; a generally higher torque is observed for the RNA system due to the aforementioned differences in machine specifications. For this reason some variations of the microstructure and mechanical properties are expected with the RNA gantry system specimens.

In order to verify at which level the joints are affected by the new process conditions on the RNA, the joint's microstructure and properties were compared. A surface view of the joints is depicted in Figure 11-3. The minor equipment differences in joining curves generate a visually rougher surface on the RSM400 joint that is characterized by a more widely spread porosity; evident from the opaque appearance. In the joint from the RNA, the pores seem to be concentrated away from the joint center, nearer the chamfer border leaving the stake walls around the keyhole visually pore-free (as indicated by the white dotted circles in Figure 11-3b).

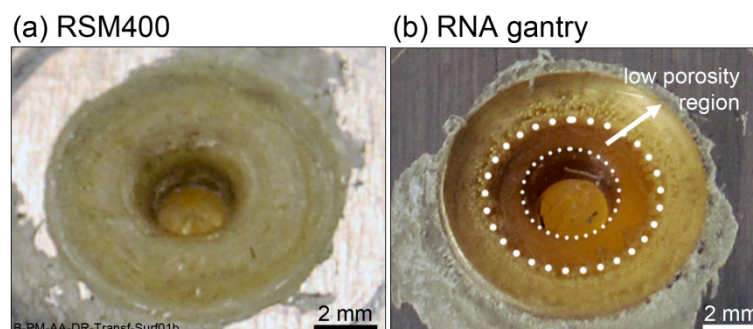


Figure 11-3: Surface view of the optimized condition produced on (a) RSM400; and (b) RNA gantry. The ring-shaped area delimited by white dotted circles represents a low porosity region.

The differences in joint microstructure are shown in Figure 11-4a. The same microstructural zones can be observed in both joints, with approximately the same shapes. The micrographs from transmitted-light optical microscopy with crossed polarizers (CP-TLOM) confirm porosity

distribution in the RSM400 joint is closer to the keyhole but in the RNA joint it is closer to the chamfer cavity (white arrows in Figure 11-4a). In Figure 11-4b-d the differences between microstructural features and local properties are shown, as measured for three replicates. The relative PTMAZ area RA_{PTMAZ} is slightly larger with the RNA gantry, while relative pore area RA_{pore} is comparable between them (Figure 11-4b). A larger PTMAZ occurs due to the higher energy input, mainly as a result of differences in equipment characteristics, which results in slightly higher torque for the RNA specimens (Appendix O). Local mechanical properties (microhardness, Figure 11-4c) in the microstructural zones and Tg in the PTMAZ (differential scanning calorimetry, Figure 11-4d) do not change significantly, and no remnant weld lines are observed in the joints. Overall, the microstructural characteristics are similar, despite the hardware differences of the machines.

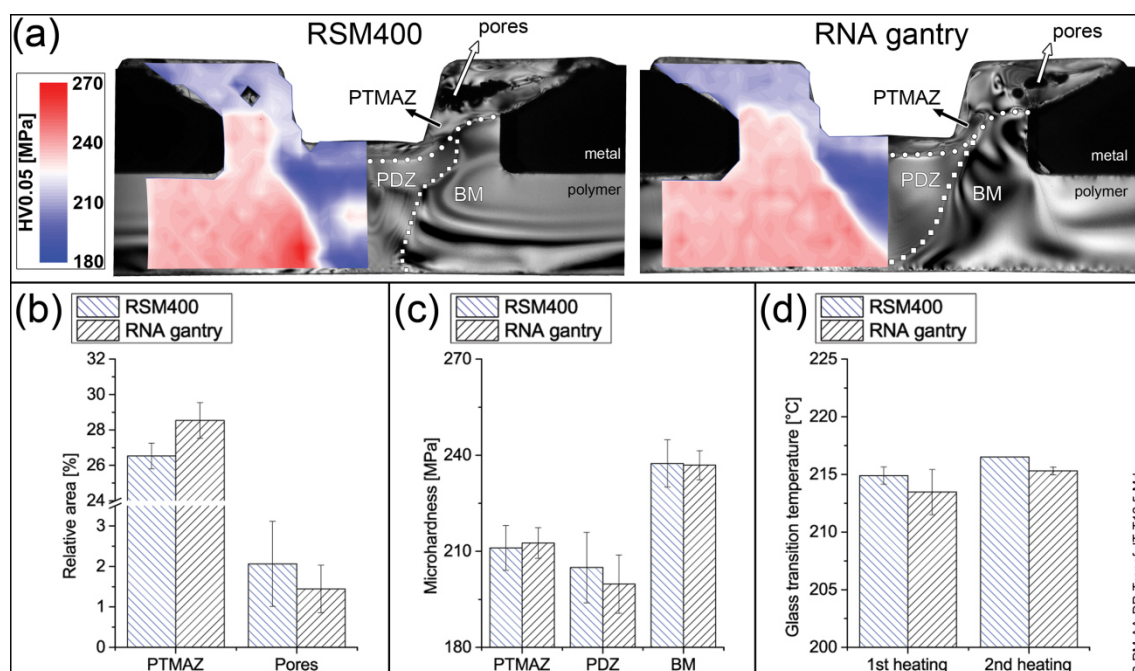


Figure 11-4: (a) Microstructure comparison of joints from the RSM400 and RNA gantry; comparison of (b) microstructural features (RA_{PTMAZ} and RA_{pore}); (c) local mechanical properties (microhardness); and (d) local physical-chemical changes (Tg from DSC).

A comparison of mechanical performance of these joints is shown in Figure 11-5. In Figure 11-5a and b the averaged force-displacement curves for LS (five specimens) and CT (seven specimens) testing are compared. The behavior in both cases is similar. In LS a higher ULSF and stiffness are achieved with the RNA joints (Figure 11-5c). The higher ULSF is the result of the RNA joints having a low-porosity stake wall, which is the preferred path for a stake-head crack (Figure 9-5a). A pore-free region delays crack growth, and since the ULSF corresponds to the point at which the stake head fails, and this contributes to improving the joint strength. The increase in joint stiffness (Stiffness-LS in Figure 11-5c) is likely due to the larger PTMAZ promoting better cavity filling, as shown in Figure 10-4c.

No change in displacement is observed for LS joints, but for CT specimens the most significant differences are seen with the displacement at UCTF and at break being larger for the RSM400 joints (Figure 11-5d). The delayed CT failure in RSM400 joints is likely due to a more intense STZ effect decelerating crack growth, as discussed in Section 10.3.3.

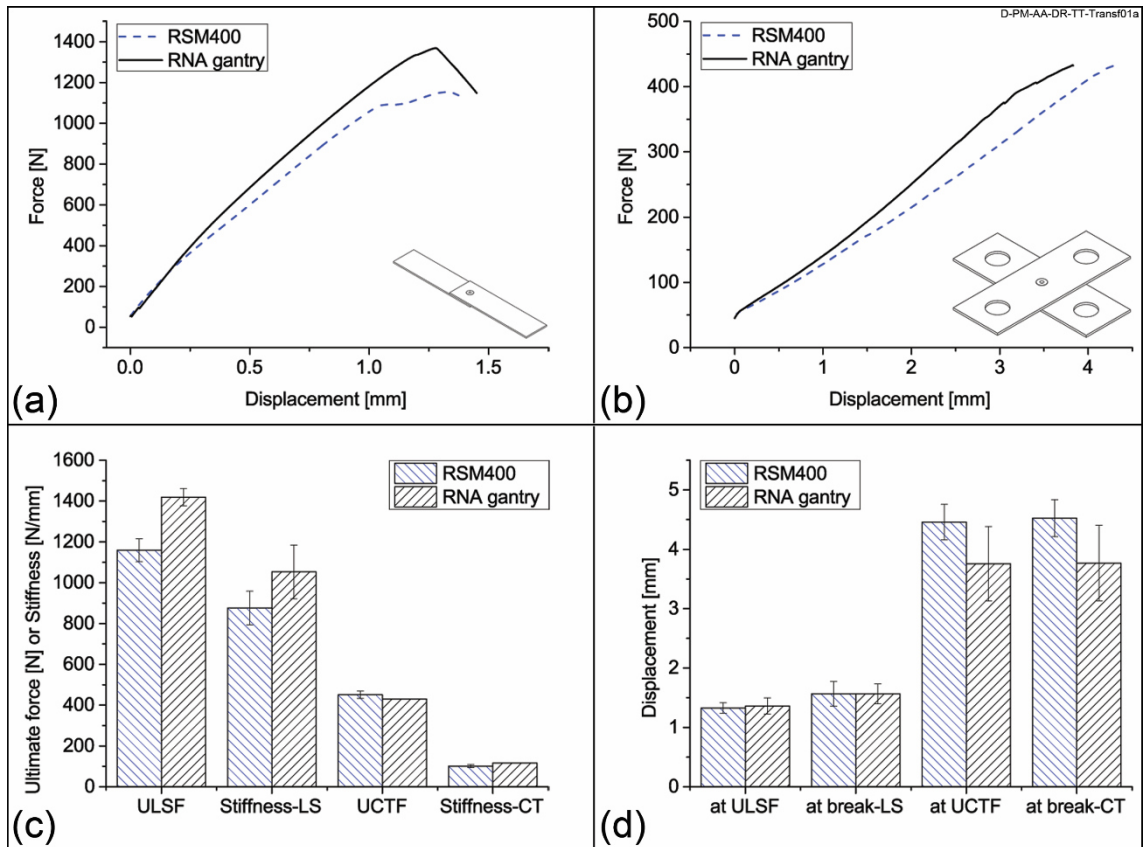


Figure 11-5: Comparison of averaged force-displacement curves for (a) Lap shear (LS) testing; and (b) cross-tensile (CT) testing; (c) comparison of average ultimate force and joint stiffness, and (d) comparison of average displacement at ultimate forces and break, for LS and CT properties.

Thus, within the limitations of the joining systems, it was possible to reproduce an optimized condition with above-average mechanical performance on the automated RNA gantry.

11.3 Comparison of F-ICJ joints to the state of the art

The optimized condition produced on the RNA gantry system was compared with state-of-the-art ultrasonic staking technology. For this comparison, the same material combination from F-ICJ (PEI and AA6082) was used. Investigations of the microstructure (according to Section 6.3.3) and quasi-static global mechanical properties (according to Section 6.3.8) were

performed. The microstructure and mechanical performance of the joints for each process are shown in Figure 11-6.

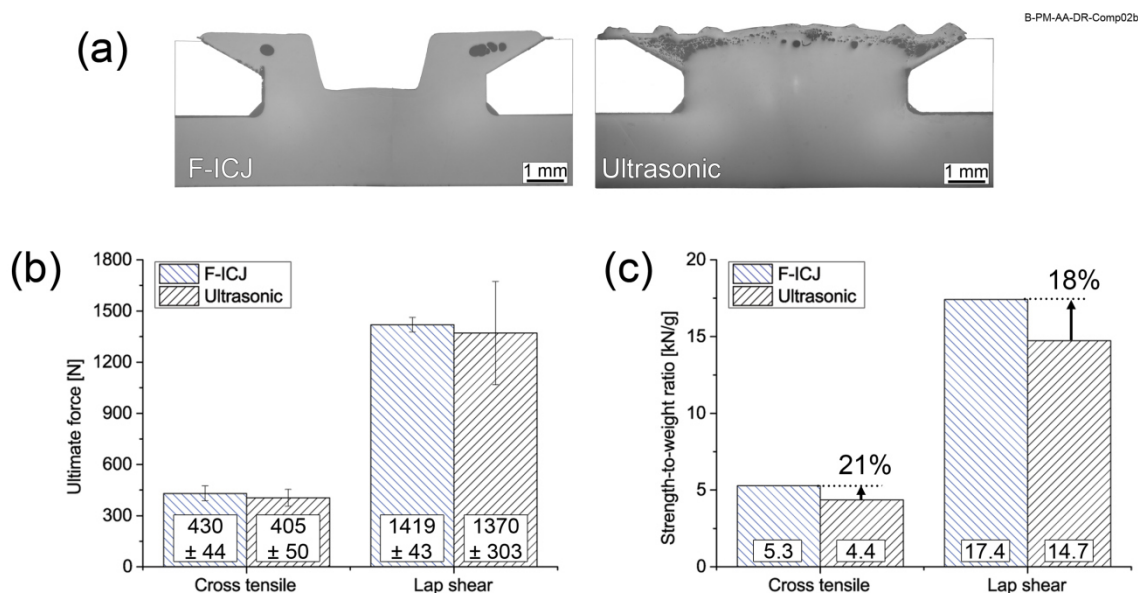


Figure 11-6: Comparison of F-ICJ to ultrasonic staking. (a) Cross-sectional view of the joints; (b) UCTF and ULSF of each process; (c) strength-to-weight ratio in CT and LS for each process. The percentages are improvements of F-ICJ over ultrasonic staking.

Both processes present similar CT and LS performances (Figure 11-6b). Taking the joint geometries shown in Figure 11-6a into account, F-ICJ uses a flush hollow stake with a keyhole, while ultrasonic staking uses a flush solid stake (knurled design, see Figure 3-9). In terms of the strength-to-weight ratio of each process, F-ICJ presents improvements of 21 % in UCTF and 18 % in ULSF better than ultrasonic staking, due to its hollow stake design. However, in this initial stage of development F-ICJ joining cycles are longer than ultrasonic staking. The F-ICJ joints from the comparison in Figure 11-6 were produced in 7.5 seconds, while the ultrasonic staking joints were produced in 2.8-2.9 seconds. These results show that the optimized F-ICJ joints in this work present comparable mechanical properties to the traditional staking method, while producing lighter joints. However, F-ICJ needs further process development to improve cycle times.

11.4 Process scaling-up

In order to assess the use of F-ICJ for the sequential joining of a multi-spot structure, investigations into the joining and mechanical behavior of a sheet and stiffener subcomponent were performed. To the best of the author's knowledge, such an analysis is the first of its kind for staked structures in the published literature. Figure 11-7a shows the pre-assembled specimen ready for the assembly process, and Figure 11-7b displays an F-ICJ subcomponent. The optimized condition for the RNA gantry was used (Table 11-2) and 20 as the number of

spots was selected, based on the work of Paz [201], which was supervised by the author of this PhD thesis (see Appendix D).

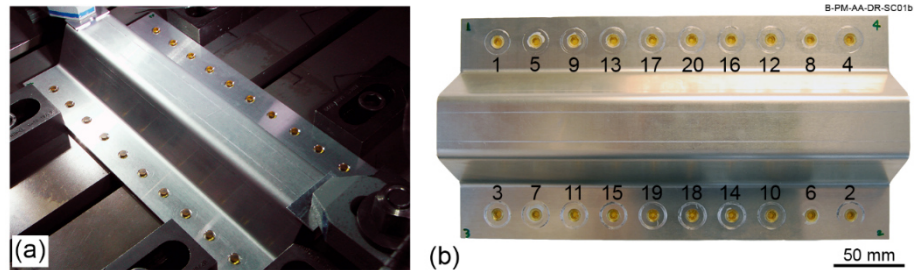


Figure 11-7: (a) Multi-spot subcomponent in position for joining; (b) joined subcomponent. The numbers represent the joining order of each individual stake.

In this scaling-up study, an automated sequential joining machine was used without an external cooling system, so repeated rubbing caused heat to build up on the tool. This effect was investigated using an infrared thermal camera, as described in Section 6.3.13. Due to the limitations of the camera's field of view and specimen geometry, only the temperatures from joining at stakes 1, 5, 9, 13, 17, and 20 (see Figure 6-14) could be directly measured. As shown in Figure 11-8, a sequential increase in temperature on the stake head is observed, and it is proportional to the increase in temperature on the tool surface. A close-up view of the stake surfaces shows that stake 1 appears to have slightly rougher surface with less pores than stakes 5, 9, 13, 17, and 20. The latter were all similar with the same visual degree of porosity and surface quality.

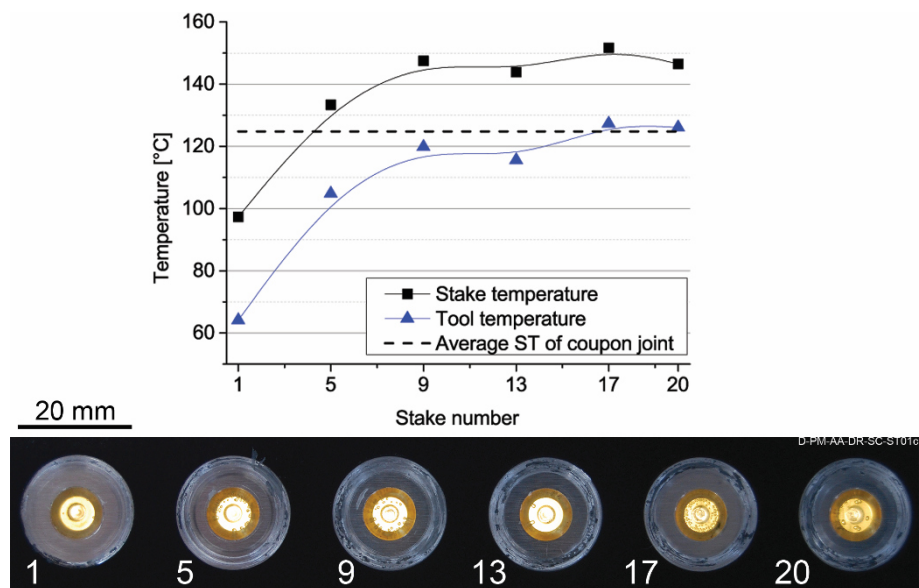


Figure 11-8: Heat build-up during sequential joining as a result of tool rubbing, and the surface appearance of the stakes from the diagram.

Compared to the single-spot joints, the process itself applies the same amount of energy on the joint, but the cooling rate during consolidation is faster due to conduction losses to the larger parts. This effect is expected with any real application, where the heat dissipation occurs under different conditions to those with laboratory coupons. Consequently the temperature of the first stake is well below the ST observed for the single-spot joints with the same condition (124.8 ± 4.5 °C). This effect is progressively compensated for by the sequential joining process, as for the subcomponent there is not enough time for the tool to cool down after each joining cycle (lacking an external tool cooling system). The heat build-up reaches a plateau after joining of the 9th stake, and the following stakes present an approximately constant stake temperature in the range 140-155 °C.

As previously discussed in Section 10.1, the main effect of the higher temperatures is it creates a larger PTMAZ. This has been proven to have little effect on LS performance, but a decrease in CT performance for the cases when the stake is susceptible to head pull-out failure (HPo) (refer to Section 10.2). The effect of heat build-up can be avoided in a more immediate way, by the implementation of tool cooling with future F-ICJ equipment. Alternatively, the heat build-up related to tool rubbing could be minimized or avoided by using a tool design with a stationary clamping system, as with the one proposed in Appendix P.

11.4.1 Quasi-static mechanical testing of the subcomponents

Subcomponent specimens were tested in quasi-static four-point bending to assess the mechanical behavior of a multi-spot F-ICJ structure for the first time. Figure 11-9a charts the force-displacement curve for four replicates of the subcomponent. The force steadily increases with displacement up to failure at ultimate force. The curves show that mechanical performance of the specimens are reproducible, with average ultimate force of 21.1 ± 1.1 kN and average displacement at ultimate force of 5.6 ± 0.8 mm. Figure 11-9b shows the deformation behavior of the subcomponent from the start of the test up to ultimate force, prior to failure. Slight bending of the polymer base plate can be seen close to the edges of the specimen (black arrows). Otherwise, no significant deformation of the specimen is observed during the test.

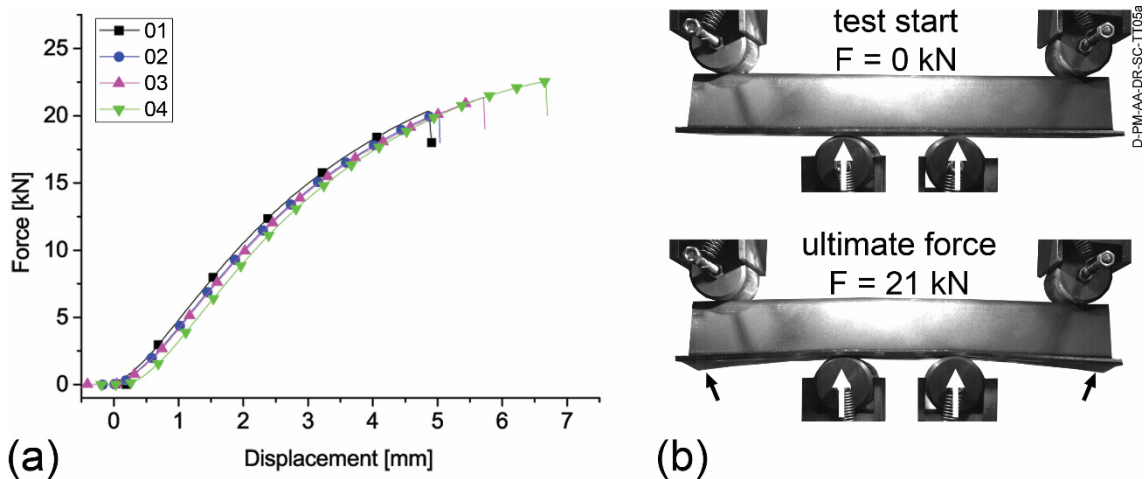


Figure 11-9: (a) Force-displacement curves for four replicates of the F-ICJ subcomponent; (b) deformation under quasi-static four-point bending of an F-ICJ subcomponent.

Figure 11-10 illustrates the typical failure surface of the tested subcomponents. Failure occurs in a mixed mode consisting of cracks through the polymer base plate (Figure 11-10a) and cracks in the stake heads (black arrows in Figure 11-10b). Failure is a catastrophic burst, which shatters the base plate. Even using a high-speed camera recording at 1000 frames per second, it is not clear if the stake-head cracks are a precursor or a consequence of the main longitudinal cracks.

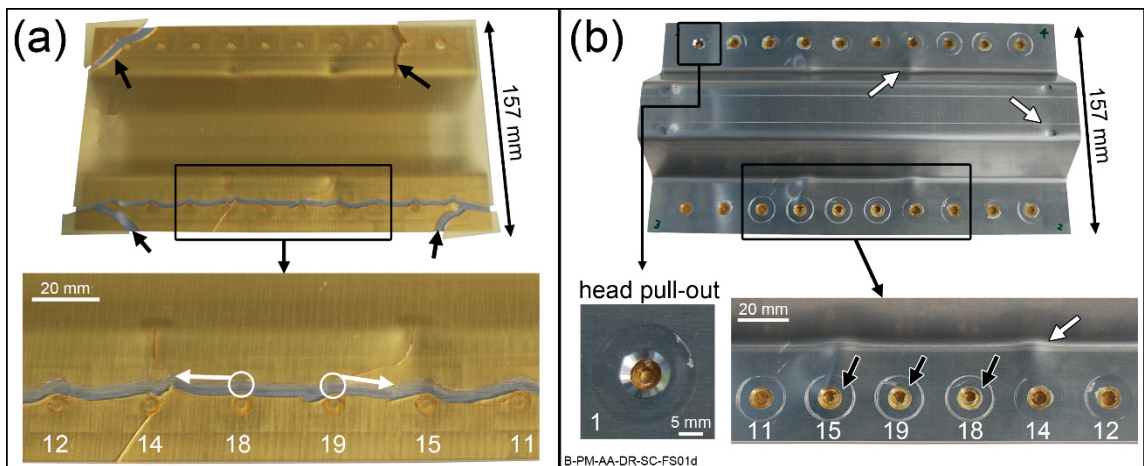


Figure 11-10: (a) Bottom surface of the subcomponent, showing a longitudinal crack. Black arrows are additional cracks from the rebound during catastrophic failure, white arrows indicate the crack propagation direction; (b) top surface of the subcomponent with details of damage to stake heads. Black arrows are cracked heads, white arrows are plastic deformation of the metal.

The bottom surface in Figure 11-10a shows a longitudinal crack that starts at the base of the central stakes (18 and 19) and propagates along the remaining stake bases until complete

plate rupture, as indicated by the white arrows in Figure 11-10a. In some cases a partial longitudinal crack is also present on the opposite row of stakes, showing that competing crack propagation occurs in both stake rows. Additional cracks, from the elastic rebound from failure, appear at the edges of the subcomponent (black arrows in Figure 11-10a). Analyzing the top surface (Figure 11-10b), it is observed that the central stake heads on both sides (17-20 in Figure 11-7b) usually present partial cracks (black arrows in Figure 11-10b). The intermediate stakes (5-16 in Figure 11-7b) present cracks less frequently, but they might still be present, as seen with stake 15 in Figure 11-10b. Although heat build-up indicated higher temperatures on the central stakes, their failure is most likely related to the geometrical constraints due to the loading noses of the rolls from the four-point bending test that created higher stresses in that region. The edge stakes 1-4 rarely show partial cracks, but can have their heads removed due to rebound from the catastrophic failure (detail in Figure 11-10b). Finally, some degree of plastic deformation in the metallic stiffener occurs at the loading and support noses (white arrows in Figure 11-10b).

This initial analysis gives an indication of how such a structure joined by F-ICJ behaves under quasi-static four-point bending. A complete analysis of mechanical behavior and failure was beyond the scope of this PhD work. A detailed understanding of the structural behavior of F-ICJ multi-component joints requires the study of different material combinations (e.g. ductile polymers and fiber-reinforced plastics) and loading conditions for a deeper assessment of the mechanical performance of F-ICJ joints in multi-spot structures.

CHAPTER 12. SUMMARY OF THE RESULTS

This chapter summarizes the main findings described in the previous chapters. The points presented here aim to assist in a fundamental understanding of the new F-ICJ technology and its scientific aspects.

Investigation of the joint formation mechanisms in F-ICJ

Monitoring of the process curves and stake temperature provided insights into the joint formation mechanisms of F-ICJ joints produced using a two-phase process configuration (Figure 4-4a). The friction phase is composed of a stud meltdown stage and a dwell time stage. The stud meltdown stage occurs from the first contact of tool and stud until complete stud meltdown is achieved. Following the stud meltdown stage, the tool rotates in position, creating a radial flow around its conical pin, characterizing a dwell time stage of the friction phase. Finally, a consolidation phase under pressure allows the stake to cool down and avoid dimensional recovery (Figure 7-2).

In sound F-ICJ joints created by the two-phase process, joint formation was mainly dependent on the material flow from the softened, fluid polymer to the chamfer cavities. This volume of flowing material characterizes a shear layer, where heat and deformation affect the stake's shape and polymer morphology (Section 7.2.1). Formation of the shear layer starts during stud meltdown due to frictional heating; this leads to a steady-state viscous dissipation that softens the polymer, and allows squeeze flow, resulting from the axial pressure imposed by the tool.

The dwell time greatly contributes to extension of the shear layer, because in this stage significant viscous heating is generated in the flowing material confined between the tool, the metal part, and the solid (unaffected) polymer volume. This lowers polymer viscosity, creating satisfactory material flow and eliminating occasional discontinuities that are formed during stud meltdown, such as shear banding, remnant weld lines, and microcracks (Section 7.2.2).

Monitoring of the stake temperature during consolidation showed that fast cooling occurs as a result of heat losses to the tool by conduction (Figure 7-10). The polymer stays only for a short time above its glass transition during consolidation. By the time the tool retreats, the polymer is well below its glass transition temperature, and experiences no significant microstructural changes (topological rearrangement of the molecules, Section 7.2.3). No dimensional recovery or loss of shape are expected after tool retreat.

Process-related changes in the materials joined by F-ICJ

Both the metallic and polymeric joining partners undergo microstructural changes, but the changes in the polymer are far more severe. Small regions of the aluminum may show metallurgical alterations, but only in cases of harsh rubbing of the tool on its surface (Section 8.1). Such changes are less relevant, as the polymer is weaker and its local changes are much more important for the mechanical behavior of the joints.

The polymeric partner typically presents a base material region (BM) and a polymer thermomechanically affected zone (PTMAZ, or shear layer). When high joining forces are used (above 2400 N), a plastically deformed zone (PDZ) is observed directly below the keyhole. The local mechanical properties in the PTMAZ and in the PDZ are lower than in the BM, indicating physical-chemical changes to these volumes (Figure 8-4).

The lower strength of the PDZ results from plastic compressive deformation as shown by residual stress fields and indentation profiles (Figure 8-6). Plastic deformation in amorphous polymers creates more free volume, reducing its local strength. The compressive stress fields around the PDZ contribute to the creation of a strengthened transition zone (STZ) between the PDZ and BM (Section 8.2.1). The local strength reduction in the PTMAZ is also an effect of less efficient chain packing (more free volume) from the thermomechanical processing and fast cooling (Section 8.2.2). The process-related shear stress and heat development in the shear layer disentangle the polymer chains, which during the consolidation phase and cooling lack the energy to translate into more packed configurations.

Post-joining annealing of a joint promotes physical aging, and yields a joint with homogeneous local strength (Section 8.2.3). This further supports the theory of free volume being responsible for loss of strength in the PTMAZ and PDZ. No evidence for extensive degradation is observed in the PTMAZ (Figure 8-8), meaning that if any thermal degradation occurs in the explored parameter range, it has no apparent effect on local mechanical properties. Analysis of the viscoelastic response of indentations in each microstructural zone indicates that the increased free volume enhances plasticity (higher loss modulus) of PEI (Section 8.3), which may negatively influence cyclic and creep loading conditions.

Typical defects in the polymeric partner were identified, and they occur mainly due to improper choices of process parameters. Porosities are products of volatile evolution in the PEI, most likely due to structural water (Section 8.4.1). Remnant weld lines can be formed under certain conditions. They are a result of material flow towards the chamfer and incomplete healing between this flowed material and the stake shaft (Section 8.4.2). If a backing surface is not used when joining with high axial forces (above 2400 N), a severely plastically deformed joint is created (“stake-shaft shearing” – SSS, Section 8.4.3).

Quasi-static mechanical behavior of F-ICJ joints

The quasi-static mechanical behavior in lap-shear (LS) and cross-tensile (CT) configurations was investigated and correlated with the microstructural changes in the polymer (Chapter 9). LS loading causes secondary bending of the polymeric plate, which in turn induces stress concentration points in the stake head and at the stake base (Figure 9-1). Failure occurs due to secondary bending, starting with a radial crack in the stake head and followed by catastrophic failure at the base plate (Figure 9-4). For the radial crack in the stake head, the remnant weld line acts as a nucleation point, and the presence of pores may influence the crack path (Figure 9-5). The ultimate lap shear force coincides with stake head failure. Fracture surface analysis shows typical micromechanisms of stable crack growth with crazes, followed by stable/unstable growth, and fast crack propagation zones (Figure 9-6). A critical crack size in the stake head transfers the load to the stake base, accelerating crack propagation (Figure 9-8).

CT loading effectively creates a tensile test of the stake head by pulling it away from the stake shaft/base plate. Most of the stress is concentrated at the stake base (Figure 9-11), but volumetric flaws in the shear layer weaken the stake head and may change its failure behavior. Both situations are active during loading and lead to two concurrent failure modes. Base plate bending (Figure 9-12b and Figure 9-13) occurs with a crack nucleating on one side of the PEI base plate and a fracture surface similar to the secondary bending failure of LS joints, but without damage to the stake head. The complete cracking of this side of the PEI plate transfers the load to the other side, which breaks catastrophically. Head pull-out failure (Figure 9-12c and Figure 9-14) is failure of the stake head. Crack nucleation may be influenced by contamination from the metallic joining partner. Pores affect the crack propagation regime, possibly accelerating crack growth. A third failure mode of stake pull-out (Figure 9-17 and Figure 9-18) was observed mostly in joints presenting stake-shaft shearing. Residual stress fields and plastic deformation create a complex local strength distribution in these joints, leading to crack path deviation and finally removal of the stake in a plug-like form. This failure mode is dominated by slow crack-propagation micromechanisms.

Process-microstructure-property relationships in F-ICJ joints

The effects of heat input on the microstructure were investigated by analyzing the PTMAZ and porosities as a function of stake temperature (ST). The relative PTMAZ area increased at higher ST, as more heat input decreases polymer viscosity and supports material flow (Figure 10-1a). Joints with smaller PTMAZ and lower heat input levels are more likely to present weld lines, and a tentative threshold can be established to avoid weld line formation (Figure 10-1a). Heat generation does not significantly change the relative pore area (Figure 10-1b), supporting the hypothesis that pores originate from structural water instead of the degradation products of PEI. The local mechanical properties (microhardness distribution, Figure 10-3) in the PTMAZ were reduced to approximately the same level for all heat inputs used, providing no clear evidence of temperature effects on local strength reduction.

The effect of microstructure on global mechanical properties was evaluated from the size of the relative PTMAZ area. Analysis of lap-shear (LS) test results showed that joint stiffness is increased with a larger PTMAZ, due to better cavity filling (Figure 10-4c). Displacement at ultimate lap shear force is decreased (Figure 10-4b) due to higher stiffness, leading to premature critical stress on the stake head. Ultimate lap shear force (Figure 10-4a) and displacement at break (Figure 10-4d) are fairly independent of microstructural changes in the stake head.

Changes to the stake head microstructure are more critical with cross-tensile (CT) testing, where the relative PTMAZ area had significant negative effects on the mechanical properties. An increased PTMAZ is a larger volume of weaker material that contains pores, thereby affecting crack nucleation and crack growth in CT loading, and undermining joint performance (Figure 10-5). Although it may influence crack nucleation, the remnant weld line does not change the average mechanical performance in LS and CT tests (Figure 10-6).

Statistical analyses of the effects of process parameters on heat development and mechanical performance were carried out (Section 10.3). The stake temperature is sensitive to the friction phase parameters (rotational speed, frictional time, frictional pressure), since they provide

frictional heating to the process (Section 10.3.1). Ultimate lap shear force does not vary greatly over the studied parameter range, and is only slightly influenced by consolidation phase parameters (forging pressure and forging time; Section 10.3.2). Ultimate cross tensile force is more sensitive to process parameters, especially the heat-contributing ones (rotational speed, frictional time, frictional pressure). This is a result of the direct dependence of the cross-tensile test configuration on changes in the stake head microstructure, which were shown to be affected by heat development (Section 10.3.3).

Proof of concept

Using the acquired process knowledge and validated statistical models an optimized condition could be produced (Section 11.1), which achieves above-average mechanical performance among the experiments in this work. A transferability study (Section 11.2) was carried out to transfer this optimized condition to an automated system (RNA gantry) for the joining of subcomponents (scaling up study). The optimized joint from the RNA gantry presents a mechanical performance comparable to traditional ultrasonic staking (Figure 11-6), with an improvement on strength-to-weight ratio of 18 % in lap-shear and 21 % in cross-tensile test configurations due to its hollow stake design.

The optimized process condition was used to join sheet and stiffener subcomponents, using an automated sequential joining program for 20 stake points using the RNA gantry (Section 11.4). Heat build-up on the tool could be observed during sequential joining (Figure 11-8), which changed the heat generation in the joints during the process in this exploratory scaling-up study. In an industrial application, the heat build-up effect could be effectively minimized or avoided by simple measures such as forced cooling or by an improved tool design to reduce the tool rubbing (Appendix P).

A quasi-static four-point-bending test was used for an exploratory analysis of the mechanical behavior of the F-ICJ multi-spot subcomponent. This mechanical test showed that the F-ICJ subcomponents present reproducible mechanical performance, and fail at ultimate force (Figure 11-9). Subcomponent failure was catastrophic (Figure 11-10), and the mechanisms leading to failure must be further investigated for application-specific cases to enable better understanding.

CHAPTER 13. CONCLUSIONS

This work has focused on the development of a new staking-based joining method for multi-material lightweight structures, ranging from coupon level to proof of concept. A fundamental understanding of the new F-ICJ technology was sought with this development. More specifically, in its scientific aspects, the work aimed at investigating the joint formation mechanisms, the physical and chemical changes affecting the materials, and micromechanisms that dictate the failure behavior. On the technological level, the study had the objectives of establishing relationships between process parameters and joint properties and optimizing the mechanical performance at the coupon level. As a further step in the technological development there was the objective of accomplishing an initial scaling-up study of the process to a multi-spot structure. This work also describes in detail for the first time a materials-science approach to understanding a staking process.

F-ICJ metal-polymer joints are formed by inducing material flow in a shear layer using frictional heat. The material flow regime was defined by investigating the microstructure of unreinforced and reinforced PEI joined by F-ICJ. These findings shed light on how the process phases can contribute to the formation of sound joints, and the role of material flow in achieving this. With this knowledge, tailoring the material flow to accomplish optimum joint formation is possible for F-ICJ.

Process-related microstructural changes in material joined by F-ICJ are related to changes to the free volume caused by thermal and mechanical effects. F-ICJ joints of amorphous polymers present microstructural zones of lower strength that are affected mainly by heat and deformation, which can fully recover with an annealing treatment (induced physical aging). The scientific descriptions of microstructure and mechanical behavior defined in this work can be adapted and extended to other staking joining processes. In this way, further progress was accomplished towards a more scientific approach in the rather technical field of staking methods.

Fundamental understanding of these effects helped to describe the relationships between process, microstructure, and quasi-static mechanical behavior of F-ICJ joints in this work. Heat development increases the size of the shear layer, thereby improving cavity filling and eliminating discontinuities such as shear bands and weld lines. To some extent, microstructural changes have an influence on the mechanical behavior of F-ICJ joints, but these are much more pronounced in cross-tensile loading of the stake head than in a lap-shear configuration. These findings will serve as a basis for future process development of F-ICJ and possibly other friction and/or staking-based processes.

Validated statistical models were successfully used to optimize joint performance at the coupon level. The best conditions produced in this work are comparable in performance to state-of-the-art ultrasonic staking, but present a better strength-to-weight ratio. This suggests that the proposed joining partner geometries, tool design, and process optimization were correct, confirming the potential of F-ICJ as a promising new staking technology.

The exploratory scaling-up study of the new technology for multi-spot structures identified solvable challenges for an industrial application. A preliminary analysis of its mechanical performance provides an initial impression of the mechanical behavior of staked

subcomponents. This first assessment of process scaling-up serves as the basis for further improvement, showing the potential of the F-ICJ process for industrial use. However, the mechanical behavior has to be further investigated with other material combinations, loading, and durability conditions required for a variety of target applications.

As far as the author of this PhD work is aware, this thesis represents the first deep scientific description ever attempted of a staking-based process and the changes it causes to the materials involved. These findings are important for the potential upcoming introduction of advanced staking methods as solutions for joining of lightweight multi-material structures. Specifically for F-ICJ, the technological development was achieved from coupon level to a preliminary proof of concept with multi-spot joints. The F-ICJ staking method shows improvement as a solution for lightweight materials compared to state-of-the-art staking and is suitable to efficiently join larger structures.

Finally, this work has demonstrated the potential of F-ICJ for future polymer-metal lightweight structural applications. This was successfully accomplished with a combined scientific and engineering approach, describing the influence of microstructure and process parameters, and going further by proposing strategies for efficient multi-spot joining.

CHAPTER 14. RECOMMENDATIONS FOR FUTURE WORK

This PhD work is a first account on development of F-ICJ. Although many of the fundamental aspects of scientific and technological development have been covered, further investigations are necessary for advancement of F-ICJ – or other innovative staking methods – enabling industrial use and weight reduction. This chapter suggests a number of important points for future investigations.

For this study, a simple tool geometry was selected that generated effective heating and material flow in the stake. However, alternative tool designs could be investigated to improve material flow and reduce the required heating time for effective joint formation. For instance, the frictional surfaces of an F-ICJ tool can be designed according to the extensive literature available on friction stir welding tool design. Moreover, the use of an outer, independently rotating clamping ring instead of the clamping surface could be tested as a solution to prevent rubbing (Appendix P). Investigations can be performed to evaluate the effectiveness of such tools to fill cavities for improved strength, reduce hole clearances for cost reduction and allow larger tolerances in staked joints.

The research should be further expanded to alternative engineering materials, such as short-fiber and long-fiber reinforced composites. The effects of F-ICJ on semicrystalline polymers should be investigated, by determining and understanding the relationships between process-related changes to crystallinity and mechanical performance. If necessary, annealing heat treatments can be defined for recovery or improvement of the local properties on process-affected regions. A beneficial contribution to process development with new materials would be the development of analytical heat input and/or computational fluid dynamics models. Such methods would supplement process development and help predict the final joint properties for different material combinations.

Under mechanical performance aspects, fatigue and durability performance remain uninvestigated. The experimental observations of quasi-static failure mode for coupon and subcomponent level would greatly benefit from numerical analysis, preferably by deeper finite element method simulations. This would support the definition of future design guidelines for F-ICJ assembled structures.

REFERENCE LIST

1. WHITE PAPER: Roadmap to a Single European Transport Area - Towards a competitive and resource efficient transport system. European Commission, 2011.
2. Marsh G., *Airbus A350 XWB update*. Reinforced Plastics, 2010. Vol. 54(6): p. 20-24.
3. Staeves J., *The right material at the right place (BMW Group)*, in *Global Automotive Lightweight Materials*. 2013: London, UK.
4. Köbler J., *Non Plus ultra*, in *Encounter*. 2014, Audi AG. p. 86-91.
5. Marsh G., *Composites in commercial jets*. Reinforced Plastics, 2015. Vol. 59(4): p. 190-193.
6. Cuenot F., *CO2 emissions from new cars and vehicle weight in Europe; How the EU regulation could have been avoided and how to reach it?* Energy Policy, 2009. Vol. 37(10): p. 3832-3842.
7. Heuss R., et al. *Lightweight, heavy impact*. McKinsey & Company, 2012. Available from: www.mckinsey.com. Accessed on: 09.07.2015.
8. *Leichtbau als Königsdisziplin*. VDI Wissensforum, 2013. Available from: www.vdi-wissensforum.de/presse. Accessed on: 09.07.2015.
9. *Leichtbau bleibt weiterhin die Königsdisziplin*. VDI Wissensforum, 2014. Available from: www.vdi-wissensforum.de/presse. Accessed on: 02.05.2015.
10. Marsh G., *Composites and metals – a marriage of convenience?* Reinforced Plastics, 2014. Vol. 58(2): p. 38-42.
11. Raugei M., et al., *A coherent life cycle assessment of a range of lightweighting strategies for compact vehicles*. Journal of Cleaner Production, 2015. Vol. 108, Part A: p. 1168-1176.
12. Duflou J.R., et al., *Environmental impact analysis of composite use in car manufacturing*. CIRP Annals - Manufacturing Technology, 2009. Vol. 58(1): p. 9-12.
13. Timmis A.J., et al., *Environmental impact assessment of aviation emission reduction through the implementation of composite materials*. The International Journal of Life Cycle Assessment, 2015. Vol. 20(2): p. 233-243.
14. Oliveux G., Dandy L.O., and Leeke G.A., *Current status of recycling of fibre reinforced polymers: Review of technologies, reuse and resulting properties*. Progress in Materials Science, 2015. Vol. 72: p. 61-99.
15. Baker D.A. and Rials T.G., *Recent advances in low-cost carbon fiber manufacture from lignin*. Journal of Applied Polymer Science, 2013. Vol. 130(2): p. 713-728.
16. Amancio-Filho S.T. and dos Santos J.F., *Joining of Polymers and Polymer-Metal Hybrid Structures: Recent Developments and Trends*. Polymer Engineering and Science, 2009. Vol. 49(8): p. 1461-1476.
17. Amancio-Filho S.T., Dos Santos J.F., and Beyer M., *US 7,780,432 B2: Method and device for connecting a plastic workpiece to a further workpiece*. 2010
18. Abibe A.B., et al., *Development and Analysis of a New Joining Method for Polymer-Metal Hybrid Structures*. Journal of Thermoplastic Composite Materials, 2011. Vol. 24(2): p. 233-249.

-
19. Mallick P.K., 8 - *Joining for lightweight vehicles*, in *Materials, Design and Manufacturing for Lightweight Vehicles*, Mallick P.K., Editor. 2010, Woodhead Publishing. p. 275-308.
 20. von Kulmiz G., *Smart application kit for lightweight multi-material body structures*, in *AluMag Lightweight Roadshow*. 2012.
 21. Braess H.-H., et al., *Aufbau*, in *Vieweg Handbuch Kraftfahrzeugtechnik*, Braess H.-H. and Seiffert U., Editors. 2013, Springer Vieweg: Wiesbaden. p. 497-630.
 22. Singh S., et al., *Lightweight design through optimized joining technology: In-depth knowledge of physical and technological properties for the most effective use of materials*. *Materialprüfung*, 2003. Vol. 45(9): p. 356-361.
 23. Fernández I., Blas F., and Frövel M., *Autoclave forming of thermoplastic composite parts*. *Journal of Materials Processing Technology*, 2003. Vol. 143-144: p. 266-269.
 24. Mallick P.K., 1 - *Overview*, in *Materials, Design and Manufacturing for Lightweight Vehicles*, Mallick P.K., Editor. 2010, Woodhead Publishing. p. 1-32.
 25. Mlekusch B. and Hambrecht T., *Lightweight design in automotive Engineering - Possibilities and Challenges*, in *4. VDI Leichtbaukongress Automobilindustrie*. 2014, VDI: Leipzig, Germany.
 26. Stewart R., *Carbon fibre market poised for expansion*. *Reinforced Plastics*, 2011. Vol. 55(2): p. 26-31.
 27. Mondo J., Wijskamp S., and Lenferink R., *Overview of thermoplastic composite ATL and AFP technologies*, in *ITHEC 2012*. 2012: Bremen, Germany.
 28. Crawford R.J., *Plastics engineering*. 3 ed. 1998: Butterworth-Heinemann.
 29. Mallick P.K., 5 - *Thermoplastics and thermoplastic-matrix composites for lightweight automotive structures*, in *Materials, Design and Manufacturing for Lightweight Vehicles*, Mallick P.K., Editor. 2010, Woodhead Publishing. p. 174-207.
 30. Feraboli P., et al. *Lamborghini "Forged Composite" Technology For The Suspension Arms Of The Sesto Elemento*. in *ASC Technical Conference 2011*. 2011. Montreal, Canada.
 31. Pudenz K. *Der neue BMW 7er mit Carbon Core: 130 kg leichter*. Springer Professional, 2015. Available from: <http://www.springerprofessional.de/der-neue-bmw-7er-mit-carbon-core-130-kg-leichter/5691238.html>. Accessed on: 01.07.2015.
 32. Moniruzzaman M. *Aircraft Weight Reduction through Materials Innovation*. SABIC Innovative Plastics, 2011. Available from: <http://www.pod-sabic-ip.com/KBAM/Reflection/Assets/20595.pdf>. Accessed on: 10.12.2013.
 33. *Carbon fibre Composite Brackets made from VICTREX® PEEK Polymer Reduce Fuel Costs on Next Generation Aircraft*. Victrex, 2013. Available from: <http://www.victrex.com/en/news/2013/03/936>. Accessed on: 01.07.2015.
 34. Caliendo H. *New bracket technology introduced to the aircraft industry*. *Composites World*, 2015. Available from: <http://www.compositesworld.com/news/new-bracket-technology-introduced-to-the-aircraft-industry>. Accessed on: 02.07.2015.
 35. *Aerospace: The economic beauty of achieving more with less*. Victrex, 2015. Available from: <http://www.victrex.com/en/news/2015/04/egmond-fusible-core-technology>. Accessed on: 01.07.2015.
 36. Kweon J.-H., et al., *Failure of carbon composite-to-aluminum joints with combined mechanical fastening and adhesive bonding*. *Composite Structures*, 2006. Vol. 75(1-4): p. 192-198.
-

-
37. Podlesak F., et al., *Spin-Blind-Riveting (SBR) - New technology to join metal with reinforced Plastic*, in *67th IIW Annual Assembly and International Conference*. 2014: Seoul, South Korea.
 38. Kolesnikov B., Herbeck L., and Fink A., *CFRP/titanium hybrid material for improving composite bolted joints*. *Composite Structures*, 2008. Vol. 83(4): p. 368-380.
 39. Camanho P.P., et al., *Hybrid titanium-CFRP laminates for high-performance bolted joints*. *Composites Part A: Applied Science and Manufacturing*, 2009. Vol. 40(12): p. 1826-1837.
 40. Baldan A., *Adhesively-bonded joints and repairs in metallic alloys, polymers and composite materials: Adhesives, adhesion theories and surface pretreatment*. *Journal of Materials Science*, 2004. Vol. 39(1): p. 1-49.
 41. Seong M.-S., et al., *A parametric study on the failure of bonded single-lap joints of carbon composite and aluminum*. *Composite Structures*, 2008. Vol. 86(1-3): p. 135-145.
 42. Goushegir S.M., dos Santos J.F., and Amancio-Filho S.T., *Friction Spot Joining of aluminum AA2024/carbon-fiber reinforced poly(phenylene sulfide) composite single lap joints: Microstructure and mechanical performance*. *Materials & Design*, 2014. Vol. 54: p. 196-206.
 43. Nagatsuka K., et al., *Direct joining of carbon-fiber-reinforced plastic to an aluminum alloy using friction lap joining*. *Composites Part B: Engineering*, 2015. Vol. 73: p. 82-88.
 44. Mitschang P., et al., *Induction Heated Joining of Aluminum and Carbon Fiber Reinforced Nylon 66*. *Journal of Thermoplastic Composite Materials*, 2009. Vol. 22(6): p. 767-801.
 45. Mitschang P., Velthuis R., and Didi M., *Induction Spot Welding of Metal/CFRPC Hybrid Joints*. *Advanced Engineering Materials*, 2013. Vol. 15(9): p. 804-813.
 46. Schmeer S., et al., *Experimental and Computational Analysis of Multi-Spot Welded Hybrid Al/CFRP-Structures on Component Level*. *Advanced Engineering Materials*, 2013. Vol. 15(9): p. 868-873.
 47. Schmeer S., et al., *Experimental and Numerical Characterization of Spot Welded Hybrid Al/CFRP-Joints on Coupon Level*. *Advanced Engineering Materials*, 2013. Vol. 15(9): p. 853-860.
 48. Balle F., Wagner G., and Eifler D., *Ultrasonic spot welding of aluminum sheet/carbon fiber reinforced polymer - joints*. *Materialwissenschaft und Werkstofftechnik*, 2007. Vol. 38(11): p. 934-938.
 49. Balle F., Wagner G., and Eifler D., *Ultrasonic Metal Welding of Aluminium Sheets to Carbon Fibre Reinforced Thermoplastic Composites*. *Advanced Engineering Materials*, 2009. Vol. 11(1-2): p. 35-39.
 50. Wagner G., Balle F., and Eifler D., *Ultrasonic Welding of Aluminum Alloys to Fiber Reinforced Polymers*. *Advanced Engineering Materials*, 2013. Vol. 15(9): p. 792-803.
 51. Balakrishnan K., Kang H., and Mallick P., *Joining Aluminum to Nylon Using Frictional Heat*. *SAE Technical Paper 2007-01-1701*, 2007.
 52. Yusof F., et al., *Utilising friction spot joining for dissimilar joint between aluminium alloy (A5052) and polyethylene terephthalate*. *Science and Technology of Welding and Joining*, 2012. Vol. 17(7): p. 544-549.
 53. Amancio-Filho S.T. and dos Santos J.F., *US 8,567,032 B2: Method for joining metal and plastic workpieces*. 2013
-

-
54. Junior W.S., et al., *Friction spot welding of PMMA with PMMA/silica and PMMA/silica-g-PMMA nanocomposites functionalized via ATRP*. *Polymer*, 2014. Vol. 55(20): p. 5146-5159.
 55. Junior W.S., et al., *Feasibility study of friction spot welding of dissimilar single-lap joint between poly(methyl methacrylate) and poly(methyl methacrylate)-SiO₂ nanocomposite*. *Materials & Design*, 2014. Vol. 64: p. 246-250.
 56. Fortunato A., et al., *Hybrid metal-plastic joining by means of laser*. *International Journal of Material Forming*, 2010. Vol. 3(1): p. 1131-1134.
 57. Bergmann J.P. and Stambke M., *Potential of Laser-manufactured Polymer-metal hybrid Joints*. *Physics Procedia*, 2012. Vol. 39: p. 84-91.
 58. Katayama S., Kawahito Y., and Mizutani M., *Latest Progress in Performance and Understanding of Laser Welding*. *Physics Procedia*, 2012. Vol. 39: p. 8-16.
 59. Katayama S. and Kawahito Y., *Laser direct joining of metal and plastic*. *Scripta Materialia*, 2008. Vol. 59(12): p. 1247-1250.
 60. Fuchs A.N., et al., *Laser-generated Macroscopic and Microscopic Surface Structures for the Joining of Aluminum and Thermoplastics using Friction Press Joining*. *Physics Procedia*, 2014. Vol. 56: p. 801-810.
 61. Wirth F.X., et al., *Analysis of the Bonding Behavior and Joining Mechanism during Friction Press Joining of Aluminum Alloys with Thermoplastics*. *Procedia CIRP*, 2014. Vol. 18: p. 215-220.
 62. Liu F.C., Liao J., and Nakata K., *Joining of metal to plastic using friction lap welding*. *Materials & Design*, 2014. Vol. 54: p. 236-244.
 63. Khodabakhshi F., et al., *Microstructure-property characterization of a friction-stir welded joint between AA5059 aluminum alloy and high density polyethylene*. *Materials Characterization*, 2014. Vol. 98: p. 73-82.
 64. Ratanathavorn W. and Melander A., *Dissimilar joining between aluminium alloy (AA 6111) and thermoplastics using friction stir welding*. *Science and Technology of Welding and Joining*, 2015. Vol. 20(3): p. 222-228.
 65. Grujicic M., et al., *An overview of the polymer-to-metal direct-adhesion hybrid technologies for load-bearing automotive components*. *Journal of Materials Processing Technology*, 2008. Vol. 197(1-3): p. 363-373.
 66. Zoellner O.J. and Evans J.A. *Plastic-metal hybrid: A new development in the injection molding technology*. in *SPE ANTEC 2002*. 2002. San Francisco, USA: Society of Plastics Engineers.
 67. Grujicic M., et al., *The Potential of a Clinch-Lock Polymer Metal Hybrid Technology for Use in Load-Bearing Automotive Components*. *Journal of Materials Engineering and Performance*, 2009. Vol. 18(7): p. 893-902.
 68. Paul H., Luke M., and Henning F., *Combining mechanical interlocking, force fit and direct adhesion in polymer-metal-hybrid structures – Evaluation of the deformation and damage behavior*. *Composites Part B: Engineering*, 2015. Vol. 73: p. 158-165.
 69. Gerstmann T. and Awiszus B., *Recent developments in flat-clinching*. *Computational Materials Science*, 2014. Vol. 81: p. 39-44.
 70. Lambiase F. and Di Ilio A., *Mechanical clinching of metal-polymer joints*. *Journal of Materials Processing Technology*, 2015. Vol. 215: p. 12-19.
-

-
71. Fratini L. and Ruisi V., *Self-piercing riveting for aluminium alloys-composites hybrid joints*. The International Journal of Advanced Manufacturing Technology, 2009. Vol. 43(1-2): p. 61-66.
 72. Settineri L., Atzeni E., and Ippolito R., *Self piercing riveting for metal-polymer joints*. International Journal of Material Forming, 2010. Vol. 3(SUPPL. 1): p. 995-998.
 73. Di Franco G., Fratini L., and Pasta A., *Analysis of the mechanical performance of hybrid (SPR/bonded) single-lap joints between CFRP panels and aluminum blanks*. International Journal of Adhesion and Adhesives, 2013. Vol. 41: p. 24-32.
 74. Rivtac. *Hochgeschwindigkeits-Bolzensetzen. Das innovative Fügeverfahren*. Böllhoff Gruppe, Available from: <http://www.boellhoff.de/static/pdf/downloadcenter/DE/RIVTAC-DE-6810.pdf>. Accessed on: 30.06.2015.
 75. Meschut G., et al., *Innovative joining technologies for multi-material structures*. Welding in the World, 2014. Vol. 58(1): p. 65-75.
 76. Amancio-Filho S.T., *Friction Riveting: development and analysis of a new joining technique for polymer-metal multi-materials structures*. Ph.D. Dissertation. Technische Universität Hamburg-Harburg, Germany. 2007.
 77. Amancio-Filho S.T., Beyer M., and dos Santos J.F., *US 7,575,149 B2: Method of connecting a metallic bolt to a plastic workpiece*. 2009
 78. Amancio-Filho S.T., *Henry Granjon Prize Competition 2009 Winner Category A: "Joining and Fabrication Technology" Friction Riveting: development and analysis of a new joining technique for polymer-metal multi-material structures*. Welding in the World, 2011. Vol. 55(1-2): p. 13-24.
 79. Rodrigues C.F., et al., *FricRiveting of aluminum 2024-T351 and polycarbonate: Temperature evolution, microstructure and mechanical performance*. Journal of Materials Processing Technology, 2014. Vol. 214(10): p. 2029-2039.
 80. Blaga L., et al., *Friction Riveting of glass-fibre-reinforced polyetherimide composite and titanium grade 2 hybrid joints*. Materials & Design, 2013. Vol. 50: p. 825-829.
 81. Altmeyer J., *Fundamental characteristics of friction riveted multi-material joints*. Technische Universität Hamburg-Harburg, Germany. 2015.
 82. Borba N.Z., et al. *Friction Riveting of pultruded thermoset glass fiber reinforced polyester composite and Ti6Al4V hybrid joints*. in SPE ANTEC 2014. 2014. Las Vegas, USA: Society of Plastics Engineers.
 83. Rotheiser J., *Joining of Plastics: Handbook for Designers and Engineers*. 1999, Munich: Carl Hanser Verlag.
 84. Endemann U., Glaser S., and Völker M., *Strong joint between plastic and metal*. Kunststoffe plast europe, 2002. Vol. 92(11): p. 38-40.
 85. Eagles D.W., *Plastic hot air stake assembly*. Assembly Automation, 2000. Vol. 20(3): p. 205-214.
 86. Abibe A.B. and Amancio-Filho S.T. *Staking-based Joining Technologies*. Lecture: Joining of Polymer-Metal Lightweight Structures, Technische Universität Hamburg-Harburg. 2015.
 87. Amancio-Filho S.T., Abibe A.B., and Dos Santos J.F., *Joining: Mechanical Fastening of Polymers, Composites, and Polymer-Metal Hybrid Structures*, in *Wiley Encyclopedia of Composites*, Nicolais L. and Borzacchiello A., Editors. 2012, John Wiley & Sons, Inc.

-
88. Brunetti M. *Joining: The Heat Is On*. 2007. Available from: <http://www.appliancedesign.com/articles/90893-joining-the-heat-is-on>. Accessed on: 19.08.2013.
 89. Dealy J.M. and Wissbrun K.F., *Melt Rheology and Its Role in Plastics Processing: Theory and Applications*. 1995, London: Chapman & Hall.
 90. Brown N., *Yield Behaviour of Polymers*, in *Failure of Plastics*, Brostow W. and Corneliussen R.D., Editors. 1986, Carl Hanser Verlag: Munich. p. 98-118.
 91. *Future of safety*. PHASA, 2012. Available from: <http://www.phasa.co.uk/itemtemplate/future-of-safety>. Accessed on: 02.07.2015.
 92. *Exterior Automotive Plastic Assembly*. PHASA, 2012. Available from: <http://www.phasa.co.uk/applications/exterior>. Accessed on: 02.07.2015.
 93. Leaversuch R.D. *Plastic-Metal Hybrids Make Headway On and Off the Road* Plastics Technology, 2003. Available from: <http://www.ptonline.com/articles/plastic-metal-hybrids-make-headway-on-and-off-the-road>. Accessed on: 29.06.2015.
 94. Sprovieri J., *Quality at stake*, in *Assembly*. 2005.
 95. Brunnecker F., Geiger R., and Pump C., *Riveting with Light*. Kunststoffe International, 2010. Vol. 10: p. 141-144.
 96. Reed B., *Shedding Light on the Staking Process*, in *Assembly*. 2014.
 97. Potente H., *Fügen von Kunststoffen: Grundlagen, Verfahren, Anwendung*, ed. Potente H. 2004, Munich: Carl Hanser Verlag.
 98. Yeh H.J., Schott C.L., and Park J.B. *Experimental study on hot-air cold staking of PC, PC/ABS and acetal samples*. in *SPE ANTEC 1998*. 1998. Atlanta, USA: Society of Plastics Engineers.
 99. Hahn O. and Finkeldey C., *Warmluftnieten von langglasfaserverstärkten Thermoplasten mit beschichteten metallischen Werkstoffen*. Vol. 63. 2004, Aachen: Shaker Verlag.
 100. Lanser M., Miller R., and Van Klompenberg A., *US 6,296,470 B1: Heat staking head with radiant heat source*. 2001
 101. Beute S. and Reed B., *Staking Plastic with Infrared Light*, in *SPE TopCon 2008*. 2008, Society of Plastics Engineers.
 102. Beute S. *Infrastake - Staking At The Speed Of Light*. in *SPE ANTEC 2009*. 2009. Chicago, USA: Society of Plastics Engineers.
 103. Grewell D.A., *Infrared and Laser Welding*, in *Plastics and composites welding handbook*, Grewell D.A., Benatar A., and Park J.B., Editors. 2003, Carl Hanser Verlag: Munich. p. 271-312.
 104. Troughton M.J., *Handbook of plastics joining: a practical guide*. 2 ed. 2008, Norwych: William Andrew.
 105. Hahn O. and Finkeldey C., *Ultrasonic Riveting and Hot-Air-Sticking of Fiber-Reinforced Thermoplastics*. *Journal of Thermoplastic Composite Materials*, 2003. Vol. 16(6): p. 521-528.
 106. Riehm U., *DE 10 2011 054 358 A1: Umformverfahren und Vorrichtung zur Durchführung des Verfahrens*. 2013
 107. Brückner E., et al., *Material and process influences during the riveting of technical plastics*. *Joining Plastics - Fügen von Kunststoffen*, 2013. Vol. 2: p. 98-103.
-

-
108. Brückner E., Friederich S., and Gehde M. *Ultrasonic Upsetting: A new method of Ultrasonic Staking to join hybrid material combinations*. in *SPE ANTEC 2015*. 2015. Orlando, USA: Society of Plastics Engineers.
 109. Brückner E., et al., *Ultrasonic upsetting - Innovative process strategy to join hybrid material combinations*. *Joining Plastics - Fügen von Kunststoffen*, 2015. Vol. 9(1): p. 40-47.
 110. Gude M., et al., *Development of novel form-locked joints for textile reinforced thermoplastics and metallic components*. *Journal of Materials Processing Technology*, 2015. Vol. 216: p. 140-145.
 111. Gude M., et al., *Thermoclinching—a novel joining process for lightweight structures in multi-material design*. *Composites Theory and Practice*, 2014. Vol. 14(3): p. 128–133.
 112. Abibe A.B., *Desenvolvimento de união de multimateriais através de "Rebitagem por Injeção" (Injection Clinching Joining)*. UFSCar, Brazil. 2011.
 113. Abibe A.B., et al., *Mechanical and failure behaviour of hybrid polymer-metal staked joints*. *Materials and Design*, 2013. Vol. 46: p. 338-347.
 114. Abibe A.B., et al., *Patent application EP14182938.2: A method for joining a plastic workpiece to a further workpiece*. 2014
 115. Abibe A.B., Dos Santos J.F., and Amancio-Filho S.T. *Friction Staking: a novel staking joining method for hybrid structures*. in *SPE ANTEC 2014*. 2014. Las Vegas, USA: Society of Plastics Engineers.
 116. Zhai Y., et al., *An experimental study on the effect of bolt-hole clearance and bolt torque on single-lap, countersunk composite joints*. *Composite Structures*, 2015. Vol. 127: p. 411-419.
 117. Rooney P. and Grewell D., *Spin Welding*, in *Plastics and Composites Welding Handbook*, Grewell D., Benatar A., and Park J.B., Editors. 2003, Carl Hanser Verlag: Munich. p. 229-248.
 118. Stokes V.K., *Analysis of the friction (spin)-welding process for thermoplastics*. *Journal of Materials Science*, 1988. Vol. 23(8): p. 2772-2785.
 119. Stokes V.K., *Vibration welding of thermoplastics. Part II: Analysis of the welding process*. *Polymer Engineering & Science*, 1988. Vol. 28(11): p. 728-739.
 120. Steijn R.P., *Friction and Wear*, in *Failure of Plastics*, Brostow W. and Corneliussen R.D., Editors. 1986, Carl Hanser Verlag: Munich. p. 357-392.
 121. Potente H. and Reinke M., *Welding parameters and properties of polyolefin parts*. *Plastics and Rubber Processing and Applications*, 1981. Vol. 1: p. 149-60.
 122. Sawai T., et al., *Evaluation of joint strength of friction welded carbon steel by heat input*. *Welding International*, 2002. Vol. 16(6): p. 432-441.
 123. Su P., et al., *Energy utilisation and generation during friction stir spot welding*. *Science and Technology of Welding and Joining*, 2006. Vol. 11(2): p. 163-169.
 124. Altmeyer J., dos Santos J.F., and Amancio-Filho S.T., *Effect of the friction riveting process parameters on the joint formation and performance of Ti alloy/short-fibre reinforced polyether ether ketone joints*. *Materials & Design*, 2014. Vol. 60: p. 164-176.
 125. Elias H.-G., *An introduction to plastics*. 2nd ed. 2003, Weinheim: Wiley-VCH.

-
126. Bauwens J.-C., *Physical Aging: Relation between free Volume and Plastic Deformation*, in *Failure of Plastics*, Brostow W. and Corneliussen R.D., Editors. 1986, Carl Hanser Verlag: Munich. p. 235-258.
 127. Rueda D.R., et al., *Order in the amorphous state of poly(ethylene terephthalate) as revealed by microhardness: Creep behavior and physical aging*. International Journal of Polymeric Materials and Polymeric Biomaterials, 2002. Vol. 51(10): p. 897-908.
 128. Flores A., Ania F., and Baltá-Calleja F.J., *From the glassy state to ordered polymer structures: A microhardness study*. Polymer, 2009. Vol. 50(3): p. 729-746.
 129. Brydson J.A., *Plastics Materials (Seventh Edition)*. 1999, Oxford: Butterworth-Heinemann.
 130. Wool R.P., Yuan B.-L., and McGarel O.J., *Welding of Polymer Interfaces*. Polymer Engineering and Science, 1989. Vol. 29(19): p. 1340-1367.
 131. Strobl G., *The Physics of Polymers*. 3rd ed. 2007, Berlin: Springer.
 132. Kim Y.H. and Wool R.P., *A theory of healing at a polymer-polymer interface*. Macromolecules, 1983. Vol. 16(7): p. 1115-1120.
 133. Boiko Y.M. and Prud'homme R.E., *Strength Development at the Interface of Amorphous Polymers and Their Miscible Blends, below the Glass Transition Temperature*. Macromolecules, 1998. Vol. 31(19): p. 6620-6626.
 134. Boiko Y.M., *On the formation of topological entanglements during the contact of glassy polymers*. Colloid and Polymer Science, 2012. Vol. 290(12): p. 1201-1206.
 135. Boiko Y.M., *Interdiffusion of polymers with glassy bulk*. Colloid and Polymer Science, 2011. Vol. 289(17-18): p. 1847-1854.
 136. Johnson R.O. and Burlhis H.S., *Polyetherimide: A new high-performance thermoplastic resin*. Journal of Polymer Science: Polymer Symposia, 1983. Vol. 70(1): p. 129-143.
 137. Carroccio S., Puglisi C., and Montaudo G., *Polyetherimide*, in *Handbook of Engineering and Specialty Thermoplastics*, Thomas S. and Visakh P.M., Editors. 2012, Scrivener Publishing LLC: Salem, MT. p. 79-110.
 138. Biron M., *Thermoplastics and Thermoplastic Composites*. 2007, Oxford: Elsevier.
 139. McKeen L.W., *Chapter 7 - Polyimides*, in *Fatigue and Tribological Properties of Plastics and Elastomers (Second Edition)*, McKeen L.W., Editor. 2010, William Andrew Publishing: Oxford. p. 149-173.
 140. Merdas I., ThomINETTE F., and Verdu J., *Humid aging of polyetherimide. I. Water sorption characteristics*. Journal of Applied Polymer Science, 2000. Vol. 77(7): p. 1439-1444.
 141. Merdas I., ThomINETTE F., and Verdu J., *Humid aging of polyetherimide. II. Consequences of water absorption on thermomechanical properties*. Journal of Applied Polymer Science, 2000. Vol. 77(7): p. 1445-1451.
 142. Sepe M.P. *The effect of absorbed moisture on the elevated temperature properties of polyetherimide*. in *SPE ANTEC 2004*. 2004. Chicago, USA: Society of Plastics Engineers.
 143. Kuroda S.-i., et al., *Degradation of aromatic polymers—I. Rates of crosslinking and chain scission during thermal degradation of several soluble aromatic polymers*. European Polymer Journal, 1989. Vol. 25(1): p. 1-7.
-

-
144. Augh L., Gillespie J.W., and Fink B.K., *Degradation of Continuous Carbon Fiber Reinforced Polyetherimide Composites During Induction Heating*. Journal of Thermoplastic Composite Materials, 2001. Vol. 14(2): p. 96-115.
 145. Amancio-Filho S.T., et al., *Thermal degradation of polyetherimide joined by friction riveting (FricRiveting). Part I: Influence of rotation speed*. Polymer Degradation and Stability, 2008. Vol. 93(8): p. 1529-1538.
 146. Ageorges C. and Ye L., *Resistance Welding of Metal/Thermoplastic Composite Joints*. Journal of Thermoplastic Composite Materials, 2001. Vol. 14(6): p. 449-475.
 147. *Ultem* and Siltem* resins - Products and markets guide*. SABIC Innovative Plastics, 2008. Available from: http://www.pod-sabic-ip.com/KBAM/Reflection/Assets/Thumbnail/14106_13.pdf. Accessed on: 24.06.2015.
 148. Stokes V.K., *Vibration welding of thermoplastics. Part IV: Strengths of poly(butylene terephthalate), polyetherimide, and modified polyphenylene oxide butt welds*. Polymer Engineering & Science, 1988. Vol. 28(15): p. 998-1008.
 149. Stokes V.K., *A phenomenological study of the hot-tool welding of thermoplastics Part 3. Polyetherimide*. Polymer, 2001. Vol. 42(2): p. 775-792.
 150. Hou M., Ye L., and Mai Y.W., *An Experimental Study of Resistance Welding of Carbon Fibre Fabric Reinforced Polyetherimide (CF Fabric/PEI) Composite Material*. Applied Composite Materials, 1999. Vol. 6(1): p. 35-49.
 151. Hou M., et al., *Resistance welding of carbon fibre reinforced thermoplastic composite using alternative heating element*. Composite Structures, 1999. Vol. 47(1-4): p. 667-672.
 152. Dubé M., et al., *Fatigue performance characterisation of resistance-welded thermoplastic composites*. Composites Science and Technology, 2008. Vol. 68(7-8): p. 1759-1765.
 153. Blaga L., et al., *Friction Riveting (FricRiveting) as a new joining technique in GFRP lightweight bridge construction*. Construction and Building Materials, 2015. Vol. 80: p. 167-179.
 154. Smock D. *The odd story of SABIC's Ultem shortage*. Updated on 08.12.2014 (accessed on 06.07.2015); Available from: <http://www.themoldingblog.com/2014/12/08/the-odd-story-of-sabics-ultem-shortage/>.
 155. Hess H. *SABIC Announces Ultem Resin Shortage Q2 2015*. Updated on 24.06.2015 (accessed on 06.07.2015); Available from: <http://newswire.net/newsroom/pr/00086184-sabic-ultem-resin-shortage-sheet-rod.html>.
 156. *Composites Selector Guide*. TenCate, 2015. Available from: http://www.tencate.com/emea/Images/TCAC_CompositeSelectGuide_V7_081115_Web_tcm28-180.pdf. Accessed on: 06.07.2015.
 157. *Overcoming elevated temperatures in a compact design space: Automotive case history*. SABIC Innovative Plastics, 2014. Available from: http://www.pod-sabic-ip.com/KBAM/Reflection/Assets/Thumbnail/23254_2.pdf. Accessed on: 24.06.2015.
 158. Birol Y., *The effect of processing and Mn content on the T5 and T6 properties of AA6082 profiles*. Journal of Materials Processing Technology, 2006. Vol. 173(1): p. 84-91.

-
159. Koumoulos E.P., et al., *Nanomechanical properties of friction stir welded AA6082-T6 aluminum alloy*. Materials Science and Engineering: B, 2011. Vol. 176(19): p. 1585-1589.
 160. Benson S., Downes J., and Dow R.S., *Load shortening characteristics of marine grade aluminium alloy plates in longitudinal compression*. Thin-Walled Structures, 2013. Vol. 70: p. 19-32.
 161. *Properties and Selection: Nonferrous Alloys and Special-Purpose Materials*. ASM Handbook. 1995: ASM International.
 162. Cabibbo M., et al., *Double side friction stir welding of AA6082 sheets: Microstructure and nanoindentation characterization*. Materials Science and Engineering: A, 2014. Vol. 590: p. 209-217.
 163. *Heat treating*. ASM Handbook. 1995: ASM International.
 164. Edwards G.A., et al., *The precipitation sequence in Al-Mg-Si alloys*. Acta Materialia, 1998. Vol. 46(11): p. 3893-3904.
 165. Holmestad R., et al., *Characterization and structure of precipitates in 6xxx Aluminium Alloys*. Journal of Physics: Conference Series, 2012. Vol. 371(1): p. 012082.
 166. Marioara C.D., et al., *Atomic model for GP-zones in a 6082 Al-Mg-Si system*. Acta Materialia, 2001. Vol. 49(2): p. 321-328.
 167. El-Danaf E.A. and El-Rayes M.M., *Microstructure and mechanical properties of friction stir welded 6082 AA in as welded and post weld heat treated conditions*. Materials & Design, 2013. Vol. 46: p. 561-572.
 168. Borsellino C., Di Bella G., and Ruisi V. *Effect of chemical etching on adhesively bonded aluminum AA6082*. in *Key Engineering Materials*. 2007. Trans Tech Publ.
 169. Borsellino C., Di Bella G., and Ruisi V.F., *Adhesive joining of aluminium AA6082: The effects of resin and surface treatment*. International Journal of Adhesion and Adhesives, 2009. Vol. 29(1): p. 36-44.
 170. Pereira A.M., et al., *Effect of process parameters on the strength of resistance spot welds in 6082-T6 aluminium alloy*. Materials & Design, 2010. Vol. 31(5): p. 2454-2463.
 171. Lucchetta G., Marinello F., and Bariani P.F., *Aluminum sheet surface roughness correlation with adhesion in polymer metal hybrid overmolding*. CIRP Annals - Manufacturing Technology, 2011. Vol. 60(1): p. 559-562.
 172. Lambiase F., *Joinability of different thermoplastic polymers with aluminium AA6082 sheets by mechanical clinching*. The International Journal of Advanced Manufacturing Technology, 2015: p. 1-12.
 173. Traglia Amancio Filho S., Dos Santos J.F., and Beyer M., *DE 10 2005 057 891 B4: Verfahren und Vorrichtung zum Verbinden eines Kunststoff-Werkstücks mit einem weiteren Werkstück*. 2007
 174. Hirasawa S., et al., *Analysis of effect of tool geometry on plastic flow during friction stir spot welding using particle method*. Journal of Materials Processing Technology, 2010. Vol. 210(11): p. 1455-1463.
 175. Lin Y.C., Liu J.J., and Lin B.Y., *Effect of Tool Geometry on Strength of Friction Stir Spot Welded Aluminum Alloys*. Advanced Materials Research, 2012. Vol. 579: p. 109-117.
 176. Bilici M.K. and Yüklér A.İ., *Influence of tool geometry and process parameters on macrostructure and static strength in friction stir spot welded polyethylene sheets*. Materials & Design, 2012. Vol. 33: p. 145-152.
-

-
177. Mu L., et al., *The effect of thermal conductivity and friction coefficient on the contact temperature of polyimide composites: Experimental and finite element simulation*. Tribology International, 2012. Vol. 53: p. 45-52.
 178. *Aluminium Alloy 6082 - T6~T651*. Aalco Metals Ltd, 2014. Available from: http://www.aalco.co.uk/datasheets/Aalco-Metals-Ltd_Aluminium-Alloy-6082-T6T651-Plate_148.pdf.ashx. Accessed on: 10.01.2014.
 179. *Duratron U1000 PEI*. Quadrant Plastics, 2011. Available from: http://www.quadrantplastics.com/fileadmin/quadrant/documents/QEPP/EU/Product_Data_Sheets_PDF/AEP/Duratron_U1000_PEI_PDS_E_28042011.pdf. Accessed on: 09.07.2014.
 180. Mutter N.J., *Characterization of Dynamic and Static Mechanical Behavior of Polyetherimide*. University of Central Florida, USA. 2012.
 181. *RTP 2187 Polyetherimide (PEI) Carbon Fiber*. RTP Company, 2005. Available from: <http://web.rtpcompany.com/info/data/2100/RTP2187.htm>. Accessed on: 20.10.2011.
 182. 316L, in *Heat Treater's Guide: Practices and Procedures for Irons and Steels*. 1995, ASM International. p. 748-749.
 183. *Properties and Selection: Irons, Steels, and High-Performance Alloys*. ASM Handbook. 1995: ASM International.
 184. Sônego M., et al., *Friction-based Injection Clinching Joining (F-ICJ) of glass-fiber-reinforced PA66 and aluminum hybrid structures*, in *21° Congresso Brasileiro de Ciência e Engenharia de Materiais*. 2014: Cuiabá, Brazil.
 185. Sônego M. *Internal Report*. Helmholtz-Zentrum Geesthacht, 2013.
 186. Oliveira P.H.F., *Estudo das propriedades e desempenho mecânico de juntas soldadas por fricção pontual de poli (metacrilato de metila) (PMMA)*. Master Thesis. UFSCar, Brazil. 2012.
 187. Schell N., et al., *The High Energy Materials Science Beamline at PETRA III*. Materials Science Forum, 2008. Vol. 571-572: p. 261-266.
 188. Huesman R., *The effects of a finite number of projection angles and finite lateral sampling of projections on the propagation of statistical errors in transverse section reconstruction*. Physics in medicine and biology, 1977. Vol. 22(3): p. 511.
 189. Schindelin J., et al., *Fiji: an open-source platform for biological-image analysis*. Nat Meth, 2012. Vol. 9(7): p. 676-682.
 190. Parlevliet P.P., Bersee H.E.N., and Beukers A., *Residual stresses in thermoplastic composites—A study of the literature—Part II: Experimental techniques*. Composites Part A: Applied Science and Manufacturing, 2007. Vol. 38(3): p. 651-665.
 191. Ajovalasit A., Petrucci G., and Scafidi M., *Review of RGB photoelasticity*. Optics and Lasers in Engineering, 2015. Vol. 68: p. 58-73.
 192. Ehrenstein G.W., Riedel G., and Trawiel P., *Thermal Analysis of Plastics: Theory and Practice*. 2004, Munich: Carl Hanser Verlag.
 193. Baltá Calleja F.J. and Fakirov S., *Microhardness of polymers*. 2007, New York: Cambridge University Press.
 194. ASTM, *E384-10e1: Standard Test Method for Knoop and Vickers Hardness of Materials*. 2010.
-

-
195. ASTM, *D5961-10: Standard Test Method for Bearing Response of Polymer Matrix Composite Laminates*. 2010.
 196. DIN, *DIN EN ISO 14272: Probenmaße und Verfahren für die Kopfzugprüfung an Widerstandspunkt- und Buckelschweißungen mit geprägten Buckeln*. 2002.
 197. Montgomery D.C. and Runger G.C., *Applied statistics and probability for engineers*. 3rd ed. 2003: John Wiley & Sons.
 198. Venter A. and Maxwell S.E., 6 - *Issues in the Use and Application of Multiple Regression Analysis*, in *Handbook of Applied Multivariate Statistics and Mathematical Modeling*, Tinsley H.E.A. and Brown S.D., Editors. 2000, Academic Press: San Diego. p. 151-182.
 199. Costa N.R., Lourenço J., and Pereira Z.L., *Desirability function approach: A review and performance evaluation in adverse conditions*. *Chemometrics and Intelligent Laboratory Systems*, 2011. Vol. 107(2): p. 234-244.
 200. Harrington E.C., *The desirability function*. *Industrial quality control*, 1965. Vol. 21(10): p. 494-498.
 201. Paz G. *Internal Report*. Helmholtz-Zentrum Geesthacht, 2014.
 202. Ettles C.M.M. and Shen J.H., *The Influence of Frictional Heating on the Sliding Friction of Elastomers and Polymers*. *Rubber Chemistry and Technology*, 1988. Vol. 61(1): p. 119-136.
 203. Schmidt H. and Hattel J. *CFD modelling of the shear layer around the tool probe in Friction Stir Welding*. in *Friction Stir Welding and Processing III - Proceedings of a Symposium sponsored by the Shaping and Forming Committee of (MPMD) of the Minerals, Metals and Materials Society, TMS*. 2005.
 204. Stachurski Z.H., *Deformation mechanisms and yield strength in amorphous polymers*. *Progress in Polymer Science*, 1997. Vol. 22(3): p. 407-474.
 205. Kausch H.-H., *Intersegmental Interactions and Chain Scission*, in *Failure of Plastics*, Brostow W. and Corneliussen R.D., Editors. 1986, Carl Hanser Verlag: Munich. p. 84-97.
 206. Threadgill P.L., et al., *Friction stir welding of aluminium alloys*. *International Materials Reviews*, 2009. Vol. 54(2): p. 49-93.
 207. Zuanetti B., *Characterization of polyetherimide under static, dynamic, and multiple impact conditions*. University of Central Florida, USA. 2013.
 208. Brown N. and Ward I.M., *Load drop at the upper yield point of a polymer*. *Journal of Polymer Science Part A-2: Polymer Physics*, 1968. Vol. 6(3): p. 607-620.
 209. Struik L.C.E., *Physical Aging : Influence on the Deformation Behavior of Amorphous Polymers*, in *Failure of Plastics*, Brostow W. and Corneliussen R.D., Editors. 1986, Carl Hanser Verlag: Munich. p. 209-234.
 210. Arruda E.M. and Boyce M.C., *Evolution of plastic anisotropy in amorphous polymers during finite straining*. *International Journal of Plasticity*, 1993. Vol. 9(6): p. 697-720.
 211. Tabor D., *The hardness of solids*. *Review of Physics in Technology*, 1970. Vol. 1(3): p. 145.
 212. Redner A.S. and Hoffman B.R., *Measuring residual stress in transparent plastics*. *Medical plastics: degradation resistance & failure analysis*, 1998: p. 45-50.
 213. Scafidi M., et al., *Review of photoelastic image analysis applied to structural birefringent materials: glass and polymers*. *Optical Engineering*, 2015. Vol. 54(8): p. 081206-081206.
-

-
214. Ajovalasit A., Barone S., and Petrucci G., *A review of automated methods for the collection and analysis of photoelastic data*. Journal of Strain Analysis for Engineering Design, 1998. Vol. 33(2): p. 75-91.
 215. Ajovalasit A., Petrucci G., and Scafidi M., *RGB Photoelasticity: Review and Improvements*. Strain, 2010. Vol. 46(2): p. 137-147.
 216. Chen X., Yan J., and Karlsson A.M., *On the determination of residual stress and mechanical properties by indentation*. Materials Science and Engineering: A, 2006. Vol. 416(1-2): p. 139-149.
 217. Xiao L., Ye D., and Chen C., *A further study on representative models for calculating the residual stress based on the instrumented indentation technique*. Computational Materials Science, 2014. Vol. 82: p. 476-482.
 218. Santa Cruz C., et al., *Plastic deformation in polyethylene crystals studied by microindentation hardness*. Philosophical Magazine A, 1993. Vol. 68(1): p. 209-224.
 219. Hutchinson J.M., *Physical aging of polymers*. Progress in Polymer Science, 1995. Vol. 20(4): p. 703-760.
 220. Baltá Calleja F.J., Flores A., and Michler G.H., *Microindentation studies at the near surface of glassy polymers: Influence of molecular weight*. Journal of Applied Polymer Science, 2004. Vol. 93(4): p. 1951-1956.
 221. Belana J., et al., *Physical ageing studies in polyetherimide ULTEM 1000*. Polymer International, 1998. Vol. 46(1): p. 29-32.
 222. *ULTEM Resin 1000*. SABIC Innovative Plastics, 2013. Available from: <https://www.sabic-ip.com/gepapp/eng/datasheetinter/dswinter>. Accessed on: 25.03.2013.
 223. Low I.M., *Effects of load and time on the hardness of a viscoelastic polymer*. Materials Research Bulletin, 1998. Vol. 33(12): p. 1753-1758.
 224. Suwanprateeb J., *A Comparison of Different Methods in Determining Load- and Time-Dependence of Vickers Hardness in Polymers*. Polymer Testing, 1998. Vol. 17(7): p. 495-506.
 225. Blunt L. and Sullivan P.J., *The measurement of the pile-up topography of hardness indentations*. Tribology International, 1994. Vol. 27(2): p. 69-79.
 226. Sakai M., *Simultaneous estimate of elastic/plastic parameters in depth-sensing indentation tests*. Scripta Materialia, 2004. Vol. 51(5): p. 391-395.
 227. Ovaert T.C., Kim B.R., and Wang J., *Multi-parameter models of the viscoelastic/plastic mechanical properties of coatings via combined nanoindentation and non-linear finite element modeling*. Progress in Organic Coatings, 2003. Vol. 47(3-4): p. 312-323.
 228. Zhang P., Li S.X., and Zhang Z.F., *General relationship between strength and hardness*. Materials Science and Engineering: A, 2011. Vol. 529: p. 62-73.
 229. Bucaille J.L., Felder E., and Hochstetter G., *Mechanical analysis of the scratch test on elastic and perfectly plastic materials with the three-dimensional finite element modeling*. Wear, 2001. Vol. 249(5-6): p. 422-432.
 230. Wei P.J. and Lin J.F., *Determination for elasticity and plasticity from time-dependent nanoindentations*. Materials Science and Engineering: A, 2008. Vol. 496(1-2): p. 90-97.
 231. Tan X., et al., *Characteristics and formation mechanism of porosities in CFRP during laser joining of CFRP and steel*. Composites Part B: Engineering, 2015. Vol. 70: p. 35-43.
-

-
232. Schuetz M., *Friction-based Injection Clinching Joining: Mechanische und röntgentomographische Untersuchung*. CAU Kiel, Germany. 2014.
 233. Tschoepke E.S. *Internal Report*. Helmholtz-Zentrum Geesthacht, 2015.
 234. Kameda J., Yokoyama Y., and Allen T.R., *Strain-controlling mechanical behavior in noncrystalline materials: I: Onset of plastic deformation*. *Materials Science and Engineering: A*, 2007. Vol. 448(1-2): p. 235-241.
 235. Chen C.-J. and Wu C.-Y. *Finite element analysis of solid stud staking design*. in *SPE ANTEC 2012*. 2012. Orlando, USA: Society of Plastics Engineers.
 236. DeSouza R., *Characterization and Guideline Development of the Heat Staking Process*. Bachelor Thesis. University of Toronto, Canada. 2009.
 237. Ekh J., Schön J., and Melin L.G., *Secondary bending in multi fastener, composite-to-aluminium single shear lap joints*. *Composites Part B: Engineering*, 2005. Vol. 36(3): p. 195-208.
 238. Ekh J., *Multi-fastener single-lap joints in composite structures*. Royal Institute of Technology, Sweden. 2006.
 239. Schürmann H., *Konstruieren mit Faser-Kunststoff-Verbunden*. 2007: Springer.
 240. Lee L.H., Mandell J.F., and McGarry F.J., *Fracture toughness and crack instability in tough polymers under plane strain conditions*. *Polymer Engineering & Science*, 1987. Vol. 27(15): p. 1128-1136.
 241. Kim K.-Y. and Ye L., *Effects of thickness and environmental temperature on fracture behaviour of polyetherimide (PEI)*. *Journal of Materials Science*, 2004. Vol. 39(4): p. 1267-1276.
 242. Nimmer R.P. and Woods J.T., *An investigation of brittle failure in ductile, notch-sensitive thermoplastics*. *Polymer Engineering & Science*, 1992. Vol. 32(16): p. 1126-1137.
 243. Hull D. and Owen T.W., *Interpretation of fracture surface features in polycarbonate*. *Journal of Polymer Science: Polymer Physics Edition*, 1973. Vol. 11(10): p. 2039-2055.
 244. Ishikawa M., Ogawa H., and Narisawa I., *Brittle fracture in glassy polymers*. *Journal of Macromolecular Science, Part B*, 1981. Vol. 19(3): p. 421-443.
 245. Agrawal C.M. and Pearsall G.W., *The fracture morphology of fast unstable fracture in polycarbonate*. *Journal of Materials Science*, 1991. Vol. 26(7): p. 1919-1930.
 246. Chang F.-C. and Chu L.-H., *Co-existence of ductile, semi-ductile, and brittle fractures of polycarbonate*. *Journal of Applied Polymer Science*, 1992. Vol. 44(9): p. 1615-1623.
 247. Faupel F., Willecke R., and Thran A., *Diffusion of metals in polymers*. *Materials Science and Engineering: R: Reports*, 1998. Vol. 22(1): p. 1-55.
 248. *Reibschweißköpfe RSM400 RK...* Harms & Wende GmbH & Co KG, 2006.

List of figures

Figure 3-1: Basis of metal-polymer welding-based joining methods.....	7
Figure 3-2: Principles of staking. (a) Pre-assembly; (b) forming; (c) staked joint. Adapted from [86]......	9
Figure 3-3: Examples of automotive staking applications: (a) Volvo XC90 seat assembly [91]; (b) fender/bumper of Renault Trafic minivan family [92]; (c) light truck front end assembly [93]; (d) Bentley Continental GT tail lights [92]......	10
Figure 3-4: Infrastake: (a) joining module; (b) process phases. Blue arrows are compressed air, red arrows are infrared radiation. Adapted from [101], as permitted by Society of Plastics Engineers.	12
Figure 3-5: Ultrasonic upsetting: (a) process steps; (b) surface view of a joint. Adapted from [108], as permitted by Society of Plastics Engineers.....	14
Figure 3-6: (a) Thermoclinching process steps; (b) cross section of a PP-GF joint and fiber orientation. Adapted from [110], with permission from Elsevier.	15
Figure 3-7: (a) Cavity filling in an ICJ process observed through μ CT; (b) electrical-heating ICJ. Adapted from [112]......	16
Figure 3-8: FricStaking: (a) tool set; (b) process steps. Adapted from [86]......	17
Figure 3-9: Conventional stake designs for metal-polymer joints.	17
Figure 3-10: Schematic curve of axial displacement during a friction welding/joining process. Based on [118]......	19
Figure 3-11: Relevant transitions and relaxation times during and after thermomechanical work.	22
Figure 3-12: (a) Chain-end disengagement leading to new chain conformations according to the reptation theory. T_r is the tube renewal time; (b) interdiffusion of chains across an interface. Adapted with permission from [132]. Copyright 1983 American Chemical Society..	23
Figure 3-13: Representation of the chemical structure from PEI.....	24
Figure 4-1: Design of F-ICJ joints with different cavities and tool profiles. (a) flat stake head created with a flat frictional surface tool and chamfer cavities (white arrows); (b) flush stake created with a conical-pin tool and chamfer cavities (white arrows); (c) flush hollow stake created with a conical-pin tool, with mechanical anchoring in the threaded cavities (black arrows) and chamfer cavities (white arrows).....	29
Figure 4-2: Schematic description of F-ICJ process.	30
Figure 4-3: (a) Surface view of an F-ICJ joint; (b) cross section of a stake observed in a stereomicroscope. A process-affected volume (shear layer) can be identified (white dotted line).	31
Figure 4-4: Schematic force-controlled F-ICJ joining diagram and process parameters for (a) a process with friction and consolidation phases (two-phase process); and (b) a process with a friction, forging and consolidation phases (three-phase process).	32
Figure 5-1: Experimental concept of this thesis.	35
Figure 6-1: (a) Microstructure of the AA6082 rolled sheets (Airbus reagent, described in Section 6.3.3); (b) geometry of the through hole in the AA6082 sheets.....	37
Figure 6-2: (a) Overlay picture showing birefringence pattern (right-hand side) and microhardness (left-hand side) distributions in the mid cross section of the stud; (b) geometry of the machined stud.	38

Figure 6-3: (a) As-molded fiber orientation at the PEI-CF specimens; (b) close-up view of the stud microstructure. White arrows represent local fiber orientation.	39
Figure 6-4: (a) Features of an F-ICJ non-consumable tool; (b) tool design used in this work.	41
Figure 6-5: (a) Overview of the RSM400 system along with the monitoring devices; (b) close-up view of the spindle, tool, and the joining specimens in the clamping system.	42
Figure 6-6: (a) RNA gantry system with a friction welding spindle and X-Y moveable table; (b) close-up of a sequential multi-spot joining process.	43
Figure 6-7: Schematics of the temperature measurement setup and snapshot of the camera's view for (a) tool surface temperature; and (b) stake temperature. White areas are the measurement regions; (c) example of the measurement curve.	44
Figure 6-8: (a) Microstructural analysis (MA) specimen; (b) schematic of the cross-section of a joint and the area used for microstructural measurements; (c) example of measurements of the PTMAZ area and the pore area in an F-ICJ joint.	45
Figure 6-9: Transmitted-light optical microscopy with crossed polarizers (CP-TLOM) of the PEI base material. Left-hand image is the original output; right-hand image is filtered for red signal only.	47
Figure 6-10: Local mechanical property measurements. (a) Standard map of five profiles; (b) detailed map; (c) microstructural zones and indentation positions observed with a stereomicroscope for a five-line profile as from (a). The black dotted line follows the shear layer boundary.	48
Figure 6-11: (a) Lap shear (LS) specimen; (b) cross tensile (CT) specimen.	49
Figure 6-12: Calculation of total torque during frictional time from the monitoring process curves.	52
Figure 6-13: (a) Subcomponent specimen geometry. Stud and hole geometry are the same as the coupon specimens; (b) schematic view of pre-assembled subcomponent; (c) joining order.	53
Figure 6-14: Schematic view and snapshot of the temperature measurement region for multi-spot subcomponents.	54
Figure 6-15: Four-point bending of multi-spot subcomponents.	54
Figure 7-1: Surface finishing in joints from: (a) two-phase process; and (b) three-phase process; and birefringence pattern in joints from: (c) two-phase process; and (d) three-phase process. Boundaries of the highly stressed cold-formed zones are marked with square dotted lines (CP-TLOM images).	56
Figure 7-2: (a) Process diagram for a two-phase F-ICJ joining configuration; (b) detail of curves during the friction phase.	57
Figure 7-3: Evolution of joint formation during stud meltdown in the friction phase of a two-phase process configuration; (a) parts before joining; and after a friction time of (b) 500 ms; (c) 1000 ms; (d) 1500 ms (Stages 1-4 from Figure 7-2b, TLOM images). Black arrows show shear banding zones; white arrows show microcracks (1) or pores (2); gray arrows show squeeze flow material; the dotted lines approximately indicate the plastically deformed zone (PDZ).	58
Figure 7-4: Microstructure after 500 ms of friction time (Figure 7-3b, Stage 2 of the friction phase). (a) Formation of the shear layer and flash material from squeeze flow (RLOM); (b) plastic deformation with increase of stud diameter and shear banding (TLOM).	59
Figure 7-5: Shear layer around the top of the stake head for (a) unreinforced PEI (TLOM); and (b) PEI-CF (RLOM). Stop-action specimens after 1000 ms of friction time (Figure 7-3c, Stage 3 of the friction phase).	60

Figure 7-6: (a) Schematic illustration of the material flow in the shear layer during dwell time; (b) schematic surface view of an F-ICJ joint showing the region of interest observed by SR- μ CT; (c) material flow in a PEI-CF joint at different positions of the shear layer. Positions S1-S4 are indicated in (a). White arrows indicate material flow in the shear layer. Dotted lines indicate boundaries between the shear layer and the unaffected base material.....	62
Figure 7-7: Effect of the dwell time on joint formation. Shear layer in a stop-action specimen (a) before the dwell time (Stage 4 of the friction phase); (b) after 1000 ms of dwell time (Stage 5 of the friction phase). TLOM images.....	63
Figure 7-8: Effect of the dwell time on the final joint microstructure. (a) Joint without a dwell time; (b) Joint with 1000 ms of dwell time (TLOM images).	64
Figure 7-9: Effect of dwell time on the polymer-polymer interface. Interface in a stop-action specimen (a) before dwell time; and (b) after 500 ms dwell time; (c) detail of the microstructure from (b), showing the healed interface (RLOM images).....	65
Figure 7-10: Cooling curves during (black squares and dashed line) and after (blue triangles and dash-dotted line) the consolidation phase of a two-phase process.	66
Figure 7-11: Evolution of joint formation during the consolidation phase: (a) stop-action specimen from the end of the friction phase, before consolidation starts (Stage 5 of the friction phase in Figure 7-2b); (b) stop-action specimen after 1 s consolidation; and (c) joint after 5 s consolidation, the end of the phase (TLOM images).....	67
Figure 8-1: Metal-polymer interface at the chamfer. Overlay of RLOM (PEI) and polarized RLOM (aluminum, Barker's reagent).	68
Figure 8-2: (a) Schematic representation of tool rubbing on the metallic partner; (b) detail of the surface of a joint with which tool rubbing took place; (c) microstructure of AA6082-T6 base material close to the surface in a non-affected area; (d) microstructure of a region of tool contact close to the surface, showing a thin process-affected layer (PTMAZ/MHAZ). Polarized RLOM images, Barker's reagent. Processing conditions: RS: 12000 rpm; FT: 5000 ms; FP: 0.5 MPa (2726 N); FoP: 1.0 MPa (5363 N); CoT: 5000 ms.....	69
Figure 8-3: Microstructural features of an F-ICJ joint created with a conical-pin tool and chamfer cavities: (a) overview of joint cross-section; (b) polymer-polymer interface; (c) pores and remnant weld lines in the PTMAZ (TLOM images). For processing conditions see Table 11-2.	70
Figure 8-4: Overlay of a microhardness map (left) on a CP-TLOM micrograph of the F-ICJ joint from Figure 8-3. Dotted lines are the boundaries of the polymer thermomechanically-affected zone (PTMAZ); dashed lines are the boundaries of the plastically deformed zone (PDZ). For processing conditions see Table 11-2.	71
Figure 8-5: (a) Behavior of PEI under uniaxial compression (based on [90, 207]); (b) yielding of PEI up to strain softening (solid curve), and reloading the yielded PEI during microhardness (dotted curve).....	72
Figure 8-6: (a) Half of a cross-sectional view of a joint featuring a PDZ; (b) birefringence of the PDZ-BM transition highlighted in (a), with number of fringes ($-\sigma_{res}$) increasing in the PDZ direction (CP-TLOM); (c) indentation profile highlighted in (b), showing the the formation of a strengthened transition zone (STZ) between the PDZ and BM. The gray horizontal lines in (c) correspond to the PEI base material's hardness.	73
Figure 8-7: (a) Microhardness distribution overlay on a CP-TLOM micrograph from an annealed F-ICJ joint (same processing condition as Figure 8-4); (b) first- and second-heating T_g (DSC), and onset of decomposition (TGA) of the PTMAZ from as-joined and annealed joints compared to the BM.....	75

Figure 8-8: (a) Thermogravimetry curve of the as-received PEI base material and the processing temperature range during the friction phase of F-ICJ; (b) Tg range of PEI base material (hatched area) compared to Tg measurements of the PTMAZ under various conditions.....	77
Figure 8-9: (a) Shape of indentations in each microstructural zone and typical profile measurement of the residual indentation depth compared to the maximum depth of the Vickers indenter; (b) measurements of relative residual depth (black solid line and symbols) and pile-up volume (blue dashed line and open symbols) as a function of local strength in the microstructural zones.....	78
Figure 8-10: (a) Overview of an F-ICJ joint (RLOM); (b) inner surfaces of the pores (SE-SEM). Processing conditions: RS: 12000 rpm; FT: 5000 ms; FP: 0.3 MPa (1525 N); FoP: 0.7 MPa (3733 N); CoT: 5000 ms.....	80
Figure 8-11: Example of 3D visualization through μ CT of pore distribution in an F-ICJ joint (RS: 7500 rpm; FT: 2500 ms; FF: 1525 N; FoF: 3733 N; CoT: 2500 ms). Results adapted from [232].....	81
Figure 8-12: (a) Remnant weld line between PTMAZ and BM (RLOM image; RS: 8000 rpm; FT: 2500 ms; FP: 0.3 MPa (1525 N); FoP: 0.7 MPa (3733 N); CoT: 5000 ms); and stress distribution on the stake head for (b) joint without weld line; (c) with a remnant weld line, indicated by gray arrows. FEM results adapted from [233]. The white arrow indicates loading direction.	82
Figure 8-13: Joint produced with high frictional force (2551 N) and without a backing surface, featuring stake-shaft shearing: (a) TLOM micrograph; (b) overlay of microhardness distribution on the stress field image by CP-TLOM (see text for description of the zones indicated by arrows); (c) severe shear banding (TLOM) and schematic orientation of slip planes; (d) 3D surface scan of the shear banding at the stake base (LSCM, 4000 % height magnification). Shear bands indicated by black arrows, shearing of the stake shaft indicated by white half-arrows. Processing conditions: RS: 8000 rpm; FT: 2500 ms; FP: 0.45 MPa (2551 N); FoP: 1.0 MPa (5363 N); CoT: 5000 ms.	83
Figure 9-1: (a) Schematic description of the forces acting during lap-shear loading of F-ICJ joints, based on the analysis by Ekh [238]. Red disks are the main stress concentration spots; (b) finite element method (FEM) simulation of the contact pressure on both stress concentration regions, adapted from [233]. FEM LS models followed the same test setup as the actual experiments (see Section 6.3.8).....	85
Figure 9-2: (a) Lateral view of specimens at the start of a lap-shear test and prior to failure, with an overlay of the deflection in the x-axis; (b) deflection from secondary bending for PEI (blue solid line) and aluminum (black dashed line) in relation to their original position (gray dash-dotted line).....	86
Figure 9-3: (a) Deflection of the polymer plate from secondary bending; (b) stresses on the base plate in an F-ICJ metal-polymer overlap joint.....	86
Figure 9-4: Mechanical behavior in lap-shear testing. Snapshots of the strain in y-direction at selected stages of the force-displacement curve show increasing localized compressive stresses $-\epsilon_y$ (hourglass-shaped boundaries). The position of the stake is indicated by a dark circle in the snapshots.	87
Figure 9-5: (a) Micrograph of a LS joint failure by secondary bending. PTMAZ boundary is marked by the white-dotted line; (b) detail of the radial crack on the stake head. White arrows indicate weld line interfaces; (c) detail of deformation at the stake base (RLOM images). Processing conditions: RS: 8000 rpm; FT: 2500 ms; FP: 0.3 MPa (1525 N); FoP: 0.7 MPa (3733 N); CoT: 5000 ms.....	88

Figure 9-6: Example of the crack propagation regions in secondary bending failure (RS: 8000 rpm; FT: 2500 ms; FP: 0.3 MPa (1525 N); FoP: 0.7 MPa (3733 N); CoT: 5000 ms). See text for a description of the zones.....	90
Figure 9-7: (a) Crack initiation region. White arrows indicate crack propagation direction; (b) crack nucleation point (black arrow) below the stake surface. For processing conditions see Table 11-2.....	91
Figure 9-8: (a) Boundaries between crack initiation zone A, transition zone B, and stable/unstable growth zone C; (b) detail of the boundary between zones B and C. White arrows show patches, gray arrows show conical markings, black arrows show hackles. Processing conditions: RS: 8000 rpm; FT: 2500 ms; FP: 0.3 MPa (1525 N); FoP: 0.7 MPa (3733 N); CoT: 5000 ms.....	91
Figure 9-9: (a) Transition between zones C and D. Black arrows are patch patterns, white arrows are hackles; (b) end-bands in the fast-propagation banded zone D. Processing conditions: RS: 8000 rpm; FT: 2500 ms; FP: 0.3 MPa (1525 N); FoP: 0.7 MPa (3733 N); CoT: 5000 ms.....	92
Figure 9-10: (a) Incomplete bending failure (IB) in the base plate, white arrow indicates the end of the crack (RS: 8000 rpm; FT: 5000 ms; FP: 0.5 MPa (2726 N); FoP: 1.0 MPa (5363 N); CoT: 2500 ms.); (b) Example of a specimen showing complete removal of the stake head as a result of the rebound from catastrophic SB failure (RS: 12000 rpm; FT: 5000 ms; FP: 0.5 MPa (2726 N); FoP: 1.0 MPa (5363 N); CoT: 5000 ms). White arrows show SB fracture surfaces, black arrows show the fracture surfaces of stake head removal; (c) comparison of average mechanical properties between SB and IB failures.....	93
Figure 9-11: (a) Forces acting on the joint in cross-tensile loading. The red disk and orange square represent the main stress concentration points in CT joints; (b) FEM simulation of the maximum principal stresses acting in the joint, adapted from [233]. FEM CT models followed the same test setup as the actual experiments (see Section 6.3.8).....	94
Figure 9-12: (a) Example of linear force-displacement behavior in cross-tensile testing. Overview of (b) base-plate bending failure – BPB (RS: 12000 rpm; FT: 2500 ms; FP: 0.5 MPa (2726 N); FoP: 1.0 MPa (5363 N); CoT: 2500 ms); (c) head pull-out failure – HPo (RS: 8000 rpm; FT: 5000 ms; FP: 0.5 MPa (2726 N); FoP: 0.7 MPa (3733 N); CoT: 5000 ms).....	95
Figure 9-13: (a) BPB failure of a CT specimen (RS: 8000 rpm; FT: 2500 ms; FP: 0.45 MPa (2551 N); FoP: 1.0 MPa (5363 N); CoT: 5000 ms); (b) fracture surface on the stable crack-growth side; (c) fracture surface on the unstable crack-growth side. White arrows are shear micromechanisms shown in detail in (d), black arrows are end-banded regions shown in detail in (e). See text for description of the zones.....	97
Figure 9-14: (a) Overview of the HPo fracture surface, the black arrow indicates a crack nucleation point; (b) example of fracture regime transitions around a pore; (c) interaction of the crack behavior with proximity to pores. White arrows show crack propagation direction, the dotted line shows transition to unstable crack propagation; (d) detail of the fracture surface close to the high-pore-content region in (a). Processing conditions: RS: 8000 rpm; FT: 2500 ms; FP: 0.45 MPa (2551 N); FoP: 1.0 MPa (5363 N); CoT: 5000 ms.....	98
Figure 9-15: (a) Crack nucleation point on the stake head; (b) crack nucleation point at higher magnification, and spots for EDS analyses; (c) EDS spectra for the spots in (b). Processing conditions: RS: 8000 rpm; FT: 2500 ms; FP: 0.45 MPa (2551 N); FoP: 1.0 MPa (5363 N); CoT: 5000 ms.....	99

Figure 9-16: Cross-sectional view of a joint with excessive tool rubbing, with white arrows showing contamination by aluminum particles in the PTMAZ (RS: 8000 rpm; FT: 5000 ms; FP: 0.3 MPa (1525 N); FoP: 1.0 MPa (5363 N); CoT: 5000 ms).....	100
Figure 9-17: (a) Example of a force-displacement curve for stake pull-out (SPo) failure in cross-tensile testing; (b) cross-sectional view of an SPo failure, indicating crack initiation points (red disks) and propagation direction (black arrows); (c) microhardness distribution on high frictional force joints and interaction of the crack path with the STZ (RLOM images). Processing conditions: RS: 12000 rpm; FT: 5000 ms; FP: 0.5 MPa (2726 N); FoP: 0.7 MPa (3733 N); CoT: 2500 ms.....	101
Figure 9-18: (a) 3D view of the stake and plate fracture surfaces; (b) overview of the fracture surface on the plate. The white-dotted line shows the boundary between stable crack growth (A) and fast crack propagation (C+D) zones; (c)-(f) are details of the fracture surface from (b). The white arrows indicate the local crack propagation direction. For processing conditions see Table 11-2. Joint annealed at 200 °C for 24 hours.	102
Figure 9-19: Mechanical performance comparison between the CT failure modes.....	103
Figure 10-1: (a) Effect of heat input on the size of PTMAZ and weld line formation. The box indicates conditions with a high frequency of weld lines; (b) effect of stake temperature on relative pore area; (c) correlation of pore area to PTMAZ area.	105
Figure 10-2: Effect of dwell time on relative PTMAZ area. Measurements from two replicates of the conditions from the FF-DoE (Table 6-7).....	106
Figure 10-3: Effect of process parameters on microstructural zones. Parameters highlighted in bold in (b)-(d) are changes to those for the reference joint in (a).	107
Figure 10-4: Effects of relative PTMAZ area on LS properties: (a) ULSF; (b) displacement at ULSF; (c) joint stiffness; (d) displacement at break.	109
Figure 10-5: Effects of relative PTMAZ area on CT properties, indexed by most frequent failure mode: (a) UCTF; (b) displacement at UCTF; (c) joint stiffness; (d) displacement at break.	110
Figure 10-6: Effects of a remnant weld line on LS and CT relevant properties.....	111
Figure 10-7: Results of preliminary investigations: (a) comparison of mechanical behavior of joints produced with a conical-pin tool and flat tool (adapted from [184]); (b) comparison of average ULSF for two conical-pin tool geometries in a one-factor-at-a-time experiment (adapted from [185]).....	112
Figure 10-8: Validation diagrams for the reduced models of (a) ST; (b) ULSF; and (c) UCTF...	113
Figure 10-9: Analysis of ST: (a) Pareto chart of standardized effects; (b) plots of significant main effects (RS, FT, FP); (c) effect of the FT*FP interaction; (c) effect of the FoP*FP interaction on the stake temperature.	115
Figure 10-10: Analysis of ULSF: (a) Pareto chart of standardized effects; (b) effect of the FoT*FoP interaction; (c) effect of the FT*FoT interaction.	117
Figure 10-11: Analysis of UCTF: (a) Pareto chart of standardized effects; (b) plots of significant main effects (RS, FT, FP); (c) effect of the FT*FP interaction.....	118
Figure 11-1: Mechanical performance of the optimized condition (with and without backing plate) compared to the predicted value. The dashed lines represent the standard error of the regression around the model's target value (specimens produced at RSM400 equipment)..	121
Figure 11-2: Joining diagrams for the transferability study of replicating the RSM400's optimized joining conditions on the RNA gantry system.....	122
Figure 11-3: Surface view of the optimized condition produced on (a) RSM400; and (b) RNA gantry. The ring-shaped area delimited by white dotted circles represents a low porosity region.	123

Figure 11-4: (a) Microstructure comparison of joints from the RSM400 and RNA gantry; comparison of (b) microstructural features (RAPTMAS and RApore); (c) local mechanical properties (microhardness); and (d) local physical-chemical changes (Tg from DSC).....	124
Figure 11-5: Comparison of averaged force-displacement curves for (a) Lap shear (LS) testing; and (b) cross-tensile (CT) testing; (c) comparison of average ultimate force and joint stiffness, and (d) comparison of average displacement at ultimate forces and break, for LS and CT properties.....	125
Figure 11-6: Comparison of F-ICJ to ultrasonic staking. (a) Cross-sectional view of the joints; (b) UCTF and ULSF of each process; (c) strength-to-weight ratio in CT and LS for each process. The percentages are improvements of F-ICJ over ultrasonic staking.....	126
Figure 11-7: (a) Multi-spot subcomponent in position for joining; (b) joined subcomponent. The numbers represent the joining order of each individual stake.....	127
Figure 11-8: Heat build-up during sequential joining as a result of tool rubbing, and the surface appearance of the stakes from the diagram.	127
Figure 11-9: (a) Force-displacement curves for four replicates of the F-ICJ subcomponent; (b) deformation under quasi-static four-point bending of an F-ICJ subcomponent.	129
Figure 11-10: (a) Bottom surface of the subcomponent, showing a longitudinal crack. Black arrows are additional cracks from the rebound during catastrophic failure, white arrows indicate the crack propagation direction; (b) top surface of the subcomponent with details of damage to stake heads. Black arrows are cracked heads, white arrows are plastic deformation of the metal.....	129
Figure A-1: Patent application of the F-ICJ process.	X
Figure C-1: (a) Overview of the clamping system; (b) back view of the clamping system.....	XII
Figure D-1: Preliminary FEM analysis of number of stakes in the subcomponent. Models with symmetry in two axes for configurations with (a) 10 stakes; (b) 14 stakes; (c) 20 stakes. Results adapted from [201]	XIII
Figure E-1: (a) Process diagram of a three-phase F-ICJ joining cycle; (b) cooling regime during (black squares and dashed line) and after (blue triangles and dash-dotted line) the forging and consolidation phases of a three-phase process.....	XIV
Figure E-2: Evolution of joint formation during the forging phase of a three-phase process. Stop-action specimens at forging times of (a) 100 ms, Stage 1; (b) 300 ms, Stage 2; and (c) finished joint microstructure (TLOM images). Arrows indicate squeeze flow (gray), shear banding (black), microcracks (white). Dotted lines indicate the PDZ.	XIV
Figure F-1: Colored images from (a) Figure 7-1c; (b) Figure 7-1d; (c) Figure 8-7a; (d) Figure 8-13b; (e) Figure 8-4 and Figure 11-4a (RNA gantry); (f) Figure 11-4a (RSM400); (g) detail from (e) used in Figure 8-6b.	XV
Figure G-1: Glass transition temperatures (DSC) measured from (a) first heating; (b) second heating. “RNA gantry”, “Annealed” and “BM” correspond to the data showed in Figure 8-7b. “RNA gantry” and “RSM400” measurements correspond to the data showed in Figure 11-4d.	XVI
Figure G-2: Measurements of onset of decomposition (TGA). (a) Average curves; (b) detail of the onset of decomposition for three replicates. “RNA gantry”, “Annealed” and “BM” correspond to the data showed in Figure 8-7b. “RNA gantry” and “RSM400” measurements correspond to the transferability study from Section 11.2.....	XVII
Figure H-1: Effect of the use of a backing surface on quasi-static mechanical performance: (a) ultimate force; (b) displacement at break.....	XVIII

Figure I-1: (a) Non-joined CT specimen testing; (b) non-joined LS specimens testing; (c) mechanical performance results.....	XIX
Figure J-1: Lap shear force-displacement curves for the specimens of the design of experiments.....	XX
Figure J-2: Cross tensile force-displacement curves for the specimens of the design of experiments.....	XXI
Figure J-3: Measurements from the fractional factorial design of experiments for all three specimen geometries.....	XXII
Figure K-1: Descriptive statistics of weld line formation: (a) presence of weld line depending on temperature; (b) presence of weld line depending on relative PTMAZ area.....	XXIII
Figure K-2: Correlation of microhardness of the PTMAZ with stake temperature.....	XXIII
Figure L-1: Differences in stake temperature measurements for the three specimen geometries used in this work.....	XXIV
Figure L-2: Effect of relative pore area RApore on properties of LS joints.....	XXV
Figure L-3: Effect of relative pore area RApore on properties of CT joints.....	XXV
Figure M-1: Stake temperature (ST) statistical model: (a) Normal probability plot; (b) effects, coefficients, and significance of predictors; (c) plot of residuals versus fitted values.....	XXVI
Figure M-2: Ultimate lap shear force (ULSF) statistical model: (a) Normal probability plot; (b) effects, coefficients, and significance of predictors; (c) plot of residuals versus fitted values.....	XXVII
Figure M-3: Ultimate cross tensile force (UCTF) statistical model: (a) Normal probability plot; (b) effects, coefficients, and significance of predictors; (c) plot of residuals versus fitted values.....	XXVII
Figure N-1: Microstructure and local mechanical properties of optimized joints produced at the RSM400 (a) with a backing plate; and (b) without a backing plate. The absence of a backing plate creates a stake-shaft shearing (SSS) defect, as described in Section 8.4.3. Processing condition from Table 11-1.....	XXIX
Figure O-1: (a) Difference in torque response at both equipments. The torque curves correspond to the matching curves of each equipment from Figure 11-2; (b) energy input at each equipment. The differences are a result of the hardware dissimilarities explained in Section 11.2.....	XXX
Figure P-1: Improved tool design for F-ICJ: (a) external overview; (b) cross-sectional view.....	XXXI

List of tables

Table 3-1: Advantages and limitations of state-of-the art staking methods for dissimilar materials [83, 87].	9
Table 3-2: Chemical composition of AA6082 [161].	27
Table 6-1: Physical and mechanical properties of AA6082 in T6 condition.	38
Table 6-2: Physical and mechanical properties of PEI (Duratron U1000).	39
Table 6-3: Physical and mechanical properties of PEI-CF (RTP2187) [181].	39
Table 6-4: Chemical composition of 316L stainless steel [182].	40
Table 6-5: Physical and mechanical properties of 316L stainless steel [182, 183].	40
Table 6-6: Equations for measurement of microstructural features.	46
Table 6-7: Levels of the fractional factorial design of experiments.	50
Table 10-1: Microstructural changes for selected conditions. Bold parameters in (b)-(d) are changes to those for the reference joint in (a).	107
Table 11-1: Process parameters for the optimized condition, as predicted by the desirability function (Section 6.3.11).	120
Table 11-2: Parameters for reproduction of the optimized condition with the RNA gantry.	122
Table B-1: Data sheet of the RSM400 system [248].	XI
Table B-2: Data sheet of the RNA gantry [81].	XI
Table M-1: Validation experiments for the ST model (three replicates).	XXVIII
Table M-2: Validation experiments for the ULSF model (five replicates).	XXVIII
Table M-3: Validation experiments for the UCTF model (five replicates).	XXVIII

APPENDIX A. F-ICJ PATENT APPLICATION

Date		22.10.14
Reference	Application No./Patent No. 14182938.2 - 1706	
Applicant/Proprietor Helmholtz-Zentrum Geesthacht Zentrum für Material- und Küstenforschung GmbH		

Designation as inventor - communication under Rule 19(3) EPC

You have been designated as inventor in the above-mentioned European patent application. Below you will find the data contained in the designation of inventor and further data mentioned in Rule 143(1) EPC:

DATE OF FILING : 29.08.14
 PRIORITY : //
 TITLE : A method for joining a plastic workpiece to a further workpiece
 DESIGNATED STATES : AL AT BE BG CH CY CZ DE DK EE ES FI FR GB GR HR HU IE IS IT LI LT LU LV MC MK MT NL NO PL PT RO RS SE SI SK SM TR

INVENTOR (PUBLISHED = 1, NOT PUBLISHED = 0):

1/Bastos Abibe, Andre [REDACTED] DE
 1/de Traglia Amancio Filho, Sergio [REDACTED] DE
 1/Sónego, Marília [REDACTED] BR
 1/F. dos Santos, Jorge [REDACTED] DE

DECLARATION UNDER ARTICLE 81 EPC:
 The applicant(s) has (have) acquired the right to the European patent as employer(s).



B-PM-AA-DR-APP-PatFICJa

Figure A-1: Patent application of the F-ICJ process.

APPENDIX B. EQUIPMENT SPECIFICATIONS: RSM400 AND RNA GANTRY

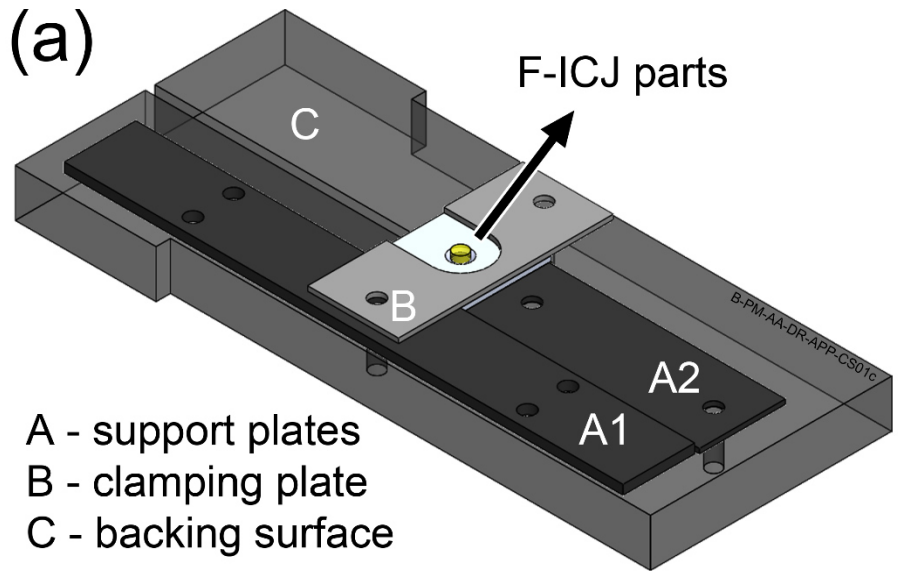
Table B-1: Data sheet of the RSM400 system [248].

Spindle feed	50 mm
Rotational speed	6000-24000 rpm
Power	1.85 kW (asynchronous)
Maximum axial force	6 kN
Motor control	Asynchronous, open-loop controlled

Table B-2: Data sheet of the RNA gantry [81].

Gantry working area (length x width x height)	1000 mm x 700 mm x 700 mm
Spindle feed	50 mm
Maximum rotational speed	21000 rpm
Maximum torque	25 N.m
Maximum axial force	24 kN
Motor control	Synchronous, field-oriented controlled

APPENDIX C. CLAMPING SYSTEM FOR SINGLE-SPOT F-ICJ SPECIMENS



(b) back view with opening

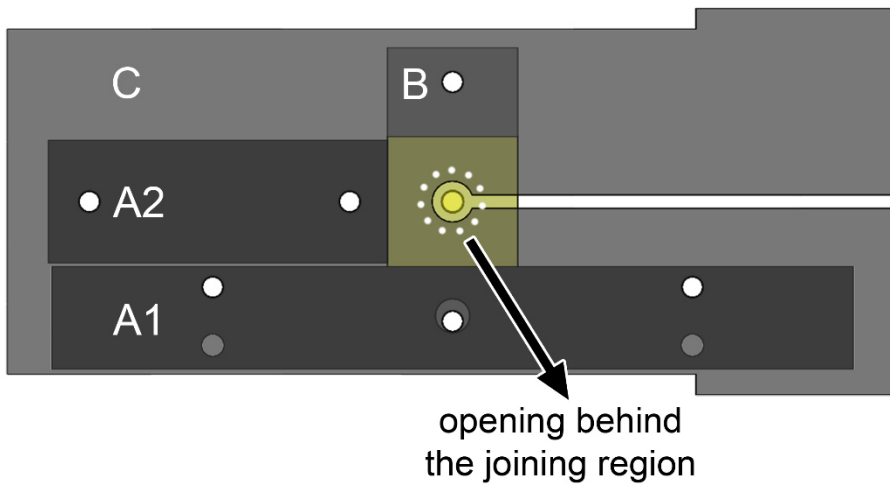


Figure C-1: (a) Overview of the clamping system; (b) back view of the clamping system.

APPENDIX D. PRELIMINARY ANALYSIS FOR THE NUMBER OF STAKES AT THE MULTI-SPOT SPECIMENS

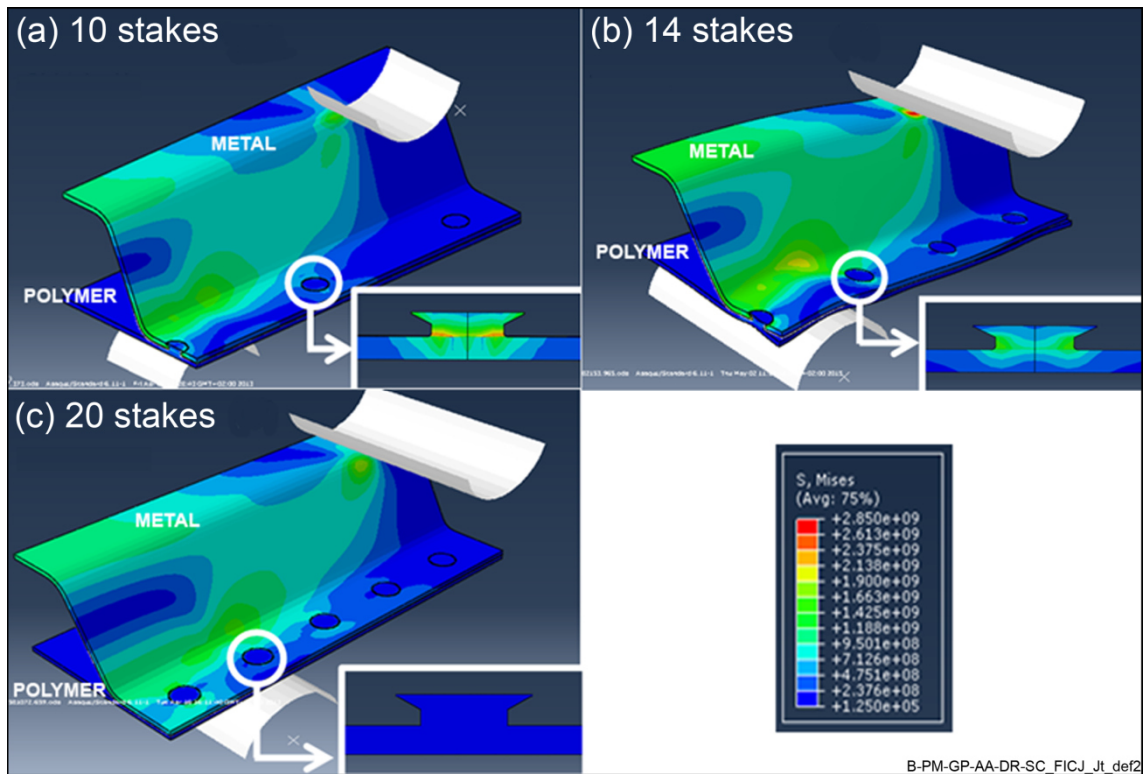


Figure D-1: Preliminary FEM analysis of number of stakes in the subcomponent. Models with symmetry in two axes for configurations with (a) 10 stakes; (b) 14 stakes; (c) 20 stakes. Results adapted from [201]

APPENDIX E. JOINT FORMATION USING A THREE-PHASE PROCESS CONFIGURATION (FRICTION, FORGING, AND CONSOLIDATION PHASES)

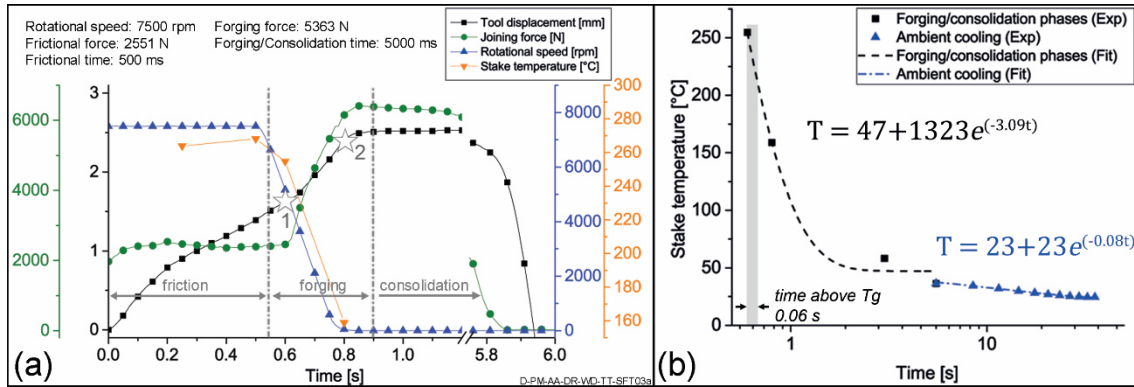


Figure E-1: (a) Process diagram of a three-phase F-ICJ joining cycle; (b) cooling regime during (black squares and dashed line) and after (blue triangles and dash-dotted line) the forging and consolidation phases of a three-phase process.

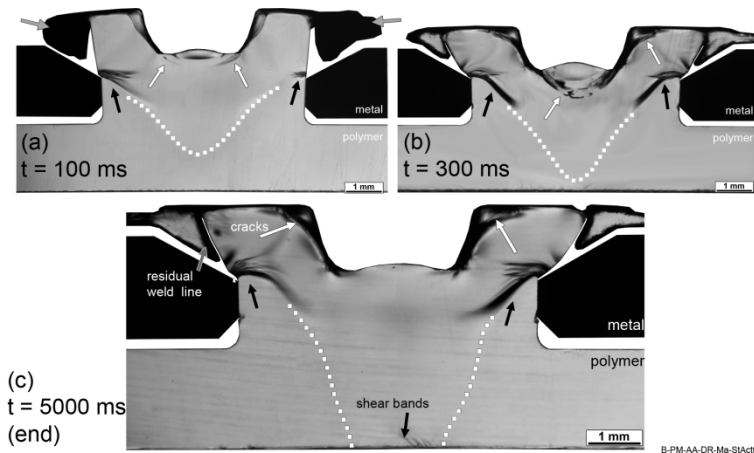


Figure E-2: Evolution of joint formation during the forging phase of a three-phase process. Stop-action specimens at forging times of (a) 100 ms, Stage 1; (b) 300 ms, Stage 2; and (c) finished joint microstructure (TLOM images). Arrows indicate squeeze flow (gray), shear banding (black), microcracks (white). Dotted lines indicate the PDZ.

APPENDIX F. COLORED BIREFRINGENCE MICROGRAPHS

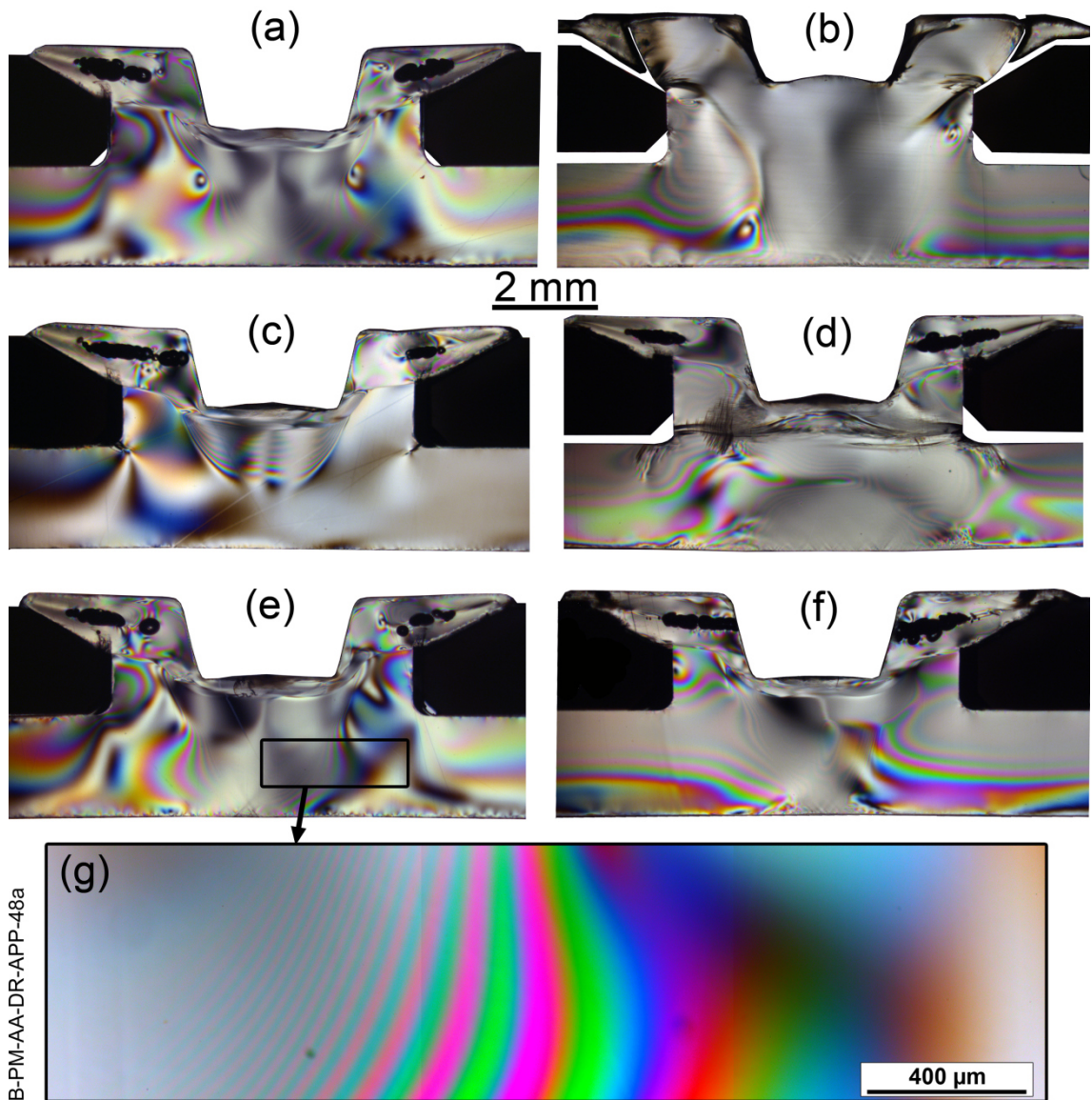


Figure F-1: Colored images from (a) Figure 7-1c; (b) Figure 7-1d; (c) Figure 8-7a; (d) Figure 8-13b; (e) Figure 8-4 and Figure 11-4a (RNA gantry); (f) Figure 11-4a (RSM400); (g) detail from (e) used in Figure 8-6b.

APPENDIX G. DETAILED THERMAL ANALYSIS CURVES

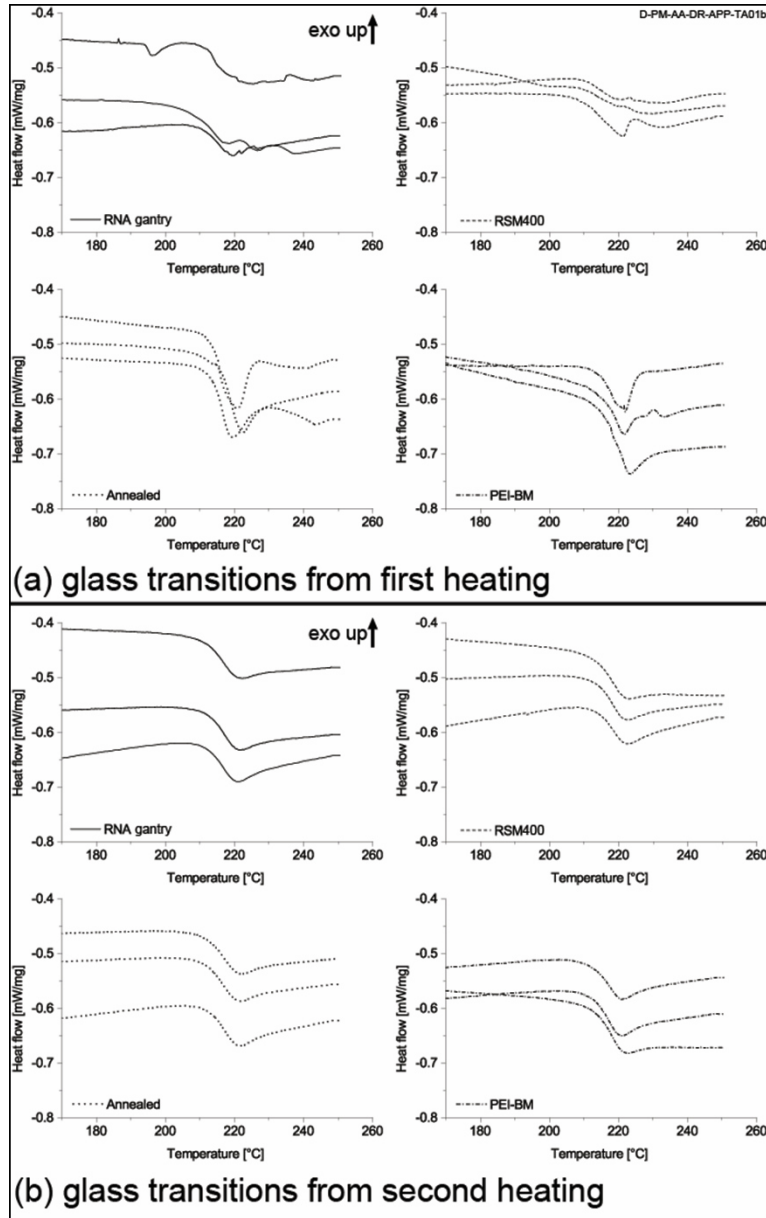


Figure G-1: Glass transition temperatures (DSC) measured from (a) first heating; (b) second heating. “RNA gantry”, “Annealed” and “BM” correspond to the data showed in Figure 8-7b. “RNA gantry” and “RSM400” measurements correspond to the data showed in Figure 11-4d.

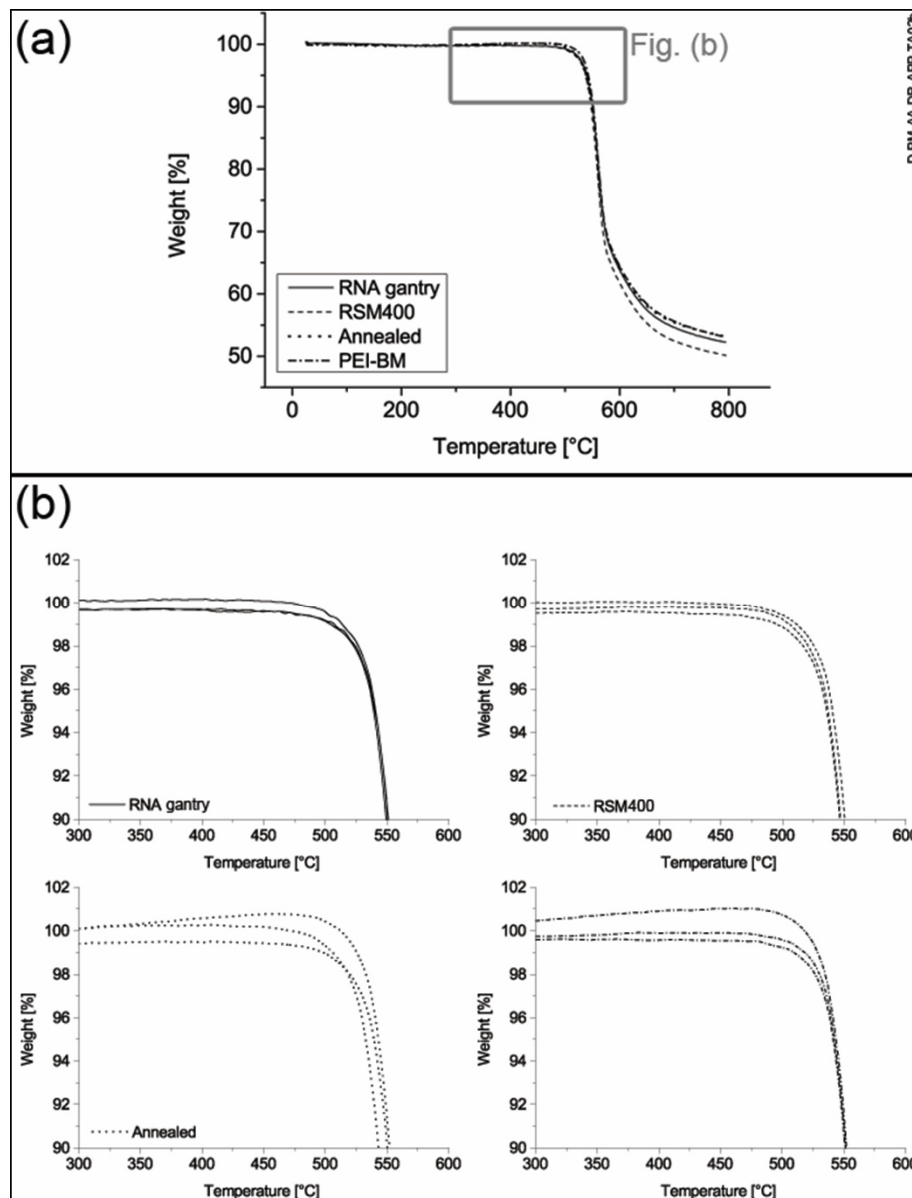


Figure G-2: Measurements of onset of decomposition (TGA). (a) Average curves; (b) detail of the onset of decomposition for three replicates. “RNA gantry”, “Annealed” and “BM” correspond to the data showed in Figure 8-7b. “RNA gantry” and “RSM400” measurements correspond to the transferability study from Section 11.2.

APPENDIX H. MECHANICAL PERFORMANCE OF JOINTS PRESENTING STAKE-SHAFT SHEARING

Figure H-1 shows a comparison for mechanical performance in lap-shear and cross-tensile testing between joints with and without presence of SSS defects (without or with a backing surface). Ultimate force is not significantly affected, and only the displacement at break for cross-tensile tests is smaller when a backing surface is used. This effect can be explained by the crack propagation regime in cross-tensile testing and the local mechanical properties (see Section 9.2).

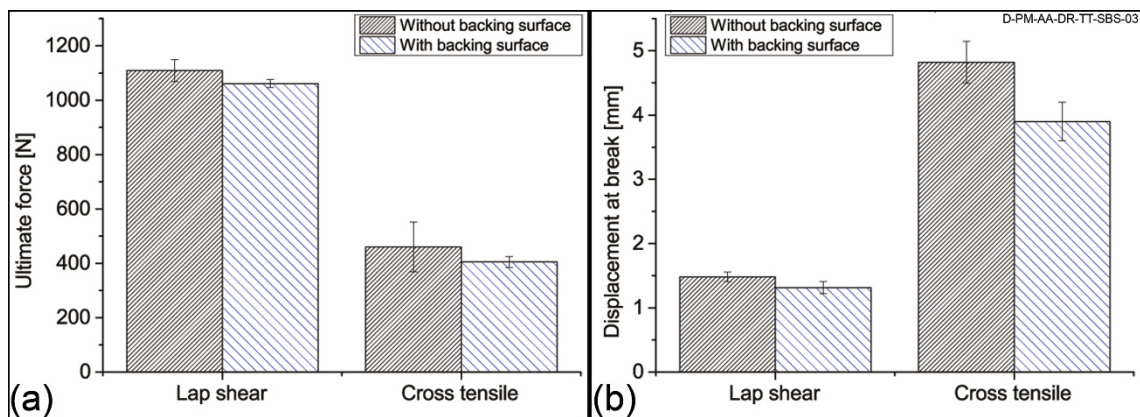


Figure H-1: Effect of the use of a backing surface on quasi-static mechanical performance: (a) ultimate force; (b) displacement at break.

APPENDIX I. MECHANICAL PERFORMANCE OF NON-JOINED F-ICJ SPECIMENS

The F-ICJ specimens were tested in the non-joined conditions to verify changes related to stake-head formation in mechanical behavior. The CT specimens were tested in three-point bending as showed in Figure I-1a. The LS specimens were tested in lap-shear with an aluminum part for load transfer as showed in Figure I-1b. The results are showed in Figure I-1c. The LS geometry without a stake head provides less resistance to secondary bending and fails by SB earlier and with lower forces. The non-joined CT specimens have lower displacement, but similar ultimate force in three-point bending as the joined F-ICJ CT specimens in cross tensile loading, and both fail by BPB. The performance of CT F-ICJ specimens is therefore comparable to the base material's resistance in a similar configuration.

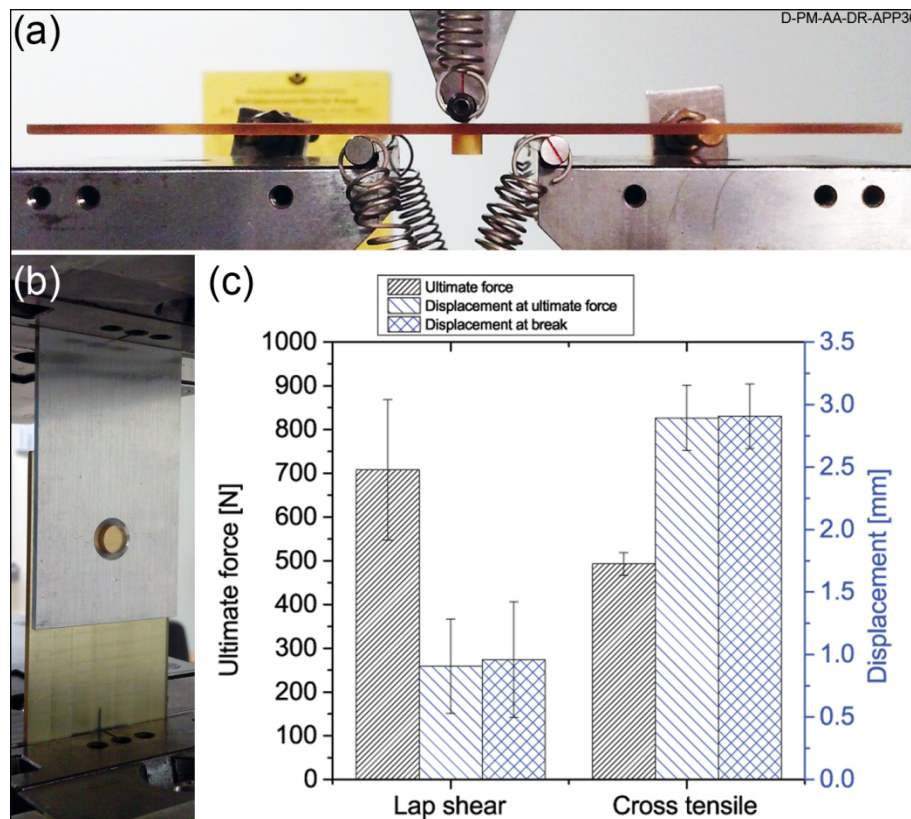


Figure I-1: (a) Non-joined CT specimen testing; (b) non-joined LS specimens testing; (c) mechanical performance results.

APPENDIX J. EXPERIMENTAL RESULTS FROM THE SPECIMENS OF THE DESIGN OF EXPERIMENTS

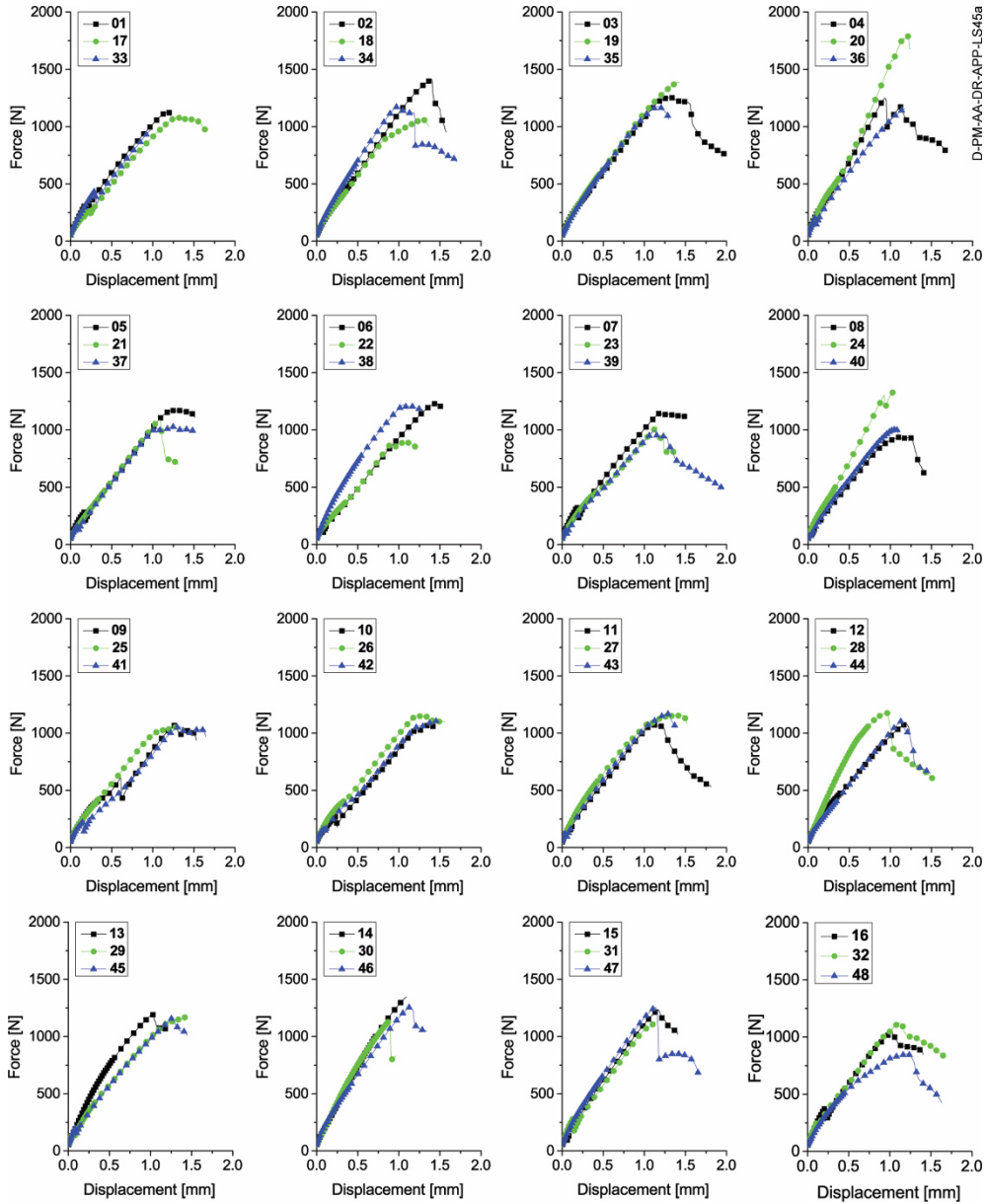


Figure J-1: Lap shear force-displacement curves for the specimens of the design of experiments.

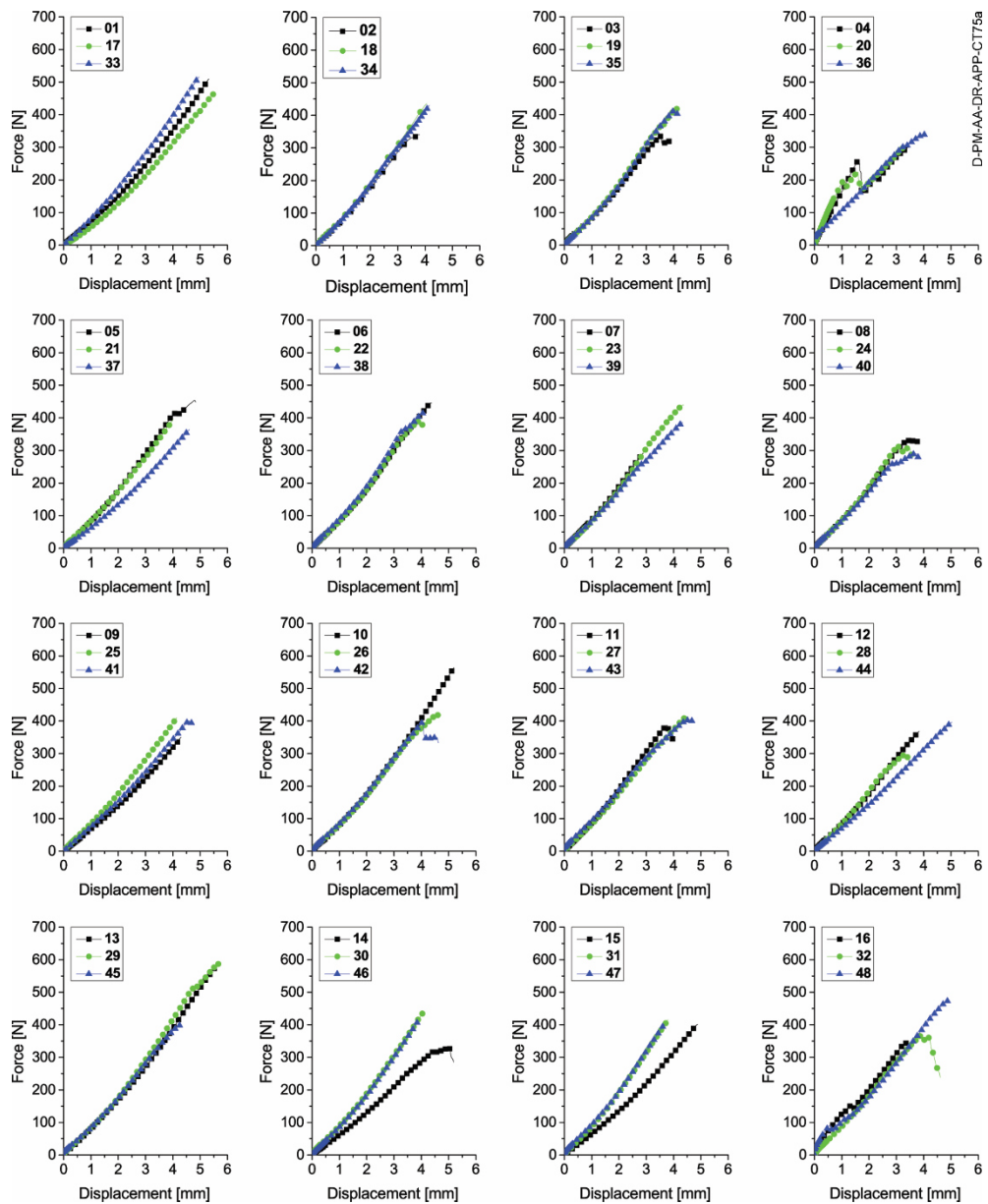


Figure J-2: Cross tensile force-displacement curves for the specimens of the design of experiments.

	Process parameters						Microstructural analysis				Lap shear				Cross tensile			
	RS [rpm]	FT [ms]	FoT [ms]	FoP [MPa]	FP [MPa]	ST [°C]	RApore [%]	RA PTMAZ [%]	ST [°C]	UJSF [N]	d (UJSF) [mm]	Stiffness [N/mm]	ST [°C]	UCTF [N]	d (UCTF) [mm]	d (break) [mm]	Stiffness [N/mm]	
1	8000	2500	2500	0.7	0.5	58.34	1.9	25.98	62.78	1124.83	1.18	1.22	954.63	49.28	509.72	5.32	5.32	95.84
2	12000	2500	2500	0.7	0.3	57.56	2.14	35.46	59.68	1410.26	1.4	1.58	1007.91	54.38	340.48	3.79	3.79	89.81
3	8000	5000	2500	0.7	0.3	67.21	1.56	41.18	57.07	1254.07	1.31	2.04	959.62	50.04	339.65	3.53	3.87	94.42
4	12000	5000	2500	0.7	0.5	99.85	3.48	49.2	122.76	1249.61	0.93	1.67	1342.93	109.42	299.12	3.44	3.44	86.9
5	8000	2500	5000	0.7	0.3	40.84	0.75	25.11	40.02	1171.34	1.23	1.51	955.17	35.09	453.91	4.8	4.84	94.65
6	12000	2500	5000	0.7	0.5	65.18	2.17	31.19	66.13	1229.04	1.44	1.51	850.59	55.58	446.16	4.38	4.88	101.88
7	8000	5000	5000	0.7	0.5	81.37	3.37	35.7	67.92	1154.53	1.19	1.49	967.77	50.68	291.84	2.89	2.89	100.88
8	12000	5000	5000	0.7	0.3	73.43	4.37	48.9	90.5	995.16	1.1	1.41	850.51	74.19	330.32	3.43	3.78	96.22
9	8000	2500	2500	1	0.3	44.78	0.46	24.08	40.56	1070.91	1.27	1.53	843.08	40.54	350.39	4.3	4.3	81.51
10	12000	2500	2500	1	0.5	62.93	2.3	32.33	70.34	1071.18	1.38	1.42	776.47	67.4	564.42	5.2	5.2	108.55
11	8000	5000	2500	1	0.5	85.01	2.44	35.79	92.47	1070.41	1.11	1.81	960.9	73.53	386.28	3.76	3.96	102.77
12	12000	5000	2500	1	0.3	57.92	3.2	45.31	78.29	1080.05	1.19	1.23	905.35	79.57	368.2	3.84	3.84	95.87
13	8000	2500	5000	1	0.5	56.02	0.88	28.15	56.64	1191.15	1.03	1.21	1159.71	48.29	573.58	5.53	5.53	103.74
14	12000	2500	5000	1	0.3	46.86	1.85	30.69	52.72	1344.39	1.09	1.09	1231.09	49.88	328.23	5	5.17	65.61
15	8000	5000	5000	1	0.3	51.26	3.01	40.1	49.38	1232.83	1.17	1.41	1050.38	55.47	401.59	4.88	4.88	82.25
16	12000	5000	5000	1	0.5	94.16	3.11	49.77	88.37	1043.06	1.02	1.41	1018.35	73.05	343.52	3.39	3.39	101.24
17	8000	2500	2500	0.7	0.5	56.16	1.32	26.75	63.58	1083.25	1.3	1.63	834.11	48.92	462.57	5.47	5.47	84.56
18	12000	2500	2500	0.7	0.3	55.77	2.17	33.98	48.3	1059.64	1.29	1.36	821.71	46.88	435.83	4.06	4.06	107.28
19	8000	5000	2500	0.7	0.3	54.17	2.49	38.79	65.69	1387.75	1.41	1.43	985.94	64.22	424.7	4.2	4.2	101.18
20	12000	5000	2500	0.7	0.5	91.06	2.28	47.56	131.97	1787.7	1.21	1.24	1473.73	128.08	297.95	3.24	3.24	92.1
21	8000	2500	5000	0.7	0.3	47.21	0.03	23.76	43.11	1086.47	1.08	1.31	1009.83	38.68	394.54	4.01	4.01	98.49
22	12000	2500	5000	0.7	0.5	67.01	2.59	31.86	69.02	892.09	0.94	1.22	953.52	54.77	390.16	3.86	4.09	100.99
23	8000	5000	5000	0.7	0.5	73.86	1.16	35.22	79.45	1027.92	1.15	1.39	894.47	64.16	439.89	4.37	4.37	100.65
24	12000	5000	5000	0.7	0.3	74.19	3.79	48.59	101.56	1325.6	1.03	1.03	1291.1	68.6	313.51	3.06	3.55	102.51
25	8000	2500	2500	1	0.3	41.58	0.93	23.13	41.2	1061.18	1.32	1.35	806.03	44.46	409.57	4.15	4.15	98.81
26	12000	2500	2500	1	0.5	77.64	2.35	30.52	79.4	1151.92	1.22	1.56	947.55	65.35	418.31	4.61	4.63	90.72
27	8000	5000	2500	1	0.5	88.72	1.94	34.02	86.74	1155.98	1.46	1.52	790.66	69	414	4.53	4.53	91.48
28	12000	5000	2500	1	0.3	64.23	3.59	47.94	84.68	1176.43	0.95	1.52	1236.56	96.48	294.99	3.27	3.45	90.29
29	8000	2500	5000	1	0.5	52.22	1.09	24.82	53.13	1169.83	1.44	1.46	809.59	42.33	586.93	5.66	5.66	103.63
30	12000	2500	5000	1	0.3	52.38	3.47	32.4	50.07	1148.58	0.89	0.97	1284.85	45.64	438.72	4.08	4.08	107.63
31	8000	5000	5000	1	0.3	50.12	0.84	40.85	54.76	1123.02	1.15	1.15	974.54	56.97	415.21	3.81	3.81	109.09
32	12000	5000	5000	1	0.5	86.9	2.61	44.27	96.76	1122.2	1.12	1.67	1002.29	77.85	368.73	3.94	4.6	93.57
33	8000	2500	2500	0.7	0.5	56.91	--	--	60.1	966.92	0.97	0.97	996.22	53.04	515.54	4.96	4.96	104
34	12000	2500	2500	0.7	0.3	56.18	--	--	52.77	1171.4	0.97	1.7	1206.93	50.19	430.05	4.15	4.15	103.7
35	8000	5000	2500	0.7	0.5	57.99	--	--	68.62	1178.4	1.17	1.3	1003.18	60.06	414.73	4.04	4.14	102.67
36	12000	5000	2500	0.7	0.5	86.6	--	--	106.42	1154.37	1.17	1.17	986.4	79.55	339.57	4.05	4.05	83.75
37	8000	2500	5000	0.7	0.3	41.72	--	--	45.66	1028.97	1.27	1.49	811.26	32.9	363.89	4.61	4.61	79.02
38	12000	2500	5000	0.7	0.5	66.06	--	--	60.7	1219.73	1.05	1.31	1157.79	61.14	416.52	4.15	4.15	100.47
39	8000	5000	5000	0.7	0.5	75.37	--	--	70.4	997.71	1.13	1.93	881.95	63.07	385.94	4.34	4.34	89.02
40	12000	5000	5000	0.7	0.3	68.4	--	--	70.81	1003.65	1.06	1.1	947.33	67	289.85	3.71	3.81	78.04
41	8000	2500	2500	1	0.3	45.49	--	--	44.05	1055.1	1.32	1.64	800.33	43.48	400.64	4.57	4.76	87.64
42	12000	2500	2500	1	0.5	78.8	--	--	73.35	1104.05	1.46	1.47	758.15	72.07	397.57	4.05	4.63	98.05
43	8000	5000	2500	1	0.5	89	--	--	69.12	1167.4	1.28	1.37	911.6	65.4	404.37	4.6	4.67	87.86
44	12000	5000	2500	1	0.3	61.46	--	--	78.93	1109.14	1.14	1.48	970.77	82.2	396.33	5.03	5.04	78.84
45	8000	2500	5000	1	0.5	51.63	--	--	53.58	1160.03	1.26	1.45	917.11	46.76	400.49	4.3	4.33	93.22
46	12000	2500	5000	1	0.3	53.06	--	--	49.57	1256.16	1.14	1.34	1106.15	44.99	410.46	3.88	3.88	105.87
47	8000	5000	5000	1	0.3	59.31	--	--	58.56	1254.78	1.13	1.65	1105.81	52.05	402.69	3.66	3.66	110.01
48	12000	5000	5000	1	0.5	105.34	--	--	89.44	850.68	1.2	1.63	706.96	101.57	474.35	4.87	4.87	97.31

Figure J-3: Measurements from the fractional factorial design of experiments for all three specimen geometries.

APPENDIX K. EFFECT OF HEAT INPUT ON WELD LINE FORMATION AND PTMAZ LOCAL STRENGTH

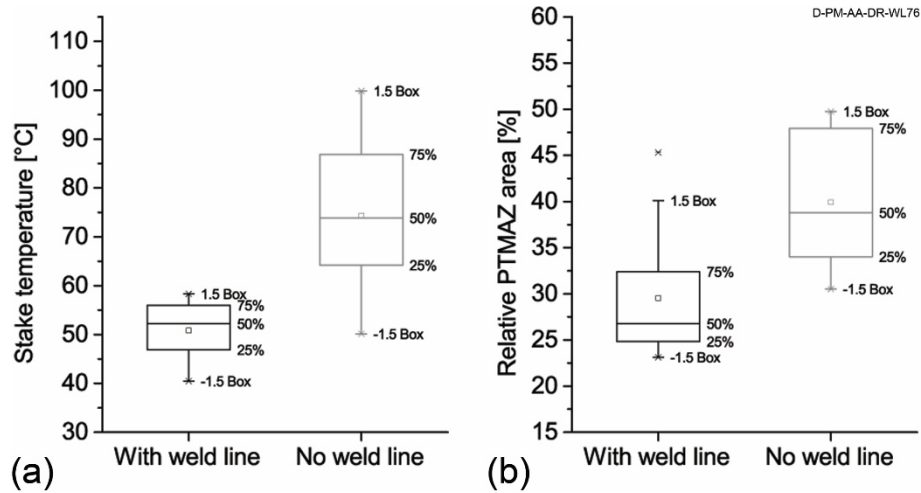


Figure K-1: Descriptive statistics of weld line formation: (a) presence of weld line depending on temperature; (b) presence of weld line depending on relative PTMAZ area.

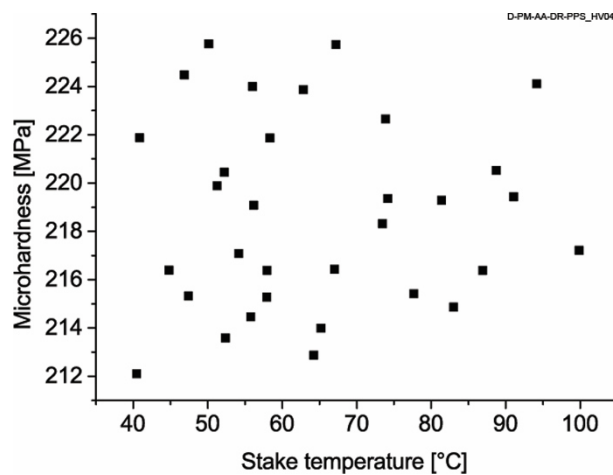


Figure K-2: Correlation of microhardness of the PTMAZ with stake temperature.

APPENDIX L. VALIDITY OF MICROSTRUCTURAL OBSERVATIONS FOR MECHANICAL TESTING SPECIMENS

Figure L-1 shows the stake temperature measurements for the three specimen geometries. No significant difference is seen between geometries; therefore microstructural observations from microstructural analysis (MA) specimens are assumed to occur in the lap shear (LS) and cross tensile (CT) specimens with the same processing conditions.

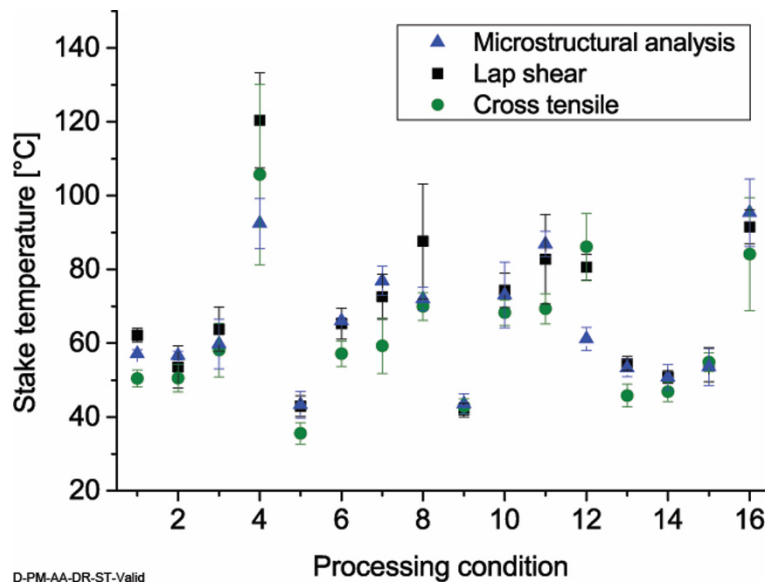


Figure L-1: Differences in stake temperature measurements for the three specimen geometries used in this work.

In Section 10.2 the effect of relative pore area RA_{pore} on mechanical properties was not explored, since the porosities are included in the PTMAZ. The significance of the influence of porosities in mechanical performance is the same of the PTMAZ, in general due to the same effects of stress concentration and/or facilitating crack growth. The only exception is the stiffness at CT specimens, which is significantly affected by the PTMAZ area but not by porosities. Since the stiffness in CT depends only on bending moments in the base plate, the porosities are not expected to affect it.

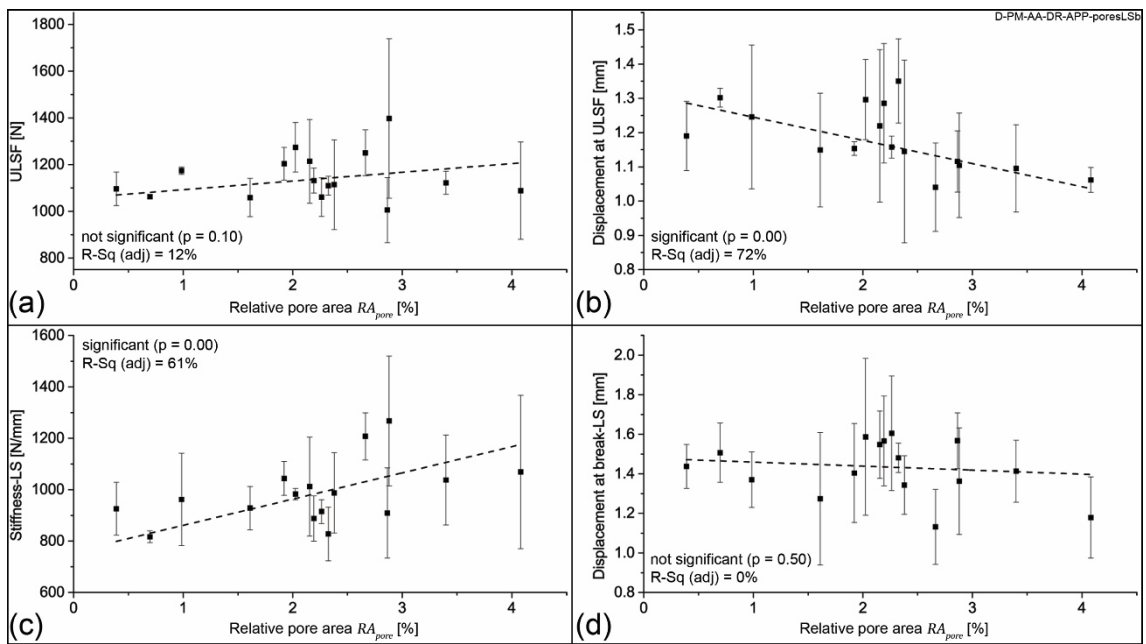


Figure L-2: Effect of relative pore area RA_{pore} on properties of LS joints.

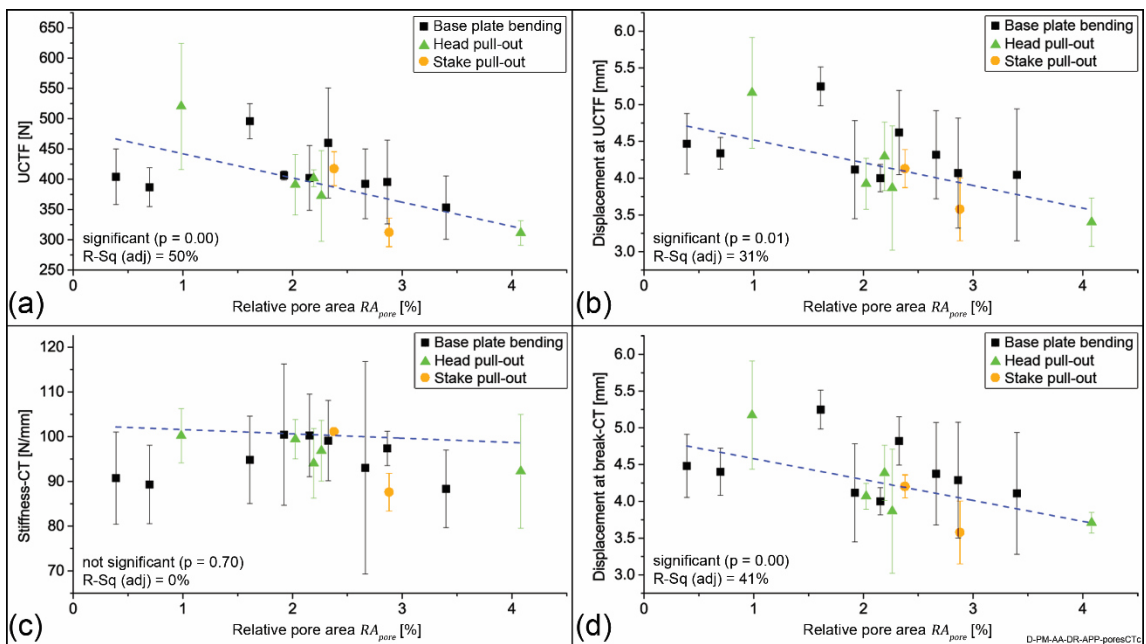


Figure L-3: Effect of relative pore area RA_{pore} on properties of CT joints.

APPENDIX M. REDUCED REGRESSION MODELS FROM THE FF-DOE AND MODEL VALIDATION TABLES

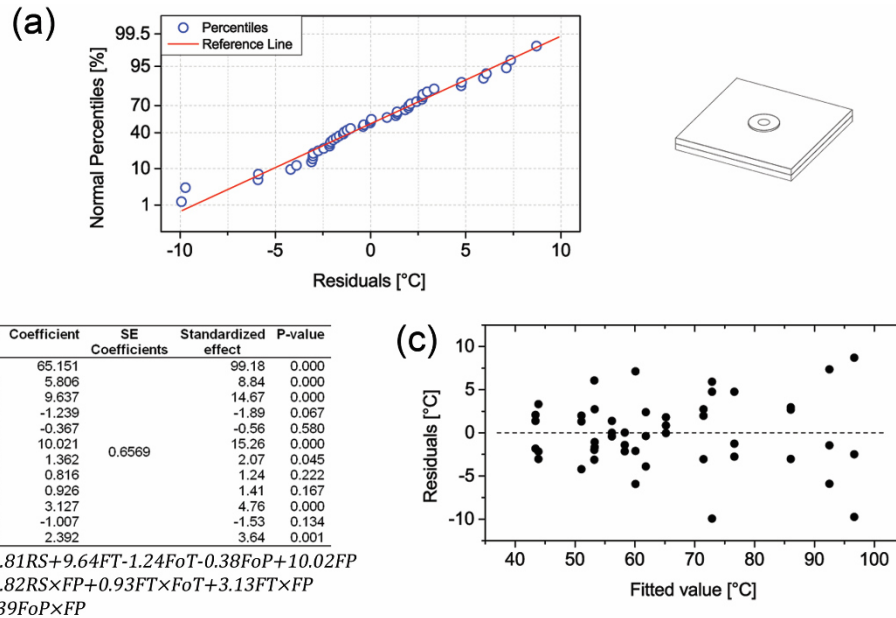


Figure M-1: Stake temperature (ST) statistical model: (a) Normal probability plot; (b) effects, coefficients, and significance of predictors; (c) plot of residuals versus fitted values.

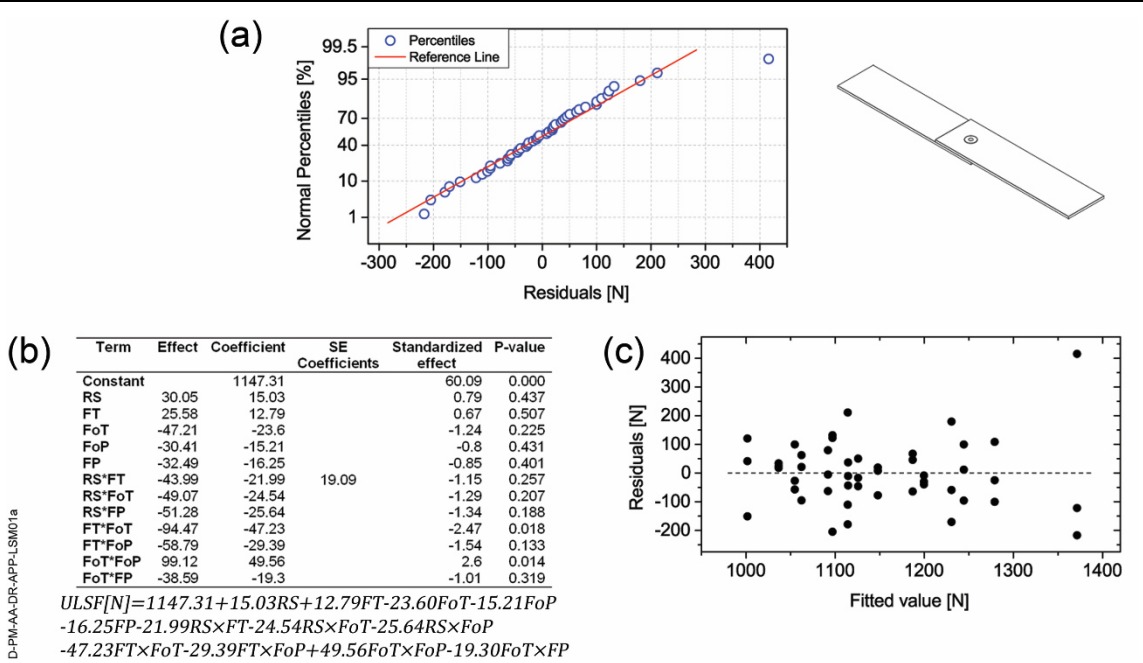


Figure M-2: Ultimate lap shear force (ULSF) statistical model: (a) Normal probability plot; (b) effects, coefficients, and significance of predictors; (c) plot of residuals versus fitted values.

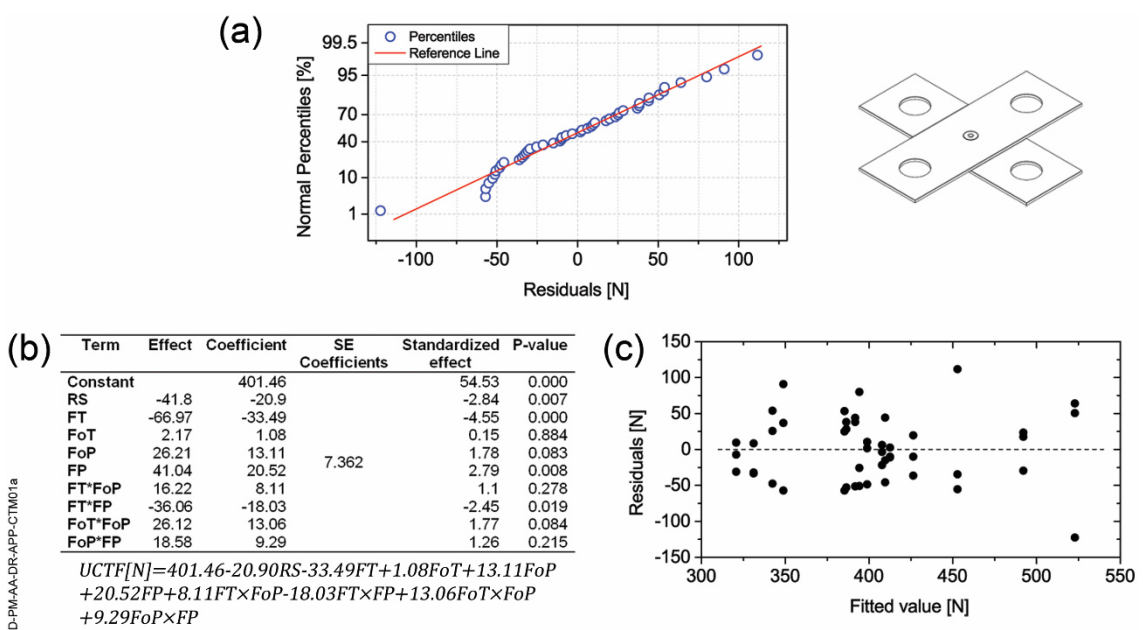


Figure M-3: Ultimate cross tensile force (UCTF) statistical model: (a) Normal probability plot; (b) effects, coefficients, and significance of predictors; (c) plot of residuals versus fitted values.

Table M-1: Validation experiments for the ST model (three replicates).

Condition	RS [rpm]	FT [ms]	FoT [ms]	FP [MPa]	FoP [MPa]	Predicted ST [°C]	Actual ST [°C]
ST-A	11000	3000	3000	0.3	0.7	56.6	50.1±0.9
ST-B	9000	5000	3000	0.3	0.8	60.0	57.5±1.9
ST-C	11500	4000	4000	0.4	0.9	71.3	79.8±2.4
ST-D	8500	2750	5000	0.35	0.75	48.2	47.6±2.1
ST-E	10000	5000	4000	0.5	0.8	87.0	87.6±0.8

Table M-2: Validation experiments for the ULSF model (five replicates).

Condition	RS [rpm]	FT [ms]	FoT [ms]	FP [MPa]	FoP [MPa]	Predicted ULSF [N]	Actual ULSF [N]
LS-A	11000	3000	3000	0.3	0.7	1203	1113±98
LS-B	9000	5000	3000	0.3	0.8	1223	1154±132
LS-C	11500	4000	4000	0.4	0.9	1137	1145±224
LS-CP	10000	3750	3750	0.4	0.85	1147	997±135
LS-6	6000	5000	500	0.2	1.0	1123	1157±55
LS-10	6000	5000	500	0.2	1.0	1131	1243±73
LS-15	6000	5000	500	0.2	1.0	1123	1103±57
LS-16	6000	5000	500	0.2	1.0	1262	1236±54

Table M-3: Validation experiments for the UCTF model (five replicates).

Condition	RS [rpm]	FT [ms]	FoT [ms]	FP [MPa]	FoP [MPa]	Predicted UCTF [N]	Actual UCTF [N]
CT-A	11000	3000	3000	0.3	0.7	388	463±82
CT-B	9000	5000	3000	0.3	0.8	374	449±43
CT-C	11500	4000	4000	0.4	0.9	385	416±77
CT-D	11500	5000	3000	0.35	0.7	342	393±35
CT-E	8000	3000	4000	0.45	0.8	453	416±59
CT-CP	10000	3750	3750	0.4	0.85	401	504±63

APPENDIX N. MICROSTRUCTURE AND LOCAL MECHANICAL PROPERTIES OF OPTIMIZED JOINTS PRODUCED AT THE RSM400

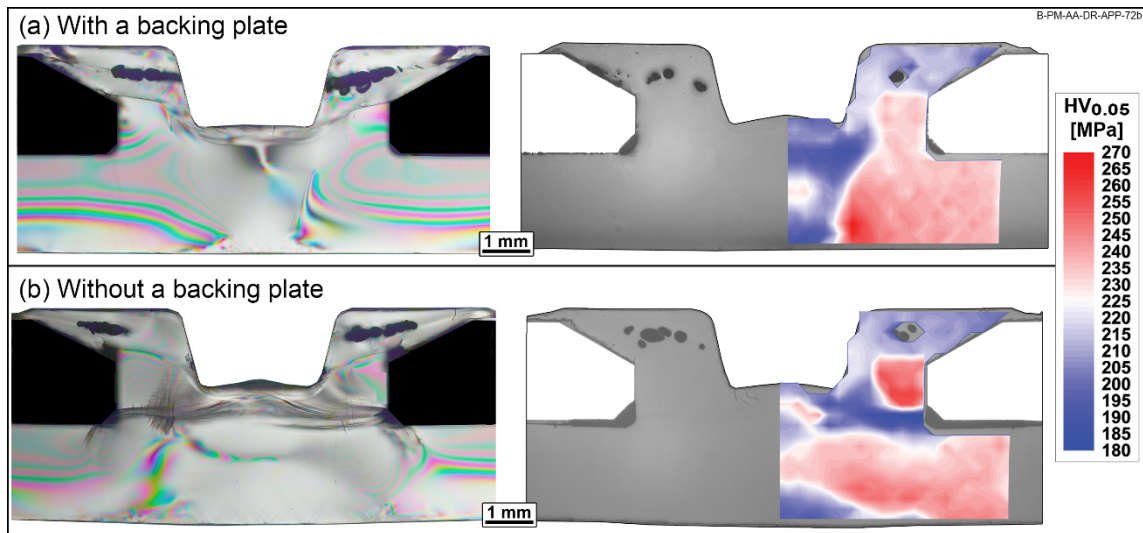


Figure N-1: Microstructure and local mechanical properties of optimized joints produced at the RSM400 (a) with a backing plate; and (b) without a backing plate. The absence of a backing plate creates a stake-shaft shearing (SSS) defect, as described in Section 8.4.3. Processing condition from Table 11-1.

APPENDIX O. TORQUE AND ENERGY INPUT RESPONSES AT THE RSM400 AND RNA GANTRY

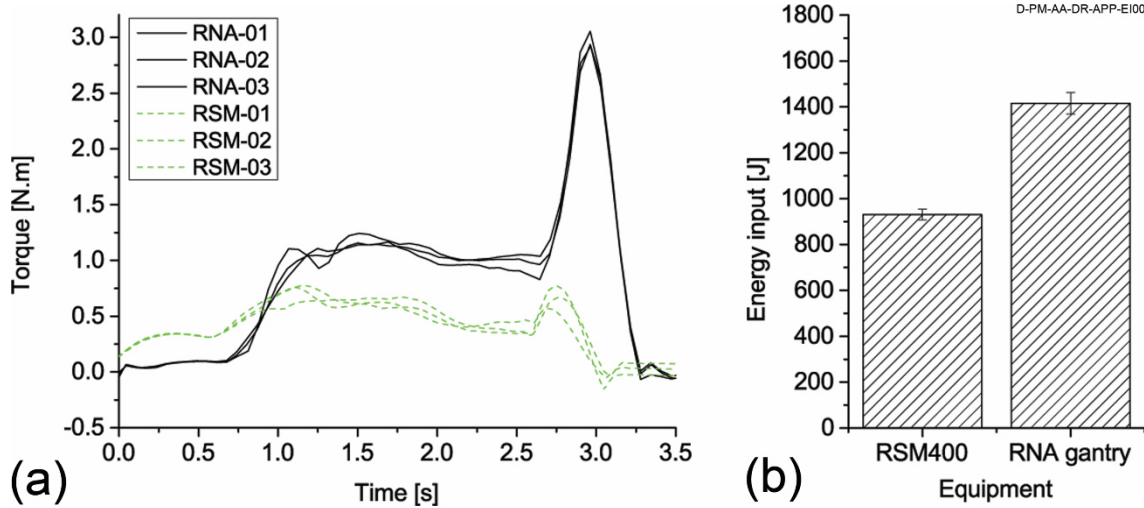


Figure O-1: (a) Difference in torque response at both equipments. The torque curves correspond to the matching curves of each equipment from Figure 11-2; (b) energy input at each equipment. The differences are a result of the hardware dissimilarities explained in Section 11.2.

APPENDIX P. IMPROVED TOOL DESIGN FOR F-ICJ

In order to avoid rubbing of the tool's clamping surface on the partner material, a clamping ring can be used which rotates independently from the frictional surfaces. A schematic concept of such a design can be seen in Figure P-1. A spring is attached to a ball bearing around the tool, and at other end of the spring a clamping ring is attached. The clamping ring is preferably of a low-friction-coefficient material such as polytetrafluoroethylene (PTFE).

The design may allow the joint to be created without loss of material, and with the softened shear layer hydrostatically holding the downward movement of the frictional surfaces. Moreover it may allow both time- and displacement-controlled processes.

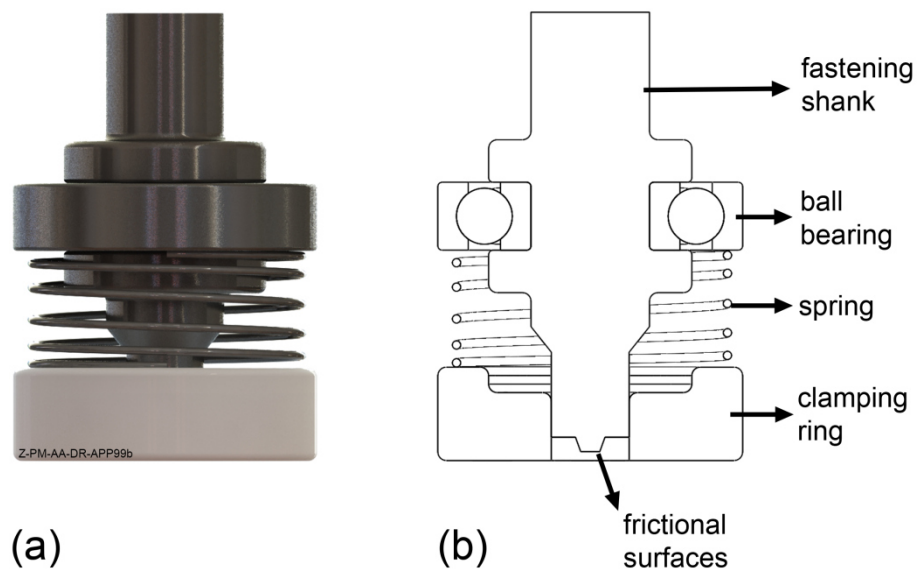


Figure P-1: Improved tool design for F-ICJ: (a) external overview; (b) cross-sectional view.

List of publications

Journal papers

Abibe A.B., Sônego M., dos Santos J.F. ; Canto L.B. ; Amancio-Filho S.T. On the feasibility of a friction-based staking joining method for polymer-metal hybrid structures. *Materials and Design*, 2016. Vol. 92: p. 632-642.

Patents

Abibe A.B., Amancio-Filho S.T., Sônego M., dos Santos J.F. Patent application EP14182938.2: A method for joining a plastic workpiece to a further workpiece. 2014.

Book chapters

Abibe A.B., Amancio-Filho S.T. Staking of polymer-metal hybrid structures, in *Joining of Polymer-Metal Hybrid Structures - Principles, Applications and Recent Developments*, Amancio-Filho S.T. and dos Santos J.F., Editors. Wiley Blackwell (To be published).

Amancio-Filho, S.T., Abibe, A.B., and Dos Santos, J.F., *Joining: Mechanical Fastening of Polymers, Composites, and Polymer-Metal Hybrid Structures*, in *Wiley Encyclopedia of Composites*, Nicolais L. and Borzacchiello A., Editors. 2012, John Wiley & Sons, Inc.

Conference proceedings

Amancio-Filho S.T., Abibe A.B., dos Santos J.F. Welding and joining of composites and composite-metal structures by frictional heating. In: 19. Nationales Symposium SAMPE Deutschland e.V. - Faserverbundwerkstoffe in der Energiewende, 2013, Hamburg. 19. Nationales Symposium SAMPE Deutschland e.V.. Hamburg: TuTech Verlag, 2013. v. 18. p. 65-67.

Conference papers

Sônego M., Abibe A.B., dos Santos J.F., Canto L.B., Amancio-Filho S.T. Chemical Changes in Polyetherimide (PEI) Joined by Friction-based Injection Clinching Joining (F-ICJ) Technique, in *Polymer Processing Society Conference*. 2015: Graz, Austria.

Sônego M., Abibe A.B., dos Santos J.F., Canto L.B., Amancio-Filho S.T. Friction-based Injection Clinching Joining (F-ICJ) of polyetherimide (PEI) and aluminum hybrid structures, in *2º Encontro de Ciência e Engenharia de Materiais de São Carlos: Transporte, Sustentabilidade e Inovação (ECEM-SanCas)*. 2014: São Carlos, Brazil.

Paz G., Blaga L., Goushegir S.M., Abibe A.B., dos Santos J.F., Mazzaferro J.A.E., Amancio-Filho S.T. Numerical simulation of the mechanical behavior of polymer-metal joints, in *21º Congresso Brasileiro de Ciência e Engenharia de Materiais*. 2014: Cuiabá, Brazil.

Sônego M., Abibe A.B., dos Santos J.F., Canto L.B., Amancio-Filho S.T. Friction-based Injection Clinching Joining (F-ICJ) of glass-fiber-reinforced PA66 and aluminum hybrid structures, in *21º Congresso Brasileiro de Ciência e Engenharia de Materiais*. 2014: Cuiabá, Brazil.

Abibe A.B., Sônego M., Amancio-Filho S.T., dos Santos J.F. Friction-based Injection Clinching Joining of plastics to metals, in *IIW Annual Assembly*. 2013: Essen, Germany.

Acknowledgments

Several people supported the successful completion of this PhD work in different ways. To them, I express here my appreciation for all the help and encouragement:

- Prof. Dr.-Ing. Sergio Amancio for the full and constant support of this research, for his trust in my abilities, and last but not least, for the friendship
 - Dr. Jorge dos Santos for providing the outstanding structure which was essential to achieve the goals of this PhD, and for his friendship
 - Prof. Dr.-Ing. Norbert Huber and Stephanie Koch for the management support within the institute
 - Prof. Dr.-Ing. Volker Schöppner for accepting to review this PhD work and contributing to its quality
 - All colleagues from the Solid State Joining department, for technical assistance, helpful discussions, and friendship. I would specially like to mention Peer-Jorge Scupin for the long life discussions, Jan Carstensen for the great times and German culture introduction, Stefanie Hanke for the cheerful company and linguistic assistance, and Menno Peters for unconditional support and for setting an example
 - Dagmar Koschek for the friendship, joyful attitude, and exceptional support in all issues
 - The colleagues from the Advanced Polymer-Metal Hybrid Structures Group for the friendship, teamwork, learning, and mutual support. I would like to specially thank my great friends Seyed Goushegir, Lucian Blaga, and Wiebke Junior, who were by my side since the start
 - Many thanks to Marília Sônego, Guilherme Paz, Laura Hsia, Madeleine Schütz and Eduardo Tschoepke for the cooperation in parts of this work and for helping me to improve myself as a tutor
 - To several HZG colleagues, among them Kay Erdmann and Jürgen Knaack for the assistance with subcomponent mechanical testing; Thomas Emmler for fruitful discussions of the polymeric material; Prof. Dr. Erica Lilleodden for helpful discussions of indentation testing; Dr. Jörg Hammel and Dr. Felix Beckmann for the μ CT measurements and related discussions
 - All my good friends from Brazil for the moral support and encouragement
 - All my family for the constant support and love
 - Natascha for the love, the contagious smile, the mutual learning, and inspiring me to do my best all this time
 - My parents Lahis and Osvaldo for the love and education, and Samira and Rebeca for the love, laughs, and mutual growth. All of you for the constant belief in me and my life path
 - Amora and Atena for keeping me cheerful during times of need
-